

Computational and experimental investigation of fluid-structure interaction with applications in energy harvesting and thermal augmentation

Submitted in partial fulfillment of the requirements

for the degree of

Doctor of Philosophy

of the

Indian Institute of Technology, Bombay, India

and

Monash University, Australia

by

Atul Kumar Soti

Supervisors:

Prof. Rajneesh Bhardwaj (IIT Bombay)

Prof. Mark C. Thompson (Monash University)



*The course of study for this award was developed jointly by
the Indian Institute of Technology, Bombay and Monash University, Australia
and given academic recognition by each of them.*

The programme was administered by The IITB-Monash Research Academy.

December 2017

Declaration

I declare that this written submission represents my ideas in my own words and where others' ideas or words have been included, I have adequately cited and referenced the original sources. I also declare that I have adhered to all principles of academic honesty and integrity and have not misrepresented or fabricated or falsified any idea/data/fact/source in my submission. I understand that any violation of the above will be cause for disciplinary action by the Institute and can also evoke penal action from the sources which have thus not been properly cited or from whom proper permission has not been taken when needed.

Notice 1

Under the Copyright Act 1968, this thesis must be used only under the normal conditions of scholarly fair dealing. In particular no results or conclusions should be extracted from it, nor should it be copied or closely paraphrased in whole or in part without the written consent of the author. Proper written acknowledgement should be made for any assistance obtained from this thesis.

Notice 2

I certify that I have made all reasonable efforts to secure copyright permissions for third-party content included in this thesis and have not knowingly added copyright content to my work without the owner's permission.



Student Name: Atul Kumar Soti



Acknowledgements

I would like to take this opportunity to express my sincere gratitude, towards my guides Prof. Rajneesh Bhardwaj and Prof. Mark Thompson for providing me this opportunity for working with them. It has been a great learning experience. I am also thankful to Prof. Atul Sharma, Prof Amit Agrawal and Prof John Sheridan for their time and suggestions which has enhanced my work and its presentation. I am thankful to all my teachers who have made me capable of reaching upto this point in life.

Abstract

Fluid-solid interaction (FSI) is studied for its applications in renewable energy and heat transfer enhancement. Specifically, two classes of FSI problems were investigated: vortex-induced vibration (VIV) was studied through numerical simulations using a spectral-element solver and through experiments performed in a water channel, and flow-induced deformation (FID) was studied through numerical simulations using a sharp-interface immersed boundary solver. VIV of a circular cylinder was studied numerically for flow energy extraction using an electromagnetic generator. The flow extraction study was extended for high Reynolds number situation by performing experiments on damper vortex-induced vibration of a circular cylinder. To improve the flow power extraction efficiency, VIV of a non-circular geometry is studied. Experiments were performed on flow-induced vibration (FIV) of a thin plate, and numerical simulations were done for the same at low Reynolds number. The work is extended using numerical simulations to account for the effect of aspect ratio of the plate on FIV response and extracted power. Heat transfer enhancement was demonstrated in a channel flow problem using FID of a flexible plate attached to the lee side of a circular cylinder. In another study, a flexible plate attached to the wall of a channel with pulsating inflow was used for heat transfer enhancement. The flexible plate attached to the cylinder was also considered for flow energy extraction capability. Apart from the FSI studies, the sharp interface immersed boundary method based FSI solver was improved for faster convergence and robustness using the Aitken's method for accelerating the fixed point iteration of the partitioned approach for the coupled solution of the flow and structure equations. Post-processing scripts were written for the energy equation solution module of the solver, and the module was validated against several benchmark problems of heat transfer.

For the first time, generation of electrical power from VIV of a cylinder using a realistic electromagnetic generator was investigated numerically. Numerical simulations were done for VIV of a circular cylinder for electricity generation using an electromagnetic electrical generator. The electrical generator consisted of a permanent magnet fixed to the cylinder and stationary conducting coil. In previous studies, the energy extraction process was modelled as a damper with constant damping ratio. The electromagnetic electrical generator, on the other hand, was modelled as a damper with spatially varying

damping ratio. The effects of the coil dimension(radius and length) and the mass ratio on the electrical power were quantified. An optimal damping ratio was found for both constant and variable damping cases for extracting maximum power. Surprisingly, the average extracted power was found to be independent of nature of damping although the temporal variations of power and displacement were very different for the two cases. The maximum power extraction efficiency was found to be an increasing function of Reynolds number and was equal to 13% at $Re = 150$. The length and radius of the coil were not found to affect the maximum average power. The possibility of using two coils positioned symmetrically about the center of the transverse direction was also examined. Mathematically, it was equivalent to changing the profile of the electromagnetic damping. Different damping profiles gave a different temporal variation of power but, surprisingly, the maximum average power was found to be independent of the nature of damping. One key advantage of the electromagnetic damping over constant damping was its better system quality which measures the insensitivity of power output to choosing the optimal system damping.

Experiments were also performed on the VIV of the circular cylinder, in the water channel facility at Monash university, to assess the power extraction at high Reynolds number. An eddy-current-based damping mechanism was constructed to provide controlled and adjustable damping values. The damper consisted of permanent magnet connected to the cylinder which moved parallel to a copper plate at some predetermined gap. The damper provided a spatially invariant damping ratio that was varied by changing the gap between the magnet and the copper plate of the damper. The increase in damping was found to reduce the range of reduced velocity for upper and lower branches and thereby the synchronization region shrinks with increasing damping. The peak amplitude data, obtained by varying the damping and keeping the Reynolds number fixed, shows a smooth variation with mass-damping. Three sets of experiments with different Reynolds number ranges were conducted to account for the Reynolds number effects. The experiments agree with the previous finding that the scatter in previously reported Griffin plots is due to the Reynolds number variation. An exponential fitting function is proposed that fits the peak amplitude data with excellent accuracy and shows a monotonic decay of peak amplitude at higher mass-damping. The extracted power is found to increase with Reynolds number.

The flow-induced vibration of an elastically mounted thin plate with aspect ratio equal to 12.0 was investigated using experiments at higher Reynolds number and numerical simulations for low Reynolds number. The vibration response of the plate differs from that of a circular cylinder. Although the plate vibration response has three branches, the three branches do not share the characteristics of the three response branches observed in the case of a circular cylinder. In first two branches, the vibration amplitude of the

plate increases linearly with the reduced velocity. The two branches differ in the slope of the linear functions. The vortex shedding frequency is locked-in with the natural frequency of the plate. The maximum vibration amplitude of the plate is $1.99D$ observed at the end of the second branch. The plate vibration amplitude is periodic in the two branches meaning it does not change significantly from one cycle to another. The third branch shows a decrease in the vibration amplitude with increasing reduced velocity. The vibration amplitude loses its periodicity in the third branch, and becomes intermittent in the later part of the branch. The plate motion becomes desynchronized with the flow at the end of the third branch and the vibration amplitude becomes small. The vortex shedding mode observed in the first and second branches are C(2S) and C(2S) + 2S, respectively. The simulations show a remarkable similarities to the experimental results.

A larger vibration amplitude is desired for better power extraction. For this purpose, VIV of thin flat plates with aspect ratio less than and equal to 0.4 is also studied numerically. Only larger aspect ratios were studied in the literature. The vibration amplitude of the plate is found to increase with decreasing aspect ratio. The 2S vortex shedding phase is observed in the initial branch and 2T mode is observed for upper and lower branches. An optimal aspect ratio of 0.2 was found for maximum power extraction. The maximum extraction efficiency was 19% which is close to 46% larger as compared to circular cylinder.

FID is studied numerically for both energy extraction and heat transfer enhancement applications. FID of a flexible plate attached to lee side of circular cylinder was used for enhancing heat transfer in a laminar channel flow. For the first time, FID of flexible structures was demonstrated as a passive means for heat transfer enhancement. The FID of a flexible plate attached to the wall of channel due to a incoming pulsating flow was also analyzed for heat transfer application. An optimal channel height was found for maximizing heat transfer with the flexible plate. The cylinder with the flexible plate is also studied from energy extraction point of view. In this case, the plate is kept at some distance from the cylinder and the whole system is kept in open domain. The plate deformation as a function of distant, plate natural frequency and bending stiffness is reported. The strain and kinetic energy of the plate was also calculated. An optimal gap exists for maximum plate deformation and total energy of the plate. There is also an optimal bending stiffness for maximum strain energy.

Contents

1	Introduction	1
1.1	Objectives	4
1.2	Organization of the Thesis	4
2	Numerical Methods	7
2.1	Continuous forcing immersed boundary method	9
2.2	Flow-induced deformation solver	11
2.2.1	Ghost-Cell based sharp interface immersed boundary method (IBM)	11
2.2.2	Heat transfer modeling	17
2.2.3	Structural solver	20
2.2.4	Fluid and structural solvers coupling	21
2.2.5	Accelerating FSI convergence	21
2.2.6	IBM based vortex-induced vibration solver	24
2.3	Flow-induced vibration solver	27
2.3.1	The spectral-element method	27
2.3.2	Flow simulation using the spectral-element method	31
3	Experimental Methodology	35
3.1	Water channel	35
3.2	Vortex-induced vibration setup	37
3.3	Damper system	37
3.4	Flow visualization	40
4	Harnessing Electrical Power from Vortex-Induced Vibration of a Circular Cylinder	43
4.1	Introduction	44
4.2	Problem definition and methodology	46
4.2.1	Governing equations	46
4.2.2	Numerical formulation	48
4.2.3	Computational domain and boundary conditions	49

4.2.4	Resolution studies and validation	49
4.3	Results	50
4.3.1	Constant versus EM damping ratio	50
4.3.2	Effect of coil length	54
4.3.3	Effect of coil radius	56
4.3.4	Effect of mass ratio	56
4.3.5	Effect of the Reynolds number	56
4.3.6	Using two coils	58
4.4	Closure	59
5	Damping effects on vortex-induced vibration of a circular cylinder and implications for power extraction	63
5.1	Introduction	64
5.2	Experimental method	66
5.2.1	VIV Experimental apparatus	66
5.2.2	Damper mechanism	67
5.2.3	Damping measurements	69
5.2.4	Experimental validation	70
5.3	Results	71
5.3.1	Effect of damping on the vibration response	71
5.3.2	Effect of damping on oscillation frequency	73
5.3.3	Effect of damping on lift force and phase	77
5.3.4	The Griffin plot	78
5.3.5	Power extraction	82
5.4	Closure	84
6	Vortex-induced vibrations of a thin plate	87
6.1	Introduction	88
6.2	Experimental method	90
6.2.1	Experimental apparatus	90
6.3	Numerical method	92
6.3.1	Solution Method	92
6.3.2	Computational domain and boundary conditions	94
6.4	Results	94
6.4.1	Response at a higher Reynolds number	94
6.4.2	Wake structures at higher Reynolds number	100
6.4.3	Numerical results	103
6.4.4	Wake structures at low Reynolds number	106
6.5	Closure	109

7	Vortex-induced vibration of thin plates: effect of aspect ratio and power extraction	113
7.1	Introduction	113
7.2	Problem definition and methodology	114
7.2.1	Governing equations	114
7.2.2	Computational domain and boundary conditions	116
7.2.3	Resolution studies and validation	116
7.3	Results	118
7.3.1	Stationary plates	118
7.3.2	Undamped response	118
7.3.3	Wake structure	121
7.3.4	Power extraction	129
7.4	Closure	130
8	Heat transfer enhancement using flow-induced deformation	135
8.1	Introduction	135
8.2	Computational model	137
8.3	Code validation	140
8.3.1	Large-scale flow-induced deformation	140
8.3.2	Conduction heat transfer	141
8.3.3	Convective heat transfer without bluff body	143
8.3.4	Convective heat transfer with stationary immersed boundary	145
8.3.5	Convective heat transfer with moving immersed boundary	145
8.4	Results and discussion	147
8.4.1	Enhanced mixing of the fluid due to FSI	148
8.4.2	Thermal augmentation due to FSI	149
8.4.3	Quantification of augmentation in heat transfer	150
8.4.4	Effect of Prandtl number	156
8.4.5	Effect of Reynolds number	156
8.4.6	Effect of Youngs modulus	157
8.4.7	Effect of channel length	157
8.5	Closure	157
9	Convective Heat Transfer Augmentation by a Fin-like Thin, Elastic Plate in a Laminar Channel Flow	159
9.1	Introduction	159
9.2	Computational model	161
9.3	Simulation Setup	162
9.4	Domain and Grid Size Independence Study	163

9.5	Results and Discussion	163
9.5.1	Mechanism of Thermal Augmentation in a Baseline Case	164
9.5.2	Effect of Plate Rigidity	168
9.5.3	Effect of Channel Height	168
9.5.4	Effect of Reynolds Number	171
9.6	Closure	173
10	Energy transfer to a flexible plate kept behind a circular cylinder	175
10.1	Introduction	175
10.2	Problem Definition and methodology	176
10.3	Results and Discussion	179
10.3.1	Effect on Drag	179
10.3.2	Energy transfer	181
10.4	Closure	182
11	Conclusions and future work	185
11.1	Conclusions	185
11.2	Future work	187

List of Figures

1.1	(a) vortex structures of a modeled hummingbird in hovering flight (Luo et al., 2012) and (b) Sedimentation of two particles (Favier et al., 2014).	2
1.2	(left) Typical human vocal tract system and (right) instantaneous vorticity contours inside the vocal tract (Seo and Mittal, 2011a).	2
1.3	(a) VIVACE (Vortex Induced Vibration Aquatic Clean Energy) (Lee and Bernitsas, 2011) and (b) a piezoelectric beam (top) kept behind a circular cylinder (Akaydin et al., 2010) and (bottom) flow visualization.	3
1.4	Park et al. (2013) used a flexible wing mounted on a heated surface in a pulsating flow (left) to improvement the heat transfer as evident from the Nusselt number (right).	4
2.1	An elastic membrane immersed in a Cartesian Mesh.	9
2.2	Approximate delta functions.	11
2.3	A representative cell.	13
2.4	Immersed boundary and labelling of computational cells (taken from (Mittal et al., 2008)).	14
2.5	Procedure for labelling the computational cells (taken from (Mittal et al., 2008)).	15
2.6	Moving IB and fresh cells treatment (taken from Mittal et al. (2008)).	17
2.7	A one dimensional Cartesian grid.	18
2.8	Implementation of boundary condition on the outer boundaries.	18
2.9	Finding temperature gradients al boundaries.	19
2.10	Flow chart of the implicit coupling.	22
2.11	y -displacement of flag tip in cylinder-flag FSI problem.	23
2.12	FSI residual variation of acceleration component in y -direction with number of iterations.	23
2.13	Comparison of maximum displacement amplitude of the undamped cylinder undergoing transverse VIV with $m = 8/\pi$ at $Re = 150$ with the published data.	26

2.14	Comparison of lift and drag coefficients of the undamped cylinder undergoing two-degree of freedom VIV with $m = 8/\pi$, $f_{nx}/f_{ny} = 2.0$ and $U_r = 4.0$ at $Re = 150$	26
2.15	1D domain and its discretization for the spectral-element method.	28
3.1	A schematic view of the water channel.	36
3.2	(a)The inlet of the water channel and (b) test section and diffuser.	36
3.3	The setup used for the VIV experiments.	38
3.4	(a) Various components of the damper system and (b) damper attached to the VIV setup.	39
3.5	The particle image velocimetry setup used for flow visualization.	41
4.1	The cylinder-magnet assembly moving along the axis of the conducting coil.	47
4.2	Computational domain for VIV of a circular cylinder.	48
4.3	a) Comparison of the cylinder response with the published data and b) effect of spectral element resolution on the cylinder displacement.	50
4.4	Top: Temporal variation of power, position and velocity of the cylinder for (a) CD ($\xi = 0.14$) and (b) EMD ($\xi_{m0} = 2.4 \times 10^{-5}$, $a = 0.6$, $L = 0.6$) cases, at $U_r = 5.2$ and $m = 2$. Vorticity contours (scale -2 to 2) corresponding to these cases are shown below each plot.	51
4.5	FFT of the cylinder displacement and power output (shown in fig. 4.4) for the CD (left) and EMD cases (right).	52
4.6	Variation of the average power (a) with ξ for CD and (b) with ξ_{m0} for EMD ($a = 0.6$, $L = 0.6$) cases, for $U_r = 5.2$ and $m = 2$	53
4.7	(a) Average power and (b) velocity amplitude versus displacement amplitude of the cylinder for CD and EMD cases at $U_r = 5.2$, $m = 2$ and $Re = 150$	53
4.8	Maximum average power versus U_r for CD and EMD cases at $m = 2$ and $Re = 150$	53
4.9	Effect of coil length on (a) average power and (b) displacement amplitude at $U_r = 5.2$, $m = 2$ and $a = 0.6$	55
4.10	Effect of coil length on EM damping ratio (a) $a = 0.6$, $L = 0.1$ and (b) $a = 0.6$, $L = 1.0$	55
4.11	Effect of coil radius on (a) average power and (b) displacement amplitude at $U_r = 5.2$, $m = 2$ and $L = 0.6$	57
4.12	Effect of coil radius on EM damping ratio (a) $a = 0.6$, $L = 0.6$ and (b) $a = 1.0$, $L = 0.6$	57
4.13	Maximum average power versus U_r for different mass ratios.	57

4.14	Effect of Re on average power and displacement amplitude for $m = 2$, $a = 0.6$ and $L = 1.0$	58
4.15	Variation of ξ_m with y for the two coil case. They are plotted for optimal cases ($\xi_{m0} = 1 \times 10^{-5}$ and 6.8×10^{-6} for $y_c = 0.10$ and 0.39 , respectively).	59
4.16	Variation of power, position and velocity of the cylinder with time for (a) $y_c = 0.39$ at $\xi_{m0} = 6.8 \times 10^{-6}$ and (b) $y_c = 0.10$ at $\xi_{m0} = 1.0 \times 10^{-5}$ at $U_r = 5.2$, $m = 2$ and $Re = 150$ for two identical coils of $a = 0.6$ and $L = 0.6$	60
4.17	Variation of average power with ξ_{m0} for (a) $y_c = 0.39$ and (b) $y_c = 0.10$ at $U_r = 5.2$ and $m = 2$ for two identical coils of $a = 0.6$ and $L = 0.6$	60
5.1	Definition sketch for the transverse vortex-induced vibration of a circular cylinder. The hydro-elastic system is idealized as a 1-DOF system constrained to move in the cross-flow direction. Here, U is the free-stream velocity, k the spring constant, D the cylinder diameter, m the oscillating mass, and c the structural damping. F_x and F_y represent the drag and the transverse lift force components acting on the body, respectively.	66
5.2	Schematic of the experimental set-up used for the VIV experiments.	67
5.3	Schematic of the damper system.	68
5.4	Damping coefficient (c) as a function of the gap (G) between the magnet and the copper plate of the damper used in the present experiments.	69
5.5	Comparison of displacement amplitude obtained by our experiment with that of Khalak and Williamson (1997) ($m^* = 2.4$, $\zeta = 4.5 \times 10^{-3}$) and Zhao et al. (2014b) ($m^* = 2.66$, $\zeta = 3.2 \times 10^{-3}$)	70
5.6	Mean of top 10% maximum amplitude response versus reduced velocity for various values of damping ratios. The mass ratio is 3.0. Blue and red regions show the upper and lower branches, respectively.	72
5.7	Time histories of the non-dimensional cylinder displacement for $U^* =$ (a) 4.0, (b) 4.6, (c) 5.8 and (d) 8.0 for the minimal damping case. The plots illustrates the time-variation of the cylinder displacement for quasi-periodic, periodic, upper branch and lower branch regions, respectively.	73
5.8	Contours of power spectral density of displacement (left) and lift force (right) plotted against the normalised frequency and reduced velocity for $\zeta =$ (a) 0.002, (b) 0.028, (c) 0.074, (d) 0.124 and (e) 0.228. Each power spectrum is plotted vertically and stacked together horizontally from each U^* to form these contour plots. A \log_{10} scale is used to highlight the variation from 0 (black) to -3 (white). The line represent $St = 0.208$, corresponding to the vortex shedding frequency of a stationary cylinder.	74
5.9	(a) RMS lift coefficients, and (b) RMS vortex force coefficients versus reduced velocity for specified damping ratios.	75

5.10	Phase difference between (a) total lift and (b) vortex force and displacement versus reduced velocity for various values of damping ratios.	76
5.11	Comparison of quadratic polynomial fit (dashed line), fit proposed by Sarpkaya (1978) (dash-dot line) and (5.7) with $n = 2$ (solid line). The data points shown as circular symbols are taken from Govardhan and Williamson (2006).	78
5.12	Griffin plot (a) showing the comparison of our results for three Re ranges with the published data, and (b) collapse of all the data points onto a single curve by considering the effect of Reynolds number. The error bars represent the standard deviation in vibration amplitude from its mean value.	80
5.13	The average extracted power versus reduced velocity for various values of damping ratios.	82
5.14	The maximum average extracted power versus damping ratio for three Reynolds number ranges given in table 5.1.	84
6.1	A representative sketch for the vortex-induced vibration in the transverse direction of a thin plate of thickness d and width D . The free stream velocity of the fluid is U . The symbols k and c represent the spring constant and damping coefficients, respectively.	91
6.2	Schematic of the experimental set-up used for the VIV experiments.	92
6.3	Low damping response of a thin plate with aspect ratio $\alpha = 12$ with $m^* = 34.4$ and $\zeta = 1.33 \times 10^{-3}$. (a) vibration amplitude, (b) RMS lift coefficient and (c) phase difference between lift and displacement versus reduced velocity.	95
6.4	(a) Displacement and (b) lift frequency response of the thin plate at low damping.	97
6.5	Non-dimensional displacement of the plate versus non-dimensional time at $U^* =$ (a) 7.4 and (b) 8.0. Obtained from experiments.	98
6.6	Non-dimensional displacement (broken lines) and lift (solid lines) of the plate versus non-dimensional time at $U^* =$ (a) 2.0, (b) 4.4 and (c) 6.2. Obtained from experiments.	99
6.7	Snapshots of vorticity contours at four equispaced time instants in a cycle of oscillation of plate for $U^* = 2.0$. The plate is at its mean position at instant a . The vorticity scale is from -1(blue) to 1(red) with an increment of 0.2. Obtained from experiments.	100
6.8	Snapshots of vorticity contours at eight equispaced time instants in a cycle of oscillation of plate for $U^* = 4.4$. The plate is at its mean position at instant a . The vorticity scale is from -1(blue) to 1(red) with an increment of 0.2. Obtained from experiments.	101

6.9	Snapshots of vorticity contours at eight equispaced time instants in a cycle of oscillation of plate for $U^* = 6.2$. The plate is at its mean position at instant a . The vorticity scale is from -1(blue) to 1(red) with an increment of 0.2. Obtained from experiments.	102
6.10	Vibration amplitude of a thin plate with aspect ratio $\alpha = 12$ at $Re = 150$	103
6.11	Displacement of the plate versus time at $Re = 150$ and $U^* = 6.2$ for $m^* =$ (a) 34.4 and (b) 3.0.	104
6.12	RMS pressure, viscous and total lift forces on the plate for (a) $m^* = 34.4$ and (b) $m^* = 3.0$ at $Re = 150$	105
6.13	Mean phases of pressure, viscous and total lift forces on the plate for (a) $m^* = 34.4$ and (b) $m^* = 3.0$ at $Re = 150$	105
6.14	(a) Displacement and (b) lift frequency response of the thin plate at $Re =$ 150 and $m^* = 34.4$	107
6.15	(a) Displacement and (b) lift frequency response of the thin plate at $Re =$ 150 and $m^* = 3.0$	107
6.16	Vorticity contours at six time instants for the plate with $m^* = 34.4$ at $U^* =$ 2.6 and $Re = 150$. The time instants are shown by filled circular markers in figure 6.17a. The vorticity scale is from -1(blue) to 1(red).	108
6.17	(a) Temporal variation of the lift force on the thin plate with $m^* = 34.4$ at $Re = 150$ and $U^* = 2.6$ and (b) FFT of the lift force.	108
6.18	Vorticity contours at six equispaced time instants in a cycle of oscillation of the plate with $m^* = 34.4$ at $U^* = 5.8$ and $Re = 150$. The plate is at its mean position at instant a . The vorticity scale is from -1(blue) to 1(red).	109
6.19	Vorticity contours at six time instants, shown by filled circular markers in figure 6.20, for $U^* = 6.2$ and $Re = 150$. The vorticity scale is from -1(blue) to 1(red).	110
6.20	Temporal variation of the displacement of the thin plate with $m^* = 34.4$ at $Re = 150$ and $U^* = 6.2$	110
6.21	Temporal variation of the displacement of the thin plate with $m^* = 34.4$ at $Re = 150$ and $U^* = 6.2$	110
7.1	Computational domain for the transverse VIV of the plate.	116
7.2	Domain independence study.	117
7.3	Mesh independence study.	117
7.4	Vorticity contours for stationary plates with different thickness a) $\alpha = 0.05$ b) $\alpha = 0.1$, c) $\alpha = 0.2$, d) $\alpha = 0.3$ and e) $\alpha = 0.4$ at $Re = 150$. The vorticity level ranges between -2 (red) to 2 (blue).	118
7.5	(a) RMS drag and lift coefficients and (b) Strouhal number for stationary plates with different thickness at $Re = 150$	119

7.6	a) Displacement amplitude, b) rms lift coefficient, c) normalized vibration frequency and d) phase difference between lift force and displacement versus reduced velocity for various thickness values of the plate for $Re = 150$. . .	120
7.7	Transverse VIV response regions of the plate with $d = 0.4$ (IB - initial branch, UB- upper branch, LB - lower branch).	122
7.8	Variation of the lift coefficient(pressure and viscous) with the vibration amplitude for different plates.	123
7.9	Phase difference between pressure force and displacement of the plates for $Re = 150$	124
7.10	Contours of Amplitude spectral density of the lift coefficient for plate with $\alpha = 0.4$ at $Re = 150$ (IB - initial branch, UB- upper branch, LB - lower branch).	125
7.11	Top: Lift coefficient (solid lines) and displacement (broken lines); middle: FFT of displacement and lift force; bottom: Vorticity contours at the instances shown by dots for the plate with $\alpha = 0.4$ at $U_r = 3.0$ and $Re = 150$.	126
7.12	Top: Lift coefficient (solid lines) and displacement (broken lines); middle: FFT of displacement and lift force; bottom: Vorticity contours at the instances shown by dots for the plate with $\alpha = 0.4$ at $U_r = 6.2$ and $Re = 150$.	127
7.13	Top: Lift coefficient (solid lines) and displacement (broken lines); middle: FFT of displacement and lift force; bottom: Vorticity contours at the instances shown by dots for the plate with $\alpha = 0.4$ at $U_r = 7.5$ and $Re = 150$.	128
7.14	Contours of Amplitude spectral density of the lift coefficient for plate with $\alpha = 0.05$ at $Re = 150$ (IB - initial branch, UB- upper branch, LB - lower branch).	130
7.15	Top: Lift coefficient (solid lines) and displacement (broken lines); middle: FFT of displacement and lift force; bottom: Vorticity contours at the instances shown by dots for the plate with $\alpha = 0.05$ at $U_r = 5.4$ and $Re = 150$.	131
7.16	Vorticity contour for (a) $\alpha = 0.05$, (b) $\alpha = 0.1$, (c) $\alpha = 0.2$, (d) $\alpha = 0.3$ and (e) $\alpha = 0.4$ at $Re = 200$	132
7.17	(a) Average power versus damping ratio at $U_r = 5.8$ and (b) Average power versus reduced velocity at $\xi = 0.36$ for CD case for the plate with $\alpha = 0.2$ at $Re = 150$	133
7.18	maximum average power versus aspect ratio of the plate for different mass ratios at $Re = 150$	133

8.1	Schematic and boundary conditions (BC) of the FSI benchmark problem with heat transfer. The FSI benchmark was first proposed by Turek and Hron (2006) and later Bhardwaj and Mittal (2012) validated their FSI solver with the benchmark. In present work, coupled convective heat transfer is considered with insulated cylinder and plate in a heated channel. Adapted with permission from (Bhardwaj and Mittal, 2012). Copyright (2011) Professor Rajat Mittal.	141
8.2	Comparison between the present work and published results of Turek and Hron (2006) for the stationary-state time-variation of X and Y displacement of the tip of the plate. Adapted with permission from (Bhardwaj and Mittal, 2012). Copyright (2011) Professor Rajat Mittal.	142
8.3	Schematic of 1D conduction heat transfer in a slab with initial and boundary conditions (a) Comparisons of simulated time- and space-varying temperature in the slab for Peclet numbers, $Pe = 1$ (b), and $Pe = 4$ (c) with 1D analytical theory.	143
8.4	2D conduction heat transfer in a square block with boundary conditions shown in (a). Qualitative comparison of isotherms for $Pe = 1$ obtained using (a) MATLAB PDE Toolbox, and (b) the present numerical model. (c) Comparison of steady-state x -varying temperature at $y = 0.5$	144
8.5	Comparison of local Nusselt number along channel length with analytical theory. Two cases, constant wall temperature and constant wall flux are considered.	145
8.6	(a) Schematic and boundary conditions for flow past a heated and stationary cylinder. (b) Comparison of local Nusselt number for $Re = 120$, $Pr = 0.7$ as function of azimuthal angle (shown in inset) at the surface of the cylinder with published numerical and experimental results.	146
8.7	Comparison of local Nusselt number as function of azimuthal angle (shown in inset of fig. 8.6b) at the surface of a transversely oscillating cylinder with numerical results of Fu and Tong (2002) for $Re = 200$ and $Pr = 0.71$. Results are compared at different time instances, $t = \tau/4$ and $3\tau/4$, where τ is the time-period of the oscillation of the cylinder.	147
8.8	Vorticity contours in a channel with a cylinder attached to an elastic plate at different time instances for $Re = 100$. The time instances are shown in the inset as black dots on time-varying position of the tip of the plate during a typical cycle of the plate oscillation.	148

8.9	Isotherms in a channel with a cylinder attached to an elastic plate at different time instances for $Re = 100$ and $Pr = 1$. The time instances are shown in the inset of fig. 8.8 as black dots on time-varying position of the tip of the plate during a typical cycle of the plate oscillation.	150
8.10	Instantaneous Nusselt numbers at the bottom ($Nu_{bw}(x, t)$) and top ($Nu_{tw}(x, t)$) channel walls at different time instances, $Re = 100$, $Pr = 1$. The time instances are shown in the inset of fig. 8.8 as black dots on time-varying position of the tip of the plate during a typical cycle of the plate oscillation.	151
8.11	Variation of temperature in a channel with a cylinder attached to an elastic plate along y -axis at (a) $x = 8$ and (b) $x = 27$ for $Re = 100$, $Pr = 1$. The time instances are shown in the inset of fig. 8.8 as black dots on time-varying position of the tip of the plate during a typical cycle of the plate oscillation.	152
8.12	Vorticity contours obtained at $t = 80$, for configurations CHL, CYL, CRP and CDP, defined in table 8.1 at $Re = 100$	153
8.13	Isotherms obtained at $t = 80$, for configurations CHL, CYL, CRP and CDP, defined in table 8.1 at $Re = 100$, and $Pr = 1$	154
8.14	Time-averaged Nusselt number (Nu_{avg}) for $Re = 100$ and $Pr = 1$, for configurations CHL, CYL, CRP and CDP, defined in table 8.1.	154
8.15	(a) Time- and space-average Nusselt number, (b) Time-average pumping power, and (c) efficiency index for configurations CHL, CYL, CRP and CDP, defined in table 8.1. The Reynolds number, Prandtl number and Young Modulus of the plate are varied in separate cases keeping other two parameters as constant.	155
9.1	Computational domain and boundary conditions.	163
9.2	(a) Domain length independence and (b) Grid size independence study: Time variation of x and y coordinates of tip of the plate is plotted for one cycle of pulsation for different channel lengths and grid resolutions.	164
9.3	Time variation of x and y coordinates of the tip of the plate over a pulsation cycle for a channel height of $H = 3$ and $Re_H = 400$	165
9.4	Vorticity contours for channel height $H = 3$ and $Re_H = 400$ with A) an elastic and B) a rigid plate. Plots are shown at four equispaced times (P1-P4 from fig. 9.3) over a pulsation cycle.	166
9.5	Temperature contours for channel height $H = 3$ and $Re_H = 400$ with A) an elastic and B) a rigid plate. Plots are shown at four equispaced times over a pulsation cycle.	167

9.6	Instantaneous Nusselt number for channel height $H = 3$ and $Re_H = 400$ with A) an elastic and B) a rigid plate. Plots are shown at four equispaced times over a pulsation cycle.	167
9.7	Time-averaged Nusselt numbers for channel height $H = 3$ at $Re_H = 400$. Three cases are compared: (a) pulsating channel flow without a bluff body (CHL); (b) pulsating channel flow with a rigid plate (CRP); and (c) pulsating channel flow with a deformable plate (CDP).	168
9.8	Vorticity contours for channel height $H = 2$ and $Re_H = 400$ with A) an elastic and B) a rigid plate. Plots are shown at four equispaced times over a pulsation cycle.	169
9.9	Temperature contours for channel height $H = 2$ and $Re_H = 400$ with A) an elastic and B) a rigid plate. Plots are shown at four equispaced times over a pulsation cycle.	170
9.10	Instantaneous Nusselt number for channel height $H = 2$ and $Re_H = 400$ with A) an elastic and B) a rigid plate. Plots are shown at four equispaced times over a pulsation cycle.	170
9.11	Time-averaged Nusselt numbers for channel height $H = 2$ at $Re_H = 400$. Three cases are compared: (a) pulsating channel flow without a bluff body (CHL); (b) pulsating channel flow with a rigid plate (CRP); and (c) pulsating channel flow with a deformable plate (CDP).	171
9.12	Variation of mean Nusselt number (top row), pumping power (middle row) and efficiency index (bottom row) with channel height. The data for three Reynolds numbers is plotted columnwise: $Re_H = 400$ (left column), 600 (middle column), 1200 (right column).	172
10.1	Dimensions of the plate.	177
10.2	Computational domain for VIV of a circular cylinder.	179
10.3	(a) Drag coefficient and (b) Strouhal number versus G for four cases mentioned in table 10.2.	180
10.4	Vorticity contours for (a) a fixed plate with $d = 0.1$, (b) a hinged plate with $d = 0.1$, (c) a fixed plate with $d = 0.2$ and (d) a hinged plate with $d = 0.2$ at $G = 4$	181
10.5	(a) Y-coordinate of right end and (b) Strain energy of the plate versus G for four cases.	182
10.6	(a) Kinetic and (b) total energy of the plate versus G for four cases.	183

Nomenclature

\ddot{y}	Transverse acceleration of the cylinder
\dot{y}	Transverse velocity of the cylinder
\mathbf{u}	Fluid velocity vector
μ_m	Magnetic moment of the magnet
ν	Kinematic viscosity of the fluid
\bar{P}	Average power
\bar{P}_{max}	Maximum average power
ρ	Fluid density
ρ_f	Density of fluid
ρ_s	Density of solid
σ_{ij}	Stress tensor
ξ	Damping ratio
ξ_{m0}	Electromagnetic damping constant
ξ_m	Electromagnetic damping ratio
a	Radius of the conducting coil
c	Damping coefficient for the linear damping
c_m	Damping coefficient for the electromagnetic damping ($= c_{m0}g^2$)
C_L	Lift coefficient
c_{m0}	Electromagnetic constant ($= \mu_m^2/(RD^4)$)
D	Cylinder diameter

F_m	Electromagnetic force
f_N	Natural frequency of the system in fluid
f_n	Natural frequency of the system in vacuum
g	A non-linear function of a , L , y_{cm} and N
H	Channel height
k	Stiffness of the spring
L	Length of the conducting coil
L_c	Cylinder length
m	Mass ratio
m_{cm}	Total mass of the cylinder-magnet assembly
m_f	Mass of the displaced fluid
N	Number of turns in the conducting coil
Nu	Nusselt number
P	Instantaneous power
p	Fluid kinematic pressure
Pe	Peclet number
Pr	Prandtl number
R	Net electrical load resistance
Re	Reynolds number
T	Temperature
t	Time
U	Free stream velocity
u	Flow velocity in x-direction
U_r	Reduced velocity
v_i	Flow velocity components

y Transverse displacement of the cylinder

y_{cm} Distance between the magnet and coil

Chapter 1

Introduction

All engineering flow problems involve the interaction of a fluid with solid surfaces. The simplest form of the fluid-solid interaction (FSI) is when all the solid surfaces are rigid and stationary, for example, pipe flow, flow across stationary bluff bodies, etc. The complexity of the problem increases when some of the solid surfaces can move along a predetermined path, for example, flow across oscillating cylinder, turbines, birds flight (fig. 1.1a). In both of these situations, the interaction between the solid and fluid takes the form of well known ‘No-slip’ boundary condition at the fluid-solid interface. A more complex form of FSI occurs when the motion of the rigid solid surfaces is governed by the fluid forces acting on them. This class of problems is also known as flow-induced motion (FIM). The example of FIM includes vortex-induced vibrations(VIV), wind turbines, aircraft, naval ships, falling objects (fig. 1.1b) etc. Lastly, the most complex and general type of FSI problems involve the interaction of the fluid with deformable solid surfaces. These problems are also known as flow-induced deformation (FID). In this situation, an additional condition of continuity of stresses at the fluid-solid interface is imposed. The examples of FID are cardiovascular flow, phonation (fig. 1.2) etc.

The focus of the present work is on the application of FSI to energy harvesting and heat transfer systems. It is possible to convert the flow energy into a usable form of energy, such as electricity, using FIM. For example, wind turbines turn the wind kinetic energy into rotational motion which is used to run an electrical generator. Dams use the potential energy of the fluid to drive a water turbine connected to an electrical generator. The water turbines are also used to convert the kinetic energy of river currents into electricity. A relatively new concept of harvesting flow energy using vortex-induced vibration (VIV) of bluff bodies is also promising. Any bluff body kept in a flowing fluid experiences a periodic alternating lift (perpendicular to the direction of fluid flow) and drag (in the direction of fluid flow) forces due to the well-known phenomenon of ‘vortex shedding.’ If the body is allowed to move along traverse or/and stream-wise direction, then the fluctuating fluid forces acting on the body causes it to undergo an oscillatory

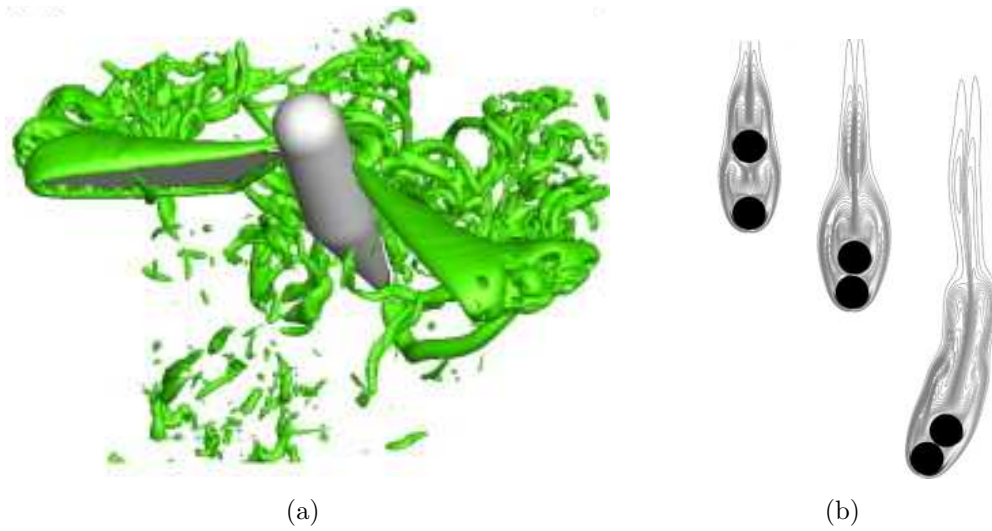


Figure 1.1: (a) vortex structures of a modeled hummingbird in hovering flight (Luo et al., 2012) and (b) Sedimentation of two particles (Favier et al., 2014).

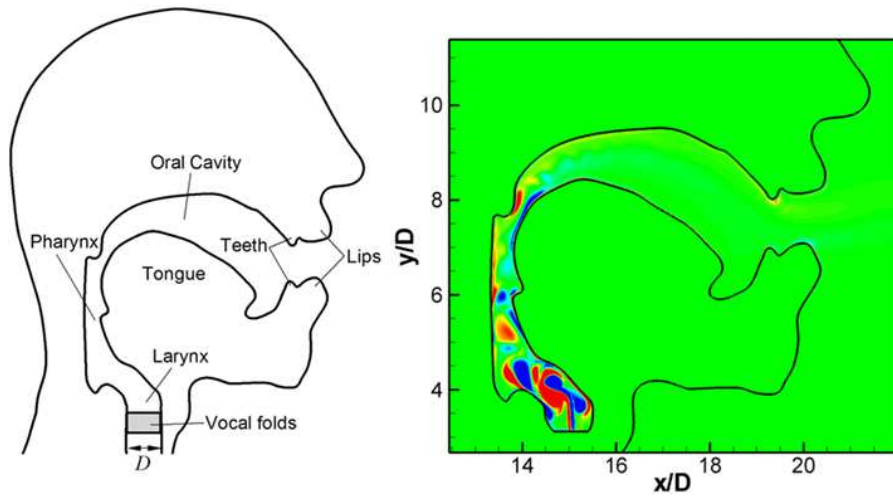


Figure 1.2: (left) Typical human vocal tract system and (right) instantaneous vorticity contours inside the vocal tract (Seo and Mittal, 2011a).

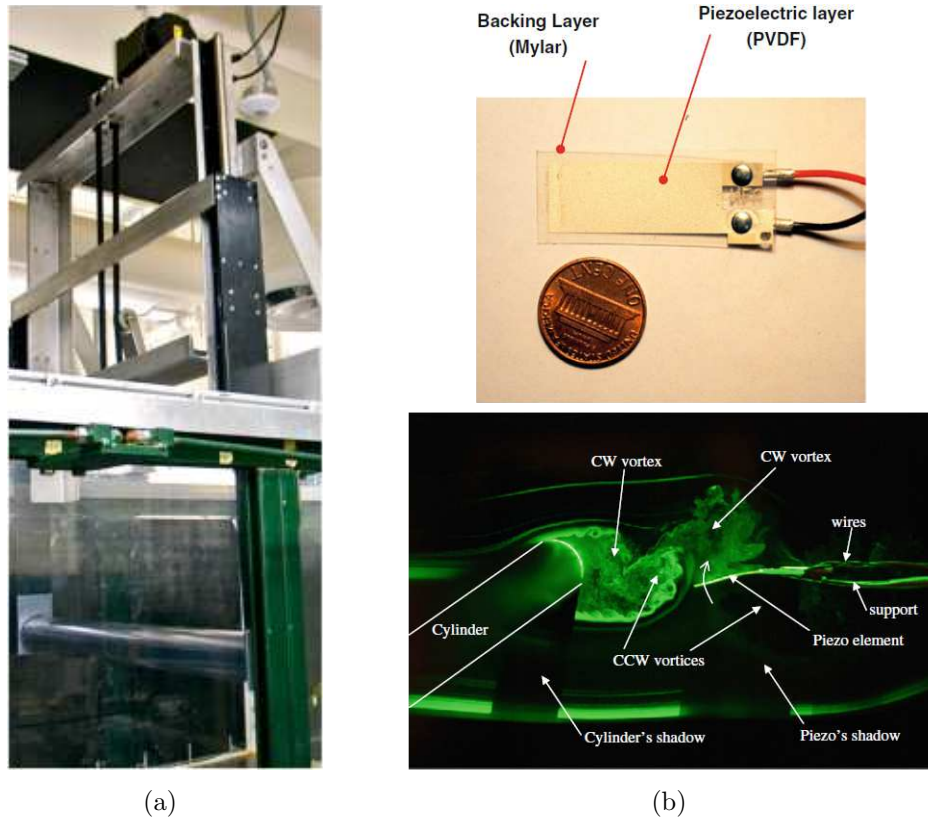


Figure 1.3: (a) VIVACE (Vortex Induced Vibration Aquatic Clean Energy) (Lee and Bernitsas, 2011) and (b) a piezoelectric beam (top) kept behind a circular cylinder (Akaydin et al., 2010) and (bottom) flow visualization.

motion known as ‘vortex-induced vibration.’ The VIV of the bluff-body can be used to produce electrical energy. The VIV of a circular cylinder has been studied extensively both experimentally and numerically. The effects of VIV can be catastrophic when the vortex shedding frequency becomes close to the natural frequency of the structure, also known as ‘lock-in,’ resulting in large amplitude vibrations. From safety point of view, an engineer tries to avoid lock-in from happening by keeping the system natural frequency far from the vortex shedding frequency. On the other hand, the lock-in is desired for energy harvesting purpose because the energy output is proportional to the square of the vibration amplitude. The vortex-induced vibration aquatic clean energy (VIVACE) converter (fig. 1.3a) is one example of generating renewable energy from fluid flow using VIV. The FID of flexible structures can also be used to convert flow energy into electricity. For example, a beam of piezoelectric material can be placed behind a circular cylinder (fig. 1.3b) so that the vortex shedding behind the cylinder causes the plate to deform periodically. The deformation of piezoelectric material gets converted into electricity due to the ‘piezoelectric effect.’

The FID of flexible structures can also be used for enhancing heat transfer. The

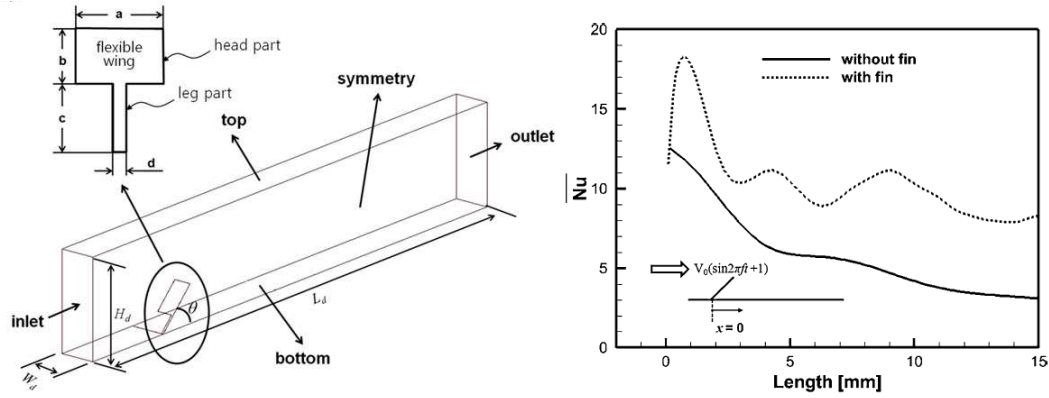


Figure 1.4: Park et al. (2013) used a flexible wing mounted on a heated surface in a pulsating flow (left) to improve the heat transfer as evident from the Nusselt number (right).

deformation of the structures promotes mixing inside the fluid and thereby heat transfer. One example of heat transfer enhancement via FID is shown in fig. 1.4. A flexible wing is mounted on a heated surface and a pulsating flow is applied at the inlet. The flexible wing undergoes periodic deformation cycles due to the pulsating nature of the incoming flow. The up and down motion of the wing directs the flow towards the heated surface which results in enhanced heat transfer as shown by the time-averaged Nusselt number in fig. 1.4. A flexible plate can attain self-sustained oscillation in a free-stream flow due to vortex shedding. Therefore, it can also be used to enhance heat transfer in a heat exchanger. The VIV of the cylinder can also be used to promote heat transfer inside a channel. In both FIM and FID cases, the moving surfaces create strong vortices which interact with the heated surfaces and increase the heat transfer.

1.1 Objectives

The focus of the present work is on both flow-induced vibration (FIV) and flow-induced deformation (FID). Specifically, FIV of a circular cylinder and rectangular plates is studied both experimentally and numerically for energy extraction from fluid flow. The FID is investigated numerically for both energy extraction and heat transfer enhancement applications.

1.2 Organization of the Thesis

The thesis is organized into eleven chapters. Chapter 1 provides an introduction to the area of current research. Chapter 2 provides the details of the numerical methods, the spectral-element method and the sharp-interface immersed boundary method, used for

simulating FSI. The acceleration of the FSI solver using Aitken's method is also presented in this chapter. Chapter 3 provides the description of the experimental setup that was used for performing VIV experiments. Chapter 4 reports the numerical study on low Reynolds number VIV of a circular cylinder for energy extraction using an electromagnetic generator. Chapter 5 is the extension of the study reported in chapter 4 for high Re using experiments. Chapter 6 presents a study on flow-induced vibration study of a thin plate done using both experiments and numerical simulations. Chapter 7 extends the work presented in chapter 6 by studying the effect of aspect ratio of the thin plate on vibration and power extraction characteristics. The thin plates are demonstrated as a better means of energy extraction due to their large oscillations as compared to the circular cylinder. Chapter 8 presents a numerical study on using FID for heat transfer enhancement in a laminar channel flow. Chapter 9 reports the use of FID for heat transfer enhancement in a pulsating channel flow. Chapter 10 revisits the problem presented in chapter 8 for energy extraction application. The conclusions and scope for future work is reported in chapter 11.

Chapter 2

Numerical Methods

The spectral-element method was used for the case of the Vortex-induced vibration (VIV) simulations, and the sharp interface immersed boundary (IB) method was used for simulating flow-induced deformation (FID) problems. Two different numerical methods for the discretization of the Navier-Stokes equation were used in the present work for the reasons explained as follows. The spectral-element method is very efficient for fixed mesh problems. Since the method has a higher order of spatial accuracy as compared to that of the immersed boundary method, it requires less number of mesh nodes as compared to that for the IB method for reducing the error in the solution upto same level. A smaller amount of mesh nodes result in less computational time for the spectral-element solver. In addition, the governing equations for the VIV simulations are solved numerically in the frame of the bluff-body, and therefore the mesh remains fixed. The resulting linear system of equations, arising from the discretization of the governing equations, has a fixed coefficient matrix which can be inverted before time-stepping begins. These advantages of the spectral-element method for fixed mesh problems results in huge computational time savings. On the other hand, the computational mesh changes with time for FID problems and hence the coefficient matrix also changes from one time step to another. The coefficient matrix for the IB method is tridiagonal which can be inverted using the Thomas algorithm (TDMA) whereas the coefficient matrix for the spectral-element method is denser which is computationally more expansive to invert. The immersed boundary method uses a fixed Cartesian mesh which is intersected by the immersed boundary at locations that may not coincide with the mesh nodes. The boundary conditions are imposed using interpolation which will be explained in details later in this chapter. The present spectral-element solver, on the contrary, uses a body-fitted mesh which will require some form of re-meshing/mesh movement techniques which is an extra computational overhead. The generation of body-fitted meshes is also a time-consuming task while the Cartesian meshes are simpler to generate. Therefore, the IB method is used for FID problems in the present work.

The sharp interface immersed boundary method (IBM) based FSI solver is a parallel code. After getting familiar with the parallel programming and underlying principle of the IBM solver, the following modifications/development in the IBM solver were done in the present work

- Vortex-induced vibration capability was added to the IBM solver. The solver was then validated against published data. Initially, VIV simulations were done using the IBM solver but later the spectral-element solver was chosen because of its computational efficiency in performing those calculations.
- The computational speed of the FSI solver was increased by a factor of 2.7 by using the Aitken's method to accelerate the fixed point iteration of the implicitly coupled solver. Earlier, it used to take a lot of trials to find the optimal under-relaxation parameter for a particular FSI problem. In the new approach, the under-relaxation parameter was determined by the Aitken's method and hence additional computational and person hours were saved.
- The implicit coupling was made more robust by adding a check for the divergence of the iterations. A safe under-relaxation parameter was defined which was activated for few iterations whenever the implicit coupling failure was detected. This avoided the need for one to regularly check on the simulations since the nonlinearities could cause the implicit coupling to fail.
- Originally, only pressure forces were being applied to the structures in the FSI solver. The shear force calculations were added to the solver.
- The heat equation solution module was modified to account for different types of temperature boundary conditions on different immersed boundaries and calculating the Nusselt number. The mixed convection capability was also added to the IBM solver.
- The implicit coupling had few logical mistakes. For example, the flow was not solved after convergence of the implicit coupling causing a higher level of divergence in the solution. These mistakes were identified and corrected.

In the following sections, the IB and the spectral-element method will be described in more details. First a brief background on the original diffused interface immersed boundary method is presented. It is followed by a detailed description of the sharp interface immersed boundary method used in the present study. Finally, a short introduction of the spectral-element solver is provided.

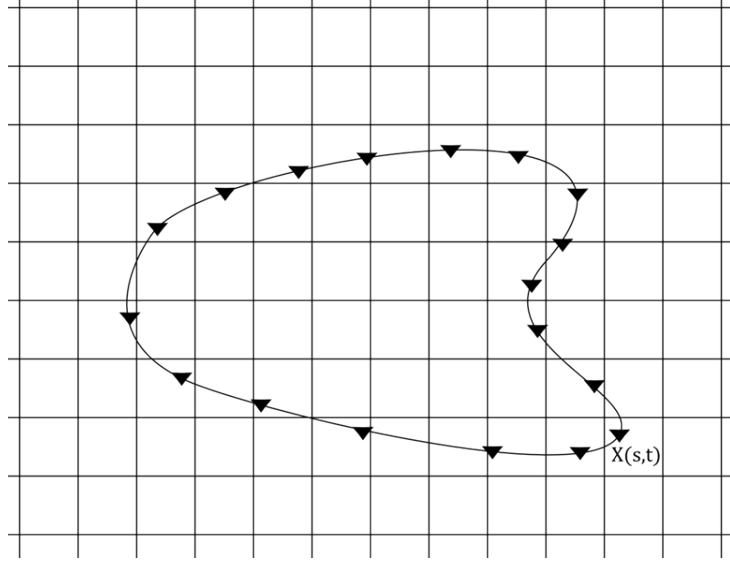


Figure 2.1: An elastic membrane immersed in a Cartesian Mesh.

2.1 Continuous forcing immersed boundary method

The first variant of the immersed boundary method was proposed by [Peskin \(1972\)](#) for simulation FSI of blood flow with human heart valve. The method employed a fixed Cartesian mesh for simulating the fluid flow. The immersed boundary (IB) moved with the fluid flow and the surface forces exerted by the IB was converted into the volumetric fluid forces with the help of the dirac-delta function. Let us consider a two-dimensional (2D) elastic boundary overlapping with the Cartesian mesh as show in fig. 2.1. The elastic boundary is discretized using a finite number of points with position vectors $\mathbf{X}(s, t)$ where $0 < s < L$ is the arc length along the boundary and L is the unstressed length of the boundary. The fluid surrounding the boundary is assumed to be incompressible and viscous whose motion is governed by the following Navier-stokes equations

$$\rho \left(\frac{\partial \mathbf{u}}{\partial t} + \mathbf{u} \cdot \nabla \mathbf{u} \right) = -\nabla p + \mu \nabla^2 \mathbf{u} + \mathbf{F}, \quad (2.1)$$

and the continuity equation

$$\nabla \cdot \mathbf{u} = 0, \quad (2.2)$$

where ρ , \mathbf{u} , p , μ and \mathbf{F} represent the fluid density, velocity, pressure, dynamic viscosity and body force, respectively. The presence of the elastic IB is incorporated in to the governing equation (eq. 2.1) using the body force term (\mathbf{F}) as follows. Let \mathbf{f} denoted the elastic force inside the IB due to its deformations which is given by some known constitutive law such as Hookes law. This force is transmitted to the fluid by converting it into the body

force using the Dirac-delta function

$$\mathbf{F}(\mathbf{x}, t) = \int \mathbf{f}(s, t) \delta(\mathbf{x} - \mathbf{X}(s, t)) ds, \quad (2.3)$$

On a discrete IB, the integration in eq. 2.3 converts to a summation over all the point on the IB

$$\mathbf{F}(\mathbf{x}, t) = \sum_k \mathbf{f}_k \delta(\mathbf{x} - \mathbf{X}_k) ds, \quad (2.4)$$

The points on the IB, which moves with the local fluid velocity, are tracked in the Lagrangian fashion by the relation

$$\frac{d\mathbf{X}}{dt} = \mathbf{u}(\mathbf{X}, t) = \int \mathbf{u}(\mathbf{x}, t) \delta(\mathbf{x} - \mathbf{X}) d\mathbf{x}, \quad (2.5)$$

which, for the discrete IB, converts to

$$\frac{d\mathbf{X}_k}{dt} = \mathbf{u}(\mathbf{X}_k, t) = \sum_i \mathbf{u}(\mathbf{x}_i, t) \delta(\mathbf{x}_i - \mathbf{X}_k) d\mathbf{x}_i, \quad (2.6)$$

This way the IB is replaced by a body force term added to the Navier-Stokes equations with no internal boundary conditions. In general, location of the points on the IB will not coincide with the Cartesian mesh nodes. Therefore, we need to use an approximate delta function, distributed over few grid points, to transmit the elastic force of the IB to the fluid. Many approximate delta functions have been proposed. All have the following form in 3D

$$\delta_h(x, y, z) = \frac{1}{h^3} \phi\left(\frac{x}{h}\right) \phi\left(\frac{y}{h}\right) \phi\left(\frac{z}{h}\right), \quad (2.7)$$

Equation 2.7 is for a mesh size of h . There are many choices for function ϕ , one was given by Peskin (1977)

$$\phi(r) = \begin{cases} \frac{1}{4} (1 + \cos \frac{\pi r}{2}), & |r| < 2. \\ 0, & \text{otherwise.} \end{cases} \quad (2.8)$$

An alternate which satisfies a set of axioms was given by Peskin (2002)

$$\phi(r) = \begin{cases} \frac{1}{8} (3 - 2|r| + \sqrt{1 + 4|r| - 4r^2}), & 0 \leq |r| < 1. \\ \frac{1}{8} (5 - 2|r| - \sqrt{-7 + 12|r| - 4r^2}), & 1 \leq |r| < 2. \\ 0, & \text{otherwise.} \end{cases} \quad (2.9)$$

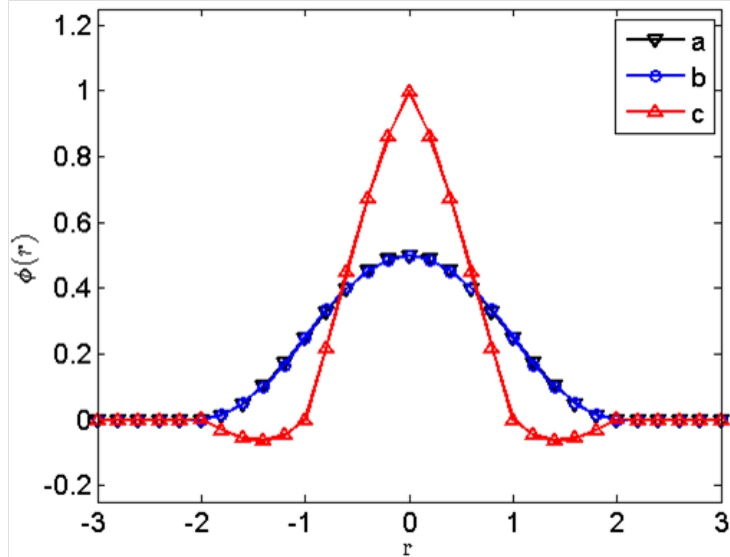


Figure 2.2: Approximate delta functions.

Another piecewise cubic approximation to the delta function was given by [Tornberg and Engquist \(2004\)](#)

$$\phi(r) = \begin{cases} 1 - \frac{1}{2}|r| - r^2 + \frac{1}{2}|r^3|, & 0 \leq |r| < 1. \\ 1 - \frac{11}{6}|r| + r^2 - \frac{1}{6}|r^3|, & 1 \leq |r| < 2. \\ 0, & \text{otherwise.} \end{cases} \quad (2.10)$$

Figure 2.2 shows the graphs of the three approximate delta functions. Symbols ‘a’, ‘b’ and ‘c’ are used for eq. 2.8, 2.9 and 2.10 respectively. Graphs of eq. 2.8 and 2.9 are overlapping with each other. The numerical algorithm of the continuous forcing approach of the IB method is as follows

1. Calculate the force \mathbf{f}_k at each point $\mathbf{X}_k(s, t)$ on the IB.
2. Transform the forces calculated in step 1 to the force density \mathbf{F} on the Cartesian mesh using an approximate delta function (eq. 2.4).
3. Solve the governing equations for the fluid, eq. 2.1 and 2.2.
4. Move the IB points to a new location using eq. 2.6.

2.2 Flow-induced deformation solver

2.2.1 Ghost-Cell based sharp interface immersed boundary method (IBM)

In the continuous forcing approach, the elastic forces of the IB are distributed over a number of fluid mesh points surrounding the IB point with help of an approximate delta

function. The method is also called the diffused interface method since the information about the interface location and forces applied by the IB is diffused over some mesh nodes. But in reality the interface is a sharp boundary between the two mediums (fluid-solid or fluid-fluid). Boundary conditions for the diffused interface, for example no slip at the solid IB, are not satisfied at the actual location of the boundary and also the accuracy of solution is compromised near the IB. This could be troublesome for some flow situations like flow at high Reynolds number where boundary layers need to be captured properly. For these reasons efforts have been made to come up with methods which retain sharp representation of the IB. These methods fall in the category of discrete forcing approach.

There are further two subcategories in discrete forcing approach: a) Direct BC imposition and b) Indirect BC imposition. The current section describes the first approach. In these methods computational stencil is modified near the IB to implement boundary conditions. Both finite difference (Mittal et al., 2008) and finite volume (Ye et al., 1999a) techniques exist in the literature.

Ghost-cells based finite difference method, given by Mittal et al. (2008), will be described here in details. Consider a 3D unsteady incompressible flow with constant properties which is governed by Navier-Stokes equation, written in tensor notation as:

$$\frac{\partial u_i}{\partial x_i} = 0, \quad (2.11)$$

$$\frac{\partial u_i}{\partial t} + \frac{\partial u_i u_j}{\partial x_j} = -\frac{1}{\rho} \frac{\partial p}{\partial x_i} + \nu \frac{\partial}{\partial x_j} \left(\frac{\partial u_i}{\partial x_j} \right), \quad (2.12)$$

where i and j varies from 1 to 3. u_i are the Cartesian velocity components, p is the pressure and ρ and ν are fluid density and kinematic viscosity respectively. Above equations can be solved by various methods. In Mittal et al. (2008) these equations were discretized on a collocated grid where all variables are stored at cell centres. Apart from cell-centre velocity u_i , the face-centre velocities U_i are required in collocated grid formulation. Fractional step method of Van Kan (1986) is used for time integration. In the first step, momentum equation is solved for intermediate velocity U^* using Adams-Bashforth and Crank-Nicolson schemes for convective and diffusion terms respectively

$$\frac{u_i^* - u_i^n}{\Delta t} + \frac{1}{2} (3C_i^n - C_i^{n-1}) = -\frac{1}{\rho} \frac{\delta p^n}{\delta x_i} + \frac{1}{2} (D_i^* + D_i^n), \quad (2.13)$$

where $C_i = \frac{\delta}{\delta x_j} (U_j u_i)$ and $D_i = \nu \frac{\delta}{\delta x_j} \left(\frac{\delta u_i}{\delta x_j} \right)$.

Note that both convective and diffusion term are discretized using a second order central difference scheme. Intermediate face-centre velocities are obtained by averaging the intermediate cell-centre velocities as follows

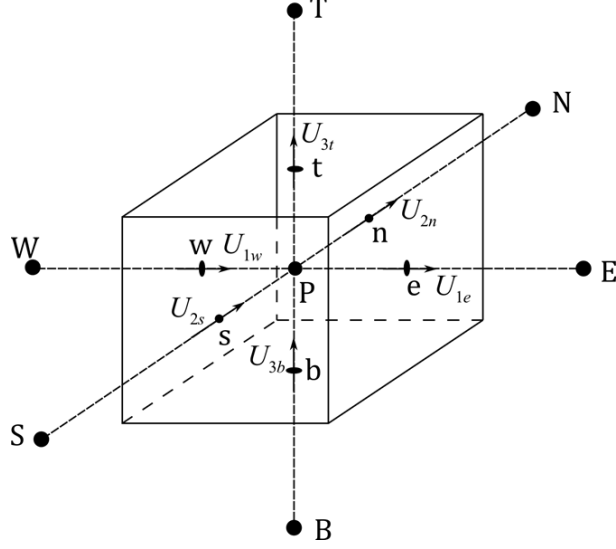


Figure 2.3: A representative cell.

$$\tilde{u}_i = u_i^* + \Delta t \frac{1}{\rho} \left(\frac{\delta p^n}{\delta x_i} \right)_{cc}, \quad (2.14)$$

$$\tilde{U}_{1w} = \gamma_w \tilde{u}_{1P} + (1 - \gamma_w) \tilde{u}_{1W}; \tilde{U}_{1e} = \gamma_e \tilde{u}_{1P} + (1 - \gamma_e) \tilde{u}_{1E}, \quad (2.15)$$

$$\tilde{U}_{2s} = \gamma_s \tilde{u}_{2P} + (1 - \gamma_s) \tilde{u}_{2S}; \tilde{U}_{2n} = \gamma_n \tilde{u}_{2P} + (1 - \gamma_n) \tilde{u}_{2N}, \quad (2.16)$$

$$\tilde{U}_{3b} = \gamma_b \tilde{u}_{3P} + (1 - \gamma_b) \tilde{u}_{3B}; \tilde{U}_{3t} = \gamma_t \tilde{u}_{3P} + (1 - \gamma_t) \tilde{u}_{3T}, \quad (2.17)$$

$$U_i^* = \tilde{U}_i - \Delta t \frac{1}{\rho} \left(\frac{\delta p^n}{\delta x_i} \right)_{fc}, \quad (2.18)$$

In eq. 2.15, 2.16 and 2.17 $\gamma_w, \gamma_e, \gamma_s, \gamma_n, \gamma_b$, and γ_t are the weights for linear interpolation at west, east, south, north, bottom and top faces respectively. Also, ‘fc’ and ‘cc’ stands for face-centre and cell-centre. Next, following Poisson equation is solved for pressure correction

$$\frac{1}{\rho} \frac{\delta}{\delta x_i} \left(\frac{\delta p'}{\delta x_i} \right) = \frac{1}{\Delta t} \frac{\delta U_i^*}{\delta x_i}, \quad (2.19)$$

Again central difference scheme is used for discretization. Neumann boundary conditions are applied for pressure correction at all boundaries. In third and final step, intermediate velocity and pressure are updated as follows

$$p^{n+1} = p^n + p', \quad (2.20)$$

$$u_i^{n+1} = u_i^* - \frac{\Delta t}{\rho} \left(\frac{\delta p'}{\delta x_i} \right)_{cc}, \quad (2.21)$$

$$U_i^{n+1} = U_i^* - \frac{\Delta t}{\rho} \left(\frac{\delta p'}{\delta x_i} \right)_{fc}, \quad (2.22)$$

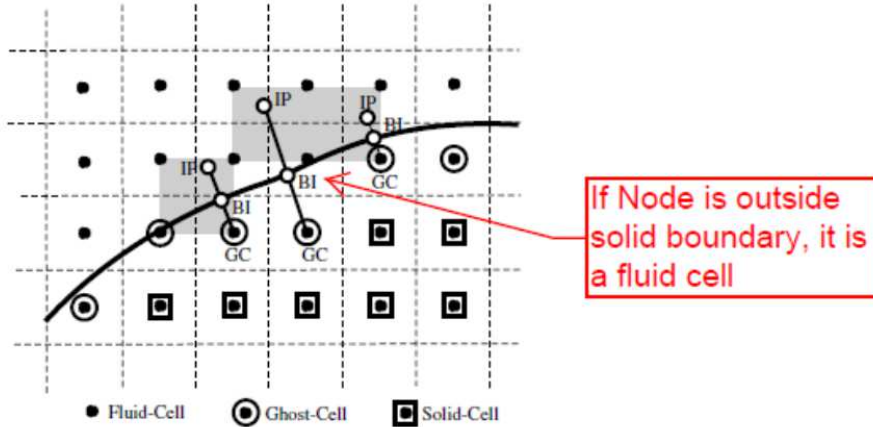


Figure 2.4: Immersed boundary and labelling of computational cells (taken from (Mittal et al., 2008)).

This completes the solution procedure for one time step. IB can be represented by variety of ways such as level set field and unstructured mesh. To account for the presence of IB, proper boundary conditions should be applied at the location of IB. For this purpose, computational cells are divided into following categories a) Fluid cells, b) Solid cells and c) Ghost cells. Cells whose centre lies outside the IB are labelled as ‘fluid cells’ and others are labelled as ‘solid cells’. Further solid cells whose at least one neighbour out of 6 (4 in 2D) is a fluid cell is relabelled as ‘ghost cell’. Figure 2.4 (taken from (Mittal et al., 2008)) shows an IB in a Cartesian grid with different kind of cells. If IB is represented using a level set field (signed distance function in particular) then fluid cells will have positive value of level set field. For IB represented by unstructured mesh a procedure was suggested in Mittal et al. (2008). As shown in Figure 2.5 (taken from (Mittal et al., 2008)), to determine whether a node is inside or outside the IB one finds a surface element on the IB which is closest to the node and then takes the dot product of two vectors p and n where p is a vector originating from the nearest surface element of IB and pointing towards the node and n is the surface normal vector. If dot product is positive then cell lies outside the IB and is labelled as fluid cell and vice-versa. Note that for stationary IB this labelling needs to be done only once in the start of the solution procedure but for moving IB we need to repeat this labelling procedure after each time step.

Once all cells are labelled, next job is to find appropriate values of different variables at the ghost cells such that boundary conditions are satisfied at the location of IB. For this a normal is drawn on to the IB from ghost cell which cuts the IB at a point called the ‘boundary intercept’ (BI) and extends into the fluid region up to a point called the ‘image point’ (IP). IP is chosen such that BI is midpoint of IP and ghost cell centre. After determining the IP for a ghost cell, a trilinear (bilinear in 2D) interpolation is used to

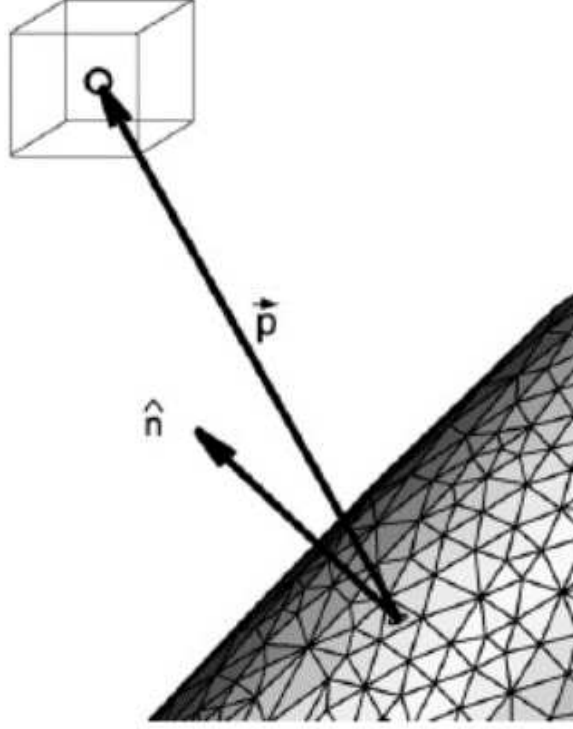


Figure 2.5: Procedure for labelling the computational cells (taken from (Mittal et al., 2008)).

interpolate the value of any variable, let us say ϕ , at IP. Any variable ϕ can be expressed by the following expression in the neighbourhood of 8 (4 in 2D) cells which surrounds the IP

$$\phi(x, y, z) = c_1xyz + c_2xy + c_3yz + c_4xz + c_5x + c_6y + c_7z + c_8, \quad (2.23)$$

There are eight unknown coefficients in eq. 2.23 which can be determined by the fact that ϕ is known at 8 neighbouring cells

$$\phi_i = c_1(xyz)_i + c_2(xy)_i + c_3(yz)_i + c_4(xz)_i + c_5x_i + c_6y_i + c_7z_i + c_8; \forall i = 1, 2, \dots, 8. \quad (2.24)$$

Above equation can be written in matrix form as

$$\{\phi\} = [V]\{c\}, \quad (2.25)$$

where V is the Vandermonde matrix given by

$$[V] = \begin{pmatrix} (xyz)_1 & (xy)_1 & (yz)_1 & (xz)_1 & x_1 & y_1 & z_1 & 1 \\ (xyz)_2 & (xy)_2 & (yz)_2 & (xz)_2 & x_2 & y_2 & z_2 & 1 \\ \vdots & \vdots \\ (xyz)_8 & (xy)_8 & (yz)_8 & (xz)_8 & x_8 & y_8 & z_8 & 1 \end{pmatrix} \quad (2.26)$$

Equation 2.25 gives the value of coefficients

$$\{c\} = [V]^{-1}\{\phi\}, \quad (2.27)$$

After determining the coefficients, eq. 2.25 can be used to find the value of ϕ at IP as

$$\phi_{IP} = \sum_{i=1}^8 \beta_i \phi_i, \quad (2.28)$$

In eq. 2.28 β_i are function of coefficients c_i and the coordinates of IP. As discussed in Mittal et al. (2008), sometimes one cell out of 8 neighbours of IP can be the ghost cell itself. In that situation the row corresponding to the ghost node in eq. 2.27 is replaced by the boundary condition at BI. In the case when Neumann boundary condition is specified at the immersed boundary, we need to find gradient of ϕ at BI as follows

$$\begin{aligned} \left. \frac{\partial \phi}{\partial n} \right|_{BI} &= (\nabla \phi)_{BI} \cdot \vec{n}_{BI} \\ &= c_1(n_1 y z + n_2 x z + n_3 x y) + c_2(n_1 z + n_2 x) + c_3(n_2 z + n_3 y) \\ &\quad + c_4(n_1 z + n_3 x) + c_5 n_1 + c_6 n_2 + c_7 n_3, \end{aligned} \quad (2.29)$$

In eq. 2.29 n_1, n_2 and n_3 are components of unit normal at BI. Also x, y and z are coordinates of BI.

Now the value of ϕ is available at IP, a linear extrapolation is used along the normal from ghost cell to IB to find the value of ϕ at ghost cell centre. For example, consider the Dirichlet boundary condition for velocity at IB. Since BI is midway between IP and ghost cell, we have

$$\phi_{BI} = \frac{1}{2} (\phi_{IP} + \phi_{GC}), \quad (2.30)$$

In an implicit solution procedure all the neighbouring values of ϕ are not known hence above equation is written as

$$\phi_{GC} + \sum_{i=1}^8 \beta_i \phi_i = 2\phi_{BI}, \quad (2.31)$$

For Neumann boundary condition for pressure on IB following central difference scheme is used

$$\left(\frac{\delta \phi}{\delta n} \right)_{BI} = \frac{\phi_{IP} - \phi_{GC}}{\Delta l}, \quad (2.32)$$

Here Δl is the distance between ghost cell centre and IP and n stands for normal direction. Again above equation is written as

$$\phi_{GC} - \sum_{i=1}^8 \beta_i \phi_i = -\Delta l \left(\frac{\delta \phi}{\delta n} \right)_{BI}, \quad (2.33)$$

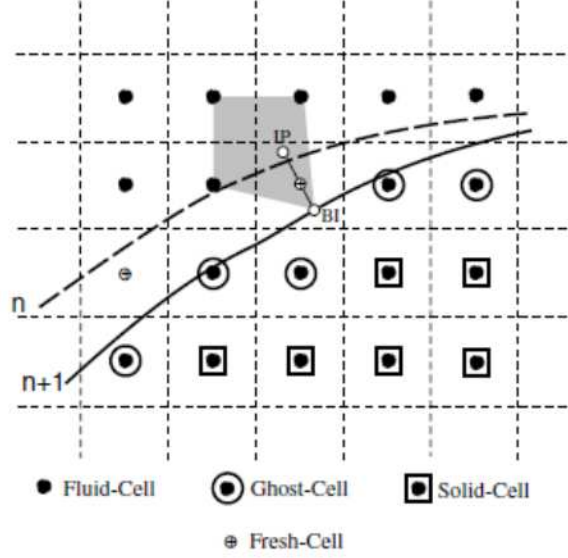


Figure 2.6: Moving IB and fresh cells treatment (taken from [Mittal et al. \(2008\)](#)).

Equations 2.31 and 2.33 are solved with 2.13 and 2.19 for all fluid cells.

When IB is moving then so called ‘fresh cells’ are being created in fluid domain. Fresh cells are those cells which were labelled as the solid cell in the previous time step but become fluid cell for the current time step due to motion of IB. An example is shown in fig. 2.6 (taken from [Mittal et al. \(2008\)](#)) for 2D problem. Problem is that values of flow variables, such as velocities and pressure, are not available from previous time steps for fresh cells since these were in solid domain. A solution to this problem was proposed in [Ye et al. \(1999b\)](#). During the solution procedure for next time step, intermediate velocities for fresh cells are interpolated from their neighbouring cells using a similar trilinear interpolation procedure that was used for ghost cells. As shown in fig. 2.6 (taken from [Mittal et al. \(2008\)](#)), a normal is drawn to the IB from fresh cell centre which cuts the IB at point called boundary intercept ‘BI’. Then image point ‘IP’ is found such that fresh cell lies midway between IP and BI. 8 (4 in 2D) neighbours of IP are identified, among which one is the fresh cell itself. Finally fresh cell intermediate velocities are interpolated from 7 neighbours of IP (fresh cell is excluded) and BI. After obtaining the intermediate velocities and pressure, pressure correction for fresh cells is obtained by solving pressure correction eq. 2.19 and final velocity and pressure is obtained by eq. 2.20 to 2.22.

2.2.2 Heat transfer modeling

The heat transfer inside the fluid is governed by the following non-dimensional energy equation

$$\frac{\partial T}{\partial t} + \mathbf{u} \cdot \nabla T = \frac{1}{Pe} \nabla^2 T, \quad (2.34)$$

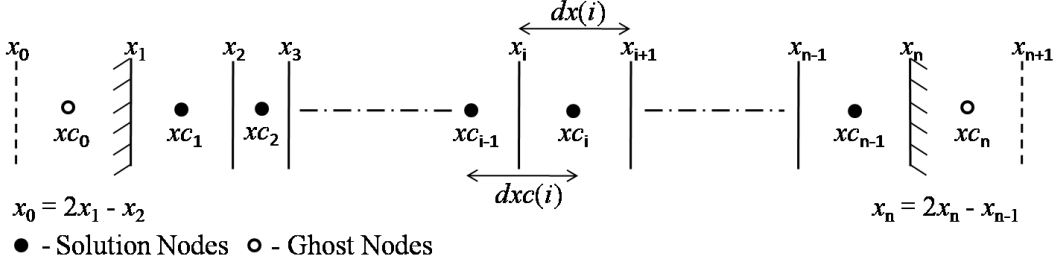


Figure 2.7: A one dimensional Cartesian grid.

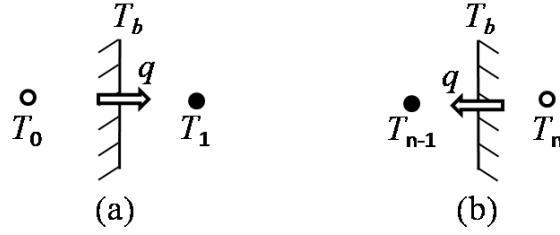


Figure 2.8: Implementation of boundary condition on the outer boundaries.

where Pe represent the Peclet number which is the product of Reynolds and Prandtl number. The Prandtl number (Pr) is ratio of momentum diffusivity (ν) to thermal diffusivity (α). The non-dimensional temperature is defined as

$$T = \frac{T^* - T_{ref}^*}{T_w^* - T_{ref}^*}, \quad (2.35)$$

where $*$ in the superscript denotes the dimensional quantities. The symbols T_w^* and T_{ref}^* represent the dimensional wall temperature and the reference temperature (equal to the inlet temperature in the channel flow case), respectively.

In the previous section, the implementation of boundary conditions on immersed boundaries was discussed. Now we briefly describe the way boundary conditions are applied at outer boundaries i.e. boundaries of Cartesian grid. The representative 1D Cartesian grid, used in our simulations, is shown in fig. 2.7. Solid vertical lines and dots represent the cell boundaries and centers, respectively. Also x and x_c stands for x -coordinates of cell boundaries and centers, respectively. Domain boundaries are located at x_1 and x_n where n is an integer given by the expression $n = (2^m)k + 1$ (for $m, k = 1, 2, \dots$) which is necessary for the multigrid method used for the solution of the pressure Poisson equation. In cell centered collocated grid, all variables are stored at cell centers. Dashed lines are for outer ghost cells boundaries. These outer ghost cells are used for applying boundary conditions at domain boundaries. The sizes of these left and right outer ghost cells are equal to the sizes of first and last cell, respectively. Using the linear interpolation,

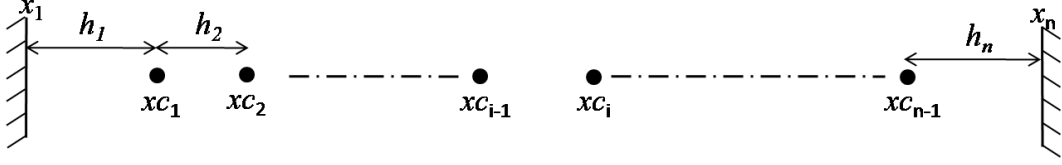


Figure 2.9: Finding temperature gradients at boundaries.

we can write the left boundary temperature as

$$T_b = \frac{T_0 + T_1}{2}, \quad (2.36)$$

In case of Dirichlet boundary condition, the boundary temperature is known and hence, we can write outer ghost cell temperature as

$$T_0 = 2T_b - T_1, \quad (2.37)$$

If a given heat flux q (non-dimensional) is prescribed at the left boundary, we can write

$$q = - \left. \frac{\partial T}{\partial x} \right|_{x=x_1} = \frac{T_0 - T_1}{dx_c(1)}, \quad (2.38)$$

where the first derivative is approximated using the second-order central difference scheme. The ghost cell temperature can be calculated from eq. 2.38. Similar treatment is done at the right boundary.

To quantify the heat transfer, we calculate the instantaneous Nusselt number (Nu), based on hydraulic diameter, on channel walls as follows

$$Nu(x, t) = \frac{2H}{T_m - 1} \left. \frac{\partial T}{\partial y} \right|_{\text{wall}}, \quad (2.39)$$

where H is the height of the channel and the bulk mean temperature, T_m , is defined as

$$T_m(x, t) = \frac{\int_0^H uT dy}{\int_0^H u dy}, \quad (2.40)$$

The temperature gradients at the domain boundaries are calculated using a third order accurate approximation to first derivative (fig. 2.9). For example, the temperature gradient at the left boundary is given by the following expression

$$\left. \frac{\partial T}{\partial x} \right|_{x=x_1} = aT_b + bT_1 + cT_2, \quad (2.41)$$

where

$$a = -\frac{2h_1 + h_2}{h_1(h_1 + h_2)}, b = \frac{h_1 + h_2}{h_1 h_2}, c = -\frac{h_1}{h_2(h_1 + h_2)}. \quad (2.42)$$

Similarly, for the right boundary

$$\left. \frac{\partial T}{\partial x} \right|_{x=x_n} = dT_b + eT_{n-1} + fT_{n-2}, \quad (2.43)$$

where

$$d = \frac{2h_n + h_{n-1}}{h_n(h_n + h_{n-1})}, e = -\frac{h_n + h_{n-1}}{h_n h_{n-1}}, f = \frac{h_n}{h_{n-1}(h_n + h_{n-1})}. \quad (2.44)$$

2.2.3 Structural solver

An open source finite-element based structure dynamics solver [Tahoe](#)[©] is employed. The governing equations are the Navier equations, written as

$$\rho_s \frac{\partial^2 d_i}{\partial t^2} = \frac{\partial \sigma_{ij}}{\partial x_j} + \rho_s f_i, \quad (2.45)$$

where ρ_s , $\boldsymbol{\sigma}$ and \mathbf{d} represent the structure density, Cauchy stress tensor and structure displacement, respectively. The indices i and j range from 1 to 3. The structure is considered as Saint Venant-Kirchhoff material in which the elasticity of the material is characterized by the Young Modulus (E) and the Poisson ratio (ν_s). This model takes the compressibility of the structure into account. In this model, the fourth order isotropic tensor of elastic constants, C can be expressed as

$$C = \begin{pmatrix} \lambda + 2\mu & \lambda & \lambda & 0 & 0 & 0 \\ \lambda & \lambda + 2\mu & \lambda & 0 & 0 & 0 \\ \lambda & \lambda & \lambda + 2\mu & 0 & 0 & 0 \\ 0 & 0 & 0 & \mu & 0 & 0 \\ 0 & 0 & 0 & 0 & \mu & 0 \\ 0 & 0 & 0 & 0 & 0 & \mu \end{pmatrix}. \quad (2.46)$$

The Lam constants λ and μ are related to Young Modulus E and Poisson ratio ν_s by the following expressions

$$\lambda = \frac{\nu_s E}{(1 + \nu_s)(1 - 2\nu_s)}, \quad (2.47)$$

$$\mu = \frac{E}{2(1 + \nu_s)}, \quad (2.48)$$

For small deformations, the stress and strain are related by $\sigma_{i,j} = C_{ijkl}\epsilon_{ijkl}$ where ϵ is the infinitesimal strain tensor. For large deformations, the constitutive relation between the stress and the strain is based on Green-Lagrangian strain tensor \mathbf{E} and second Piola-

Kirchhoff stress tensor $\mathbf{S}(\mathbf{E})$ as a function of \mathbf{E} . The second Piola-Kirchhoff stress tensor can be expressed in terms of the Cauchy stress tensor $\boldsymbol{\sigma}$ as follows

$$\mathbf{S} = J\mathbf{F}^{-1}\boldsymbol{\sigma}\mathbf{F}^{-T}, \quad (2.49)$$

where J is the determinant of the deformation gradient tensor \mathbf{F} . The Green-Lagrangian strain tensor \mathbf{E} is defined as

$$\mathbf{E} = \frac{1}{2}(\mathbf{F}^T\mathbf{F} - \mathbf{1}), \quad (2.50)$$

2.2.4 Fluid and structural solvers coupling

There are two approaches for numerical solution of FSI problems (Hou et al., 2012) Monolithic and partitioned approach. Both fluid and structure governing equations are solved simultaneously in former approach whereas fluid and structure solver are called separately in an iterative fashion in later case. The advantage of partitioned approach is that existing black-box fluid and structure solver can be coupled together with relatively ease. This approach was used by Bhardwaj and Mittal (2012) to couple a sharp interface Immersed boundary method based fluid solver with a Finite element method based structure solver called Tahoe[©]. One major drawback of this approach is the large computational time due to many FSI iterations. In partitioned approach an initial guess of fluid-solid interface location is continuously refined by iterative procedure till convergence is reached. This is also referred to as fixed-point iteration. Many methods have been proposed to reduce the number of iteration of fixed point iteration (Degroote et al., 2010).

The flow solver is coupled with an open source finite-element structural solver, Tahoe[©], via implicit partitioned approach. This ensures stability of the FSI solver at low solid to fluid density ratios. A flow chart of the strongly coupled partitioned approach is given in fig. 2.10.

2.2.5 Accelerating FSI convergence

One simple way to accelerate the convergence of FSI iterations is to use dynamic under-relaxation factor (ω) instead of constant one. As discussed in Degroote et al. (2010) this can be achieved using Aitkens method. In this method, two previous iterations are used to predict a better value of ω . The final expression for ω is given by

$$\omega_k = -\omega_{k-1} \frac{(R_{k-1})^T(R_k - R_{k-1})}{\|R_k - R_{k-1}\|^2}, \quad (2.51)$$

where \mathbf{R} is the interface residual vector. We can start the iteration with a small initial guess of ω (ω_0). As one can see in flow chart in fig. 2.10, we use different ω for different

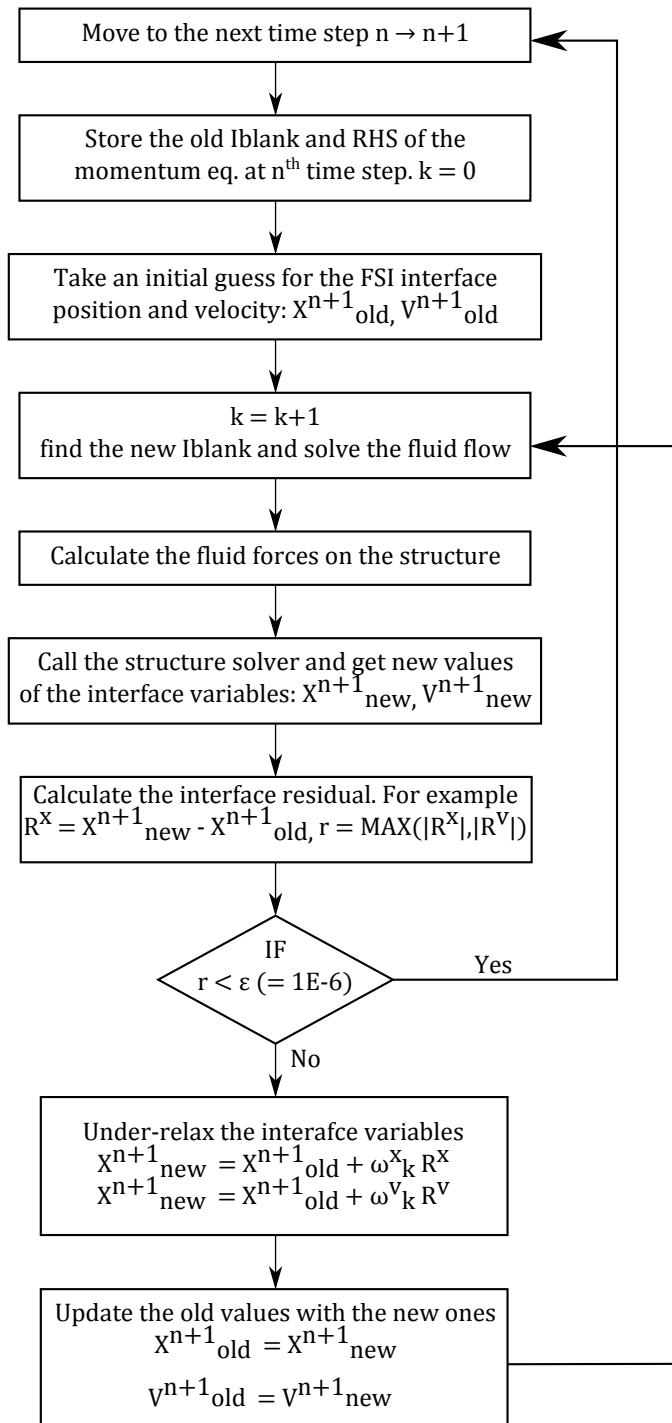


Figure 2.10: Flow chart of the implicit coupling.

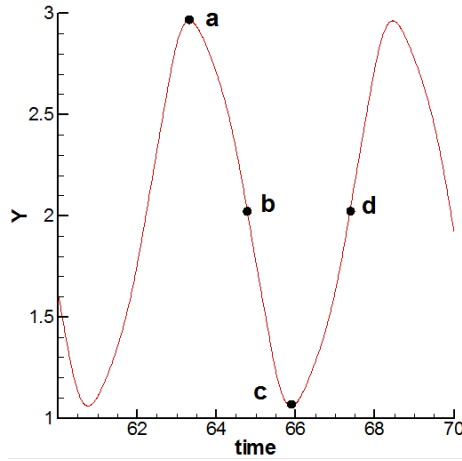


Figure 2.11: y -displacement of flag tip in cylinder-flag FSI problem.

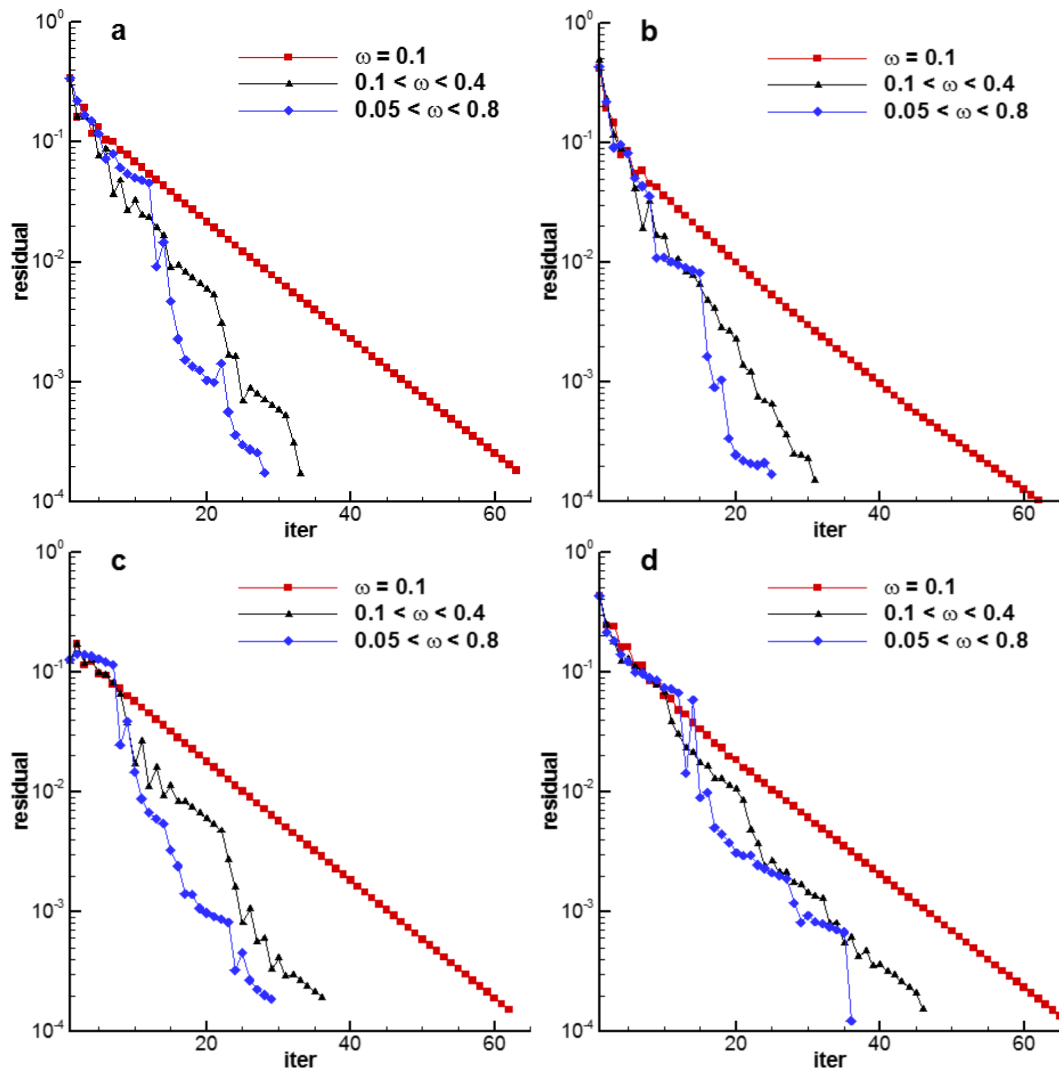


Figure 2.12: FSI residual variation of acceleration component in y -direction with number of iterations.

interface variables. There are three interface variables: position (x), velocity (v) and acceleration (a) of interface. Each variable has 2 (3 in 3D) components and hence we use 6 (9 in 3D) different ω . Aitkens relation is exact only for linear systems. It means that iteration will converge in just 3 iterations (2 previous guess plus 1 Aitkens) for linear system. Hence, due to non-linearity of the FSI system the coupling may diverge due to high value of ω predicted by Aitkens relation. In this situation, we switch to constant under-relaxation for few numbers of iterations, N_{safe} (we choose $N_{safe} = 5$). We need a small under-relaxation parameter (ω_{safe}) which can ensures converges. We have taken $\omega_{safe} = \omega_0$. We switch back to dynamic under-relaxation after N_{safe} number of iterations.

To evaluate the performance of Aitkens method, we consider the FSI benchmark problem used by [Bhardwaj and Mittal \(2012\)](#) for code validation. In this problem a deformable plate of length $3.5D$ and thickness $0.2D$ is attached to the lee side of a rigid cylinder of diameter D . The structure is kept in a channel of height $4.1D$ and length $41D$. A fully developed velocity profile is applied at left boundary of the channel. Velocity boundary conditions (BC) at bottom and top walls are No-slip. At right boundary zero Neumann BC is applied. The plate is modelled as Saint VenantKirchhoff material. Reynolds number, Youngs modulus, solid to fluid density ratio and Poisson ratio are take as 100, 1.4×10^3 , 10 and 0.45, respectively.

As the flow develops the plate attains a constant amplitude wave like deformation after sufficient time. The y -displacement of the tip of the plate is show in fig. 2.11. The plate oscillation frequency is 0.19. We plot the FSI convergence history in fig. 2.12 at four time instances in a cycle of plate oscillations. These four instances are show by black dots in fig. 2.11. We have compared the performance of dynamic vs. constant under-relaxation. The maximum value of ω for which the constant under-relaxation converges is found to be 0.1. We have taken following three cases to comparison: (a) Constant under-relaxation with $\omega = 0.1$, (b) Dynamic under-relaxation with ω in the range of 0.1 to 0.4 and (c) Dynamic under-relaxation with ω in the range of 0.05 to 0.8. The interface residual is decreasing much faster with dynamic ω as compared to constant case. The tolerance for convergence is set to 2×10^{-4} . Average numbers of iterations for one cycle of plate oscillation in cases (a), (b) and (c) is found to be 76, 39 and 28, respectively. Hence we are getting a maximum speed up of 2.7 using Aitkens method.

2.2.6 IBM based vortex-induced vibration solver

Vortex-induced vibration (VIV) of an elastically supported circular cylinder of mass m and diameter D kept in a uniform flow with the free stream velocity U is considered. The support has stiffness k and damping coefficient c . The motion of the cylinder is governed by the following equations

$$m\ddot{\mathbf{r}} + c\dot{\mathbf{r}} + k\mathbf{r} = \mathbf{F}, \quad (2.52)$$

where $\mathbf{r} = (x, y)$ represents the displacement vector of the cylinder and \mathbf{F} is the net external force acting on it. The natural frequency of the system, described by eq. 2.52, in vacuum is given by

$$f_n = \frac{1}{2\pi} \sqrt{\frac{k}{m}}, \quad (2.53)$$

We define the damping ratio as $\zeta = c/c_c$. The critical damping (c_c) for the system is given by the expression $c_c = 2m\omega_n$ where ω_n is the angular frequency ($\omega_n = 2f_n$). Using these definitions, eq. 2.52 can be re-written as

$$\ddot{\mathbf{r}} + 4\pi\zeta f_n \dot{\mathbf{r}} + 4\pi^2 f_n^2 \mathbf{r} = \frac{\mathbf{F}}{m}, \quad (2.54)$$

We take D and U as the reference length and velocity, respectively, to obtain the non-dimensional form of eq. 2.54. The other non-dimensional parameters are

$$\mathbf{r}^* = \frac{\mathbf{r}}{D}, \quad t^* = \frac{U}{D}t, \quad f_n^* = \frac{D}{U}f_n, \quad m^* = \frac{m}{\pi\rho D^2 L/4}$$

where L is the length of the cylinder taken as unity in the case of two-dimensional flow. The non-dimensional form of eq. 2.54 is

$$\ddot{\mathbf{r}}^* + 4\pi\zeta f_n^* \dot{\mathbf{r}}^* + 4\pi^2 f_n^{*2} \mathbf{r}^* = \frac{2}{\pi} \frac{\mathbf{F}^*}{m^*}, \quad (2.55)$$

where $\mathbf{F}^* = 2\mathbf{F}/(\rho U^2 DL)$. The solution of eq. 2.55 depends on the fluid forces acting on the cylinder which in turn depend on the velocity of the cylinder. Therefore, the cylinder motion is coupled with the fluid flow. One easy way to solve this coupled problem is to use a loose coupling (staggered approach) in which the fluid forces from previous time steps are used to find the solution of eq. 2.55 at the new time step and then this solution is used to find the new flow field. The coupling scheme is stable for relatively large mass ratios (Placzek et al., 2009) and is computationally efficient. An explicit numerical integration scheme is used for solution of eq. 2.55. In following, we will drop the star from the superscript for the non-dimensional variables. First, the acceleration of the cylinder at new time step is calculated using the variables from the previous time step

$$\ddot{\mathbf{r}}^{n+1} = \frac{2}{\pi} \frac{\mathbf{F}^n}{m} - 4\pi\zeta f_n \dot{\mathbf{r}}^n - 4\pi^2 f_n^2 \mathbf{r}^n, \quad (2.56)$$

then the displacement and velocity of the cylinder at the new time step are calculated as (Bao et al., 2012)

$$\dot{\mathbf{r}}^{n+1} = \dot{\mathbf{r}}^n + \Delta t \ddot{\mathbf{r}}^{n+1}, \quad (2.57)$$

$$\mathbf{r}^{n+1} = \mathbf{r}^n + 0.5\Delta t(\dot{\mathbf{r}}^n + \dot{\mathbf{r}}^{n+1}), \quad (2.58)$$

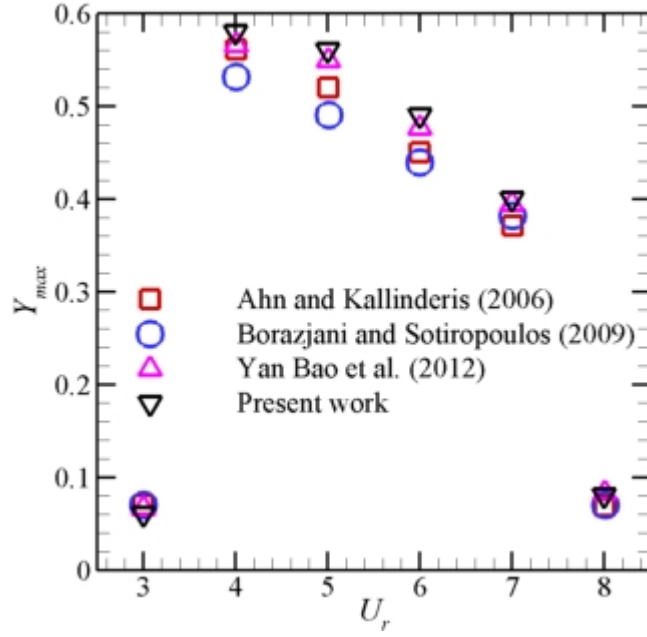


Figure 2.13: Comparison of maximum displacement amplitude of the undamped cylinder undergoing transverse VIV with $m = 8/\pi$ at $Re = 150$ with the published data.

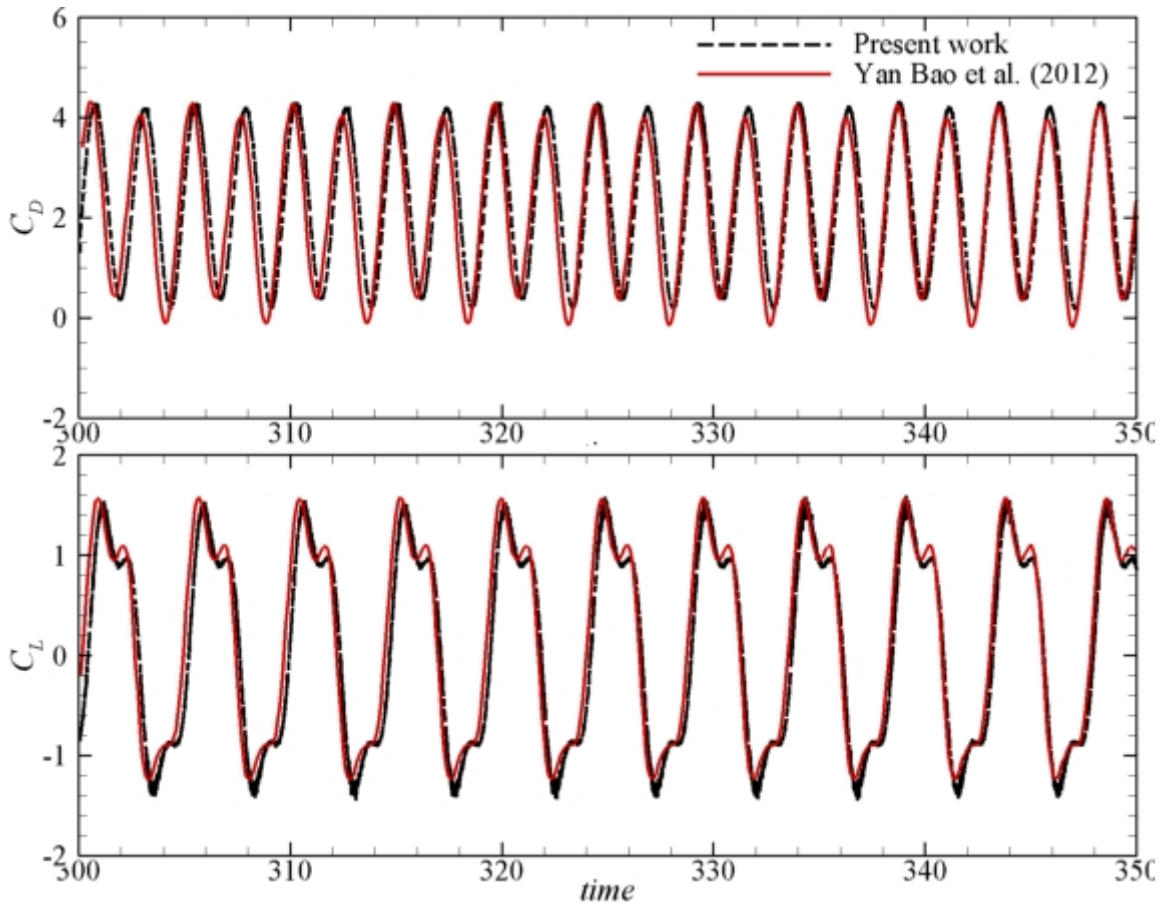


Figure 2.14: Comparison of lift and drag coefficients of the undamped cylinder undergoing two-degree of freedom VIV with $m = 8/\pi$, $f_{nx}/f_{ny} = 2.0$ and $U_r = 4.0$ at $Re = 150$.

Figure 2.13 shows the comparison of our work with published data against the displacement amplitude of the cylinder which is free to vibrate only in transverse direction for various reduced velocities $U_r (= U/Df_n)$ at $\text{Re} = 150$. Our results agree well with the published data. To further validate our solver, we compare the lift and drag coefficients for a two-degree of freedom cylinder having $m = 8/\pi$ with that of Bao et al. (2012). The ratio of frequencies in x and y -directions (f_{nx}/f_{ny}), reduced velocity and Reynolds number are equal to 2.0, 4.0 and 150, respectively. As seen in fig. 2.14, we get a good agreement with the results of Bao et al. (2012).

2.3 Flow-induced vibration solver

2.3.1 The spectral-element method

In the spectral-element method, the computational domain is divided into a set of non-overlapping regions which are called elements. On each element the solution is approximated using higher order basis functions. The approximate solution is then put into the governing equation. Since the solution is approximate it does not satisfy the governing equations exactly and produces a residual. A weighted integral of the residual is equated to zero on each element. This operation, also called discretization, produces a set of linear equations for each element of the computational mesh. Every set of the linear system obtained from each elements are combined into one larger linear system. When the basis functions (trial functions) and the weighting functions are the same, the method is also called a Galerkin method. Let us consider the following one-dimensional (1D) wave equation for explaining the method in more details,

$$\frac{\partial q}{\partial t} + \frac{\partial f}{\partial x} = 0, \quad (2.59)$$

where $f = qu$ and u is the wave velocity. The physical domain is divided into N_e number of N^{th} order elements having $1 + N$ number of nodes (see fig. 2.15). We map the physical coordinate (x) of each element Ω_e into a representative computational element ($\xi \in [-1, 1]$) for reason that will become clear later. A linear mapping is given by the following expression

$$\xi = \frac{2}{\Delta x}(x - x_0) - 1, \quad (2.60)$$

where $\Delta x = x_N - x_0$ is the size of the 1D element. The symbols x_0 and x_N denotes the physical coordinates of the first and last node of the element, respectively. Notice that, depending on the problem, any higher order mapping can also be used. On each element, the solution is approximated as a linear combination of some higher order basis functions as

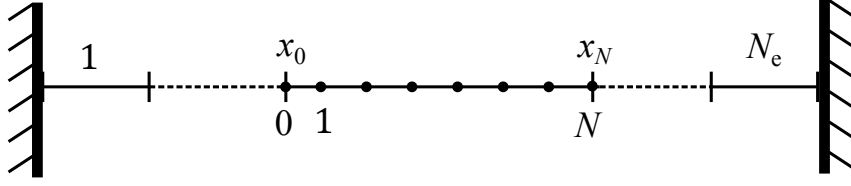


Figure 2.15: 1D domain and its discretization for the spectral-element method.

$$q_N(x, t) = \sum_{j=0}^N q_j(t) \psi_j(x), \quad (2.61)$$

and the basis functions are taken as the Lagrange polynomials defined as follows

$$\psi_i(r) = \prod_{\substack{j=0 \\ j \neq i}}^1 \frac{r - r_j}{r_i - r_j}, \quad (2.62)$$

Following the method of weighted residual, the approximate solution (eq. 2.61) is substituted into the governing equation (eq. 2.59) which produces a residual. The integrals of the product of the residual with the basis functions (Lagrange polynomials for the Galerkin approach) are equated to zero on each element

$$\int_{\Omega_e} \psi_i \left(\frac{\partial q_N}{\partial t} + \frac{\partial(q_N u)}{\partial x} \right) dx = 0 \text{ for } i = 0, 1, \dots, N \quad (2.63)$$

Substituting the expression of the approximate solution (eq. 2.61) into the previous equation yields

$$\sum_{j=0}^N \int_{\Omega_e} \left(\psi_i \psi_j \frac{dq_j}{dt} + \psi_i \frac{d\psi_j}{dx} q_j u \right) dx = 0, \quad (2.64)$$

The above equation can be written in the following matrix form

$$M_{i,j}^e \frac{d\mathbf{q}_j}{dt} + D_{i,j}^e \mathbf{q}_j u = 0, \quad (2.65)$$

where \mathbf{q}_j represents the column vectors of nodal unknowns q_j . The matrices $M_{i,j}^e$ and $D_{i,j}^e$ are called the mass and differentiation matrices, respectively. The expression of the mass matrix is

$$M_{i,j}^e = \int_{x_0}^{x_N} \psi_i(x) \psi_j(x) dx, \quad (2.66)$$

Transformation of the physical space to the computational space, using the relation $d\xi = \frac{2}{\Delta x} dx$, gives

$$M_{i,j}^e = \frac{\Delta x}{2} \int_{-1}^1 \psi_i(\xi) \psi_j(\xi) d\xi, \quad (2.67)$$

The above equation shows the advantage of mapping the physical element to a representative computational element. The integral in the equation is independent of the element and hence need to be calculated only once. The nodes points are distributed according to the Gauss-Legendre-Lobatto points and the same are used for evaluating the integral in the equation numerically using the quadrature rule as follows

$$M_{i,j}^e = \frac{\Delta x}{2} \sum_{k=0}^N w_k \psi_i(\xi_k) \psi_j(\xi_k), \quad (2.68)$$

where w_k are the quadrature weights. The size of the mass matrix is $(N + 1) \times (N + 1)$. The differentiation matrix is given by the following expression

$$D_{i,j}^e = \int_{x_0}^{x_N} \psi_i(x) \frac{d\psi_j(x)}{dx} dx = \int_{-1}^1 \psi_i(\xi) \frac{d\psi_j(\xi)}{d\xi} d\xi, \quad (2.69)$$

This completes the spatial discretization process using the spectral-element method. The resulting algebraic equations from each element are collected into a single linear system. For further demonstration, consider a linear element ($N = 1$). The basis functions are

$$\psi_0(\xi) = \frac{1}{2}(1 - \xi) \text{ and } \psi_1(\xi) = \frac{1}{2}(1 + \xi), \quad (2.70)$$

The mass and differentiation matrices are 2×2 matrices. For example, the mass matrix is

$$M_{i,j}^e = \frac{\Delta x}{2} \int_{-1}^1 \begin{pmatrix} \psi_0\psi_0 & \psi_0\psi_1 \\ \psi_1\psi_0 & \psi_1\psi_1 \end{pmatrix} d\xi, \quad (2.71)$$

which evaluates to

$$M_{i,j}^e = \frac{\Delta x}{6} \begin{pmatrix} 2 & 1 \\ 1 & 2 \end{pmatrix}, \quad (2.72)$$

Similarly, the differentiation matrix for the linear element is given by

$$D_{i,j}^e = \frac{1}{2} \begin{pmatrix} -1 & 1 \\ -1 & 1 \end{pmatrix}, \quad (2.73)$$

Assuming that the domain is divided into two linear elements of same size, there will be three nodes at which the dependent variable q needs to be evaluated. The second node ($i = 1$) will be shared by both the elements. The discretized equations for the first element are

$$\frac{\Delta x}{6} \begin{pmatrix} 2 & 1 \\ 1 & 2 \end{pmatrix} \frac{d}{dt} \begin{pmatrix} q_0 \\ q_1 \end{pmatrix} + \frac{1}{2} u \begin{pmatrix} -1 & 1 \\ -1 & 1 \end{pmatrix} \begin{pmatrix} q_0 \\ q_1 \end{pmatrix} = 0, \quad (2.74)$$

and for the second element are

$$\frac{\Delta x}{6} \begin{pmatrix} 2 & 1 \\ 1 & 2 \end{pmatrix} \frac{d}{dt} \begin{pmatrix} q_1 \\ q_2 \end{pmatrix} + \frac{1}{2}u \begin{pmatrix} -1 & 1 \\ -1 & 1 \end{pmatrix} \begin{pmatrix} q_1 \\ q_2 \end{pmatrix} = 0, \quad (2.75)$$

Since the second node is shared by both the elements, both contribute to the solution at $i = 1$. The final global assembly of the individual elemental equations results into the following linear system

$$\frac{\Delta x}{6} \begin{pmatrix} 2 & 1 & 0 \\ 1 & 4 & 1 \\ 0 & 1 & 2 \end{pmatrix} \frac{d}{dt} \begin{pmatrix} q_0 \\ q_1 \\ q_2 \end{pmatrix} + \frac{1}{2}u \begin{pmatrix} -1 & 1 & 0 \\ -1 & 0 & 1 \\ 0 & -1 & 1 \end{pmatrix} \begin{pmatrix} q_0 \\ q_1 \\ q_2 \end{pmatrix} = 0. \quad (2.76)$$

The resulting global matrix equation can be solved either by any direct (such as LU decomposition) or iterative method (for example Gauss-Seidel).

Next, let us consider the following Poisson equation in 1D

$$\frac{d^2q}{dx^2} = f, \quad (2.77)$$

Substituting the approximate solution into the above equation and multiplying it with the weighting function gives

$$\left[\psi_i \frac{dq_N}{dx} \right]_{x_0}^{x_N} - \int_{x_0}^{x_N} \frac{d\psi_i}{dx} \frac{dq_N}{dx} dx = \int_{x_0}^{x_N} \psi_i f_N dx, \quad (2.78)$$

where integration by parts was used. The first term on the left hand side of the above equation is a boundary term which can be absorbed into the boundary conditions and will be ignored. Substituting the expression of the approximate solution (eq. 2.61) into the above equation gives

$$-L_{i,j}^e \mathbf{q}_j = M_{i,j}^e \mathbf{f}_j, \quad (2.79)$$

where $L_{i,j}^e$ is the Laplacian operator given by the following expression

$$L_{i,j}^e = \int_{x_0}^{x_N} \frac{d\psi_i}{dx} \frac{d\psi_j}{dx} dx = \frac{2}{\Delta x} \int_{-1}^1 \frac{d\psi_i}{d\xi} \frac{d\psi_j}{d\xi} d\xi, \quad (2.80)$$

and $M_{i,j}^e$ is mass matrix given by eq. 2.67. For a linear element, the Laplacian operator evaluates to

$$L_{i,j}^e = \frac{1}{\Delta x} \begin{pmatrix} 1 & -1 \\ -1 & 1 \end{pmatrix}, \quad (2.81)$$

For higher dimensions, the basis functions are taken as the tensor product of the 1D Lagrange polynomials (eq. 2.62).

2.3.2 Flow simulation using the spectral-element method

In this section, the procedure for the solution of the governing equations of vortex-induced vibration problems will be described. As discussed, the flow field is solved in the reference frame of the body. The flow field is governed by the following non-dimensional Navier-Stokes equation written in the reference frame of the body

$$\frac{\partial \mathbf{u}}{\partial t} + \mathbf{u} \cdot \nabla \mathbf{u} = -\nabla p + \frac{1}{Re} \nabla^2 \mathbf{u} + \mathbf{a}_F, \quad (2.82)$$

where $\mathbf{a}_F = \frac{d\mathbf{V}_F}{dt}$ and \mathbf{V}_F are the non-dimensional acceleration and velocity of the reference frame, respectively. The time integration of eq. 2.82 is done in three stages. In each stage, one term of the Navier-Stokes equation is integrated. In the first step, the convective term is integrated to provide an intermediate velocity (\mathbf{u}')

$$\mathbf{u}' - \mathbf{u}^n - \Delta \mathbf{V}_F = \int_t^{t+\Delta t} \mathbf{u} \cdot \nabla \mathbf{u} dt, \quad (2.83)$$

where \mathbf{u}^n is the flow velocity field at the previous time step and $\Delta \mathbf{V}_F = \int_t^{t+\Delta t} \mathbf{a}_F dt$. This intermediate velocity is then used for the pressure sub-step

$$\mathbf{u}'' - \mathbf{u}' = - \int_t^{t+\Delta t} \nabla p dt. \quad (2.84)$$

The final velocity for the new time step is obtained in the third step by using the intermediate velocity found in the pressure sub-step

$$\mathbf{u}^{n+1} - \mathbf{u}'' = \frac{1}{Re} \int_t^{t+\Delta t} \nabla^2 \mathbf{u} dt. \quad (2.85)$$

The motion of the body is coupled with the fluid flow and hence the governing equations need to be solved in a coupled manner. Therefore, an iterative predictor-corrector scheme is used. The predictor step begins by getting an initial estimate for the velocity of the body at the next time step using a quadratic extrapolation of the body velocity from previous three time steps

$$\mathbf{V}_F^{(n+1)'} = 3\mathbf{V}_F^n - 3\mathbf{V}_F^{n-1} + \mathbf{V}_F^{n-2}, \quad (2.86)$$

The change in the body velocity ($\Delta \mathbf{V}_F$) can then be calculated by subtracting the body velocity at the current time step (\mathbf{V}_F^n) from the approximation of the velocity at next time step ($\mathbf{V}_F^{(n+1)'}$). Using the approximate body velocity at the next time step, the new

position of the body is calculated using a third-order Adams-Moulton method

$$\mathbf{r}_F^{(n+1)'} = \mathbf{r}_F^n + \frac{\Delta t}{12}(5\mathbf{V}_F^{(n+1)'} + 8\mathbf{V}_F^n - \mathbf{V}_F^{n-1}), \quad (2.87)$$

Using the prediction for the change in the body velocity ($\Delta\mathbf{V}_F'$), the convection step can be completed. A third-order Adams-Bashforth method is used for integration of eq. 2.83

$$\mathbf{u}' = \mathbf{u}^n + \Delta\mathbf{V}_F' + \frac{\Delta t}{12}(23C^n - 16C^{n-1} + 5C^{n-2}), \quad (2.88)$$

where $C^n = \mathbf{u}^n \cdot \nabla\mathbf{u}^n$ is the non-linear convection term at n^{th} time step. Notice that the above equation represents an explicit integration method which is used only for the first iteration. A modified semi-implicit version of eq. 2.88 is used for next iterations which will be explained later.

Moving on to the pressure sub-step, the integration of eq. 2.84 is done using a second-order Adams-Moulton method

$$\frac{\mathbf{u}'' - \mathbf{u}'}{\Delta t} = -\frac{1}{2}(\nabla p^n + \nabla p^{n+1}) = -\nabla p^{n+1/2}, \quad (2.89)$$

Both fluid pressure and velocity are unknowns in the above equation. Taking the divergence of the above equation and enforcing continuity condition on the intermediate velocity ($\nabla \cdot \mathbf{u}'' = 0$) results in the following Poisson equation for the pressure field

$$\nabla^2 p^{n+1/2} = \frac{\nabla \cdot \mathbf{u}'}{\Delta t}, \quad (2.90)$$

After calculating the pressure field, the second intermediate velocity can be obtained from eq. 2.89. In the third diffusion sub-step, an implicit second-order Adams-Moulton method is used for obtaining the flow velocity at the next time step

$$\frac{\mathbf{u}^{(n+1)'} - \mathbf{u}''}{\Delta t} = \frac{1}{2Re}(\nabla^2 \mathbf{u}^{n+1} + \nabla^2 \mathbf{u}^n). \quad (2.91)$$

This completes the predictor part of the iterative solution procedure. The corrector step updates the approximation for the body velocity ($\mathbf{V}_F^{(n+1)'}$). This is done by calculating the fluid forces acting on the body using the approximation of the flow velocity at the next time step obtained from eq. 2.91. The fluid forces along with the approximate body position at the next time step is used for obtaining the acceleration of the body (\mathbf{a}_F^{n+1}). The body acceleration is then integrated over the time step to update the approximation for the body velocity

$$\mathbf{V}_F^{(n+1)'} = \mathbf{V}_F^n + \frac{\Delta t}{24}(25\mathbf{a}_F^{n+1} - 2\mathbf{a}_F^n + \mathbf{a}_F^{n-1}), \quad (2.92)$$

With the updated body velocity, the position of the body is also updated using eq. 2.87. This completes the one iteration of the predictor-corrector method.

As mentioned previously, the convective sub-step is different for subsequent iterations. Since the approximation of the flow velocity at the next time step ($\mathbf{u}^{(n+1)'}$) is available, a third-order Adams-Moulton method is used for the numerical integration of eq. 2.83

$$\mathbf{u}' = \mathbf{u}^n + \Delta \mathbf{V}_F' + \frac{\Delta t}{12}(5C^{(n+1)'} + 8C^n - C^{n-1}), \quad (2.93)$$

The pressure and diffusion sub-steps are performed similar to the first iteration. The corrector step produces a new approximation of the body velocity ($\mathbf{V}_F^{(n+1)''}$). Instead of using the new approximation for subsequent calculations, it is under-relaxed for numerical stability

$$\mathbf{V}_F^{(n+1)} = \mathbf{V}_F^{(n+1)'} + \omega(\mathbf{V}_F^{(n+1)''} - \mathbf{V}_F^{(n+1)'}), \quad (2.94)$$

where $\mathbf{V}_F^{(n+1)''}$ and $\mathbf{V}_F^{(n+1)'}$ are representing the body velocity approximations obtained from the current and previous iterations, respectively. The under-relaxation parameter ($0 < \omega \leq 1.0$) determines the amount of correction added to the existing approximation. The iterations continue till the body velocity, lift and fluid velocity converge to a specified tolerance. Following pressure boundary condition is applied at the body surface and free stream boundaries

$$\frac{\partial p^{n+1/2}}{\partial \mathbf{n}} = \mathbf{n} \cdot \left[C^n + \frac{1}{Re}(\nabla \times (\nabla \times \mathbf{u})^n) \right], \quad (2.95)$$

where \mathbf{n} is the unit normal vector to the boundary.

Chapter 3

Experimental Methodology

Vortex-induced vibration experiments were performed for a circular cylinder and flat plates at FLAIR laboratory of Monash University. The experiments served as a higher Reynolds number extension of the numerical studies. The details of the experimental techniques used in performing the experiments and collecting data are discussed in this chapter. The details of the flow system is first discussed in the section 3.1. The details of the structural part of the fluid-solid interaction is discussed in section 3.2. A passive eddy current based damping system was made which is described in section 3.3. Finally, the flow visualization method is discussed in section 3.4.

3.1 Water channel

The vortex-induced vibration (VIV) experiments were performed in the recirculating free surface water channel facility at FLAIR laboratory of Monash University. A schematic of the water channel is shown in fig. 3.1. It consists of three main section: a inlet section, a test section and a diffuser. The inlet contains a series of flow conditioning sections to reduce the turbulence. The flow turbulence is reduced using vane, mesh, settling chamber, honeycomb and fine mesh. The turbulence level in the test section was less than 1%. The test section is where the experimental setup of VIV is kept. The test section is 4 m long, 0.6 m wide and 0.8 m deep. Its walls are made of glass walls for flow visualization. The diffuser collects the fluid for recirculating it back to the inlet using a centrifugal pump. The flow velocity in the test section is controlled by the rotational speed of the pump. The test section velocity can be varied in a range of 0.048 – 0.456 m/s. The pump speed and thereby the flow velocity in the test section is controlled using the LabVIEW™ software. The calibration of the test section flow velocity as a function of the pump rotational speed was done using particle image velocimetry (PIV). The measurements showed a linear relationship between the two quantities which was used in the experiments to maintain a particular flow velocity.

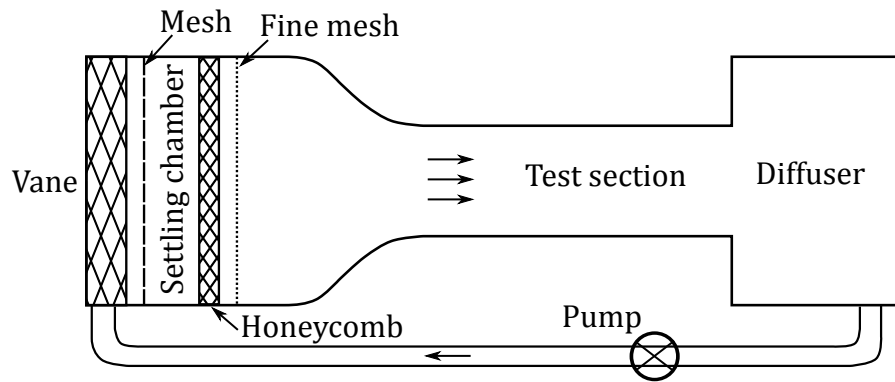


Figure 3.1: A schematic view of the water channel.

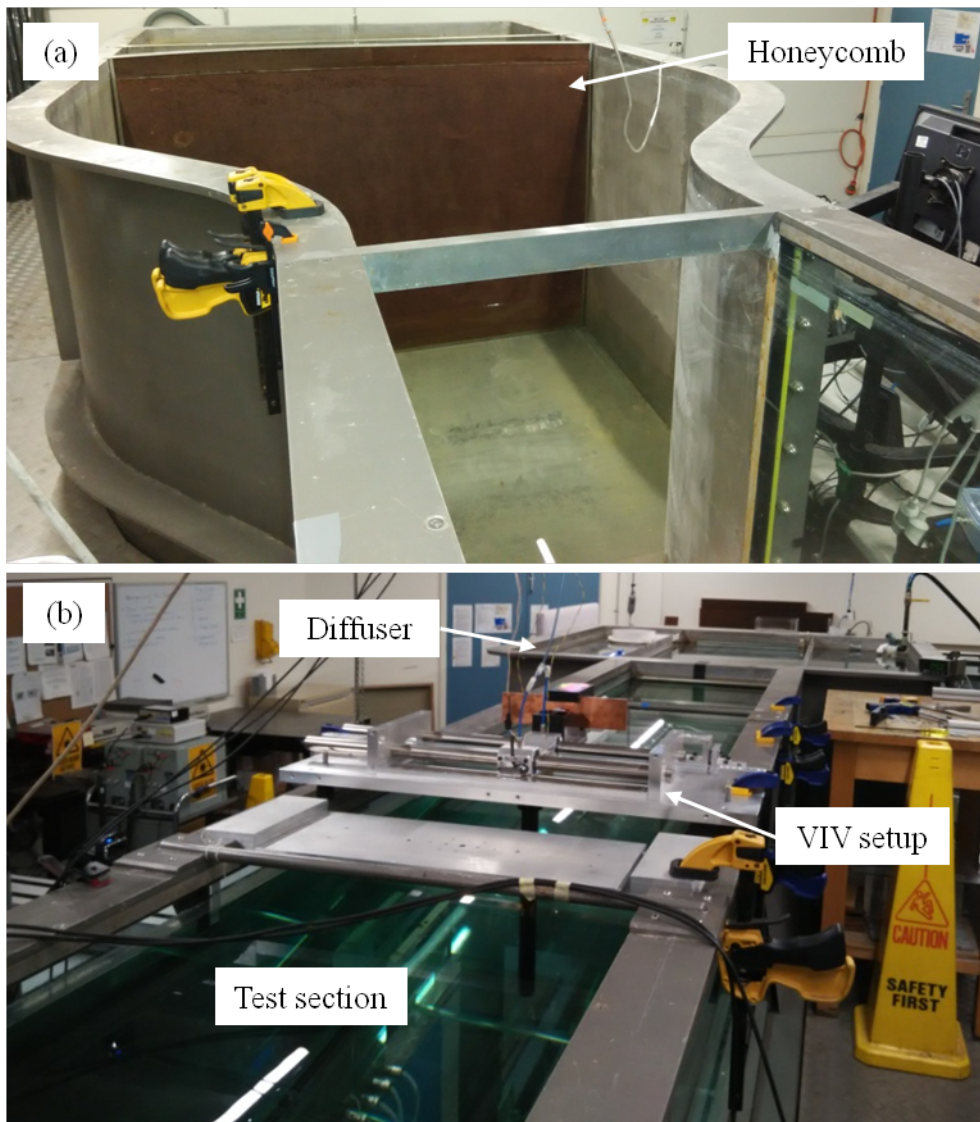


Figure 3.2: (a)The inlet of the water channel and (b) test section and diffuser.

3.2 Vortex-induced vibration setup

The experiments involve a bluff body (a circular cylinder or a flat plate) kept in a free stream of fluid flow with only one-degree of freedom transverse to the incoming flow. The mechanical arrangement of the structural part of the experiment will be described in this section. The VIV setup is shown in fig. 3.3. It consisted of a carriage to which the bluff body is attached. A strain gauge based force sensor is attached between the carriage and the body for measuring the lift force. The sensor and the body are attached at the center of the carriage using screws. Springs are attached at both side of the carriage. The carriage has two holes on both sides which are fitted with air bushings. The air bushings are part of the air bearing system which allow very low friction motion of the body. The air bearing is composed of the air bushing, guide shafts and compressed air. The air bushings are supplied with the compressed air which is injected between the small space between the bushing and the shaft. The thin sheet of air acts as a lubricant allowing low friction relative motion. In the present case, the guide shafts are stationary and the bushings moves along with the carriage. Compressed air is injected into the bushings from holes drilled into the carriage. The low friction feature allows small structural damping and therefore allows to observe maximum possible vibration amplitude in VIV. The displacement of the carriage (and thereby the body) is measured using a non-contact digital linear optical encoder having $1.0\ \mu\text{m}$ resolution. It uses an optical ribbon with micrometer gratings. The optical encoder shines light at the ribbon and the reflected light is processed to calculate the displacement information. The optical encode is mounted on the side of the carriage and the ribbon is pasted on a fixed flat surface. Everything is mounted on a base plate. The base plate is kept on the test section. A damper system consisting of a permanent magnet and a copper plate is also shown in fig. 3.3. The details of the damper system will be described in the next section.

3.3 Damper system

A damping mechanism was introduced into the existing VIV setup for power extraction studies. It worked on the principle of eddy currents. The damper system that was made for the current experiments is shown in fig. 3.4. Primarily, it was composed of a moving permanent magnet and a stationary copper plate. The magnet moved parallel to the copper plate at a fixed gap. The relative motion results in creation of the eddy currents inside the copper plate. The eddy currents creates a magnetic field which applies an opposing force on the magnet whose magnitude is proportional to the velocity of the magnet. The value of the damping coefficient was controlled by changing the gap between the magnet and the plate. A cylindrical shaped neodymium permanent magnet

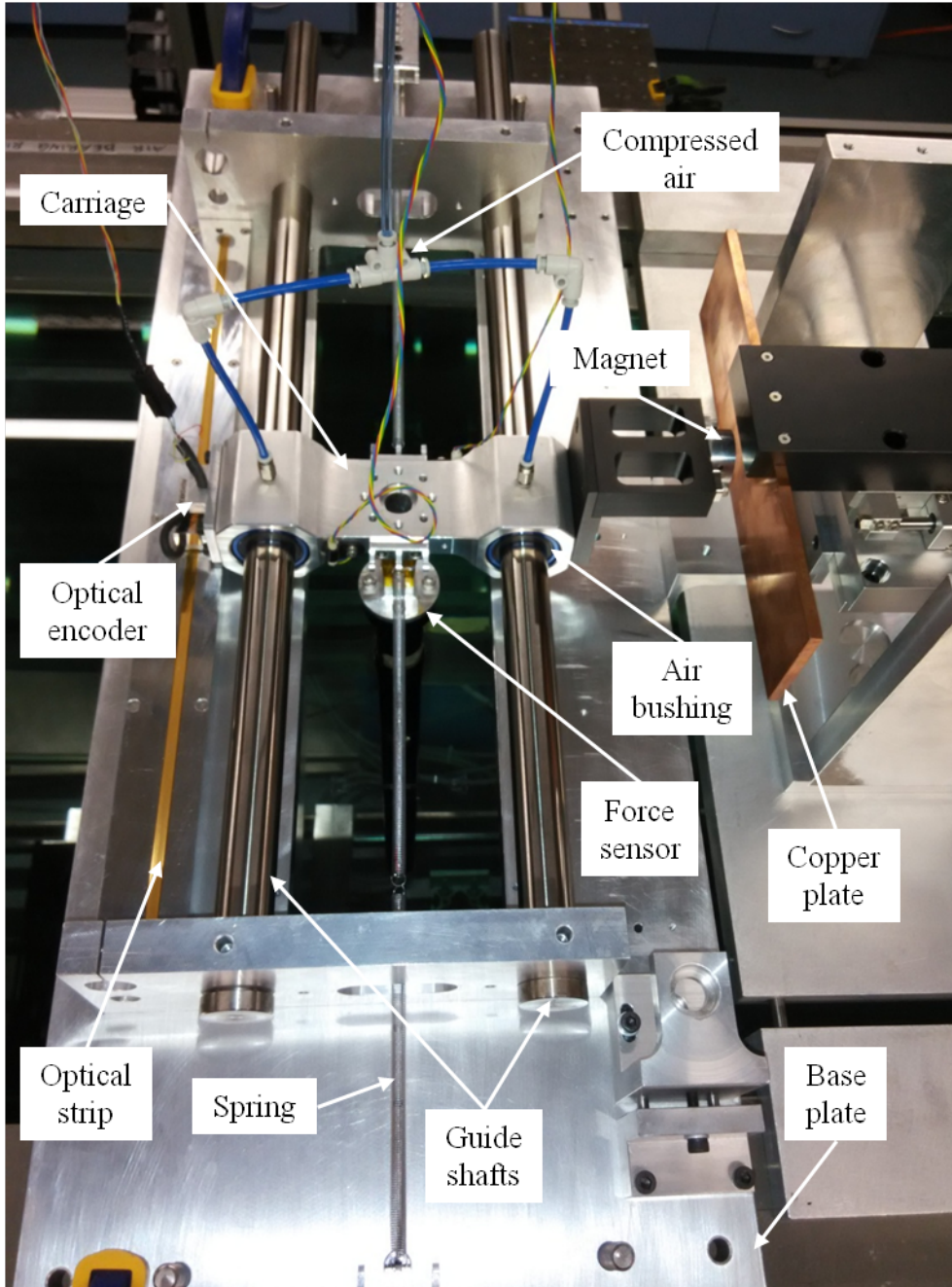


Figure 3.3: The setup used for the VIV experiments.

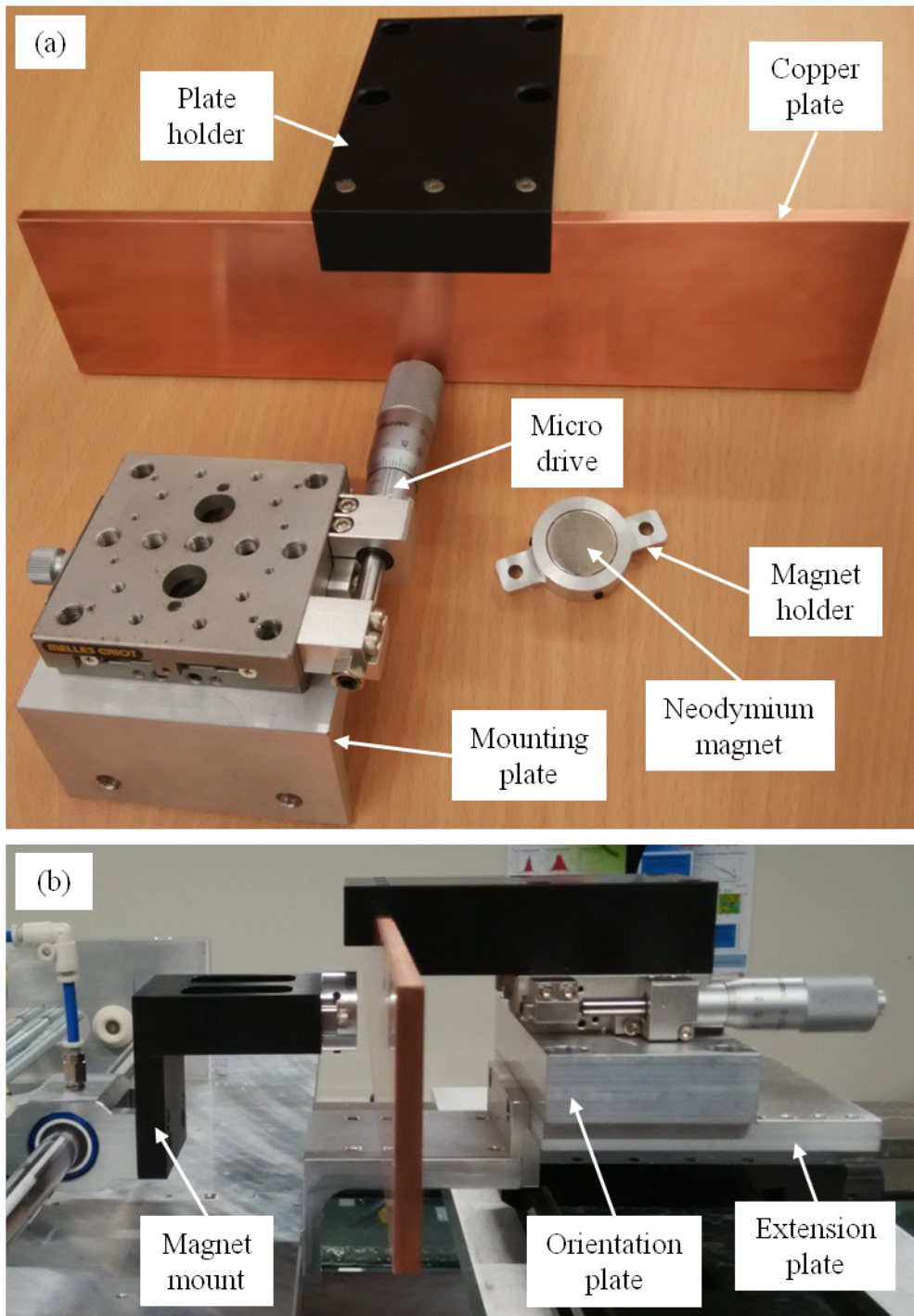


Figure 3.4: (a) Various components of the damper system and (b) damper attached to the VIV setup.

was attached to the carriage with the help of a magnet mount and a magnet holder so that the magnet followed the motion of the body. The stationary copper plate was mounted on a manual linear stage, with the help of a plate holder, that was driven by a micrometer having 0.01 mm resolution. The linear stage allowed the gap between the magnet and the plate to be controlled in a precise manner. The magnet needed to remain at the same gap irrespective of its transverse location so that the damping ratio was a constant at any fixed chosen gap. This was achieved by mounting the linear stage on an orientation plate having some degree of freedom to rotate about the vertical axis. The orientation plate was locked in a position where the line of movement of the magnet was parallel to the plate. This ensured that the damping coefficient did not vary with the transverse location of the body. The orientation plate was mounted on an extension plate which had series of holes to mount the orientation plate at various locations of desired gap. The extension plate was attached to the mounting plate which was screwed to the base plate. The damping coefficient values at various gaps were measured via performing free decay experiments. The damping ratio versus the gap relationship was found to be non-linear with sharp changes in the damping ratio at smaller gaps.

3.4 Flow visualization

The flow velocity and vortex structures were measured using particle image velocimetry (PIV) technique. In this method, micro-sized particles are introduced into the flow which are almost mass less as compared to the fluid and therefore they follow a path determined by the local flow velocity. The particles are illuminated with a laser and a pair of photographs with milliseconds of time delay are captured from a high speed camera. The pair of images are processed using cross-correlation techniques to determine the instantaneous flow velocity. The PIV setup of the current experiments is shown in fig. 3.5. A Nd:YAG (Neodymium-doped Yttrium Aluminium Garnet) continuous green laser was used in the experiments. The laser beam was converted into a planar sheet using a cylindrical lens. The laser was mounted on a positioning system that was used for placing the laser sheet at the middle of the immersed length of the bluff body. A high speed camera was mounted underneath the test section to capture the particles images. The camera shutter was triggered via a TTL signal generator and the image pairs with 2016×2016 pixels resolution were captured at 0.1 s of interval. The time interval (Δt) between the images of a image pair was controlled using a timing controller. The two images of the image pair are divided into equal number of interrogation windows. For two interrogation windows from the two images, cross-correlation is used to find the displacement of the particles from one image to the second. Fast Fourier Transform (FFT) is used for cross-correlation calculations to speed up the computations. The calculated distances are in

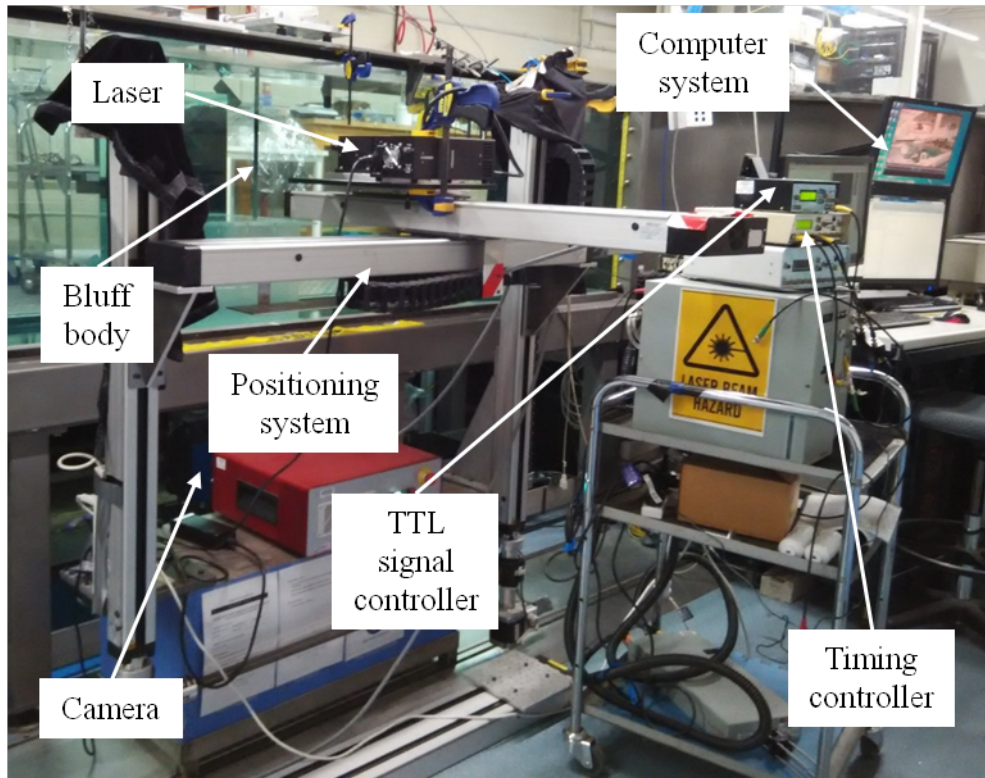


Figure 3.5: The particle image velocimetry setup used for flow visualization.

pixels which are converted into the physical units by finding out the magnification factor. It is measured by placing a ruler at the laser plan and counting the number of pixels for a known unit of distance. The local fluid velocity then can be calculated with the help of cross-correlation calculations, magnification factor and the time interval (Δt). A phase-averaging method was used for finding the average vorticity field. Since the motion of the freely vibration bluff body was periodic in most of the cases, its motion was divided into a number of phases (for example 24). Then based on the trigger time and corresponding body position in its cycle of oscillation, the image pairs were sorted into those phases. Finally, image pairs that lied in the same phase were averaged to give an average vorticity field corresponding to that phase.

Chapter 4

Harnessing Electrical Power from Vortex-Induced Vibration of a Circular Cylinder

Renewable energy sources are likely to become essential due to continuously increasing energy demands together with the depletion of natural resources that are currently used for power generation, such as coal and gas. They are also advantageous in terms of their reduced environmental impact. Here, the generation of electrical power from Vortex-Induced Vibration (VIV) of a cylinder is investigated numerically. The cylinder is free to oscillate in the direction transverse to the incoming flow. The cylinder is attached to a magnet that can move along the axis of a coil made from conducting wire. The magnet and the coil together constitute a basic electrical generator. When the cylinder undergoes VIV, the motion of the magnet creates a voltage across the coil, which is connected to a resistive load. By Lenz's law, induced current in the coil applies a retarding force to the magnet. Effectively, the electrical generator applies a damping force on the cylinder with a spatially varying damping coefficient. For the initial investigation reported here, the Reynolds number is restricted to $Re \leq 200$, so that the flow is laminar and two-dimensional (2D). The incompressible 2D Navier-Stokes equations are solved using an extensively validated spectral-element based solver. The effects of the electromagnetic (EM) damping constant ξ_m , coil dimensions (radius a , length L), and mass ratio on the electrical power extracted are quantified. It is found that there is an optimal value of ξ_m (ξ_{opt}) at which maximum electrical power is generated. As the radius or length of the coil is increased, the value of ξ_{opt} is observed to increase. Although the maximum average power remains the same, a larger coil radius or length results in a more robust system in the sense that a relatively large amount of power can be extracted when ξ_m is far from ξ_{opt} , unlike the constant damping ratio case. The average power output is also a function of Reynolds number, primarily through the increased maximum oscillation amplitude that

occurs with increased Reynolds number at least within the laminar range, although the general qualitative findings seem likely to carry across to high Reynolds number VIV.

4.1 Introduction

Renewable energy sources, such as wind, solar, geothermal and gravitational, are receiving increased attention due to the continuing depletion of natural resources used for coal or gas-fired electrical power generation together with the associated environmental emissions. An alternative approach to electrical power generation is to convert the available flow energy of a free-flowing fluid into electrical energy. Wind turbines provide one example (Carli et al., 2010; Vermeer et al., 2003), although the effect of their low-frequency noise on health is debated (Knopper et al., 2011). Another example is the use of flexible piezoelectric structures. Michelin and Doaré (2013) studied the efficiency of the electrical power generation due to flutter of a flexible flag with piezoelectric patches attached. They used a semi-analytical approach where the fluid forces were modelled assuming potential flow and the Euler-Bernoulli model was used for the flag. A maximum 12% efficiency was reported for the largest mass ratio and flow velocity considered in their work. Akcabay and Young (2012) numerically studied the fully coupled fluid-solid interaction of a thin beam in incompressible viscous flow. The effect of the ratio of solid to fluid inertia forces on the flutter was investigated and the possibility of power extraction was demonstrated. Akaydin et al. (2010) performed experiments for energy extraction from a piezoelectric beam located in the wake of a circular cylinder. The length of the beam was equal to the cylinder diameter (D). The power output was examined as a function of transverse and downstream beam location. Maximum power was produced when the beam was positioned on the centreline at $2D$ from the rear of the cylinder. Wang et al. (2012) exploited pressure fluctuations in the wake of a trapezoidal bluff body to oscillate a flexible diaphragm connected to a permanent magnet. A theoretical model was developed to study the effects of the system parameters on power generation. A prototype was constructed that produced several micro-watts of electrical power.

Vortex-induced vibration (VIV) of a bluff body provides another method for extracting power from flow energy that has received considerable attention; see the review by Xiao and Zhu (2014) on flapping-foil based energy harvesters. Mehmood et al. (2013) numerically investigated energy harvesting from VIV of a circular cylinder using a piezoelectric transducer. It was found that there is an optimal load resistance for harvesting maximum power but the optimal case does not coincide with the largest amplitude of oscillations. In their experiments, Nishi et al. (2014) considered two identical cylinders separated by a fixed distance in the streamwise direction. Two cases, for which one then the other cylinder was kept fixed, were compared with the isolated cylinder case. An

electromagnetic transducer was used to convert the cylinder motion into electrical energy. It was found that the case with the rear cylinder fixed produced the largest vibration amplitude and the highest efficiency of 15%. [Dai et al. \(2016\)](#) experimentally investigated four different installations of a cylinder on a piezoelectric beam for harnessing energy. Out of the four, three configurations had the cylinder axis aligned with the beam and for the fourth the cylinder had its axis perpendicular to the beam. The fourth configuration was reported to produce the maximum power. [Hobbs and Hu \(2012\)](#) experimentally investigated energy extraction from a linear array of four cylinders. Each cylinder was attached to a piezoelectric energy transducer. They studied the effect of cylinder spacing and flow speed on extracted power. Downstream cylinders were found to produce a larger amount of power than upstream cylinders. They also found that power increased only until the third cylinder for low wind speeds but continued to increase for the fourth cylinder for higher wind speeds. This suggests that the optimal number of power harvesting devices depends on the Reynolds number, at least for a certain range. [Barrero-Gil et al. \(2012\)](#) undertook a semi-analytical analysis of power harvesting from transverse VIV of a circular cylinder. The energy extraction process was modelled as a linear damper. Data from forced vibration experiments were used as input for the governing equations of motion of the cylinder. The effects of mass and damping ratios were studied, and it was found that relatively high efficiency can be achieved over a large range of reduced velocity for lower mass ratios.

From the above review, it is clear that there has been considerable valuable research undertaken on this important problem. Given the complexity of the system and flow physics involved, it is understandable that simplifications have been made in the modelling undertaken. To-date there has been no attempt to match the form of the extracted power output to more realistic damping models. To do so is important for two reasons — it could affect the power output if the form of its extraction is not constant versus variable damping, and indeed the variable damping could also affect the flow physics of this vortex-induced vibration system and consequently the incoming power input available for extraction. Hence, the validity of the assumption that power output predictions based on constant damping ratio provides a good predictor for the variable damped case has not been investigated in the literature. In addition, a detailed analysis of a magnet-coil type energy harvester based on the principle of electromagnetic induction appears yet to have been reported. The aim of the present work is to address these open questions.

The layout of this chapter is as follows. In section [4.2](#), the governing theory for the fluid-structure interaction problem is presented, followed by the specifics of the electromagnetic energy-extraction system. The numerical approach to solve this coupled system is then presented. Key results are given in section [4.3](#). In section [4.3.1](#) the extracted power is quantified and compared for systems having constant and electromagnetically

based variable damping coefficients. Following this, the details of the EM damping system are discussed. Next the influences of tuneable parameters on system behaviour are quantified, these include: the length and radius of the coil, mass ratio, and Reynolds number. Finally the influence of using dual generators is determined in section 4.3.6, before providing conclusions.

4.2 Problem definition and methodology

4.2.1 Governing equations

A vertical elastically mounted circular cylinder of diameter $D (= 1)$ and length L_c is placed in a free-stream flow. The cylinder is free to oscillate in the transverse (y) direction, with the cylinder displacement denoted by y . The Reynolds number is chosen so that the flow is two-dimensional (2D), and the fluid is incompressible. The computational problem is set in the reference frame of the cylinder. The governing equations are the non-dimensional Navier-Stokes equations in an accelerated frame of reference

$$\frac{\partial \mathbf{u}}{\partial t} + (\mathbf{u} \cdot \nabla) \mathbf{u} = \nabla p + \frac{1}{Re} (\nabla^2 \mathbf{u}) + \mathbf{a}_F, \quad (4.1)$$

where \mathbf{u} and p are the fluid velocity and kinematic pressure, respectively, and \mathbf{a}_F is the acceleration of the reference frame. The freestream velocity U and the cylinder diameter D are used as the reference scales, respectively, and to define the Reynolds number, $Re = UD/\nu$, where ν is the kinematic viscosity of the fluid. The cylinder is attached to a magnet (magnetic moment μ_m) that can move along the axis of an electrically conducting coil of non-dimensional radius a , length L , and composed of N turns (see fig. 4.1). According to Faraday's law of electromagnetic induction, the motion of the magnet produces an emf (ϵ) across the coil. If the coil is connected to a resistive load R then the induced current in the coil is $i = \epsilon/R$. The induced current opposes the motion of the magnet by applying an electromagnetic force (F_m), given by the following expression

$$F_m^* = c_{m0} g^2 \dot{y}^*, \quad (4.2)$$

where $*$ is used to represent dimensional variables. Also, $c_{m0} = \mu_m^2 / (RD^4)$ is a constant and $g = g(y(t))$ is a function of dimensions of the coil and its distance from the magnet. It is given by the following equation based on the single magnetic dipole approximation (Donoso et al., 2010)

$$g = \left(\frac{2\pi N a^2}{L} \right) \left[\frac{1}{(a^2 + (y_{cm} - L/2)^2)^{3/2}} - \frac{1}{(a^2 + (y_{cm} + L/2)^2)^{3/2}} \right], \quad (4.3)$$

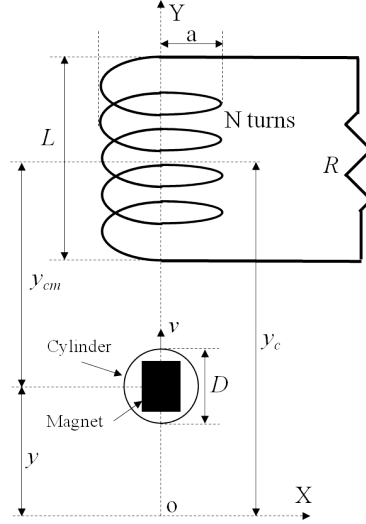


Figure 4.1: The cylinder-magnet assembly moving along the axis of the conducting coil.

with y_{cm} the non-dimensional distance between the magnet and coil. The electromagnetic force can be considered as a damping force with a non-constant damping coefficient $c_m = c_{m0}g^2$. The motion of the cylinder-magnet assembly is governed by the following equation

$$m_{cm}\ddot{y}^* + c\dot{y}^* + ky^* = F_l^* + F_m^*, \quad (4.4)$$

where m_{cm} is the mass of the cylinder-magnet assembly and F_l^* is the lift force on the cylinder. The second term on the left-hand side of eq. 4.4 represents a power transducer based on a constant damping (CD) assumption, i.e., $c = \text{constant}$ (Barrero-Gil et al., 2012). Notice that when the constant damping (CD) transducer is used then the electromagnetic damping (EMD) transducer is turned off and vice-versa. The natural frequency of the above system in a vacuum is given by $f_n = \frac{1}{2\pi}\sqrt{k/m_{cm}}$. Following the standard procedure of nondimensionalization of eq. 4.4, the damping and mass ratios are defined as $\xi = c/c_c$ and $m = m_{cm}/m_f$, respectively, where $m_f = \rho\frac{\pi}{4}D^2L_c$ is the mass of the displaced fluid and $c_c = 4\pi m_{cm}f_n$ is the critical damping, below which the system response has a decaying sinusoidal variation. Similarly, the electromagnetic damping constant is defined as $\xi_{m0} = c_{m0}/c_c$, so that the non-dimensional expression for the electromagnetic force is given by

$$F_m = 2\pi^2 m \xi_m f_n \dot{y}, \quad (4.5)$$

with $\xi_m = \xi_{m0}g^2$ the EM damping ratio. Using above definitions, the following non-dimensional form of eq. 4.4 is obtained as

$$\ddot{y} + 4\pi(\xi + \xi_m)f_n\dot{y} + 4\pi^2 f_n^2 y = \frac{2}{\pi} \frac{C_L}{m}. \quad (4.6)$$

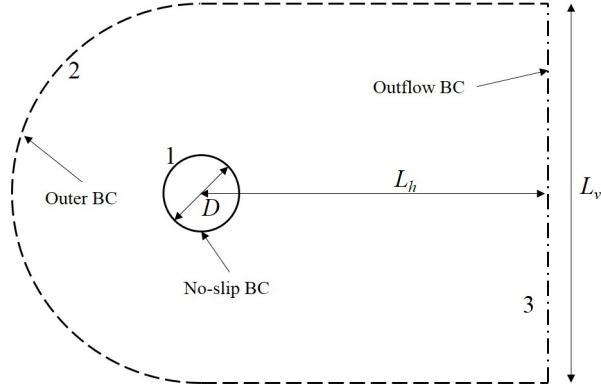


Figure 4.2: Computational domain for VIV of a circular cylinder.

Here, $C_L = F_l^* / (\frac{1}{2}\rho U^2 D L_c)$ is the lift coefficient for the cylinder. In addition, the natural frequency of the cylinder-magnet assembly in the fluid is given by $f_N = \frac{1}{2\pi} \sqrt{k/m_{eff}}$. The *effective mass* of the system in the fluid (m_{eff}) is given by the sum $m_{eff} = m_{cm} + m_a$, where m_a is the added mass of the fluid which the cylinder accelerates. The added mass can be expressed as $m_a = c_a m_f$ with $c_a = 1$ from potential flow theory. The non-dimensional reduced velocity is defined as $U_r = U/(f_N D)$. The dimensionless power is defined as the ratio of the power dissipated by the damper to the power available over the fluid region occupied by the cylinder ($\frac{1}{2}\rho U^3 D L_c$). It can also be considered as the efficiency of the system. The electrical power can be calculated by multiplying the electromagnetic force with the velocity of the magnet $P(t) = F_m \dot{y}$. The average power over a period of oscillation (T) of the cylinder is calculated as

$$\bar{P} = \frac{1}{T} \int_T P(t) dt. \quad (4.7)$$

4.2.2 Numerical formulation

The fluid equations and cylinder equations of motion are solved in a coupled manner using a previously validated spectral-element code (e.g., see [Leontini et al., 2006b,a](#); [Thompson et al., 2006](#), and references therein). More details on the method can be found in those papers, so only a brief description will be given here. The spatial discretisation uses the nodal spectral-element approach ([Karniadakis and Sherwin, 1999](#)), which is essentially a high-order Galerkin finite-element method. The *shape and weighting* functions are tensor product Lagrangian interpolating polynomials based on node points distributed according to the Gauss-Legendre-Lobatto quadrature integration points, which in turn is used to approximate the integrals from application of the weighted residual method. Importantly, the method achieves spectral (or exponential) convergence as the order of the interpolating

polynomials is increased (Karniadakis and Sherwin, 1999). The time-integration of the spatially discretised equations is achieved by a fractional step or time-splitting method (e.g., Chorin, 1968a; Karniadakis and Sherwin, 1999; Thompson et al., 2006), in which the convective, pressure and diffusion terms of the Navier-Stokes equations are integrated sequentially, using an explicit Adam-Bashforth method for the convective substep and the θ -corrected implicit Crank-Nicholson method for the diffusive substep (Canuto et al., 2006). The pressure substep is used to satisfy continuity and is also treated implicitly. The higher-order pressure boundary condition applied at the cylinder surface is derived from the Navier-Stokes equations to provide the pressure-normal derivative (see Karniadakis et al., 1991). A fuller description can be found in Thompson et al. (2006). For the coupled problem, the acceleration of the frame is added to the convective substep, and iteration proceeds during each full timestep until the fluid velocity field, cylinder velocity and the cylinder applied force converge. Testing was performed to ensure that each of these three convergence criteria are small enough to achieve 1% accuracy or better in predicting the oscillation amplitude evolution. It has been previously been used to model vortex-induced vibrations of inline (Leontini et al., 2013, 2011), transverse (Leontini et al., 2006a,b), and rotationally (Lo Jacono et al., 2010) oscillating cylinders, and even tethered spheres (Lee et al., 2013).

4.2.3 Computational domain and boundary conditions

The computational domain, shown in fig. 4.2, extends $L_h = 25D$ and $L_v = 40D$ in the downstream and transverse directions, respectively. Thus the cross-stream blockage is 2.5%. The inlet is semicircular with diameter L_v . The fluid velocity is prescribed as $u = U, v = -\dot{y}$ at the inlet, top and bottom boundaries, where \dot{y} is the velocity of the cylinder. No-slip conditions are applied at the cylinder boundary. Neumann conditions is applied at the outlet for the fluid velocity and the pressure is taken as constant.

4.2.4 Resolution studies and validation

The base computational mesh is the same as that used by Leontini et al. (2006b) for their studies of transverse oscillations of a circular cylinder at $Re = 200$, except that the blockage has been reduced by adding an extra layer of cells to extend the transverse dimension from 30 to $40D$. It was verified that the same amplitude/reduced-velocity response curve was reproduced from that study for the constant damping case. For the current work, the majority of simulations were undertaken at $Re = 150$, ensuring that the flow remained two-dimensional. Leontini et al. (2007) showed through stability analysis that the wake does not undergo transition to three-dimensionality prior to $Re = 250$, at least in the high-amplitude lock-in region. For the bulk of the simulations reported in

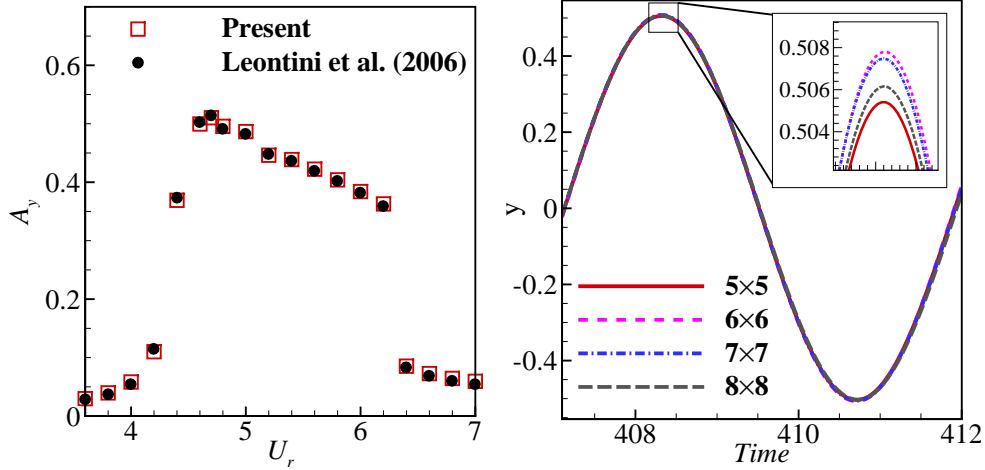


Figure 4.3: a) Comparison of the cylinder response with the published data and b) effect of spectral element resolution on the cylinder displacement.

this chapter, 5×5 noded elements were used for the macro-elements of the mesh. This is sufficient to guarantee the prediction of the peak oscillation amplitude of vibrations to better than 1% for the Reynolds numbers considered.

To provide more confidence in the predictions, validation and resolution tests are presented in fig. 4.3a and 4.3b, respectively. In fig. 4.3a, the cylinder displacement amplitude (A_y) obtained by the present solver is compared with that of the Leontini et al. (2006b) for a range of reduced velocities (U_r) at $\text{Re} = 200$, $m = 10$ and $\xi = 0.01$. Individual values of A_y differ by less than 1% from the published data. For the resolution study $U_r = 4.7$ was chosen, which was the reduced velocity leading to maximum cylinder displacement. To perform the resolution study, the number of elements in the computational mesh was fixed while varying the number of nodes per element. In fig. 4.3b, the temporal variation of the cylinder displacement is shown for different numbers of nodes per element. This indicates the 5×5 element-based mesh predicts the maximum displacement to within better than 1% of the most resolved mesh tested. Hence, this mesh was used for subsequent simulations.

4.3 Results

4.3.1 Constant versus EM damping ratio

In this section, the behaviour of using the electromagnetic damping (EMD) is compared with the constant damping (CD) in terms of energy extraction. The average power (\bar{P}) is a function of damping ratio, reduced velocity and mass ratio. Initially, the mass ratio is fixed at $m = 2$, and the reduced velocity is taken as $U_r = 5.2$ which corresponds

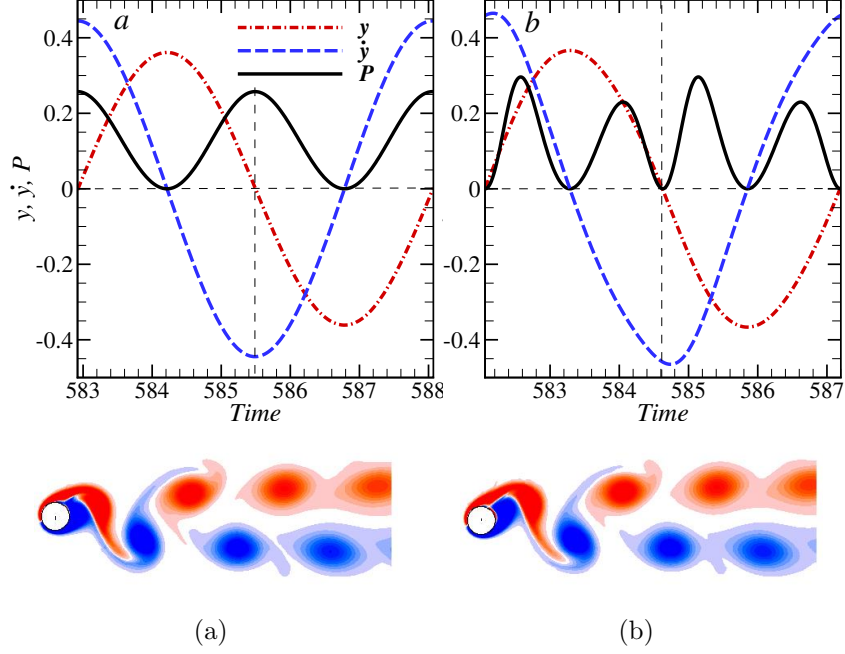


Figure 4.4: Top: Temporal variation of power, position and velocity of the cylinder for (a) CD ($\xi = 0.14$) and (b) EMD ($\xi_{m0} = 2.4 \times 10^{-5}$, $a = 0.6$, $L = 0.6$) cases, at $U_r = 5.2$ and $m = 2$. Vorticity contours (scale -2 to 2) corresponding to these cases are shown below each plot.

to the lock-in condition at $Re = 150$ (Leontini et al., 2006b). For the EMD case, the length and radius of the coil are both taken as $0.6D$. Time variations of power, transverse displacement (y) and transverse velocity (\dot{y}) of the cylinder over an oscillation cycle are shown in fig. 4.4 for the CD and EMD cases. The plots correspond to a value of the damping ratio that produces the maximum average power (\bar{P}_{max}). Let f_p and f_c be the fundamental frequencies of power and cylinder transverse displacement, respectively. As seen in fig. 4.5, f_p is 2 and 4 times f_c for the CD and EMD cases, respectively. In the CD case, peak electrical power is generated when the cylinder passes through its mean position ($y = 0$), where it has the maximum speed. The same is not true for the EMD case, where peak power is generated when the cylinder displacement is $y = \pm 0.23$. There are two distinct local maxima for power, as seen in fig. 4.4b. Also notice that the velocity profile of the cylinder is not sinusoidal in the EMD case. The instant of maximum velocity does not coincide with that of the mean position. Therefore the two peaks of power have different magnitude even though they occur when the cylinder is at the same distance from its mean position. The lower and higher peaks occur when the cylinder is moving towards and away from its mean position, respectively. The peak power in the EMD case (0.30) is higher than that of the CD case (0.26).

The vorticity patterns for both the cases are also compared in fig. 4.4. In both cases the $C(2S)$ vortex shedding mode is observed (e.g., Williamson and Govardhan, 2004),

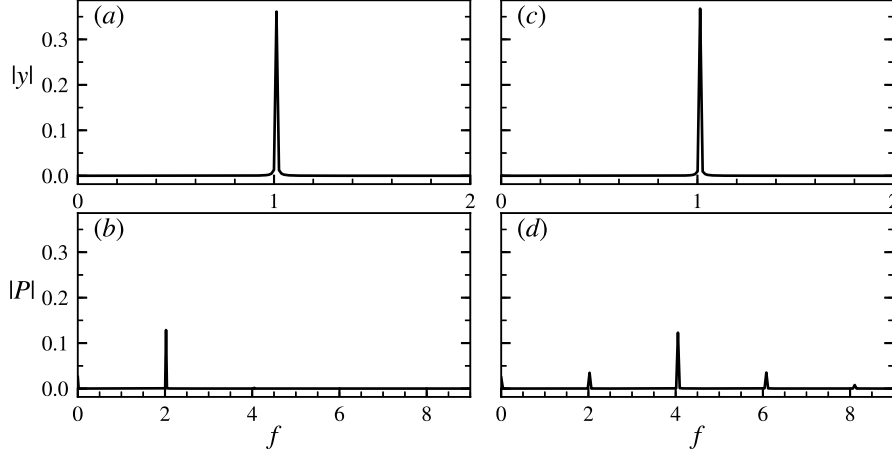


Figure 4.5: FFT of the cylinder displacement and power output (shown in fig. 4.4) for the CD (left) and EMD cases (right).

and indeed there is little difference between the shedding patterns.

Figure 4.6a shows the variation of the average power with damping ratio (ξ) for the CD case. Also plotted are the displacement and velocity amplitudes of the cylinder, which are seen to monotonically decrease with increasing ξ . This behaviour is expected since the role of damping is to apply a retarding force on the cylinder, hence, a larger damping value results in a larger retarding force and thereby a smaller oscillation amplitude. Since the oscillation amplitude of the cylinder decreases with ξ , and the power is proportional to the product of ξ and the square of the velocity amplitude, it is expected that there is an optimal value of ξ (ξ_{opt}) at which maximum power is harnessed. This is seen in fig. 4.6a, where $\xi_{opt} = 0.14$ and the maximum average power (\bar{P}_{max}) is 0.13. A similar plot is shown in fig. 4.6b for the EMD case. The maximum average power in this case is also close to 0.13, but note that more power is obtained compared to the CD case when the damping ratio is greater than its optimal value. To quantify this effect, the *quality* of the system is defined as

$$Q = \frac{\Delta\xi}{\xi_{opt}}. \quad (4.8)$$

Here $\Delta\xi$ is the half-width at half-maximum (HWHM), i.e., $\Delta\xi = \xi_{1/2} - \xi_{opt}$, where $\xi_{1/2}$ represents the value of damping at which the power is half of its maximum value. In effect, Q signifies how far, relative to the optimal condition, the system can operate and still produce more than half of the maximum average power. The values of Q at $U_r = 5.2$ for CD and EMD cases are 2.1 and 12.8, respectively. The value of maximum average power at $U_r = 6.7$ is close to half of \bar{P}_{max} at $U_r = 5.2$. The values of Q at $U_r = 6.7$ for the CD and EMD cases are 4.1 and 31.0, respectively. Thus, the EMD system is considerably less sensitive to tuning.

In fig. 4.7, the data of fig. 4.6 is replotted with different axes. This reveals the relationship of power and velocity amplitude with the displacement amplitude of the cylinder

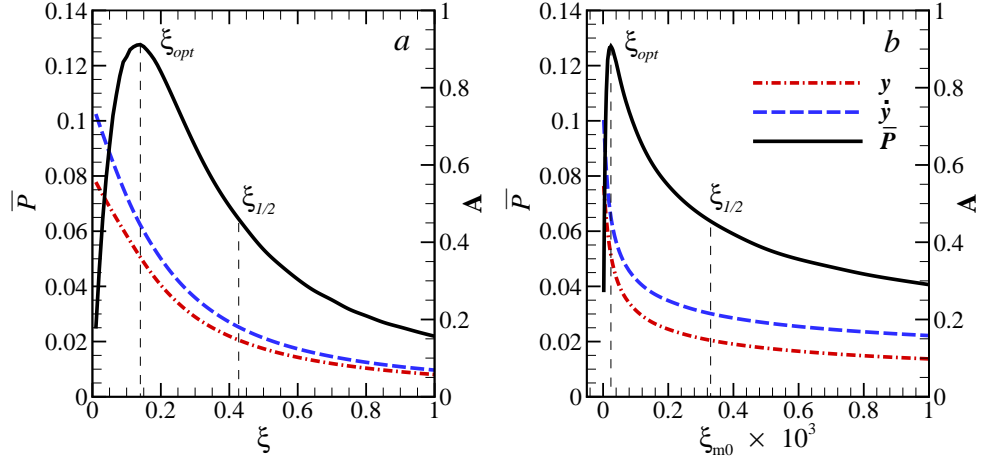


Figure 4.6: Variation of the average power (a) with ξ for CD and (b) with ξ_{m0} for EMD ($a = 0.6, L = 0.6$) cases, for $U_r = 5.2$ and $m = 2$.

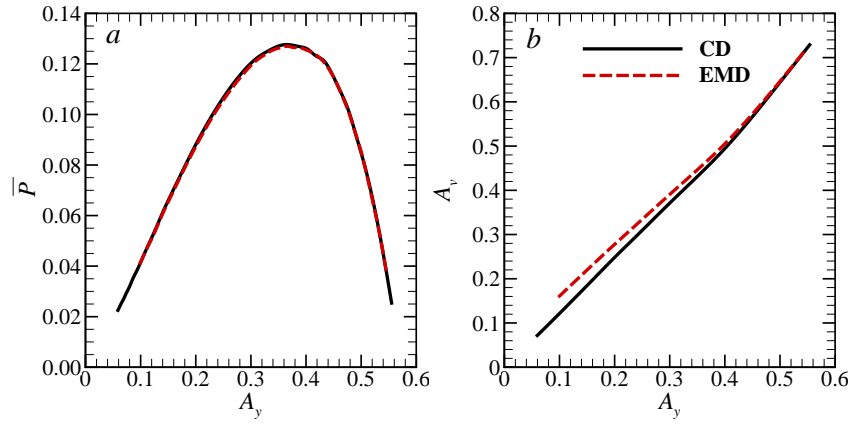


Figure 4.7: (a) Average power and (b) velocity amplitude versus displacement amplitude of the cylinder for CD and EMD cases at $U_r = 5.2$, $m = 2$ and $Re = 150$.

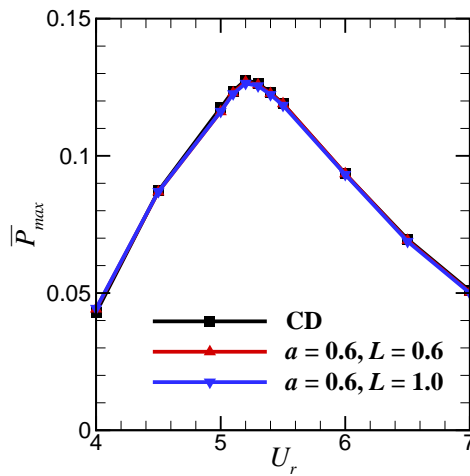


Figure 4.8: Maximum average power versus U_r for CD and EMD cases at $m = 2$ and $Re = 150$.

for both the cases. While fig. 4.7a shows the similarity between the two cases, fig. 4.7b points out the differences. Although the temporal variation of power is different for each case, surprisingly, the average power is seen to depend only on the displacement amplitude of the cylinder in fig. 4.7a. There is an optimal amplitude for the maximum average power. On the other hand, the velocity amplitude of the cylinder is larger for the EMD case at smaller displacement amplitude. This happens because the EMD case has smaller damping at the mean position ($y = 0$), which allows a larger acceleration of the cylinder.

Figure 4.8 shows the variation of maximum average power (\bar{P}_{max}) with reduced velocity for both CD and EMD cases. Two EMD cases with different coil lengths are considered. All the curves in fig. 4.8 are effectively indistinguishable implying that the variation of maximum average power with reduced velocity is independent of the nature of damping used. Therefore, a constant damping ratio can be used to calculate the *average* power that can be extracted from the system under non-constant electromagnetic damping; whilst noting that the temporal variation for the two cases is quite different.

4.3.2 Effect of coil length

Now details of the EMD setup are examined while retaining the same mass ratio ($m = 2$) and choosing the lock-in condition ($U_r = 5.2$) at $Re = 150$. In this section, the effect of the length of the coil on the power output is considered. In addition to the value of 0.6 already considered, L is varied in the range $[0.1, 1.0]$. The radius of the coil is kept at $a = 0.6$. The variations of average power and displacement amplitude of the cylinder with ξ_{m0} are shown in fig. 4.9 for the different lengths of the coil (L). There is no significant effect of the coil length on the maximum average power, but the value of optimal ξ_{m0} increases with L . It is worth mentioning that the relationships of power and the velocity amplitude with the displacement amplitude of the cylinder (not shown here) are unaffected by the L . The displacement amplitudes of the cylinder at optimal ξ_{m0} for $L = 0.1, 0.6$ and 1.0 are 0.39, 0.37 and 0.38, respectively. The corresponding velocity amplitudes of the cylinder are 0.49, 0.46 and 0.48, respectively. It is seen that at a particular value of ξ_{m0} , greater than the optimal value, larger values of power and velocity amplitude of the cylinder are produced for a larger L . This behaviour can be explained by the relationship of ξ_m with L , which is plotted in fig. 4.10. In fig. 4.10a and b, the variation of ξ_m with y is plotted, at three values of ξ_{m0} , for $L = 0.1$ and 1.0 , respectively. As seen in fig. 4.10, a small value of L results in a large value of ξ_m at the same ξ_{m0} . Since increased damping ratio is expected to reduce the vibration amplitude, a small L produces a smaller displacement amplitude and power at a particular value of ξ_{m0} . The values of Q for $L = 0.1, 0.6$ and 1.0 are 11, 12.8 and 19.6, respectively.

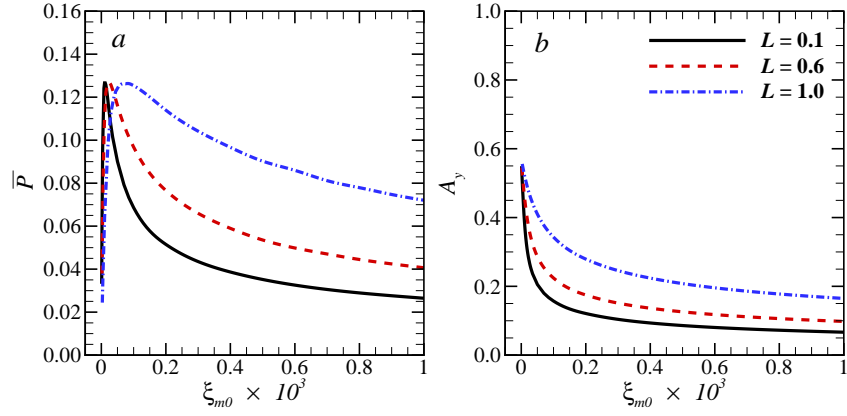


Figure 4.9: Effect of coil length on (a) average power and (b) displacement amplitude at $U_r = 5.2$, $m = 2$ and $a = 0.6$.

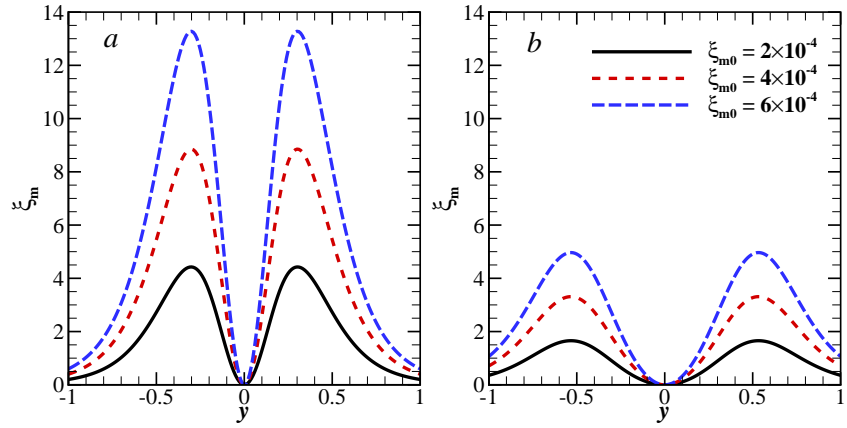


Figure 4.10: Effect of coil length on EM damping ratio (a) $a = 0.6$, $L = 0.1$ and (b) $a = 0.6$, $L = 1.0$.

4.3.3 Effect of coil radius

This section studies the effect of the coil radius on the power output. Coil radius values of $a = 0.4, 0.8$ and 1.0 are used, in addition to the already considered value of 0.6 , while the length of the coil is kept at $L = 0.6$. The other parameters are kept unchanged, i.e. $m = 2, U_r = 5.2$ and $Re = 150$. The effect of coil radius on power can be seen in fig. 4.11, where the variations of average power and displacement amplitude of the cylinder with ξ_{m0} are plotted for the four aforementioned values of a . Similar to what was seen in section 4.3.2, the value of maximum average power is unaffected by the coil radius, but the value of optimal ξ_{m0} increases with an increase in a . The displacement amplitudes of the cylinder at optimal ξ_{m0} for $a = 0.4, 0.6, 0.8$ and 1.0 are $0.37, 0.39, 0.36$ and 0.36 , respectively. The effect of coil radius on damping ξ_m is shown in fig. 4.12 where the variation of ξ_m with y is plotted, at three values of ξ_{m0} , for $a = 0.6$ and 1.0 , respectively. The damping ξ_m is higher for smaller a and therefore more power is produced for larger a at same ξ_{m0} (fig. 4.11a). The values of Q for $a = 0.4, 0.6, 0.8$ and 1.0 are $13.2, 12.8, 13.4$ and 13.8 , respectively. Again, the relationships of power and the velocity amplitude with the displacement amplitude of the cylinder (not shown here) are unaffected by the coil radius.

4.3.4 Effect of mass ratio

Next the effect of mass ratio of the cylinder-magnet assembly on the power output is discussed. In this case the coil radius (a) and length (L) are set to 0.6 and 1.0 , respectively. As discussed in section 4.3.1, the values of a and L do not affect the maximum average power \bar{P}_{max} . Figure 4.13 shows the variation of \bar{P}_{max} with U_r for different mass ratios m . It is seen that the \bar{P}_{max} versus U_r curve becomes flatter as the mass ratio is decreased, implying that the synchronization region for the VIV of the cylinder becomes larger for smaller m . This phenomenon has been reported previously in the literature (Govardhan and Williamson, 2000). The results show only a very small effect of m on the peak value of \bar{P}_{max} .

4.3.5 Effect of the Reynolds number

Lastly, the effect of the Reynolds number on the power output of the system is briefly considered. For this the value of Re is varied to take values 100 and 200 , in addition to the value of 150 already considered. Similarly to before, the mass ratio is kept as $m = 2$, and a coil of length $L = 1.0$ and radius $a = 0.6$ is kept at $y = 0$. The variations of average power with ξ_{m0} for three Reynolds numbers are shown in fig. 4.14a. The maximum average power is obtained at $U_r = 5.3$ and 5.2 for $Re = 100$ and 200 , respectively. The average power is seen to increase with Re . Two reasons could account for this increase

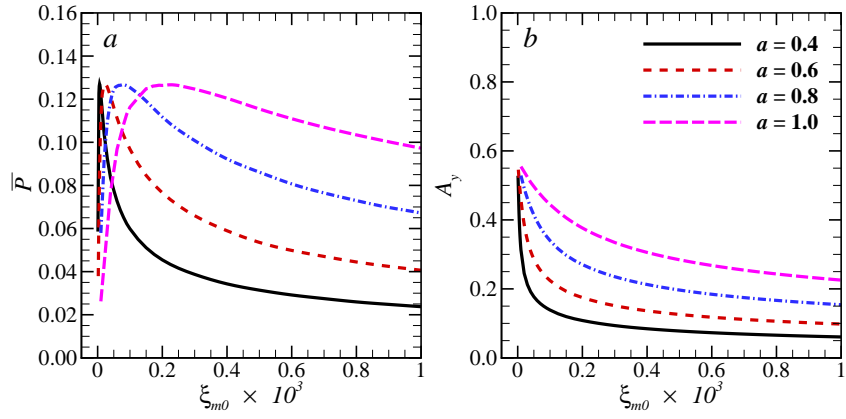


Figure 4.11: Effect of coil radius on (a) average power and (b) displacement amplitude at $U_r = 5.2$, $m = 2$ and $L = 0.6$.

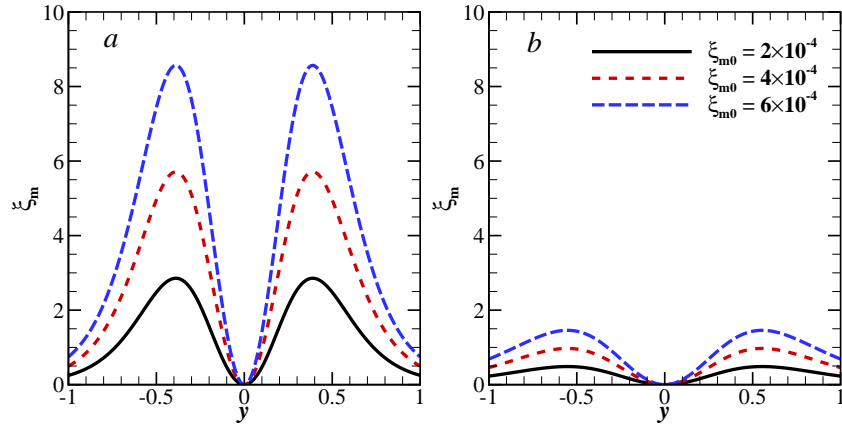


Figure 4.12: Effect of coil radius on EM damping ratio (a) $a = 0.6$, $L = 0.6$ and (b) $a = 1.0$, $L = 0.6$.

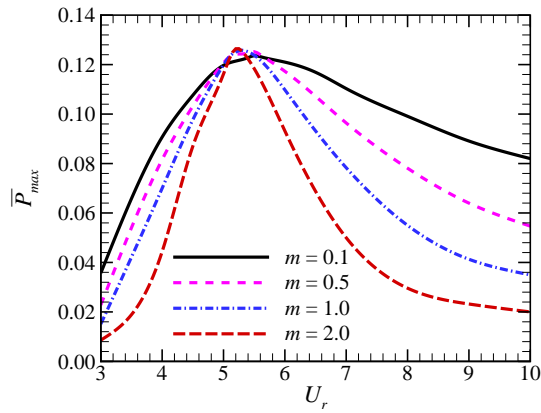


Figure 4.13: Maximum average power versus U_r for different mass ratios.

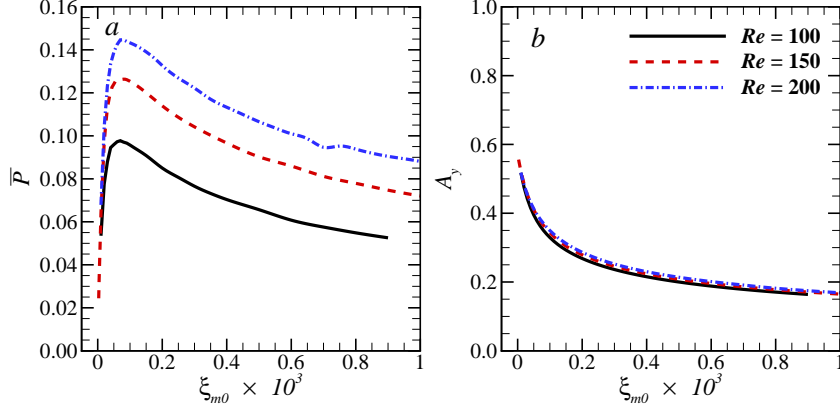


Figure 4.14: Effect of Re on average power and displacement amplitude for $m = 2$, $a = 0.6$ and $L = 1.0$.

in \bar{P} with Re : increase in Strouhal number and increase in the vibration amplitude (see fig. 4.14b) with Re . The values of \bar{P}_{max} for $Re = 100, 150$ and 200 are $0.10, 0.13$ and 0.145 , respectively.

4.3.6 Using two coils

In the previous sections the electrical generator consisted of only one coil, which was located at the magnet centre $y = 0$. Another possibility is to use two identical coils that are kept at equal distances, $\pm y_c$, along the transverse direction. In this case the net EM damping force is the sum of the damping forces due to each coil. Therefore, the effective EM damping ratio for the two coils case can be written as

$$\xi_m = \xi_{m0} (g_1^2 + g_2^2). \quad (4.9)$$

Two values of y_c , 0.10 and 0.39 , are considered. The variations of ξ_m with y for these two values of y_c are shown in fig. 4.15. The plot of ξ_m for $y_c = 0.10$ is similar to that for one coil case, except that it has a non-zero value at the centre $y = 0$. On the other hand, the $y_c = 0.39$ case shows an entirely different behaviour where the maximum damping occurs at the centre.

The effect of the two y_c values on power for mass ratio $m = 2$ at lock-in ($U_r = 5.2$) is investigated. The Reynolds number is kept at 150 , and the length and radius of the coils are taken as 0.6 and 0.6 . The variations of power with time for the two cases are plotted in fig. 4.16. The plots corresponds to the their optimal damping situations. The instantaneous power for the $y_c = 0.39$ case is shown in fig. 4.16a. The peak value of power (P_p) is 0.39 , and is generated when the cylinder is located near the centre. Although the frequency of power is the same as that of the CD case presented in section 4.3.1, i.e., $f_p = 2f_c$, the temporal variation shows some dissimilarity. The power does not

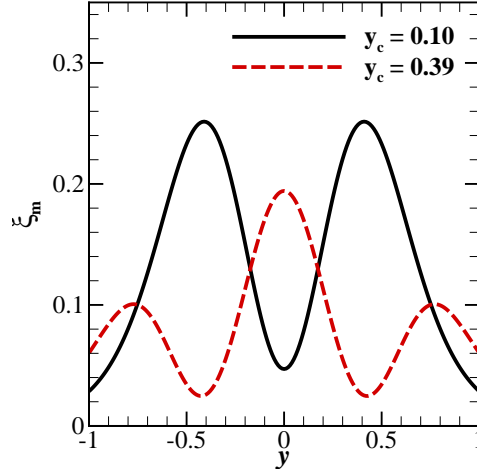


Figure 4.15: Variation of ξ_m with y for the two coil case. They are plotted for optimal cases ($\xi_{m0} = 1 \times 10^{-5}$ and 6.8×10^{-6} for $y_c = 0.10$ and 0.39 , respectively).

vary in a sinusoidal fashion in this case. In a cycle, the duration for which power is more than $P_p/2$ is smaller than the duration for which the power is less than $P_p/2$. The instantaneous power for the $y_c = 0.10$ case is shown fig. 4.16b. The peak power for this case is $P_p = 0.24$, which is smaller than that for the single coil EMD case presented in section 4.3.1. The peak power is generated when the cylinder displacement is $y = \pm 0.22$. Similar to the single coil case, there are two unequal peaks for the power, and the lower and higher peaks occurs when the cylinder is moving towards and away from its mean position, respectively. However unlike the single coil case, the power is not zero at the centre because $\xi_m \neq 0$ there, and therefore $f_p = 2f_c$ for this case. In section 4.3.1, it was shown that the CD case had a lower Q value compared to the single coil EMD case. Figure 4.17a shows the variation of average power with ξ_{m0} for $y_c = 0.39$. The value of Q for this case is 1.4, which is smaller than that for the CD case. The reason for this small value of Q is the rapid decrease in the displacement and velocity amplitudes with ξ_{m0} , as seen in fig. 4.17a. This occurs due to a higher value of ξ_m at the centre, resulting in a strong damping force. The variation of average power for $y_c = 0.10$ with ξ_{m0} is shown in fig. 4.17b. The value of Q in this case is 5.8, which is smaller than the one coil EMD case, and this can be attributed to the fact that ξ_m is non-zero at the centre. Again, the maximum average power for both y_c values is 0.13. The displacement amplitudes of the cylinder at optimal ξ_{m0} for $y_c = 0.10$ and 0.39 are 0.38 and 0.37, respectively, with corresponding cylinder velocity amplitudes of 0.47 and 0.46.

4.4 Closure

The problem of harvesting power from VIV of a circular cylinder was investigated numerically using a spectral-element based FSI solver. Specifically, the average power production

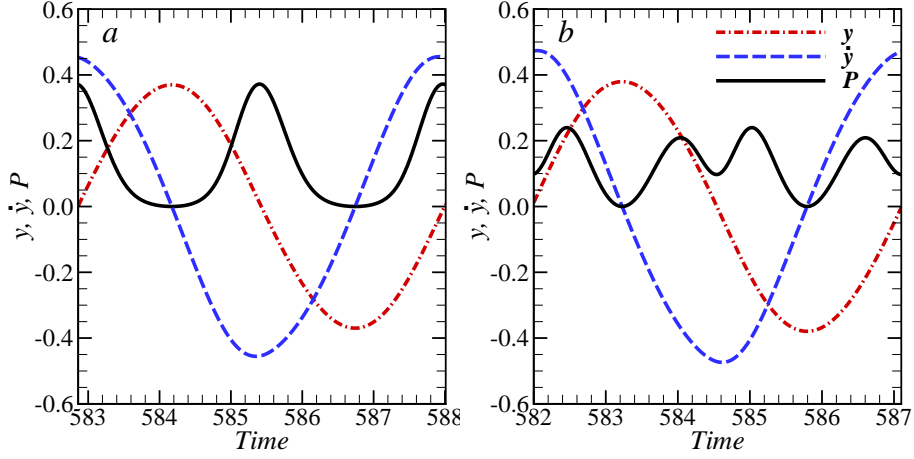


Figure 4.16: Variation of power, position and velocity of the cylinder with time for (a) $y_c = 0.39$ at $\xi_{m0} = 6.8 \times 10^{-6}$ and (b) $y_c = 0.10$ at $\xi_{m0} = 1.0 \times 10^{-5}$ at $U_r = 5.2$, $m = 2$ and $Re = 150$ for two identical coils of $a = 0.6$ and $L = 0.6$.

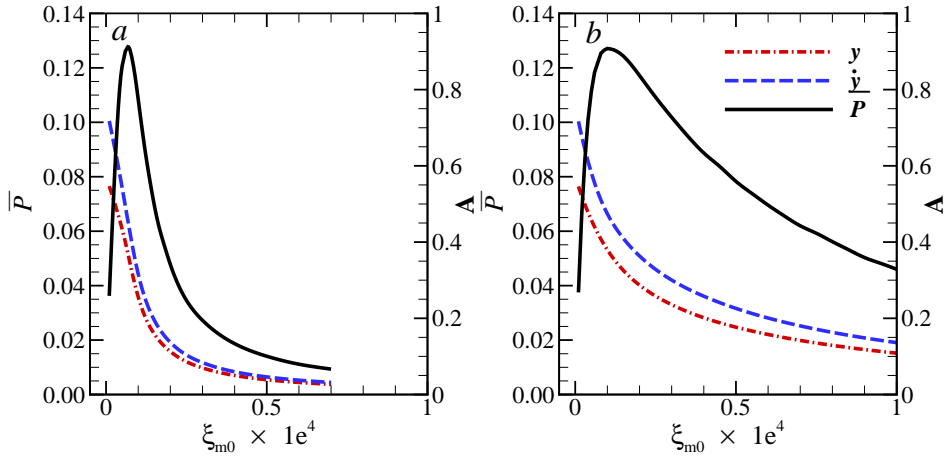


Figure 4.17: Variation of average power with ξ_{m0} for (a) $y_c = 0.39$ and (b) $y_c = 0.10$ at $U_r = 5.2$ and $m = 2$ for two identical coils of $a = 0.6$ and $L = 0.6$.

was compared for constant damping (CD) ratio and a realistic electromagnetic induction-based magnet-coil energy transducer. The magnet-coil system was modelled as a damper having spatially varying electromagnetic damping (EMD) ratio. There was an optimal damping ratio, for both the systems, at which maximum power was harnessed. The results show that the temporal variation of instantaneous power is quite different for the two cases but, perhaps surprisingly, both systems produce the same maximum average power (non-dimensional value of 0.13 at $Re = 150$). The EMD case produced a larger value of peak power as compared to the CD case. The frequency of the power signal for the EMD case was twice of that of CD case. In terms of the range of damping values for which a significant amount of power is extracted from the flow, the EMD setup is superior compared with the constant damping case.

The effects of coil length, radius and mass ratio were also explored and quantified. It was found that both length and radius of the coil do not affect the maximum average power although the average power versus damping ratio relation does change. The value of optimal damping ratio increases with increases in both length and radius of the coil. The increase in mass ratio increases the maximum average power by a small amount. The more significant effect of mass ratio is on the range of reduced velocity for synchronization of the cylinder. A smaller mass ratio cylinder is seen to have a larger synchronised region, and thereby can produce a significant amount of power over a large range of reduced velocities.

The effect of Reynolds number on power output was also studied over the range leading to two-dimensional periodic flow. The average power increases with an increase in Re . There was a 30% and 45% increase in maximum average power when Re was increased from 100 to 150, and to 200, respectively. The increase in average power can be attributed to the combined increases in vibration amplitude and frequency of the cylinder with Re .

The possibility of using two coils positioned symmetrically about the centre of the transverse direction was also examined. Two values of the distance between the coils were studied. These distances were chosen such that the resultant damping ratios had different variations with spatial coordinate. Both the cases give different temporal variation of power due to the difference in the nature of damping. The case where damping was highest at the centre, produced the largest peak power. The average power decreased faster with the damping ratio for this case compared with the case where damping is not highest at the centre. The maximum average power was the same (non-dimensional value of 0.13 at $Re = 150$) for both the cases. The systems with zero damping at the center were found to be less sensitive (have higher Q values) to variation in damping from its optimal value.

To summarise, the constant and electromagnetic damping cases produce entirely different temporal variations of instantaneous power output. In addition, the fundamental

frequency of power is different between the two cases. On the other hand, the average power does have a strong dependence on the vibration amplitude of the cylinder, which depends on Reynolds number, despite showing little dependence on the nature of damping. Of potential importance is that the system quality, which measures the insensitivity of power output to choosing the optimal system damping, is considerably better with the spatial-varying damping associated with the electromagnetic damping system.

Chapter 5

Damping effects on vortex-induced vibration of a circular cylinder and implications for power extraction

The effect of damping on vortex induced vibration (VIV) of a circular cylinder of a fixed mass ratio ($m^ = 3.0$) was studied through water-channel experiments. To achieve this, an eddy-current-based damping mechanism was constructed to provide controlled and adjustable damping values. This consisted of a permanent magnet connected to the cylinder that moves parallel to a copper plate at some predetermined gap, which determines the damping in the system. Increased damping was found to reduce the reduced-velocity range of the upper and lower branches, thus reducing the synchronization region. As the damping was increased, the lower branch remains easy to identify from the amplitude response curves, but the boundary between the initial and upper branch becomes less clear. However, the frequency variation with reduced velocity under higher damping shows similarities to that at the lowest damping and these similarities can be used to delimit the different response branches. This data was assembled to plot the peak amplitude response as a function of the mass-damping parameter in a “Griffin plot”. Due to a restricted variation in Reynolds number in the experiments, the measured data shows negligible scatter compared to the assembled literature data. Three sets of experiments using different sets of springs were conducted to quantify the Reynolds number effect. An exponential fitting function was then used to successfully fit the data on the Griffin plot. Under higher damping, it was found that the total and vortex phases are no longer at either 0° or 180° , and take intermediate values throughout the response branches. The power extracted by the damping mechanism was also calculated. Maximum power extraction occurs for a combination of optimal damping and reduced velocity. The power was also found to increase with Reynolds number, correlated with the increase in vibration amplitude. At the highest Reynolds number examined, the dimensionless energy conversion ratio is 0.2, indicating that approximately*

20% of the flow energy approaching the cylinder frontal cross-section can be converted to useful electrical energy. This factor increased substantially with Reynolds number from approximately 15 to 20% over the Reynolds number range considered ($Re \sim 1700\text{--}5900$).

5.1 Introduction

Vortex-induced vibration may occur when a bluff body, having some degree of flexibility, is placed in a fluid stream. Stationary bluff bodies experience vortex shedding above a critical Reynolds number. In this state, vortical structures form at the rear of the bluff body and are typically shed in an alternating fashion. This causes fluctuations in the lift and drag forces experienced by the body. A flexible body can vibrate due to these fluctuating forces, which is known as *vortex-induced vibration* (VIV). Indeed, VIV is encountered in many important situations, for example, marine risers, bridges, transmission lines, buildings, heat exchangers, etc. Often the flexibility of the structure can be modelled as a linear spring for simplicity. Such a simplified model focuses on the resonant vibration of an elastically mounted bluff body with one or two degrees of freedom (DOF) of movement due to the oncoming fluid flow.

Vortex-induced vibration (VIV) of a circular cylinder has been studied extensively by many researchers, for example see the reviews by [Khalak and Williamson \(1999\)](#), [Williamson and Govardhan \(2004\)](#), [Sarpkaya \(2004\)](#), [Gabbai and Benaroya \(2005\)](#), and [Bearman \(2011\)](#). The focus of many of these studies has been to identify the maximum cylinder response by minimizing the structural damping. This is important because of the possible structural failure that may occur due to large deformations. [Khalak and Williamson \(1999\)](#), in their experiments with a 1-DOF elastically mounted circular cylinder, found three branches in the amplitude response: the *initial*, *upper* and *lower* branches, as the ratio of shedding frequency to body oscillation frequency was varied. The maximum vibration amplitude is close to one cylinder diameter (D) and is observed to occur in the upper branch. The transition from one branch to another was found to be associated with the changes in the vortex shedding mode and phases of the lift and vortex forces. The transition from the initial branch to the upper branch occurs when the phase of the vortex force jumps from 0° to 180° , which is associated with the vortex shedding mode changing from $2S$ (refer to [Williamson and Roshko \(1988\)](#) for a description of the different vortex shedding modes) to $2P_o$ (similar to the $2P$ vortex shedding mode but the secondary vortex is much weaker). The upper to lower branch transition is associated with a jump from 0° to 180° in the phase of the lift force and a change in the vortex-shedding pattern from $2P_o$ to $2P$. [Jauvtis and Williamson \(2004\)](#) conducted 2-DOF VIV experiments on a circular cylinder by using a pendulum arrangement. For mass ratios 6.0 or greater, the transverse direction response was found to be close to a 1-DOF circular cylinder. How-

ever, a super-upper branch was observed for mass ratios less than 6.0. In that state, a maximum vibration amplitude of $1.5D$ and a corresponding $2T$ vortex shedding mode were observed.

Some results on the oscillatory response have also been reported on the effect of damping. [Feng \(1968\)](#) used an electromagnetic-eddy-current-based damper for studies of circular and D-shaped cylinders in a wind tunnel. Due to the large mass-damping parameter (described below), only two branches, the initial and lower branches, were observed. [Klamo \(2009\)](#) proposed a variable magnetic eddy-current damping system to study VIV of a circular cylinder. [Govardhan and Williamson \(2006\)](#) controlled the damping by applying an external force to the cylinder proportional to the cylinder velocity. In their setup, the measured cylinder velocity was applied to the support of a spring connected to the cylinder to mimic the damping force. A functional fit was proposed for maximum vibration amplitude as a function of the mass-damping parameter and Reynolds number.

Studying damping effects is also important as VIV can be used for converting flow energy into electrical energy (see [Bernitsas et al., 2008](#); [Barrero-Gil et al., 2012](#); [Soti et al., 2017](#)). A cylinder undergoing VIV has kinetic energy and part of it can be extracted using a power transducer such as an electromagnetic generator ([Soti et al., 2017](#)). The power-extraction process from VIV introduces additional damping into the system. Therefore, the power extraction process can be modelled by adding a damper to the system.

The main focus of the previous studies on VIV of circular cylinders has been on the effect of damping on the peak amplitude response. This is summarized in a “Griffin plot”, which plots peak vibration amplitude as a function of mass-damping. Literature studied showed considerable scatter about the underlying functional variation. [Govardhan and Williamson \(2006\)](#), using a mechanical damping system, have shown that the scatter is mostly due to the Reynolds number differences between different measurements. In the present work, an accurate physical damping mechanism is used to confirm that the data points on the Griffin plot show no scatter for a fixed Reynolds number. By conducting experiments for three different Reynolds numbers, it is shown that the scatter is due to Reynolds number differences. Apart from the Griffin plot, which focuses on peak amplitude response, the effects of damping on the amplitude response as a function of reduced velocity appears to have been insufficiently documented in the literature. The aim of the present work is also to report the effects of damping on various parameters of VIV response of the circular cylinder, namely, the amplitude, frequency, lift and phase. Finally, the power extracted by the damper from VIV of the circular cylinder is investigated.

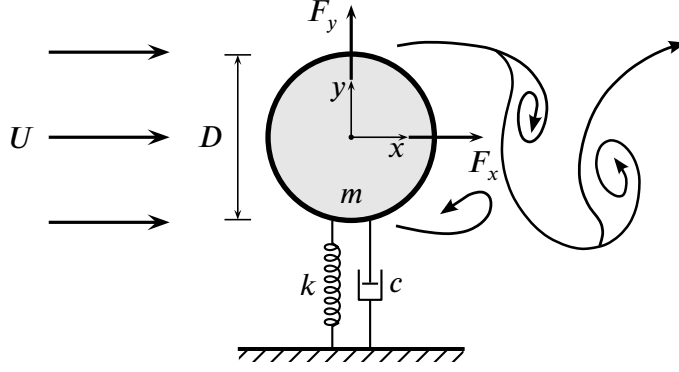


Figure 5.1: Definition sketch for the transverse vortex-induced vibration of a circular cylinder. The hydro-elastic system is idealized as a 1-DOF system constrained to move in the cross-flow direction. Here, U is the free-stream velocity, k the spring constant, D the cylinder diameter, m the oscillating mass, and c the structural damping. F_x and F_y represent the drag and the transverse lift force components acting on the body, respectively.

5.2 Experimental method

5.2.1 VIV Experimental apparatus

The experiments reported on here were conducted in the free-surface recirculating water channel of the *Fluids Laboratory for Aeronautical and Industrial Research* (FLAIR) group at Monash University. The water channel has a test section with dimensions of 600 mm in width, 800 mm in depth and 4000 mm in length. Figure 5.1 shows a schematic of transverse VIV of a circular cylinder, which defines key parameters to the problem. The elastically mounted cylinder is free to oscillate in only one direction transverse to the oncoming free-stream. The governing equation of the oscillating system can be expressed as

$$m\ddot{y} + c\dot{y} + ky = F_y, \quad (5.1)$$

where m is the total oscillating mass of the system, c is the structural damping, k is the structural stiffness, y is the body displacement in the transverse (cross-flow) direction and F_y is the transverse lift force.

In the present experiments, the hydro-elastic VIV set up employed a low-friction air-bearing system. A schematic of the experimental set up is shown in figure 5.2. The air bearing consisted of two air bushings that moved along two stationary precision guiding shafts. The air bushings were mounted on a carriage to which the cylinder was attached (see Sareen et al., 2017). The test circular cylinder, precision-made from hollow aluminium tubing, had a diameter of $D = 30 \pm 0.01$ mm. The immersed length in water was $L = 615$ mm, giving the mass of displaced fluid of $m_f = \rho\pi D^2 L/4 = 434$ g and a length-to-diameter aspect ratio of 20.5. The total oscillating mass was $m = 1301.5$ g, yielding an

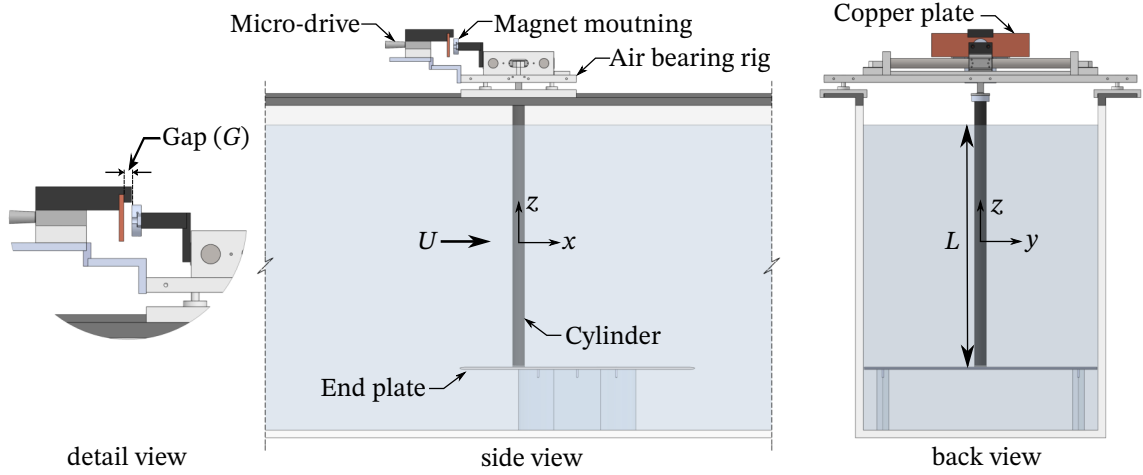


Figure 5.2: Schematic of the experimental set-up used for the VIV experiments.

overall mass ratio of $m^* = m/m_f = 3.0$. A non-contact digital optical encoder with a resolution of $1\ \mu\text{m}$ (model: RGH24, Renishaw, UK) was mounted to the side of the carriage to measure the displacement of the cylinder. An end-conditioning platform was used to reduce end effects at the bottom edge of the cylinder as shown in the schematic (see Zhao et al., 2014b,c; Wong et al., 2017). A force balance based on strain gauges was mounted between the carriage and the cylinder for directly measuring the fluid forces. However, it should be noted the transverse lift was derived based on the body displacement signal and other system parameters in (5.1), since it was found that the accurate digital displacement signal produced a more reliable and accurate lift force than attainable from the force balance signal because of electrical noise. The method and approach have been further described and validated in Zhao et al. (2014c); Wong et al. (2017).

The data acquisition (DAQ) system consisted of a USB DAQ device (model: USB6218-BNC, National Instruments, US) and customised LabVIEW programs that controlled the water-channel flow velocity and automation of measurements. For each U^* case, the DAQ measurements were sampled at 100 Hz for more than 100 oscillation cycles. Spot measurements with longer sampling times verified that this signal acquisition time was sufficient to provide reliable and accurate response amplitudes.

5.2.2 Damper mechanism

An eddy-current based damping mechanism was used to achieve controlled and variable damping values. The damper consists of a stationary electrically conductive plate and a permanent magnet that can move along the length of the plate at any fixed gap (G) between the plate and the magnet. When the magnet moves relative to the plate it creates eddy currents inside the plate. These eddy currents produce their own magnetic field which opposes the motion of the magnet (Lenz's law). From an energy conversion

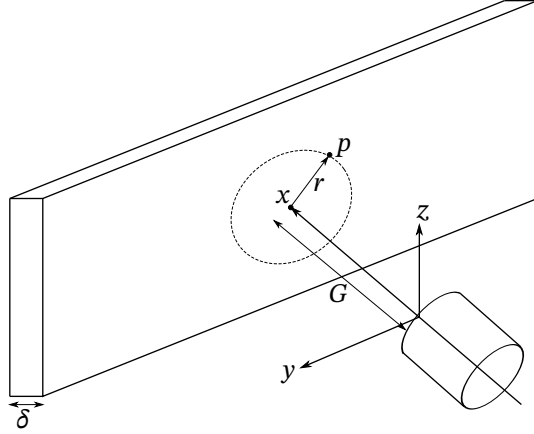


Figure 5.3: Schematic of the damper system.

point of view, the eddy currents dissipate energy in the form of heat due to the electrical resistance of the plate. The dissipated energy is deduced from the kinetic energy of the magnet. If the magnet is located at a distance G from the plate and moves with a constant velocity \dot{y} along the y -direction (see figure 5.3) then the damping force can be expressed as (Schieber, 1975; Klamo, 2009)

$$F = C\sigma\delta B_x^2 \dot{y}, \quad (5.2)$$

where σ and δ represent the electrical conductivity and thickness of the plate, respectively. The constant C is a function of various parameters such as the dimensions of the plate and the magnet. It also accounts for the variation in magnetic field along the plate and the finite width of the plate. The magnetic field strength B_x depends on the gap G , material and size of the magnet. The strength of magnetic field at any point P on the plate is given by (Donoso et al., 2009)

$$B_x = \frac{\mu_m}{(G^2 + r^2)^{3/2}} \left[\frac{3G^2}{G^2 + r^2} - 1 \right], \quad (5.3)$$

where μ_m represents the magnetic dipole moment of the magnet. Equations 5.2 and 5.3 show that the damping coefficient ($c = C\sigma\delta B_x^2$) depends upon various parameters, namely: the gap between the magnet and the plate, the magnetic field strength of the magnet, and the size, thickness and material of the conducting metal plate. A change in the damping, in the present experiments, is achieved by changing the gap between the plate and the magnet.

For the present experiments, an N42 grade rare earth Neodymium magnet of cylindrical shape with diameter 20 mm and length 10 mm was used. The magnet was mounted on the carriage to which the cylinder is attached so that it followed the motion of the cylinder. A plate made of copper of 250 mm length and 60 mm width was used. It had

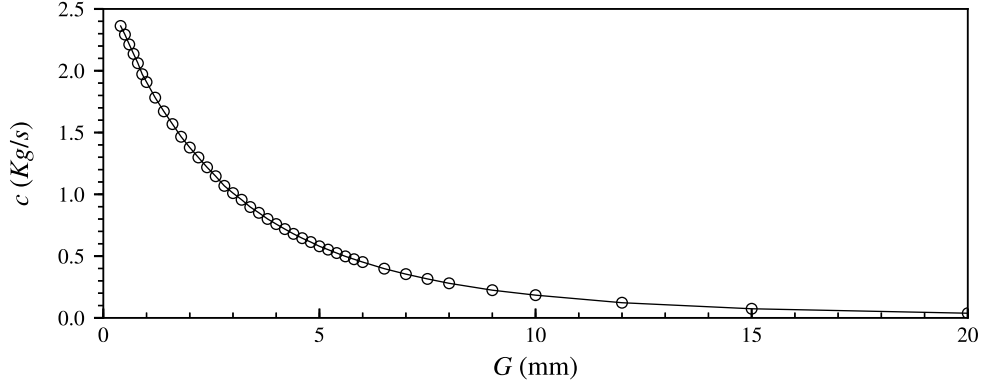


Figure 5.4: Damping coefficient (c) as a function of the gap (G) between the magnet and the copper plate of the damper used in the present experiments.

a thickness of 6 mm. The plate was attached to a micro-drive stage so that the distance between the magnet and plate can be changed in a precise and controlled manner with an accuracy of $10\ \mu\text{m}$.

5.2.3 Damping measurements

The first step of the experiment was to measure the damping coefficient for various gap values so that any desired c value can be achieved by positioning the copper plate at the corresponding gap G from the magnet. The damping coefficient was measured by conducting free decay tests in air. The cylinder was removed during the free decay test to avoid fluid forces and an equivalent mass was placed on the carriage to retain the total mass of the system. If the system is displaced by some distance A_0 from its equilibrium position and released then the motion of this one degree of freedom (DOF) freely vibrating system is governed by the following equation

$$m\ddot{y} + c\dot{y} + ky = 0, \quad (5.4)$$

where m and k represents the total mass and stiffness of the system. The behaviour of the solution of eq. 5.4 depends upon the damping ratio $\zeta = c/2m\omega_n$ where $\omega_n = \sqrt{k/m}$ is the natural angular frequency of the system. For under damper situation, $0 \leq \zeta < 1$, the system undergoes periodic sinusoidal motion of form $y = A \cos(\omega_d t)$ where $\omega_d = \omega_n \sqrt{1 - \zeta^2}$ is the damped natural angular frequency and the amplitude of vibration is given by $A = A_0 \exp(-\zeta\omega_n t)$. The two consecutive peaks of displacement would be separated by the time interval $T = 2\pi/\omega_d$. If the log decrement between two instances of peak displacement, t_n and $t_{n+1} = t_n + T$, is defined as $\delta = \ln(A_n/A_{n+1})$ then the damping ratio is given as

$$\zeta = \sqrt{\frac{\delta^2}{4\pi^2 + \delta^2}}, \quad (5.5)$$

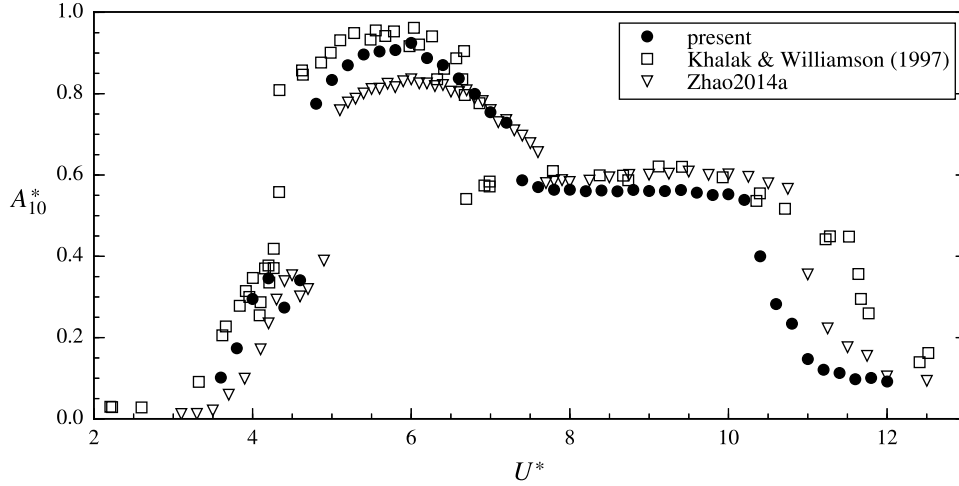


Figure 5.5: Comparison of displacement amplitude obtained by our experiment with that of [Khalak and Williamson \(1997\)](#) ($m^* = 2.4$, $\zeta = 4.5 \times 10^{-3}$) and [Zhao et al. \(2014b\)](#) ($m^* = 2.66$, $\zeta = 3.2 \times 10^{-3}$)

The natural frequency can be calculated as $f_n = 1/T$ for very low ζ . An average is taken over all the ζ values obtained by applying eq. 5.5 to all the consecutive peaks of the displacement. Since the damping coefficient is independent of mass and stiffness of the system, it is useful to convert the damping ratio values to damping coefficient. The measured values of damping coefficient as a function of gap (G) are plotted in figure 5.4.

5.2.4 Experimental validation

The experimental setup was validated by comparing the amplitude response of the circular cylinder at low damping with that of [Khalak and Williamson \(1997\)](#). The mass and damping ratio for the present case are $m^* = 3.0$ and $\zeta = 2.5 \times 10^{-3}$, respectively. Figure 5.5 shows a good match of the amplitude response (A_{10}^* represents the mean of the top 10% of displacement peaks of the displacement signal.) of the cylinder with the published results. The difference in the peak value of the amplitude could be attributed to the difference in the Reynolds number. The Reynolds number range for the data presented in figure 5.5 is given by the data set 3 in table 5.1. The synchronization region, the range of reduced velocity for which the cylinder shows significant vibration amplitude, is known to shrink with increase in mass ratio. Since the mass ratio for the present experiments is slightly higher than that of [Khalak and Williamson \(1997\)](#), the boundaries of upper and lower branches do not match exactly with the published data. Overall, a good match is obtained and the three response branches: initial, upper and lower, are captured.

Table 5.1: Three set of experiments performed in the present work

Set	Natural frequency in air f_n (Hz)	Natural frequency in water f_N (Hz)	Re range
1	0.362	0.309	1250–3750
2	0.639	0.550	2220–6661
3	1.095	0.943	3805–11416

5.3 Results

In this section, the effects of damping on the vortex-induced vibration of a circular cylinder will be discussed. There are four important independent parameters in the study of VIV: the mass ratio (m^*), damping ratio (ζ), reduced velocity (U^*) and Reynolds number (Re). The reduced velocity is defined as $U^* = U/(f_N D)$, where U is the free stream velocity and f_N is the natural frequency of the system in water. The natural frequency in water is measured by conducting free decay tests in still water with minimal damping (without the damper). The VIV response also depends (more weakly but non-negligibly) on the Reynolds number ($\text{Re} = UD/\nu$). In the present experiments, the reduced velocity was varied by changing the free-stream velocity while keeping the values of f_N and D fixed. This also resulted in a changing Reynolds number. Three sets of f_N values were used in the experiments to examine the effect of Reynolds number. The values of natural frequency and corresponding Reynolds number ranges for the three sets are shown in table 5.1. The mass ratio is kept at $m^* = 3.0$. The change in f_N was achieved by physically changing the number of springs and thereby changing the spring constant. The displacement and force data were recorded for 360 s (for more than 100 oscillation cycles) for a single reduced velocity.

5.3.1 Effect of damping on the vibration response

The effect of damping on the vibration amplitude of the circular cylinder is shown in figure 5.6 for the Reynolds number range of $\text{Re} = 2220\text{--}6661$ (referred to as set 2 in table 5.1). For small damping values, the typical three-branch VIV response is observed. The initial branch is further divided into a quasi-periodic (QP) region (see fig. 5.7(a)) for $3.6 \leq U^* < 4.4$, and a periodic (P) region for $4.4 < U^* < 4.8$ (fig. 5.7(b)). There is a visible jump in the vibration amplitude from the initial to the upper branch at $U^* \simeq 4.8$. At the start of the upper branch, which extends over $4.8 \leq U^* \leq 7.4$, the vortex shedding frequency locks onto the natural frequency of the cylinder and the amplitude response becomes significantly higher. The amplitude response reaches its peak value of $A_{10}^* \approx 0.8$ at $U^* = 5.8$ in the upper branch. Here, A_{10}^* represents the mean of the top 10% of peaks of the displacement signal. The vibration amplitudes were observed to be

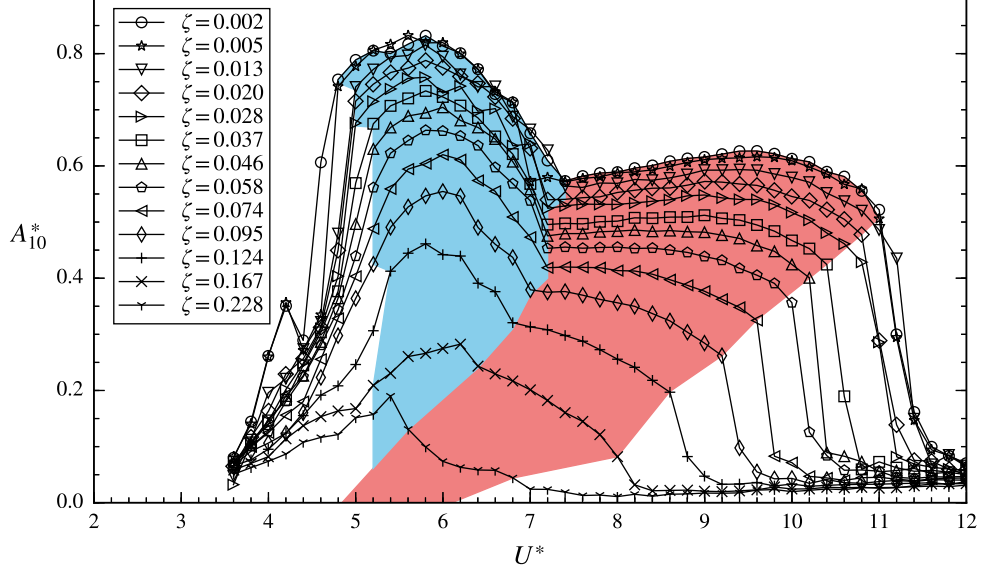


Figure 5.6: Mean of top 10% maximum amplitude response versus reduced velocity for various values of damping ratios. The mass ratio is 3.0. Blue and red regions show the upper and lower branches, respectively.

varying from one cycle to another, i.e. the vibrations are not fully periodic (see fig. 5.7(c)). With further increase in U^* , the vibration response switches to the lower branch covering $7.4 \leq U^* \leq 11.0$. The vibration amplitude response does not vary much with U^* in the lower branch and is consistently close to $A_{10}^* \approx 0.6$ (see fig. 5.7(d)). The vibration amplitude is also quite stable from one cycle to another at any U^* i.e. the vibrations are periodic. The upper and lower branch combined is called the lock-in region. The cylinder motion desynchronises from the vortex shedding frequency for $U^* > 11.0$ and the vibration amplitude jumps down to a small value. The vibration amplitude is seen to decrease with an increase in the damping ratio for any reduced velocity since the role of damping is to continuously dissipate energy.

The jump in the vibration amplitude at the lower to upper branch transition becomes smeared out with increasing damping. As the damping ratio is increased, the lock-in region becomes narrower. The transition between the branches become continuous rather than through jumps. The vibration amplitude in the lower branch tends to decrease with U^* at higher damping values. The upper and lower branches are identified by blue and red colours, respectively, in figure 5.6. The identification of boundaries of these branches, especially the upper branch, is approximate at high damping values and the proposed classification will be discussed in the next section.

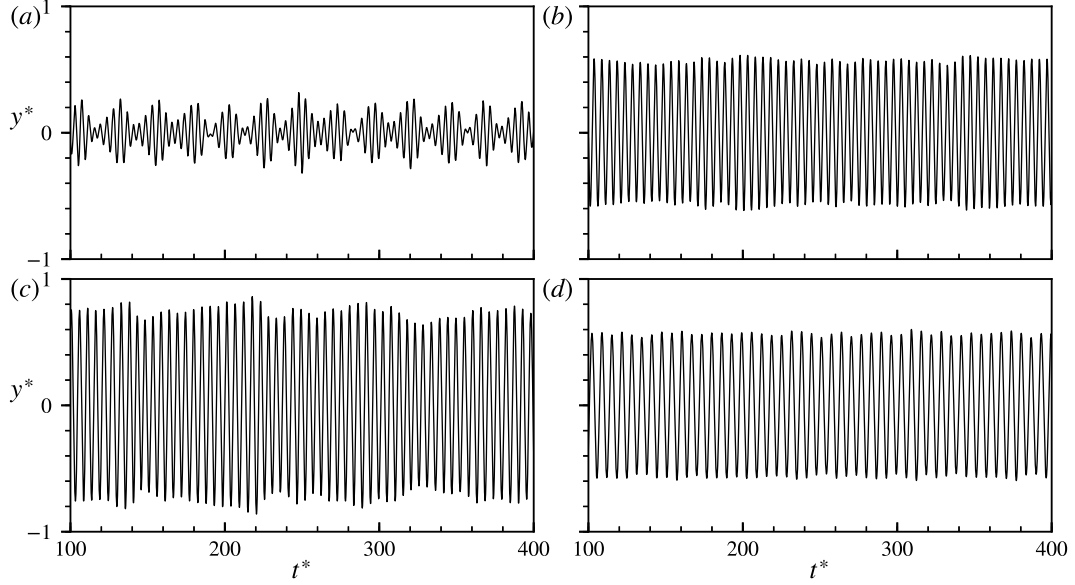


Figure 5.7: Time histories of the non-dimensional cylinder displacement for $U^* =$ (a) 4.0, (b) 4.6, (c) 5.8 and (d) 8.0 for the minimal damping case. The plots illustrates the time-variation of the cylinder displacement for quasi-periodic, periodic, upper branch and lower branch regions, respectively.

5.3.2 Effect of damping on oscillation frequency

The normalized frequency ratio of vibration frequency to the natural frequency of the cylinder in water ($f_y = f/f_N$) also shows different behaviour in the three response branches. A contour plot of power spectral density (PSD) of cylinder displacement against normalized frequency and reduced velocity is plotted on the left of figure 5.8 for five different damping values. A contour map of the PSDs of the lift force signals is also plotted on the right of figure 5.8. The log scale is chosen for the PSD in the contour plots so that weak harmonics can still be recognised. For low damping values (see figure 5.8(a)), three distinct patterns are seen for the frequency response. In the initial branch, two frequency components are present in the displacement. One is due to the vortex shedding frequency, which overlaps with the straight line representing $St = 0.208$ in figure 5.8, and the other is due to the natural frequency of the system. The two components are also visible in the lift force, as seen in figure 5.8(a). The vortex shedding frequency becomes locked to the natural frequency of the cylinder at the start of the upper branch and there is only one dominant component present in f_y . The normalized vibration frequency of the cylinder jumps to a value close to unity at the start of the upper branch. The normalized vibration frequency then increases gradually with U^* through the upper branch. A third harmonic of the fundamental frequency appears in the lift signal in the upper branch, which could be related to the change in vortex shedding pattern from $2S$ to $2P_0$. With a further increase in U^* , another jump in f_y is observed at the start of the lower branch. The normalized vibration frequency stays constant at a value greater than 1.0 (≈ 1.25) in

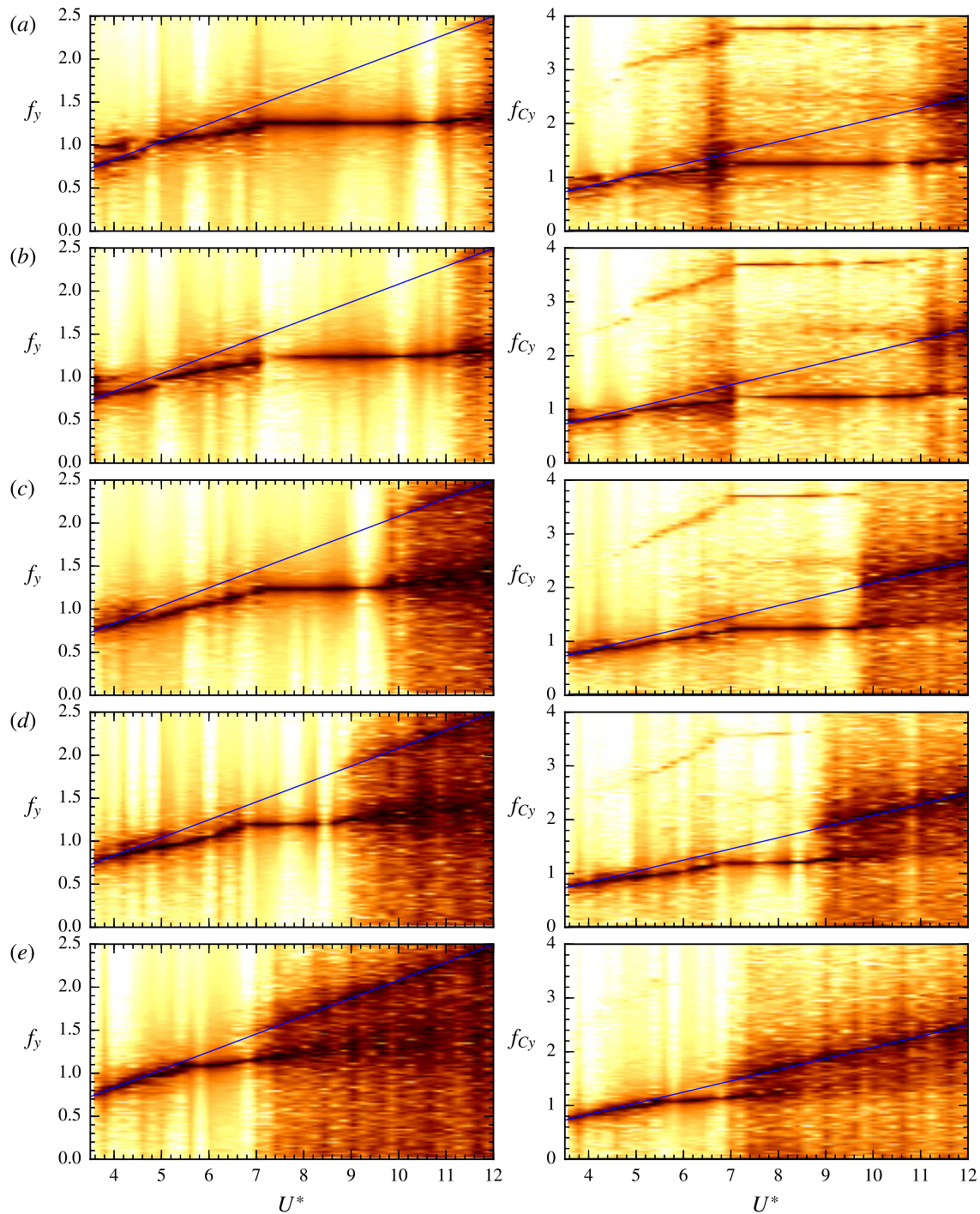


Figure 5.8: Contours of power spectral density of displacement (left) and lift force (right) plotted against the normalised frequency and reduced velocity for $\zeta =$ (a) 0.002, (b) 0.028, (c) 0.074, (d) 0.124 and (e) 0.228. Each power spectrum is plotted vertically and stacked together horizontally from each U^* to form these contour plots. A \log_{10} scale is used to highlight the variation from 0 (black) to -3 (white). The line represent $St = 0.208$, corresponding to the vortex shedding frequency of a stationary cylinder.

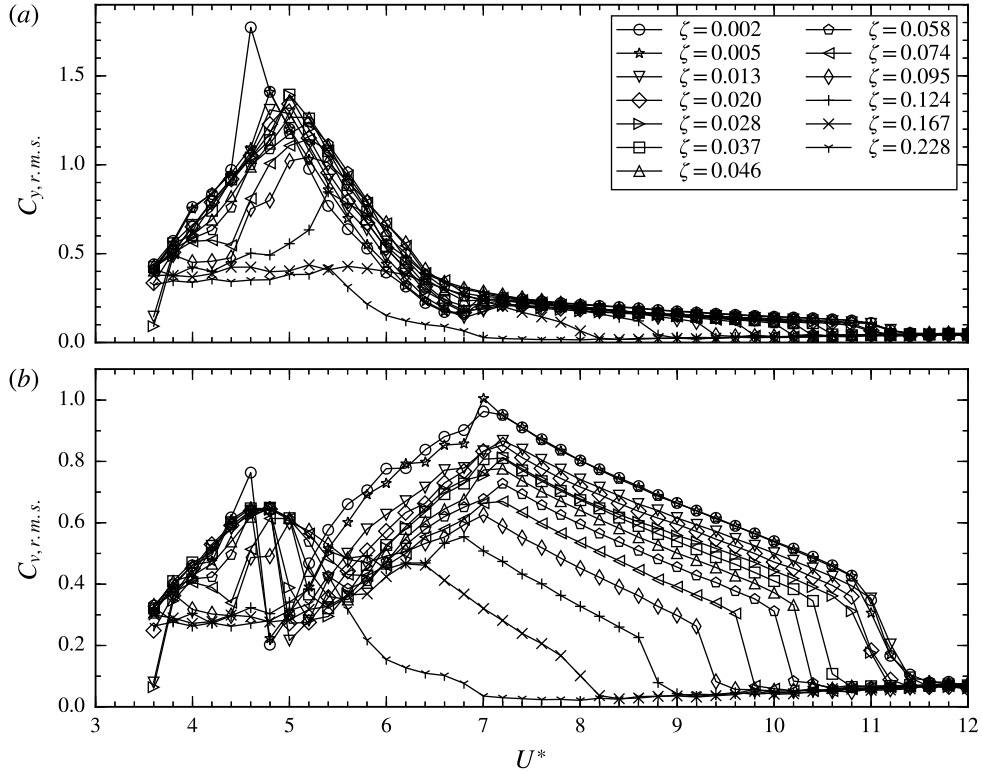


Figure 5.9: (a) RMS lift coefficients, and (b) RMS vortex force coefficients versus reduced velocity for specified damping ratios.

the lower branch. The vibration amplitude in this branch is very stable compared to the initial and upper branches and therefore, the plots show a sharp spectral peak through this lower branch. However, a relatively stronger third harmonic is present in the lift force in the lower branch indicating that the signal is not purely sinusoidal. For $U^* > 11.0$, the desynchronization region appears and the cylinder displacement shows two dominating frequencies: the vortex shedding and the natural frequencies. The lift force also has these two frequency components in this region. Note that in the contour plots the energy of the signal is distributed over a range of frequencies.

As the damping is increased, the desynchronization region begins at progressively small values of U^* . All contour plots in figure 5.8(b)-(e) show a region similar to figure 5.8(a), where the vibration and lift frequencies remain at a constant value. Following the discussion for the low damping case in the previous paragraph, this region can also be labelled as the lower branch for higher damping cases. The right-hand end of the lower branch can be identified by the distribution of the displacement and lift signal energy to a larger range of frequencies i.e. the scatter in the PSD frequency content. The left-hand end of the lower branch occurs when the vibration frequency stops changing with U^* and becomes constant. The same can be seen for the third harmonic in the lift force.

Identifying the start of the upper branch is less obvious at higher damping values. In

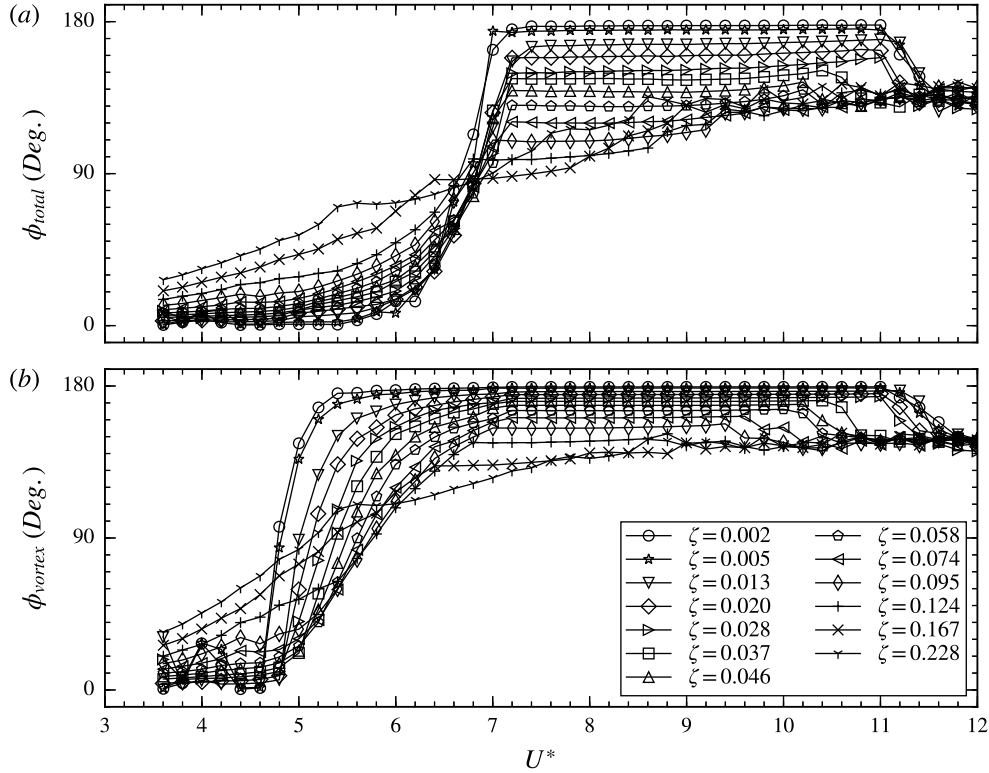


Figure 5.10: Phase difference between (a) total lift and (b) vortex force and displacement versus reduced velocity for various values of damping ratios.

figure 5.8b, which corresponds to an order of magnitude higher damping, the start of the upper branch can still be identified by a jump in the vibration frequency. Jumps in the vibration frequency are still present at the boundaries of upper and lower branches since there is a visible change in the amplitude variation with U^* across the branch boundaries (see figure 5.6). In figure 5.8(c), f_y does not show any visible jump at the upper branch boundary since the vibration amplitude increase gradually with U^* at this high damping. The vibration frequency still shows the three different trends that occur in three branches at low damping. There is a region in figures 5.8(b) to 5.8(e) resembling the initial branch for the low damping case in figure 5.8(a) where the vibration frequency matches the vortex shedding frequency for a stationary circular cylinder. The frequency content overlaps with the $St = 0.208$ line in this region. Due to the similarity, it is reasonable to designate this region the initial branch for higher damping cases. In the upper branch of the low damping case, the vibration frequency increases with U^* but no longer overlaps with the $St = 0.208$ line, and a third harmonic of the fundamental frequency appears in the lift force. These two trends are also present for the higher damping cases and, therefore, were used for identifying the upper branch at high damping.

5.3.3 Effect of damping on lift force and phase

The lift coefficient is defined by $C_y = F_y / (\frac{1}{2}\rho U^2 DL)$, where F_y represents the force acting on the cylinder in the transverse direction. The root mean square (RMS) lift coefficient as a function of reduced velocity is plotted in figure 5.9(a) for various damping ratios. The peak value of C_y is seen to decrease with an increase in damping. The maximum value of the lift coefficient (=1.8) is obtained at minimum damping for $U^* = 4.6$. For small damping values, the lift force shows a rapid increase with U^* in the initial branch and reaches a peak value at the beginning of the upper branch. In the upper branch, the lift force experiences a rapid decrease with U^* and reaches a value lower than that of the stationary cylinder case. With a further increase in U^* , the lift force shows a slow decrease in its value in the lower branch. At the end of the lower branch, a jump is seen in C_y and it reduces to an even smaller value.

The fluid force can decompose into two components: the potential force (F_{pot}) and the vortex force (F_{vor}). This decomposition reflects the fact that any velocity field can be constructed from the summation of a potential flow component plus a field due to the vorticity in the system. The potential force is the part of the fluid force that is in phase with the displacement (in the equivalent potential flow system). Physically, it is the force required to accelerate the surrounding fluid. Therefore, the magnitude of potential force is equal to the added mass times the acceleration of the cylinder

$$F_{pot} = -m_A \ddot{y} = -C_A \frac{\pi}{4} \rho D^2 L \ddot{y}, \quad (5.6)$$

where m_A and C_A (= 1.0 for the circular cylinder) are the added mass and potential added mass coefficient, respectively. The vortex force is then calculated by subtracting the potential force from the total lift force. The RMS vortex force coefficient ($C_{vortex} = F_{vortex} / (\frac{1}{2}\rho U^2 DL)$) is plotted in figure 5.9(b) against U^* for various damping values. The vortex force increases with U^* in the initial branch and reaches its peak at the start of the upper branch. There is a sudden decrease in C_{vortex} at the start of the upper branch. The vortex force increases with further increase in U^* . In the lower branch, the vortex force is seen to decay almost linearly with U^* .

It is also important to examine the phase of the fluid forces. The phase difference between lift force and cylinder displacement (ϕ_{total}) is shown in figure 5.10(a) for various damping ratios. The phase of vortex force with respect to displacement (ϕ_{vortex}) is shown in figure 5.10(b). For very low damping values, the total phase remains at 0° during the initial and upper branch. The total phase jumps to 180° during the transition from the upper branch to lower branch. The vortex phase, on the other hand, shows a jump from 0° to 180° at the start of the upper branch. These jumps in the total and vortex phase agree with those observed by Govardhan and Williamson (2000); Khalak and Williamson

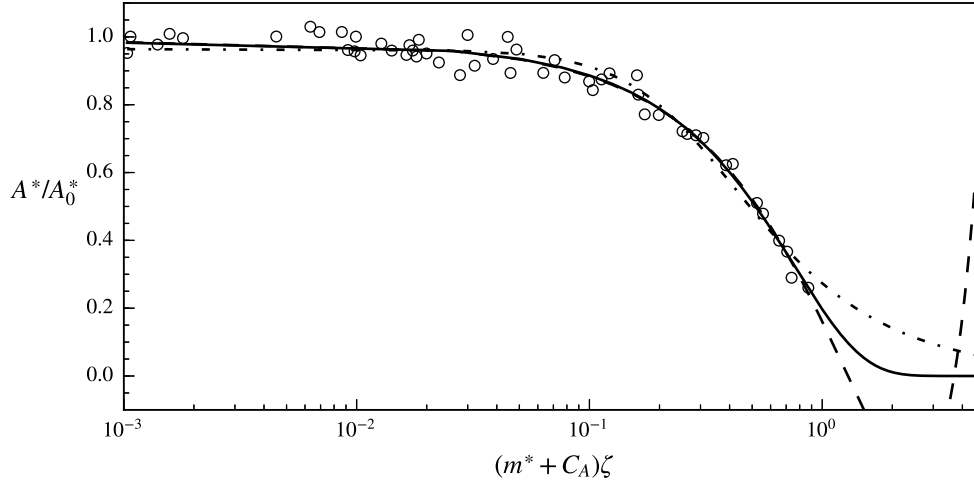


Figure 5.11: Comparison of quadratic polynomial fit (dashed line), fit proposed by [Sarpkaya \(1978\)](#) (dash-dot line) and (5.7) with $n = 2$ (solid line). The data points shown as circular symbols are taken from [Govardhan and Williamson \(2006\)](#).

(1999). The jump in the vortex phase is associated with the change in the wake structure from 2S to 2P mode. As the damping ratio is increased, the phase changes between the branches become more continuous. In addition, the phase difference between branches tends to reduce with increasing damping.

5.3.4 The Griffin plot

Previous studies have attempted to relate the peak vibration amplitude of a circular cylinder undergoing VIV with the product of mass and damping ratios ($m^*\zeta$). [Griffin \(1980\)](#) plotted the peak vibration amplitude against the Skop-Griffin parameter $S_G = 2\pi^3 S^2(m^*\zeta)$, where S is the Strouhal number for a stationary cylinder. This is known as the *Griffin plot*. [Sarpkaya \(1978\)](#) proposed the following relationship: $A^* = B/\sqrt{C + S_G^2}$ where B and C are determined from curve fit. [Govardhan and Williamson \(2006\)](#) proposed, what they called, the *modified Griffin plot*, where they plotted the peak vibration amplitude against the logarithm of mass-damping parameter $\alpha = (m^* + C_A)\zeta$. For Reynolds numbers in range of 500 to 33000, they found a fit for that the peak vibration amplitude of circular cylinder at zero damping with Re as $A_0^* = \log_{10}(0.41\text{Re}^{0.36})$. At a fixed Re, they proposed a quadratic polynomial fit between the peak vibration amplitude and mass-damping parameter. Overall, the peak vibration amplitude as a function of mass-damping and Reynolds number is written as $A^* = (1 + C_1\alpha + C_2\alpha^2) \log_{10}(0.41\text{Re}^{0.36})$ where C_1 and C_2 are constants.

The authors, independently, developed an exponential fitting function for the following reasons: a) the plot of peak vibration amplitude versus the mass-damping parameter on a linear scale looks like an exponentially decaying function and b) since the damp-

Table 5.2: Coefficients of the exponential fit, obtained by least-squares fitting method, for the peak vibration amplitude data shown in figure 5.12a

Set	Re range	A_0^*	C_0	C_1
1	1687– 2030	0.798	-0.802	-1.483
2	2995– 3440	0.878	-0.812	-0.959
3	5328– 5898	0.970	-0.966	-0.755

ing force is proportional to cylinder velocity, it should take very large (tending towards infinite) amount of damping to completely suppress the VIV. The following general exponential fitting function was conceptualized to take into account the expected asymptotic behaviour

$$A^* = A_0^* \exp \left(\sum_{i=1}^n C_i \alpha^i \right), \quad (5.7)$$

where C_i are constants determined based on a least-squares fit. A second-order form ($n = 2$) was found to give an excellent fit. Figure 5.11 is taken from Govardhan and Williamson (2006) and shows comparison of three fitting functions: quadratic fitting, the fitting proposed by Sarpkaya (1978), and (5.7) with $n = 2$. Both the quadratic and exponential fitting functions overlap over the available data range shown by the circular markers. As noted by Govardhan and Williamson (2006), the quadratic fit does not behave nicely in the high mass-damping region where it first predicts a negative peak vibration amplitude and then an increase in peak vibration amplitude with mass-damping. The exponential fit, on the other hand, predicts a slowly decaying peak vibration amplitude with mass-damping. The fitting proposed by Sarpkaya (1978) also shares the property of requiring an infinite amount of damping to completely suppress the VIV but it is less accurate in fitting the available data (see appendix B of Govardhan and Williamson (2006)).

The peak vibration amplitude of the cylinder as a function of mass-damping, for three sets of experiments reported in table 5.1, is plotted in figure 5.12a. The exponential fitting function, (5.7) with $n = 2$, is used to connect the data points. The coefficients of the fit are listed in table 5.2. The error bars represent the standard deviation in vibration amplitude from its mean value. A smaller standard deviation implies that the vibration amplitude varies little from one cycle to another. The peak vibration amplitude of the circular cylinder is seen to increase with Reynolds number. This could be related to the decrease in the viscous component of the lift force acting on the cylinder. Table 5.3 shows the root mean square (RMS) error for three types of fitting used in figure 5.11 at three

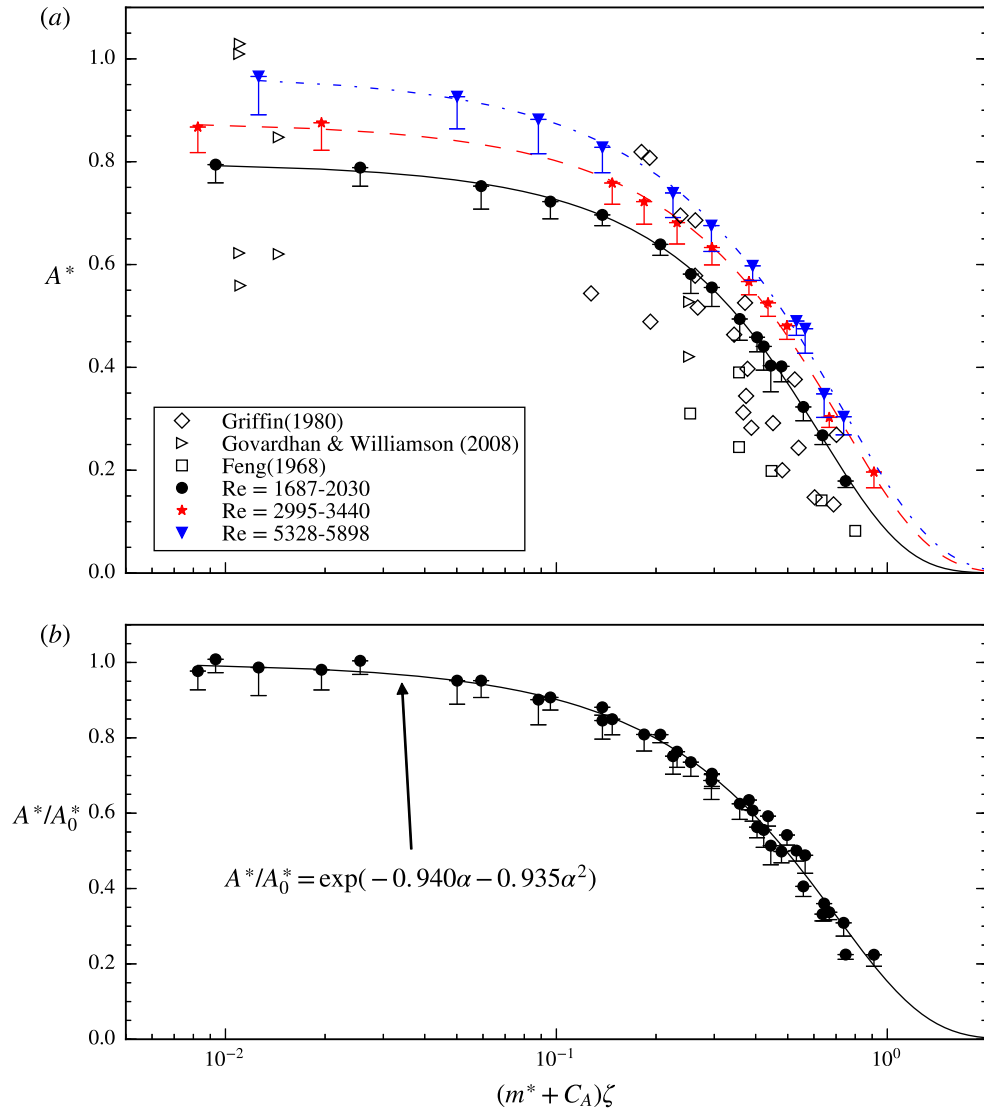


Figure 5.12: Griffin plot (a) showing the comparison of our results for three Re ranges with the published data, and (b) collapse of all the data points onto a single curve by considering the effect of Reynolds number. The error bars represent the standard deviation in vibration amplitude from its mean value.

Table 5.3: Root mean squared error of three fitting functions for the peak vibration amplitude data shown in figure 5.12a.

Set	Re range	RMS error		
		Equation 5.7 with $n = 2$	quadratic fit by Govardhan and Williamson (2006)	fitting by Sarpkaya (1978)
1	1687–2030	0.023	0.017	0.129
2	2995–3440	0.036	0.048	0.128
3	5328–5898	0.040	0.035	0.071

different Reynolds numbers. The RMS error is defined as

$$E_{rms} = \sqrt{\frac{1}{N} \sum_{i=1}^N \left(\frac{A^* - A_{fit}^*}{A^*} \right)^2}, \quad (5.8)$$

where A^* is the measured vibration amplitude, A_{fit}^* is the vibration amplitude obtained from fit and N is the total number of data set points. Both exponential and quadratic fitting give similar RMS errors while the fitting by Sarpkaya has a larger error. Therefore, the exponential fit in (5.7) performs as good as the quadratic fitting function while having a better basis, given the physical behaviour at higher mass-damping values.

Interestingly, the peak vibration amplitude occurs at different reduced velocities at different damping values. In general, the optimal reduced velocity corresponding to peak vibration amplitude increases with damping because the damped natural frequency of a linear spring-mass system is known to be smaller than the undamped one. Therefore, there is a small variation in Reynolds number corresponding to each data point in figure 5.12(a) for each set of experiments. The range of variation in Re is also shown in table 5.3. To account for the Reynolds number effect, the undamped peak vibration amplitude in (5.7) is expressed as $A_0^* = \log_{10}(DRe^E)$ where D and E are constants. The four constants in the modified form of (5.7) are then determined by a least-squares fit of all the data from three sets of experiments in figure 5.12(a). The set of values of constants obtained is $(D, E, C_1, C_2) = (0.402, 0.366, -0.940, -0.935)$. Once the constants D and E are known, the effect of Re in the Griffin plot can be eliminated by dividing the individual A_0^* data in figure 5.12a by the A_0^* corresponding to the Re value at that data point. The resulting Griffin plot is shown in figure 5.12(b) which shows a strong collapse of the peak vibration amplitude, normalized by its undamped value, on a single curve. Therefore, the following

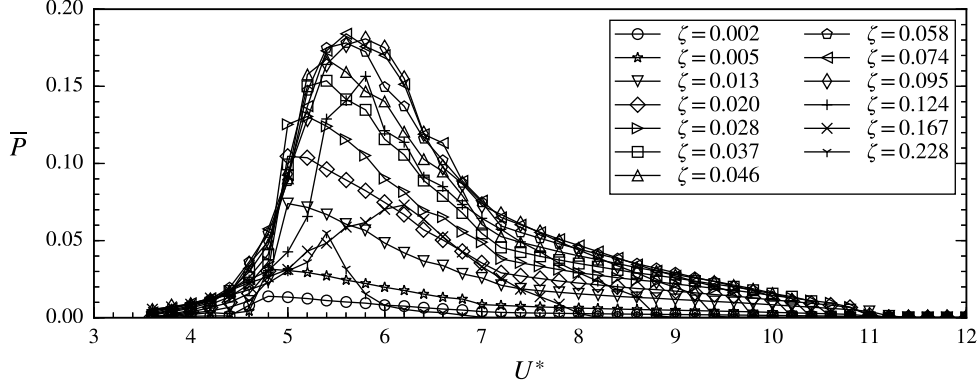


Figure 5.13: The average extracted power versus reduced velocity for various values of damping ratios.

equation can be used to predict the peak vibration amplitude (A^*) of a circular cylinder undergoing VIV as a function of mass-damping (α) and Reynolds number (at least over the range of Re considered in this study)

$$A^* = \log_{10} (0.402\text{Re}^{0.366}) \exp(-0.940\alpha - 0.935\alpha^2). \quad (5.9)$$

5.3.5 Power extraction

The fluctuating lift force acting on the cylinder, due to vortex shedding, causes the cylinder to vibrate. The vibration of the cylinder suggests a way to extract power from the fluid flow. Any power extraction process can be modelled as the addition of damping to the system. Usually, the damping coefficient for the power-harvesting device is modelled as a constant. In [Soti et al. \(2017\)](#), it was shown that a constant damping ratio model predicts the same average power that will be extracted by a more realistic electromagnetic power extraction device where the damping is far from constant. In the present experiments, different damping values were introduced to the system and then the extracted power was calculated by using the observed cylinder displacement and the preset value of damping introduced to the system. If the cylinder displacement at any instant is given by $y(t)$ then the instantaneous non-dimensional power extracted by the damper is $P(t) = cy(t)^2 / (\frac{1}{2}\rho U^3 DL)$ which can also be written as

$$P(t) = 2\pi^2 f_n^* m^* \zeta \dot{y}^{*2}, \quad (5.10)$$

where $f_n^* = f_n D/U$ and $y^* = y/D$ are the non-dimensional natural frequency in vacuum and displacement of the cylinder, respectively. Since the cylinder undergoes a periodic motion, the average extracted power over a cycle of oscillation can be defined as $\bar{P} = \int_0^T P(t) dt$ where T is the period of oscillation. The cylinder displacement can be approximated as $y^* = A_y^* \sin(2\pi f_y f_N^* t)$ where A_y^* , f_y and f_N^* are non-dimensional displace-

Table 5.4: Coefficients of the exponential fit, obtained by least-squares fitting method, for the maximum average power

Set	Re range	C_3	C_1	C_2
1	1560-1998	1.591	-3.624	-1.739
2	2662-3440	1.512	-2.222	-2.246
3	4757-5708	1.581	-1.922	-2.637

ment amplitude, normalized vibration frequency and non-dimensional natural frequency of the cylinder in water, respectively. Using this approximation, the average power can be simplified to

$$\bar{P} = 4\pi^4 f_n^* f_y^2 m^* \zeta \left(\frac{A_y^*}{U^*} \right)^2, \quad (5.11)$$

The average power varies from one vibration cycle to another because of the variation in vibration amplitude. In the present experiments, the average power was calculated over many (≈ 100) vibration cycles. The average extracted power as a function of reduced velocity is shown in figure 5.13 for various damping values for set 2. At any damping value, an optimal reduced velocity exists at which \bar{P} is maximum. Since the vibration amplitude and thereby the cylinder velocity attains its maximum in the upper branch, it is expected that \bar{P} will be maximum in the upper branch.

In general, the value of U^* at which the average power is maximum may not be same as that of the maximum vibration amplitude. The optimal U^* values for maximum power and maximum displacement amplitude are found to differ by 1.0 and 0 at minimum and maximum damping values, respectively, in the present experiments. The normalized vibration frequency is close to 1.0 in the upper branch where the average power is maximum. Since the vibration amplitude varies from one vibration cycle to another the maximum average power is approximated as $\bar{P}_m = C_0 \alpha \bar{A}^{*2}$ where C_0 is a constant and \bar{A}^* is the peak mean vibration amplitude of the cylinder. Assuming that the peak mean vibration amplitude can be related to the mass-damping using a function similar to (5.7), the maximum average power is approximated as

$$\bar{P}_m = C_3 \alpha \exp(C_1 \alpha + C_2 \alpha^2), \quad (5.12)$$

where $C_3 = C_0 (\bar{A}_0^*)^2$ and \bar{A}_0^* is the peak mean vibration amplitude at zero damping. Notice that n is taken as 2 in (5.12) as only two terms inside the exponential were found to be sufficient for accurate fitting in section 5.3.4.

The maximum average power (\bar{P}_m) obtained from the present experiments is plotted in figure 5.14 for three ranges of Reynolds number. Notice that the Re range in figure 5.14 differs from that in figure 5.12a because the optimal values of U^* for average power and

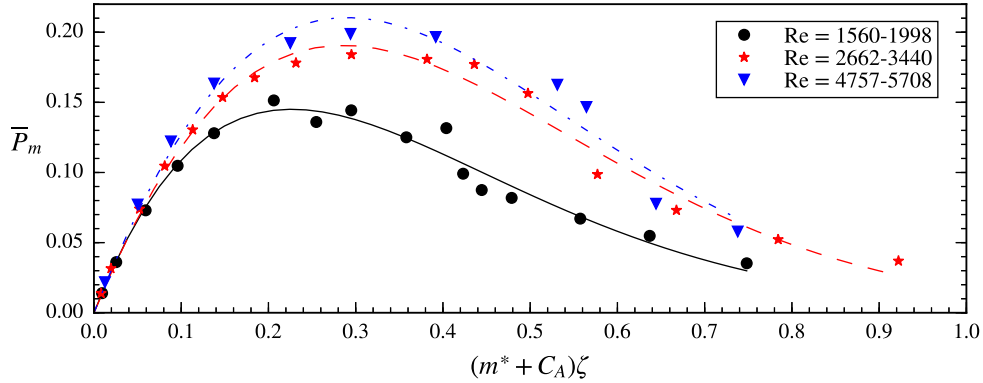


Figure 5.14: The maximum average extracted power versus damping ratio for three Reynolds number ranges given in table 5.1.

peak amplitude are different. The data is fitted to (5.12) using the least-squares method. The constants of (5.12) obtained by the least-squares fit are listed in table 5.4. From figure 5.14, it is seen that there is also an optimal damping at which \bar{P}_{max} is maximum. The existence of an optimal damping can be explained as follows: The extracted power will be zero at zero damping. on the other hand, the extracted power will also be zero at very large damping due to complete suppression of the cylinder vibration. Therefore, as the damping is increased from zero, the extracted power should first increase with damping then reach a maximum for some optimal damping before decreasing back to zero. Since the vibration amplitude increases with Reynolds number, the extracted power is expected to increase too. Figure 5.14 also shows the effect of Re on extracted power. As expected, the extracted power increases with Reynolds number. The value of optimal damping also increases by small magnitude with Reynolds number. The maximum value of \bar{P}_m for set 1, 2 and 3 are close to 0.15, 0.18 and 0.20, respectively.

Assuming that the peak mean vibration amplitude at zero damping follows a logarithmic relationship with Reynolds number similar to the one used in section 5.3.4, the average power as a function of Reynolds number and mass-damping is written as

$$\bar{P}_m = [\log_{10} (0.252\text{Re}^{0.538})]^2 \alpha \exp (-2.882\alpha - 1.779\alpha^2), \quad (5.13)$$

The coefficients in (5.13) were obtained by using a least-squares fit on the all data points in figure 5.14.

5.4 Closure

The effects of damping on the vortex-induced vibration of a circular cylinder were studied experimentally. An eddy-current-based passive damping mechanism was used to apply various damping levels to the system. The cylinder vibration response and the fluid forces

were recorded as a function of the reduced velocity over a range of damping values.

The typical three-branch VIV response (the initial, upper and lower branches) are observed at low damping values. The jumps in amplitude response at the boundaries of these branches get smeared out as the damping is increased. The frequency response also shows jumps at the boundaries of the branches at low damping but these jumps disappear at higher damping. However, there are the following similarities between frequency responses at low and high damping: there is a region of reduced velocity at higher damping similar to a) the initial branch where the vibration frequency matches with the vortex shedding frequency for a stationary circular cylinder; b) the upper branch where the vibration frequency is close to the natural frequency of cylinder and increases moderately with the reduced velocity; and c) the lower branch where the vibration frequency stays constant. Therefore, it is reasonable to also label these regions as the initial, upper and lower branches, respectively, for higher damping cases. The frequency of vibration decreases by a little with damping in all of these regions since the damped natural frequency is smaller than the undamped one. The amplitude response decreases with increasing damping due to an increase in the dissipation of the kinetic energy of cylinder by the damper. As the damping is increased, all branches are seen to shrink in terms of the range of reduced velocity. Consequently, the synchronization region also shrinks with increasing damping.

The lift force also shows a monotonic decrease with increasing damping. Since the power dissipation is proportional to the sine of the phase difference between the lift and displacement signals, the total phase remains close to 0° and 180° for low damping. As the damping is increased, the total phase tends to vary in a continuous fashion with reduced velocity.

The effect of damping on the peak vibration amplitude is quantified by plotting it against the product of mass and damping ratios (called mass-damping) in the *Griffin plot*. The peak amplitude data, obtained by varying the damping and keeping the Reynolds number fixed, shows a smooth variation with mass-damping. Three sets of experiments with different Reynolds number ranges were conducted to account for the Reynolds number effects. The experiments agree with the finding of [Govardhan and Williamson \(2006\)](#) that the scatter in previously reported Griffin plots is due to the Reynolds number variation. An exponential fitting function is proposed that fits the peak amplitude data with excellent accuracy and shows a monotonic decay of peak amplitude at higher mass-damping.

The amount of power dissipated by the damper was also calculated and was regarded as the power that can be extracted from the flow through VIV of the cylinder. At any damping value, there is an optimal reduced velocity for extracting maximum power. Also, there is an optimal damping value at any reduced velocity at which the extracted power is maximum. Therefore, there is an optimal combination of damping and reduced velocity

where the extracted power attains its global maximum value. The vibration amplitude and hence the extracted power is seen to increase with Reynolds number.

Chapter 6

Vortex-induced vibrations of a thin plate

The flow-induced vibration of an elastically mounted thin plate with aspect ratio, the ratio of width to thickness of the plate, equal to 12.0 is investigated using experiments at higher Reynolds number and numerical simulations for low Reynolds number. In the experiments, a stainless steel plate with mass ratio 34.4 was elastically mounted on an air bearing system using linear springs. The air bearing setup allows very low friction leading to a very low damping system. The experiments were performed in a water channel and the numerical results were calculated using a spectral-element based fluid-structure interaction solver. The results at low and high Re show remarkable similarities. The thin plate response is dominated by the vortex-induced vibration (VIV) and the galloping is absent at both low and higher Re. There are three branches in the vibration amplitude response of the plate. The first two branches show a linear increment, with a different slope for each branch, of the vibration amplitude with the reduced velocity. The vortex shedding mode is $C(2S)$ in the first branch and $C(2S) + 2S$ in the second branch. The vortex shedding frequency in the two branches is close to the natural frequency of the plate. At any reduced velocity in the first two branches, the vibration amplitude remains constant with respect to the time as also observed in the lower branch of a circular cylinder undergoing VIV. The maximum vibration amplitude occurs at the end of the second branch and is equal to $2.0D$ and $1.4D$ for high and low Reynolds number cases, respectively. The phase difference between the lift force and the displacement is equal to 0° for the first two branches. The third branch starts as the phase difference changes to 180° . The vibration amplitude decreases with the reduced velocity in the third branch. Intermittency in the vibration response is observed towards the end of the third branch. Three vortex shedding modes: $C(2S)$, $C(2S) + 2S$ and $P + S$, are observed in the intermittency region. Similar to a circular cylinder, a lower mass ratio (3.0) plate vibrates with significant amplitude over a wider range of reduced velocity and the peak vibration amplitude is independent of the mass ratio. On the other

hand, the range of reduced velocity over which the vortex shedding frequency is close to the natural frequency of the plate decreases for the lower mass ratio.

6.1 Introduction

Vortex-induced vibration (VIV) of bluff bodies is an important subject of study for its applications in various engineering problems such as marine risers, transmission lines, bridge design, buildings, heat exchangers, energy harvesting devices, etc. The phenomenon occurs when the natural frequency of a structure is close to the vortex shedding frequency associated with it. The fluctuating lift force due to the vortex shedding phenomenon gets locked-in with the motion of the structure and can cause large deformations leading to catastrophic structural failure. The collapse of the Tacoma narrow bridge is a real-life example of the destructive power of VIV. For this reason, researchers have focused on estimating the maximum vibration amplitude that a certain bluff body will experience in the lock-in condition. In general, the structures represent a continuous system with infinite degrees of freedom (DOF) and natural frequencies. To simplify the problem, the elastic structure is modeled as a rigid body connected to a simple linear spring. This simplified model looks at the one or two degrees of freedom vibrations of a bluff body that is kept in a free stream of fluid flow.

Many studies have been reported on VIV of a circular cylinder. A detailed description can be found in [Khalak and Williamson \(1999\)](#), [Williamson and Govardhan \(2004\)](#), [Sarpkaya \(2004\)](#), [Gabbai and Benaroya \(2005\)](#), and [Bearman \(2011\)](#). A circular cylinder with the transverse degree of freedom has three response branches of VIV ([Khalak and Williamson, 1999](#)). For very low reduced velocity, the inverse of the non-dimensional natural frequency of the structure, the cylinder does not vibrate significantly. As the reduced velocity is increased, the cylinder starts to vibrate with a small amplitude that increases with the reduced velocity. This region is called the *initial* branch. Both natural frequency of the structure and vortex shedding frequencies are present in the displacement. The phase difference between the lift force and the displacement of the cylinder is 0° . The vortex shedding is in 2S mode. There is a jump in the vibration amplitude at the end of the initial branch and the *upper* branch starts. The vortex shedding frequency gets locked-in with the natural frequency of the structure and therefore the vibration amplitude becomes large. The maximum vibration amplitude occurs in the upper branch. The value of maximum vibration amplitude is an increasing function of Reynolds number. The start of the upper branch is associated with a jump in the phase of the vortex force from 0° to 180° and the vortex shedding changes from 2S to $2P_o$. With further increase in the reduced velocity, the phase of lift force jumps to 180° as the *lower* branch starts. The vortex shedding changes to 2P mode. The vibration amplitude remains close to $0.6D$ in

the lower branch and the cylinder vibrations are quite periodic. The vibration frequency also stays constant in the lower branch. Only the initial and lower branches are said to be present (Prasanth and Mittal, 2008) at low Reynolds number. The 2S vortex shedding mode is observed at all reduced velocities. The lower limit of Reynolds number for VIV of a circular cylinder to occur has been reported to be 20 (Mittal and Singh, 2005).

For non-circular cross-sections, such as a square cylinder, the relative angle of attack changes due to the body motion. The fluid forces may become in phase with body motion which results in what is called the *galloping*. The vibration amplitude in galloping is larger than the VIV cases but the frequency of vibration is a fraction of the vortex shedding frequency. Unlike VIV, the vibration amplitude increases with the reduced velocity in galloping. Parkinson and Smith (1964) developed a quasi-steady theory for predicting the critical flow velocity for the onset of galloping for a square cylinder. Both VIV and galloping can influence the motion of a body having a non-circular cross-section. Nemes et al. (2012) experimentally studied the effects of orientation on flow-induced vibration (FIV) of a square cylinder. The cylinder was free to vibrate only in the direction transverse to the incoming flow. For zero angle of attack, the square cylinder shows the galloping response. The vibration amplitude is found to increase with the reduced velocity and the vibration frequency is smaller than the vortex shedding frequency. For the 45° angle of attack configuration, also referred as the diamond shape, the amplitude response is dominated by the VIV. The maximum vibration amplitude was $0.75H$ where H is the length of the diagonal. Both VIV and galloping were found to contribute to the cylinder response for some intermediate values of the angle of attack. Zhao et al. (2014a) conducted experiments on the transverse FIV of a square cylinder for three angles of attacks with a very fine resolution of reduced velocity. For zero angle of attack, the vibration response was dominated by the galloping instability. It was argued that the vortex shedding frequency can only synchronize to an odd-integer multiple of the oscillation frequency. For 20° angle of attack case, the so-called higher branch that was identified by Nemes et al. (2012) was also observed. The oscillation amplitude in this branch is higher than that observed in either of VIV or galloping cases.

Zhao et al. (2013) numerically investigated the fluid-structure interaction of a square cylinder having two DOF at $Re = 100$ for three angles of attack ($\alpha = 0^\circ, 22.5^\circ$ and 45°). Galloping was absent at zero angle of attack. For $\alpha = 22.5^\circ$, two galloping dominated lock-in regions were observed. Maximum vibration response was observed at $\alpha = 45^\circ$. Barrero-Gil et al. (2009) have shown the galloping for a square cylinder starts after Reynolds number 159. The maximum vibration amplitude was observed for 45° angle of attack. In contrast to a circular cylinder, the vibration frequency in the in-line direction was found to be same as that in the cross-flow direction. Zhao (2015), through numerical simulations, studied FIV of rectangular cylinders of aspect ratio, the ratio of side lengths along and

transverse to the flow, 0.3 and greater at $Re = 200$. For aspect ratios greater than 0.3, the vibration response showed both the VIV and galloping regions. The aspect ratio 0.3 case only showed the VIV response region. The maximum vibration amplitude in the VIV lock-in region and the critical velocity for the onset of galloping were found to decrease and increase, respectively, with the aspect ratio. [Sen and Mittal \(2015\)](#), using numerical simulations, studied the effect of mass ratio on free vibration of a square cylinder at zero angle of attack. For low mass ratio ($m^* = 1$), the response was dominated by VIV. On the other hand, both VIV and galloping were present at higher mass ratios.

Recently, VIV has also received attention for being a source of renewable energy. Any vibrating structure has some energy, a part of which can be converted to usable energy such as electricity. [Soti et al. \(2017\)](#), through numerical simulations, studied the power extracting capability of an electromagnetically coupled FSI system. The motion of a circular cylinder undergoing VIV was transferred to a linear electromagnetic generator. The flow power was extracted at 13% efficiency at Reynolds number 150. The extracted power is proportional to the square of the vibration amplitude. The circular cylinder may not be ideal and a better bluff body geometry may exist for power extraction. Therefore, VIV of non-circular geometries needs to be explored. Practically, a thin plate is much easier to use as compared to a circular cylinder since the raw material comes in the form of thin sheets.

There has been no previous study in literature focusing on FIV of thin plates. It is not known whether the FIV response of such geometry will be dominated by the VIV or galloping mechanism. In the present work, FIV of a thin plate with aspect ratio 12 is investigated at low and higher Reynolds numbers using numerical and experimental techniques, respectively. The thin plate is elastically mounted and is free to move only in the transverse direction. The details of the experimental method are given in section [6.2.1](#). The numerical method is described in section [6.3.1](#). The FIV response of the plate at higher Reynolds number is discussed in section [6.4.1](#) and the corresponding wake structures are presented in section [6.4.2](#). The low Reynolds number vibration response and corresponding wake structures are presented in section [6.4.3](#) and [6.4.4](#), respectively.

6.2 Experimental method

6.2.1 Experimental apparatus

The VIV experiments on a thin plate were conducted in a free-surface recirculating water channel facility of the Fluids Laboratory for Aeronautical and Industrial Research (FLAIR) at Monash University. The water channel has a width of 600 mm and depth of 800 mm. The sketch in figure [6.1](#) shows a plate of thickness d and width D kept normal to

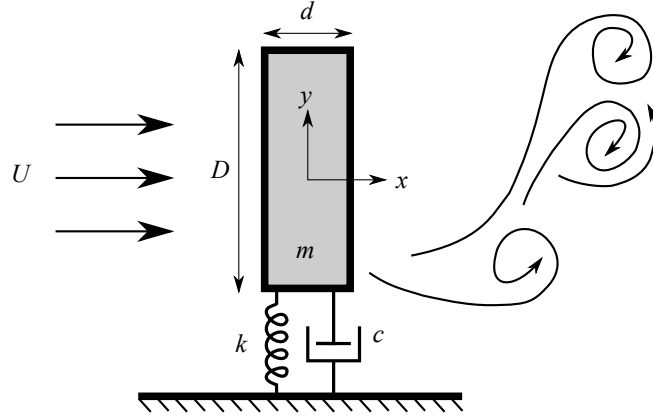


Figure 6.1: A representative sketch for the vortex-induced vibration in the transverse direction of a thin plate of thickness d and width D . The free stream velocity of the fluid is U . The symbols k and c represent the spring constant and damping coefficients, respectively.

an incoming free-stream flow of velocity U . Above some critical Reynolds number, vortex shedding will take place resulting in fluctuating forces on the plate. The motion of the plate due to the fluid forces in the transverse direction (F_y) is governed by the following equation

$$m\ddot{y}^* + c\dot{y}^* + ky^* = F_y, \quad (6.1)$$

A stainless steel plate of thickness $d = 2.5$ mm and width $D = 30.0$ mm was used for the experiments. The aspect ratio $\alpha (=D/d)$ is 12.0. The immersed length of the plate inside water was $L = 450.0$ mm. The mass of the displaced fluid $m_f = \rho D^2 L / \alpha$ was equal to 33.7 g. The total moving mass (m) was equal to 1159.6 g. Therefore, the mass ratio $m^* = m/m_f$ of the plate was 34.4. An air bearing system was used to allow almost frictionless motion in the direction transverse to the incoming flow. The air bearing system consisted of two air bushings which could move along two straight circular shafts. The air bushings were connected to a compressed and clean air supply. The air bushings were housed in a carriage to which the plate was attached. A strain gauge based force sensor was attached between the plate and the carriage for lift and drag force measurements. Springs were also attached to the carriage. An optical encoder (model: RGH24, Renishaw, UK) was mounted to the side of the carriage for monitoring the displacement of the plate. The digital optical encoder measured the displacement of the plate without making any physical contact with the carriage with an accuracy of 1 μm . A damper system is mounted on the other side of the carriage for setting various damping values in the experiments. A schematic of the experimental setup is shown in figure 6.2. An end plate is kept at the bottom of the water channel to reduce the end effects on the bottom end of the plate (Morse et al., 2008). The data acquisition was done using a USB data acquisition device (model: USB6218-BNC, National Instruments, US). LabVIEW software was used

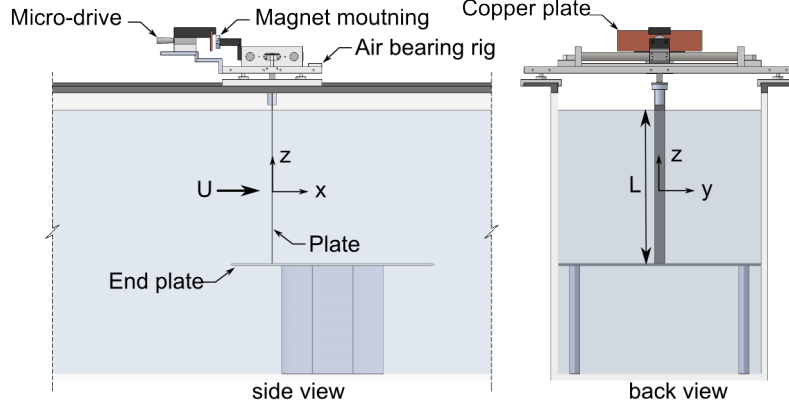


Figure 6.2: Schematic of the experimental set-up used for the VIV experiments.

to control the water channel pump for changing the free-stream velocity and thereby the reduced velocity. For each reduced velocity, the data was sampled at 100 Hz and was recorded for 300 seconds, unless specified otherwise, which was found to be sufficient for getting reliable and repeatable response amplitude and forces.

Particle image velocimetry (PIV) was used for measuring the flow velocity field in the near wake of the plate. A high-speed digital camera with 2048×2048 pixels resolution was placed at the bottom of the channel and a continuous laser sheet was shined at the middle of the immersed length of the plate with the help of a cylindrical lens. Water was seeded with micro-particles which were illuminated by the laser. Series of image pairs, separated by a very short time interval (in the order of milliseconds), was captured at 10.0 Hz and the image pairs were cross-correlated to find instantaneous flow velocity. The instantaneous flow fields were phase-average to create vorticity contours at 24 instants in one cycle of plate oscillations.

6.3 Numerical method

6.3.1 Solution Method

The VIV of the thin plate with aspect ratio ($\alpha = D/d$) 12.0 was simulated by solving the coupled equations for fluid flow and plate motion. The plate width (D) and free-stream velocity were taken as the reference length and velocity, respectively. The Reynolds number, $Re = UD/\nu$ where ν is the kinematic viscosity of the fluid, was taken as 150. The flow is solved in the reference frame of the plate which eliminates the need of re-meshing the computational domain as the plate moves. The flow was assumed to two-dimensional and is governed by the following non-dimensional Navier-Stokes equations

$$\frac{\partial \mathbf{u}}{\partial t} + (\mathbf{u} \cdot \nabla) \mathbf{u} = \nabla p + \frac{1}{Re} (\nabla^2 \mathbf{u}) + \mathbf{a}_F, \quad (6.2)$$

where \mathbf{a}_F , \mathbf{u} and p represents the transverse acceleration of the plate, flow velocity vector and fluid kinematic pressure, respectively. Equations 6.2 are discretized using a nodal spectral-element based method (Karniadakis and Sherwin, 1999). In this approach, the computational domain is divided into non-overlapping regions called *elements*. In each element, the solution of the governing equation is approximated by the *shape functions* which, in the present solver, are taken as the tensor product of Lagrange polynomials. The order of the Lagrange polynomials determines the spatial accuracy of the solution method. A n^{th} order Lagrange polynomial has $n + 1$ nodal points. The nodal points are taken as the Gauss-Legendre-Lobatto quadrature integration points. The residual is obtained by putting the approximate solution into the governing equation. Finally, the integral of the product of the residual with *weighting functions* is set to zero. The weighting functions are also the tensor product of Lagrange polynomials in the present solver. The elemental linear systems obtained from the weighted residual method are then assembled into a global linear system while imposing the continuity of solution at element boundaries. The time-integration of the discretized equations is done using the fractional step method (Chorin, 1968a; Thompson et al., 2006). First, the convective terms are integrated to arrive at an intermediate velocity using an explicit Adam-Bashforth method. The acceleration of the reference frame is added to this substep. Then the diffusive terms are integrated using the implicit Crank-Nicholson method. The pressure substep is used to correct the intermediate velocity to satisfied the continuity equation.

The motion of the plate is governed by the following non-dimensional equation

$$\ddot{y} + \frac{4\pi\zeta\dot{y}}{U^*} + \frac{4\pi^2y}{(U^*)^2} = \frac{\alpha}{2} \frac{C_y}{m^*}, \quad (6.3)$$

where y and C_y are the non-dimensional transverse displacement and lift force of the plate, respectively. The reduced velocity $U^* = U/(f_n D)$ is based on the natural frequency of plate in vacuum (f_n). The damping ratio (ζ) was taken as zero to maximize the plate vibrations. The mass ratio is defined as $m^* = m/(m_f)$ where $m_f = \rho D^2/\alpha$ is mass of the displaced fluid by the plate. The coupled equations 6.2 and 6.3 are solved using an implicit partitioned approach. The iteration starts by extrapolating the plate position and velocity from previous time steps and then the flow equations are solved to get an estimate of the fluid forces. The estimated forces are then used to correct the plate position and velocity which are then used for generating the next estimate for the fluid forces. This iteration continues till the flow field, plate position and velocity converges to a predefined limit. The solver has been used previously to model vortex-induced vibration (Leontini et al., 2006a,b, 2011; Soti et al., 2017).

6.3.2 Computational domain and boundary conditions

The computational domain was a rectangle of length $60D$ in x and $80D$ in y direction. The flow was along the positive x direction. The plate was located at $20D$ from the inlet and midway along the transverse direction. Flow is prescribed as $u = U$ and $v = -\dot{y}$ at left, top and bottom boundaries of the domain where \dot{y} is velocity of the plate. Zero Neumann boundary condition was applied at the outlet on the right boundary. No-slip boundary condition was applied to the plate surface. The size of the computational domain was determined by doing a domain independence study. Any further increase in the domain size created less than 1% change in the vibration amplitude of the plate. The computational domain was divided into 720 non-uniform quadrilateral elements. The element order was chosen to be six based on the mesh independence study. A higher order element resulted in less than 1% change in the vibration amplitude of the plate (see section 7.2.3).

6.4 Results

6.4.1 Response at a higher Reynolds number

The vortex-induced vibration (VIV) response of the thin plate with aspect ratio 12.0 at a low damping and a higher Reynolds number is presented in this section. The natural frequency of the elastically mounted plate in the air (f_n) and water (f_N) were 0.839 Hz and 0.834 Hz, respectively. The damping ratio was $\zeta = 1.33 \times 10^{-3}$ and the mass ratio was $m^* = 34.4$. The added mass coefficient $C_A = m^*((f_n/f_N)^2 - 1)$ comes out to be 0.43. The natural frequency in air and the damping ratio were measured by doing free-decay tests in which the spring-mass system is displaced away from its equilibrium position and left to vibrate. The damping ratio was calculated using the logarithmic decrement rule for free vibrations of the system governed by equation 6.1. The natural frequency in water was calculated by doing a similar free-decay test while the plate was submerged in still water. The displacement and force data were recorded for six minutes at 100 Hz for most of the cases which were equivalent to approximately 250 cycles of plate oscillation. An important parameter in the study of VIV is the reduced velocity defined as $U^* = U/(f_N D)$ where U is the free stream velocity and D is the characteristic length, equal to the width of the plate in the present case. The natural frequency of the system was kept fixed in the experiments since it required manually changing the mass or/and springs of the system. The free stream velocity, on the other hand, could be changed in an automated fashion by changing the rotation rate of the driving pump for the water channel. Therefore, the free stream velocity was changed in the experiments to vary the reduced velocity. The change in the free stream velocity also resulted in the change of the Reynolds number

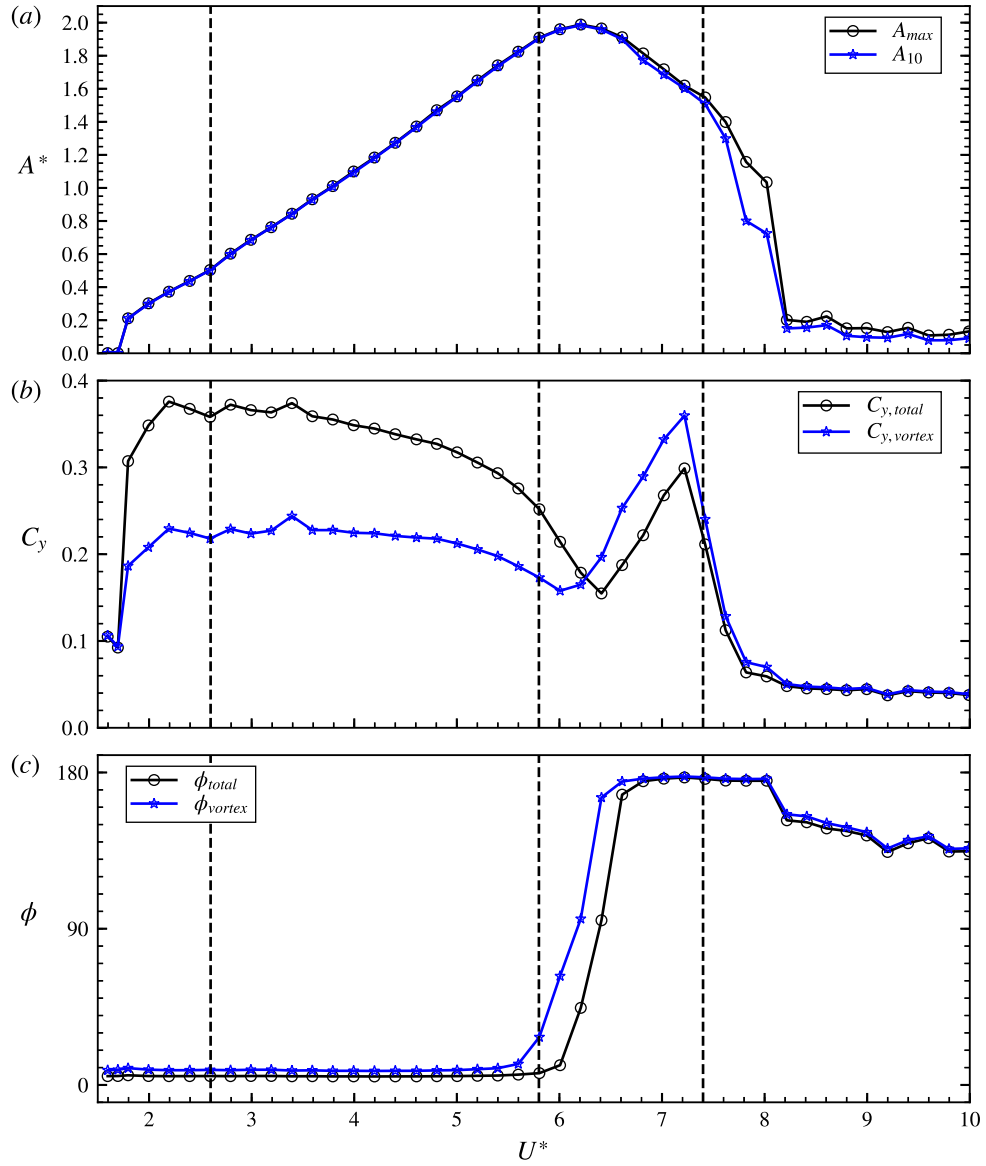


Figure 6.3: Low damping response of a thin plate with aspect ratio $\alpha = 12$ with $m^* = 34.4$ and $\zeta = 1.33 \times 10^{-3}$. (a) vibration amplitude, (b) RMS lift coefficient and (c) phase difference between lift and displacement versus reduced velocity.

$Re = UD/\nu$, where ν is the kinematic viscosity of water. The density (ρ) and viscosity (μ) of water are taken as 998 and 8.9×10^{-4} , respectively. The reduced velocity was varied between the range of 1.6–10.0 with an increment of 0.2 and correspondingly the Reynolds number varied in the range of 1343–8406.

The non-dimensional vibration amplitude response of the thin plate is plotted in figure 6.3a as a function of the reduced velocity. In figure 6.3a, A_{max} refers to the maximum value of amplitude and A_{10} denotes the mean of top 10% amplitude values (Hover et al., 1998; Morse et al., 2008). The maximum vibration amplitude (A_{max}) is important from the design point of view to know the maximum stress and A_{10} gives a better overview of the overall vibration behavior. At small reduced velocities, $U^* \leq 1.7$, the vortex shedding frequency is desynchronized from the plate natural frequency and, therefore, the plate does not vibrate with a significant amplitude. A jump is observed in the amplitude response at $U^* = 1.8$ as the non-dimensional vibration amplitude becomes close to 0.2. The variation of the vibration amplitude with the reduced velocity is close to a linear function in the range $1.8 \leq U^* \leq 5.8$. There are two branches in this linear region. The first branch for $1.8 \leq U^* < 2.6$ has a different slope compared to the second branch for $2.6 < U^* \leq 5.8$. The plate attains a maximum non-dimensional vibration amplitude of 1.99 for $U^* = 6.2$ at the end of the second branch. In the first two branches, the plate vibrations are quite periodic in the sense that the vibration amplitude does not vary significantly from one cycle to another. Therefore, the data points for A_{max} and A_{10} overlap in figure 6.3a for $U^* \leq 6.2$. For $U^* > 6.2$, there is a third branch where the vibration amplitude decreases sharply with U^* . The vibration amplitude loses its periodicity in the third branch and the difference between A_{max} and A_{10} increases with the reduced velocity. For $7.4 \leq U^* \leq 8.0$, the plate vibrations show intermittency i.e., the vibration amplitude switches between low and high values. The time variation of the plate displacement at $U^* = 7.4$ and 8.0 is shown in figure 6.5a and 6.5b, respectively. These data sets were recorded for 40 minutes. The switching between the two states happens at irregular intervals. Two hours of recording (not shown here) also did not show any pattern for the switching. A large difference between the two values indicates a short duration burst of larger amplitude vibrations followed by a long steady low amplitude vibrations as seen in figure 6.5b. For $U^* \geq 8.0$, the vortex shedding frequency desynchronizes with the natural frequency of the plate, and its vibration amplitude reduces to $0.2D - 0.1D$ range.

The variation of root mean squared (RMS) lift coefficient, $C_y = F_y/(\frac{1}{2}\rho U^2 DL)$ where F_y is the lift force, for the plate with U^* is shown in figure 6.3b. The total transverse fluid force can be decomposed into two components: potential and vortex force. The potential force is the force applied to the plate by the surrounding fluid which gets accelerated along with the plate. By definition, the potential force is the component of the total lift

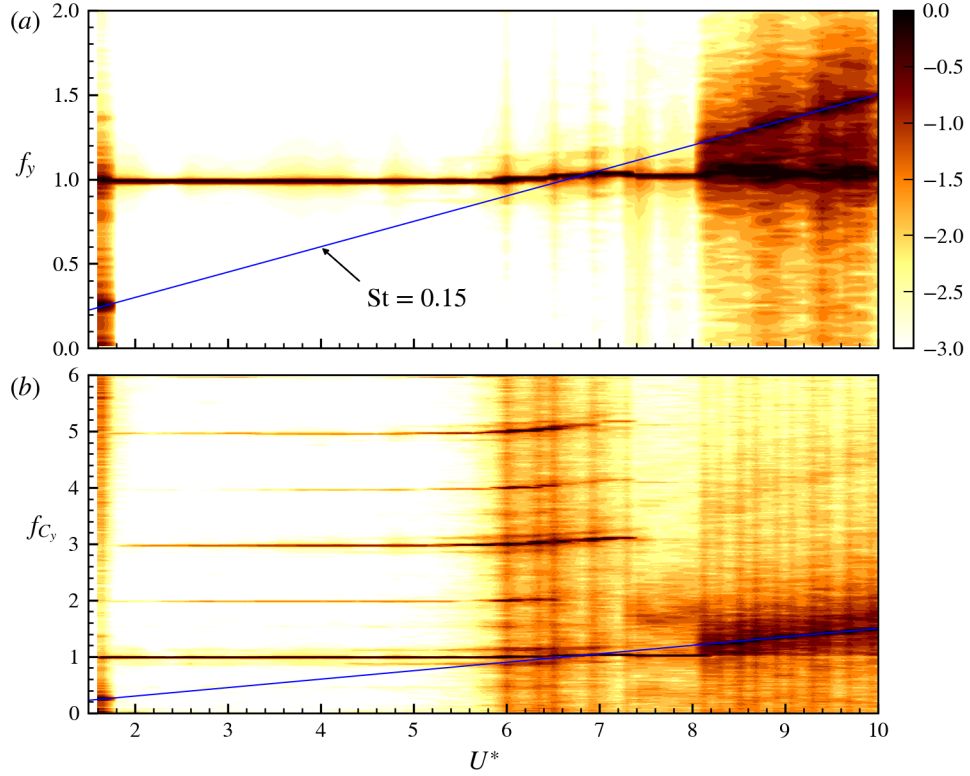


Figure 6.4: (a) Displacement and (b) lift frequency response of the thin plate at low damping.

which is in phase with the plate displacement. The potential force can be calculated as

$$F_{pot} = -m_A \ddot{y} = -C_A \frac{\rho D^2 L}{\alpha} \ddot{y}, \quad (6.4)$$

where m_A is the added mass of the plate. Once the potential force is known, the vortex force can be calculated by subtracting the potential force from the total lift force. The RMS vortex force is also plotted in figure 6.3b. Total lift and vortex force show similar M shaped variation with U^* . In the desynchronization region ($1.8 > U^* > 8.0$), where the plate does not vibrate significantly, the potential force is very small, and hence the total lift and vortex forces are equal. In the first branch, the lift force increases with the reduced velocity and reaches to a peak value at the end of the branch. The lift force then decreases with U^* in the second branch, and attains a local minimum value close to the point where the displacement amplitude is maximum. The lift force increases with U^* from starting of the third branch to the point where displacement shows intermittency ($6.2 < U^* < 7.2$). It reaches a local maximum at $U^* = 7.2$ and then decrease with U^* .

The mean phases of the total and vortex forces relative to the displacement are shown in figure 6.3c. The total phase is close to 0° in the initial lock-in region, $U^* = 1.8-5.8$. Since the total lift is in phase with the displacement and the potential force, by definition, is in phase with the displacement, the vortex force is smaller than the total force. The

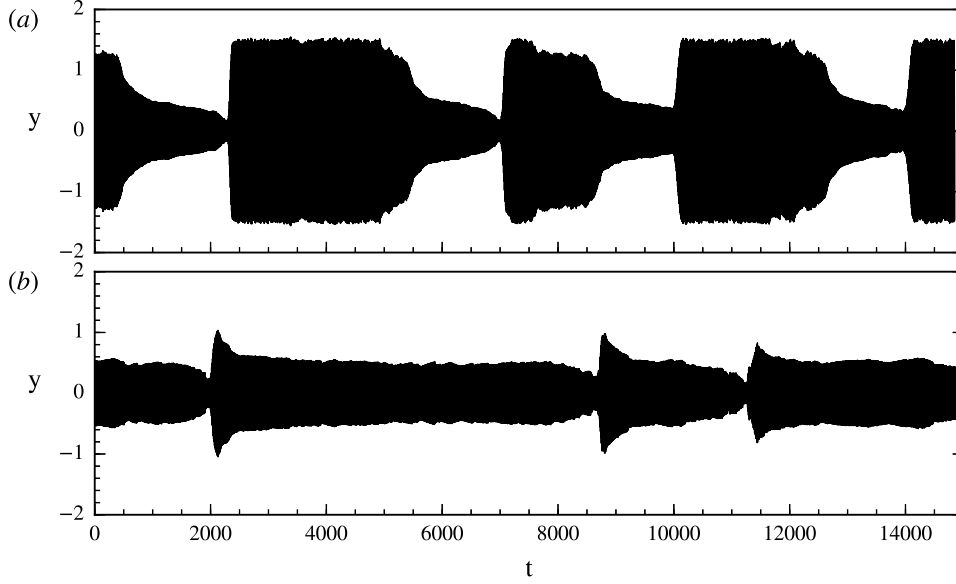


Figure 6.5: Non-dimensional displacement of the plate versus non-dimensional time at $U^* =$ (a) 7.4 and (b) 8.0. Obtained from experiments.

total phase shows a transition to 180° as the reduced velocity is increased. At $U^* = 6.2$, the total phase is close to 90° and the total lift and vortex forces have similar magnitudes. The vortex force becomes larger than the total force as the total phase becomes 180° . The vortex phase shows a similar trend as the total phase.

The contour plots of power spectral density (PSD) of plate displacement as a function of reduced velocity is shown in figure 6.4a. The log scale is used to show any weak harmonics present in the signal. The vibration frequency is normalized by the natural frequency of the system in water (f_N). Two dominant frequency components are present in the desynchronization region, which correspond to the natural frequency of the plate and the vortex shedding frequency of the stationary plate. The non-dimensional vortex shedding frequency for the stationary plate is 0.15 and is shown by the straight line in the contour plots. In the synchronization region, the plate vibrates with only one frequency that is close to its natural frequency. The contour plot for PSD of total lift on the plate is plotted in figure 6.4b. In the synchronization region, the lift has a fundamental frequency component equal to the natural frequency of the system. For $1.8 < U^* < 6.8$, odd harmonics are also present. The third harmonic becomes strongest for $6.2 \leq U^* \leq 6.6$. The temporal variations of lift for $U^* = 2.0$, 4.4 and 6.2 are shown in figures 6.6a, 6.6b and 6.6c, respectively. The third harmonic can be seen to become stronger at $U^* = 6.2$. Weak even harmonics can also be seen in the contour plot. For $U^* > 6.6$, only the fundamental and third harmonics have significant power. The vortex shedding frequency switches back to the value of 0.15 in desynchronization region.

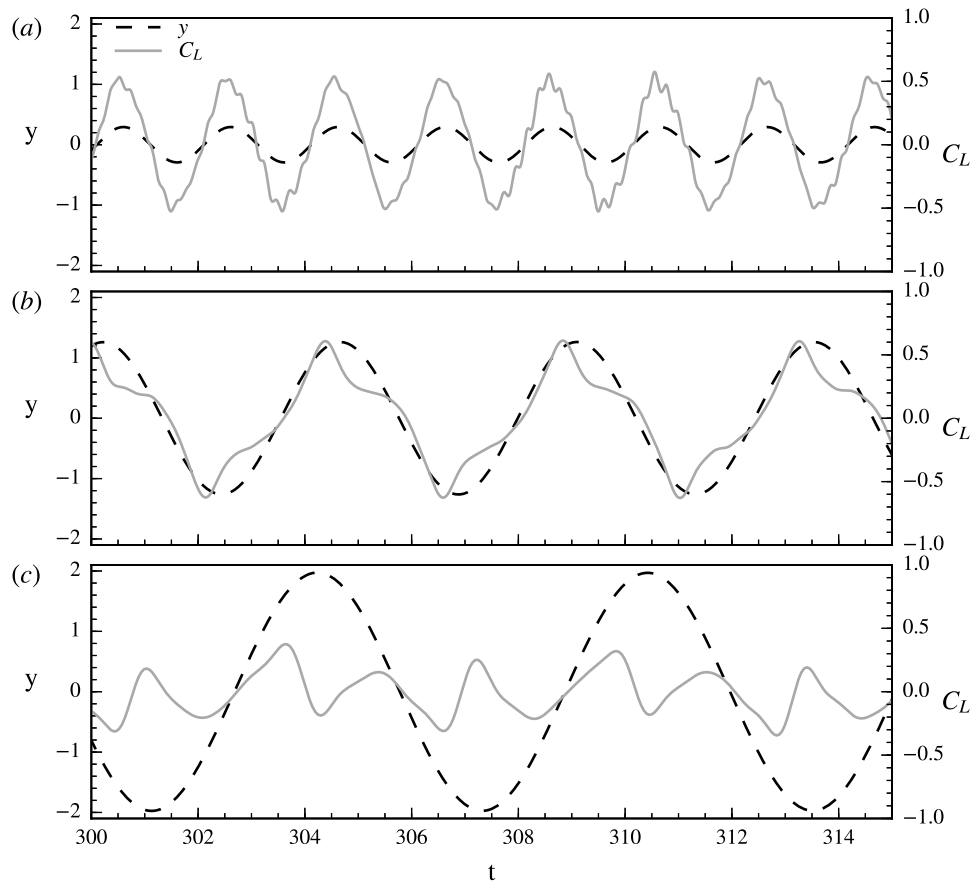


Figure 6.6: Non-dimensional displacement (broken lines) and lift (solid lines) of the plate versus non-dimensional time at $U^* =$ (a) 2.0, (b) 4.4 and (c) 6.2. Obtained from experiments.

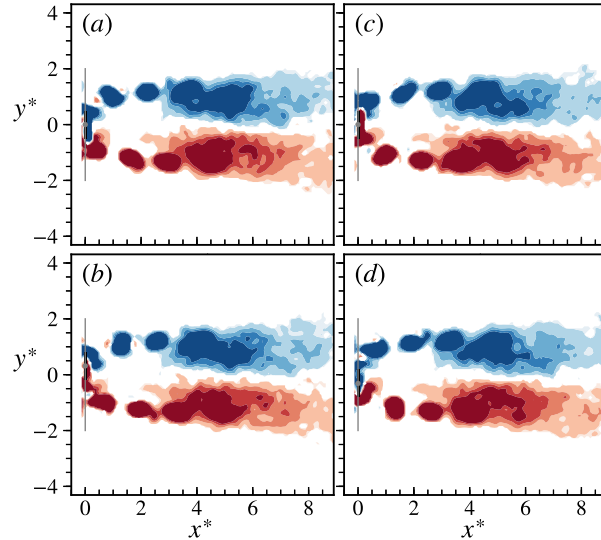


Figure 6.7: Snapshots of vorticity contours at four equispaced time instants in a cycle of oscillation of plate for $U^* = 2.0$. The plate is at its mean position at instant a . The vorticity scale is from -1(blue) to 1(red) with an increment of 0.2. Obtained from experiments.

6.4.2 Wake structures at higher Reynolds number

The flow structures observed at different vibration amplitudes of the plate are presented here. The vorticity contours at $U^* = 2.0$ is plotted in figure 6.7 at four equispaced time instants in a cycle of oscillation of plate. The vibration amplitude of the plate is $0.30D$. At instant a , a counter-clockwise rotating vortex is about to shed from the bottom of the plate, and a clockwise rotating vortex is being formed at the top of the plate. The bottom vortex has shed at instant b . From instant c to d , the top end vortex can be seen to shed. Therefore, one vortex is shed alternately from each side of the plate in one cycle of its oscillation. The vortices cores are separated by a distance along the transverse direction. This vortex shedding mode is similar to what is called the C(2S) mode in literature (Williamson and Roshko, 1988).

Next vorticity contours are plotted at $U^* = 4.4$ in figure 6.8 at eight equispaced time instants in a cycle of oscillation of plate. The vibration amplitude of the plate is $1.27D$. The plate is at its mean location at instant a and is moving towards the positive y direction. A clockwise rotating vortex is being formed the plate from instant a to c . As the plate moves, it drags the surrounding fluid and interaction of the dragged fluid with the free-stream causes the formation of a counter-clockwise rotating vortex below the bottom end of the plate. The plate is coming back from its max position at instant d and the clockwise rotating vortex has shed from top of the plate and has a circular shape. The counter-clockwise rotating vortex is still attached to the plate. From instant e to f , the counter-clockwise rotating vortex detaches from the plate and has non-circular

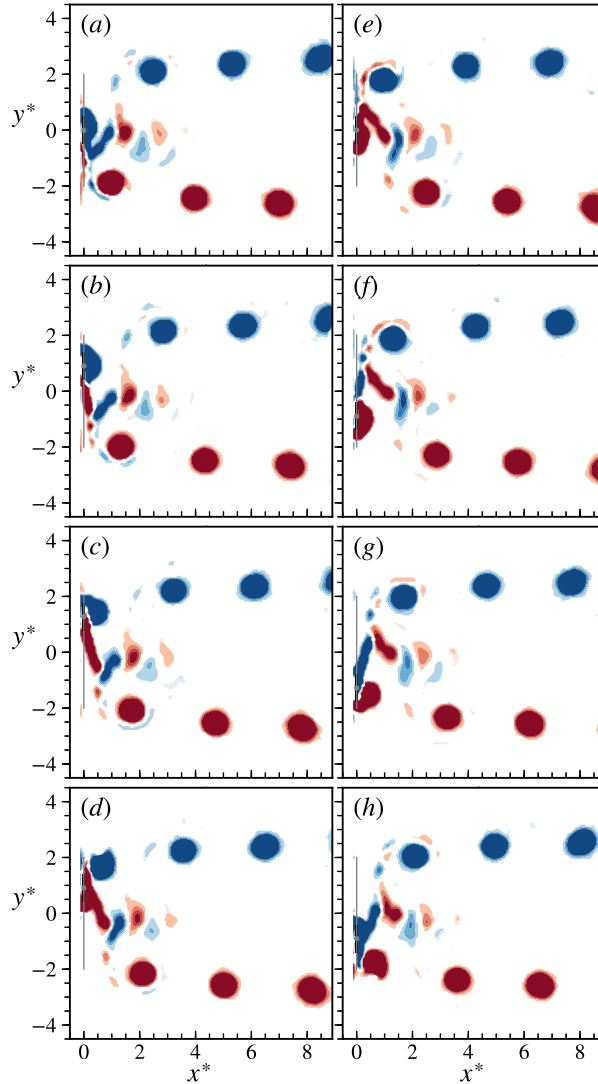


Figure 6.8: Snapshots of vorticity contours at eight equispaced time instants in a cycle of oscillation of plate for $U^* = 4.4$. The plate is at its mean position at instant a . The vorticity scale is from -1(blue) to 1(red) with an increment of 0.2. Obtained from experiments.

elongated shape. A counter-clockwise rotating vortex is being formed behind the plate and a clockwise rotating vortex forms above the top end of the plate. These vortices get shed in rest half of the cycle. Therefore, two opposite-sign vortices are shed from the plate at different time instants in one-half cycle of its oscillation. The circular vortices are shed when the plate is close to its max distance from mean location and therefore are separated by a distance along the transverse direction. The circular vortices resemble the C(2S) vortex shedding mode. The elongated vortices are shed from the plate when it is close to its mean location, and therefore these vortices do not move along with the circular vortices due to being in the wake region. These elongated vortices resemble the 2S vortex shedding mode. Therefore, the vortex shedding mode at $U^* = 4.4$ is C(2S) + 2S.

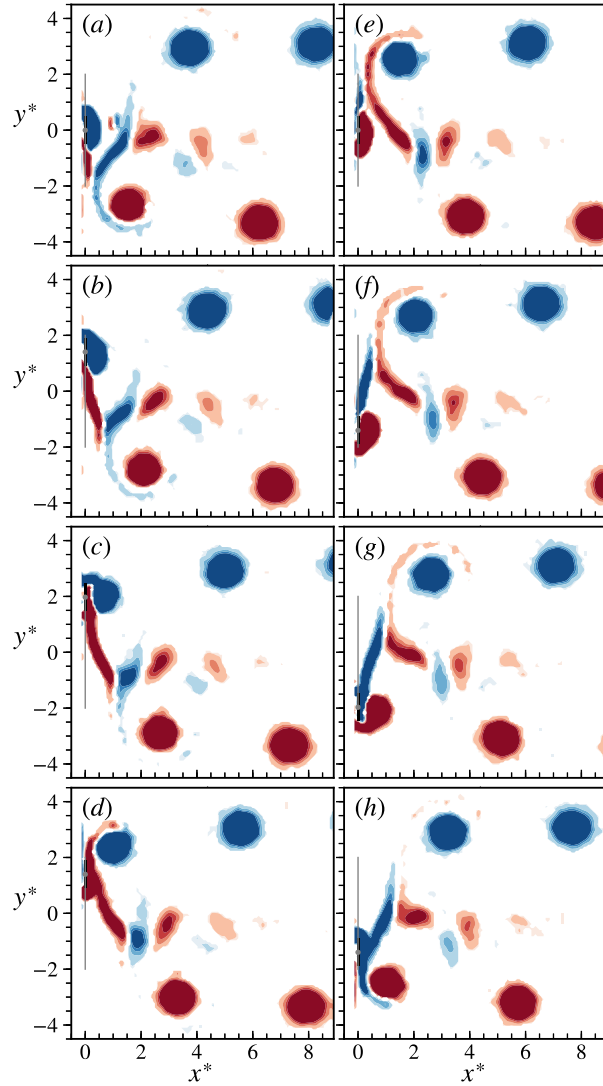


Figure 6.9: Snapshots of vorticity contours at eight equispaced time instants in a cycle of oscillation of plate for $U^* = 6.2$. The plate is at its mean position at instant a . The vorticity scale is from -1(blue) to 1(red) with an increment of 0.2. Obtained from experiments.

The vorticity contours at $U^* = 6.2$ are plotted in figure 6.9. The vibration amplitude of the plate is $1.99D$. The plate is at its mean location at instant a and is moving towards the positive y direction. Notice that the total phase changes from 0° at $U^* = 4.4$ to 180° at $U^* = 6.2$. The vortex shedding pattern is similar to that of the $U^* = 4.4$ case. In a cycle of plate oscillation, two opposite-sign vortices with circular shapes are shed which form the C(2S) vortex shedding mode and two opposite sign vortices with elongated shapes are shed which form the 2S vortex shedding mode. Therefore, the vortex shedding mode at $U^* = 6.2$ is also C(2S) + 2S.

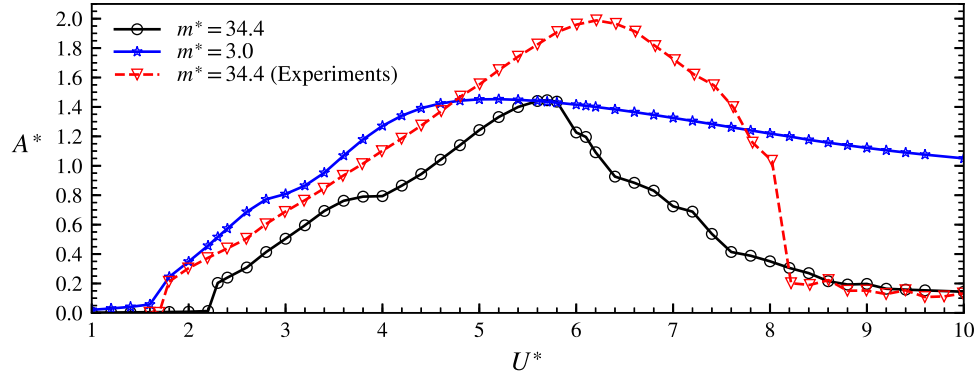


Figure 6.10: Vibration amplitude of a thin plate with aspect ratio $\alpha = 12$ at $\text{Re} = 150$.

6.4.3 Numerical results

The VIV response of the thin plate with aspect ratio $\alpha = 12$ at $\text{Re} = 150$ is presented in this section. The damping ratio is taken as zero. The amplitude response of the plate is shown in figure 6.10. Two values of the mass ratio are considered: 34.4, which matches with the experimental value, and 3.0. Notice that the reduced velocity is based on the natural frequency of the plate in the vacuum. The amplitude response for $m^* = 34.4$ shows similarities to the experimental results presented in the section 6.4.1. The plate starts to vibrate with a significant amplitude for $U^* \geq 2.2$ and attains a peak amplitude of $1.43D$ at $U^* = 5.8$. Similar to the experiments, the plate vibrations are very periodic in this range of reduced velocity. As the reduced velocity is increased further, the vibration amplitude reduces, and the displacement starts to show intermittency (switching between a low and a high amplitude vibration states). The time trace of plate displacement is shown in figure 6.11 for $U^* = 6.2$. The displacement can be seen to switch between low and high amplitude states. The plate vibration becomes periodic after $U^* = 9.0$ and gradually decreases with U^* . The amplitude response for mass ratio 3.0 case is similar to that of the $m^* = 34.4$ till $U^* = 5.8$. The peak vibration amplitude is same for both the mass ratios. The lower mass ratio plate does not show intermittency in its displacement, and the vibrations are periodic over the whole range of U^* considered (see figure 6.11b). The lower mass ratio plate also has a wider range of reduced velocity over which the plate vibrates with a significant amplitude. A circular cylinder also shows a wider range of reduced velocity for synchronization at lower mass ratios.

The RMS lift coefficient for the plate at $\text{Re} = 150$ is plotted in figure 6.12 for the two aforementioned mass ratios. The pressure and viscous components of the total lift force are also shown in the figure. Similar to the experiments, the lift for the higher mass ratio has an M shaped variation with U^* . The lift force jumps to a higher value when the plate starts to vibrate with a significant amplitude. It attains a maximum for both mass ratios but at different U^* . The maximum lift force is same for both the mass

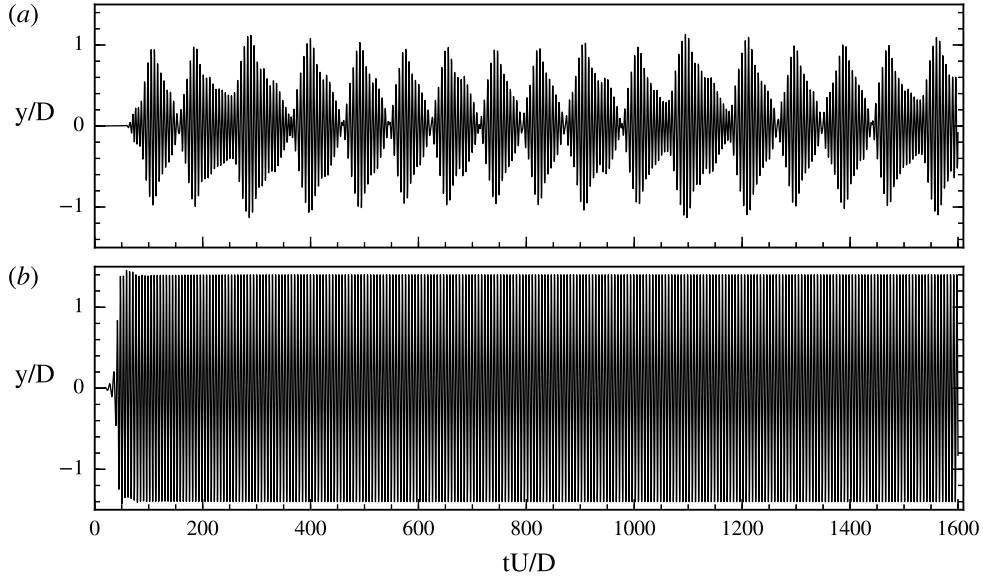


Figure 6.11: Displacement of the plate versus time at $Re = 150$ and $U^* = 6.2$ for $m^* =$ (a) 34.4 and (b) 3.0.

ratios and is greater than that at the higher Re . The amplitude response shows a shift in its trend at the reduced velocity corresponding to the maximum lift force. The viscous component of lift is stronger than the pressure component for $U^* < 5.8$. The phase of the lift force and its viscous and pressure components with respect to the displacement of the plate is plotted in figure 6.13. The total lift phase shows a jump from 0° to 180° at $U^* = 5.8$ when the lift force reaches its minimum. The transition of total phase from 0° to 180° happens over a range of reduced velocity in case of the lower mass ratio. The pressure force becomes more dominant as compared to the viscous component after the total phase has jumped to 180° . The viscous force is smaller for the lower mass ratio plate as compared to that for the higher mass ratio plate for $U^* > 5.8$ and vice-versa for the pressure force.

The power spectral densities of displacement and lift of the plate with $m^* = 34.4$ are plotted in figure 6.14. Unlike the experiments, there is only one frequency component in the plate displacement in the desynchronization regions ($2.2 > U^* \geq 9.0$) which is equal to the vortex shedding frequency for a fixed plate. The second frequency component observed at higher Re corresponds to the natural frequency of the plate. For a sinusoidal forcing, the solution of equation 6.3 is the sum of a transient and a steady state solution. The transient solution frequency is equal to the natural frequency of the spring-mass system, and the steady state solution frequency is equal to the forcing frequency. The transient solution dies out after some time for non-zero damping. Therefore, the absence of the natural frequency component for low Re situation indicates that the lift force has a significant amount of component in phase with the damping force. The vortex shedding synchronizes

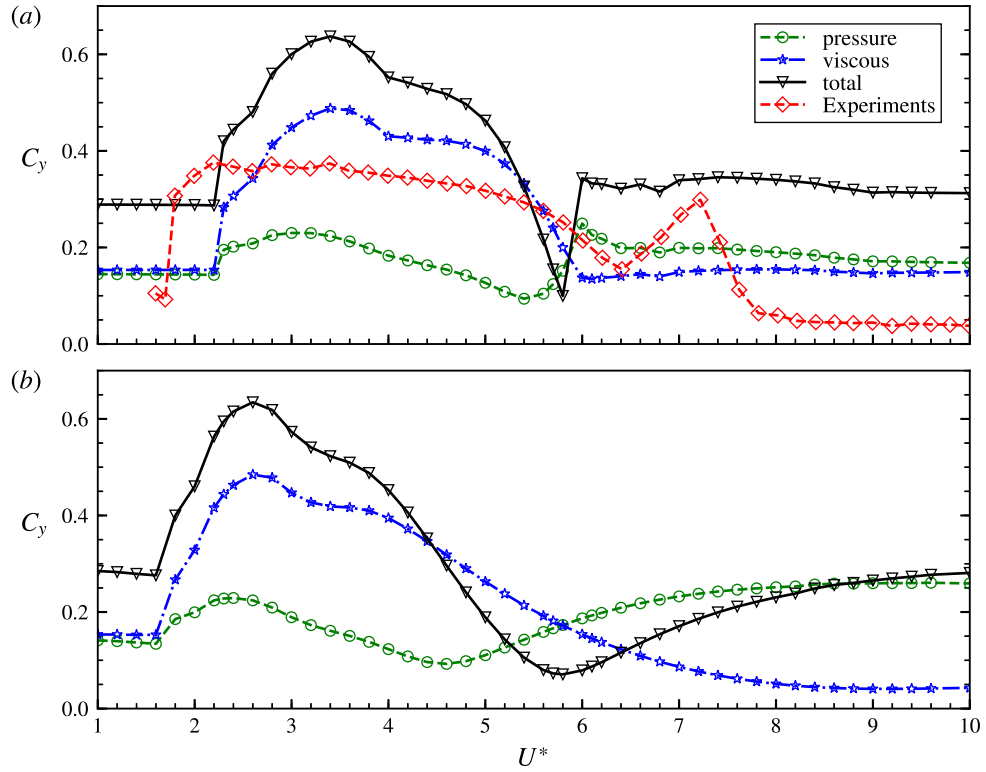


Figure 6.12: RMS pressure, viscous and total lift forces on the plate for (a) $m^* = 34.4$ and (b) $m^* = 3.0$ at $Re = 150$.

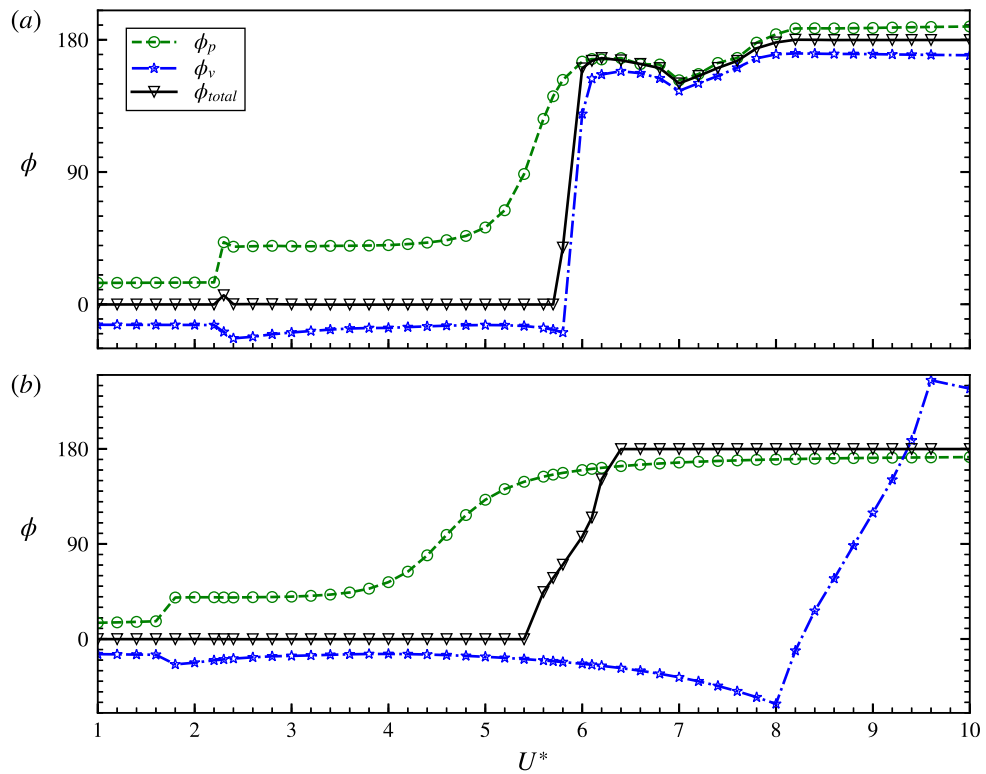


Figure 6.13: Mean phases of pressure, viscous and total lift forces on the plate for (a) $m^* = 34.4$ and (b) $m^* = 3.0$ at $Re = 150$.

with the natural frequency of the plate at $U^* = 2.2$ as the frequency ratio becomes equal to 1.0. For $2.2 \leq U^* < 6.0$, the displacement frequency has only a single component as the vortex shedding frequency has locked-in with the natural frequency of the plate. The lift has a weak third harmonic of the fundamental frequency. For $6.0 \leq U^* < 9.0$, the plate vibration frequency has multiple components which are not harmonics of any fundamental frequency. The lift also has multiple frequency components. These components are due to different vortex shedding patterns and will be discussed in the next section.

The frequency response of the lower mass ratio plate (see figure 6.15) is different from that of the higher mass ratio case (see figure 6.14). For $U^* < 1.8$, the vortex shedding frequency is equal to that for a stationary plate as in the case of the higher mass ratio plate. As the reduced velocity is increased beyond 1.8, the vortex shedding frequency gets locked with the natural frequency of the plate in the fluid. The normalized frequency is less than 1.0 during lock-in due to the added-mass. After $U^* = 6.0$, the vortex shedding frequency becomes constant and is greater than that for a stationary plate. Unlike higher mass ratio case, there is only a single frequency component in plate displacement which is equal to the vortex shedding frequency. As discussed in the previous paragraph, the absence of the natural frequency component in the displacement suggests a significant damping component of the lift. The amplitude of the steady state solution of equation 6.3 for a sinusoidal forcing is proportional to the static deflection which is the deflection of the spring-mass system under a static loading. For a fixed value of natural frequency, the static deflection is inversely proportional to the mass. Therefore, the lower mass ratio plate has a larger amplitude in the desynchronization region as compared to the larger mass ratio plate.

6.4.4 Wake structures at low Reynolds number

The different wake patterns observed at $Re = 150$ are discussed in this section. The vorticity contours for the plate with $m^* = 34.4$ at $U^* = 2.6$ are shown in figure 6.16. The lift force acting on the plate at $U^* = 2.6$ is plotted in figure 6.17a. The six circular markers shown in figure 6.17a represent the six instants at which the vorticity contours are plotted in figure 6.16. The lift force appears to have more than one frequency component which is evident in the FFT plot shown in figure 6.17b. The multiple frequency components are due to the interaction of the shed vortices in the downstream region of the plate. At instant a , a vortex is being formed behind the top end of the plate, and hence the lift force on the plate is positive. A counter-clockwise rotating vortex forms behind the bottom end of the plate at instant b causing negative lift force on the plate. These two opposite-sign vortices are shed in one cycle of the plate oscillation, and therefore the vortex shedding resembles the 2S mode. Another clockwise rotating vortex forms at instant c which coalesces with the vortex shed at instant a . The interaction of the vortices results in a decrease in the

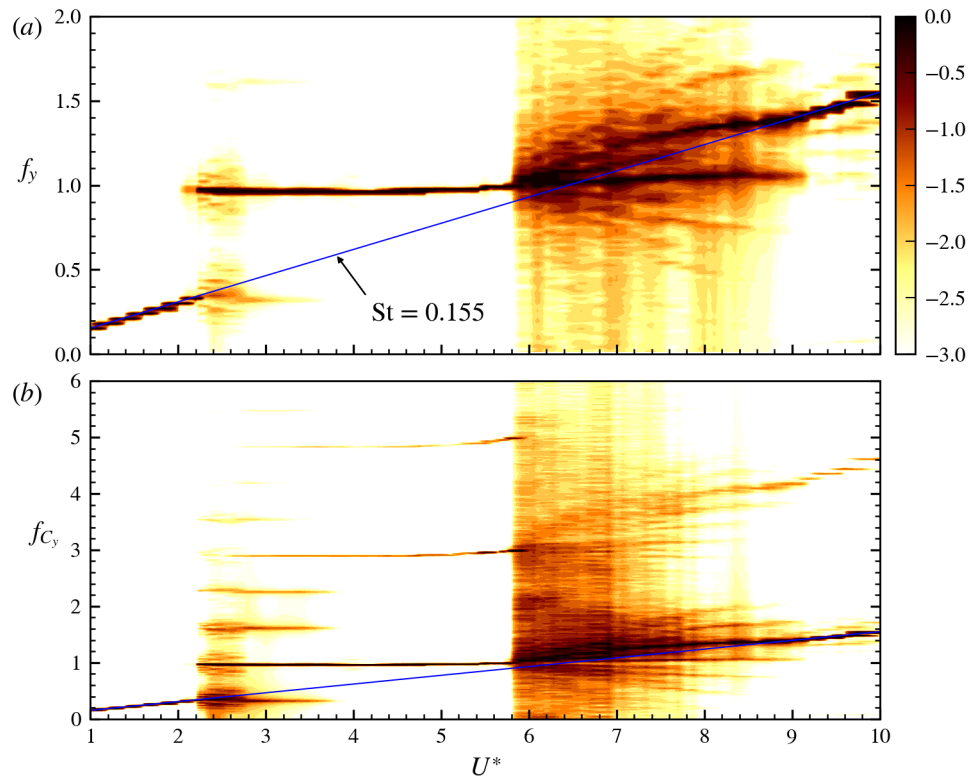


Figure 6.14: (a) Displacement and (b) lift frequency response of the thin plate at $Re = 150$ and $m^* = 34.4$.

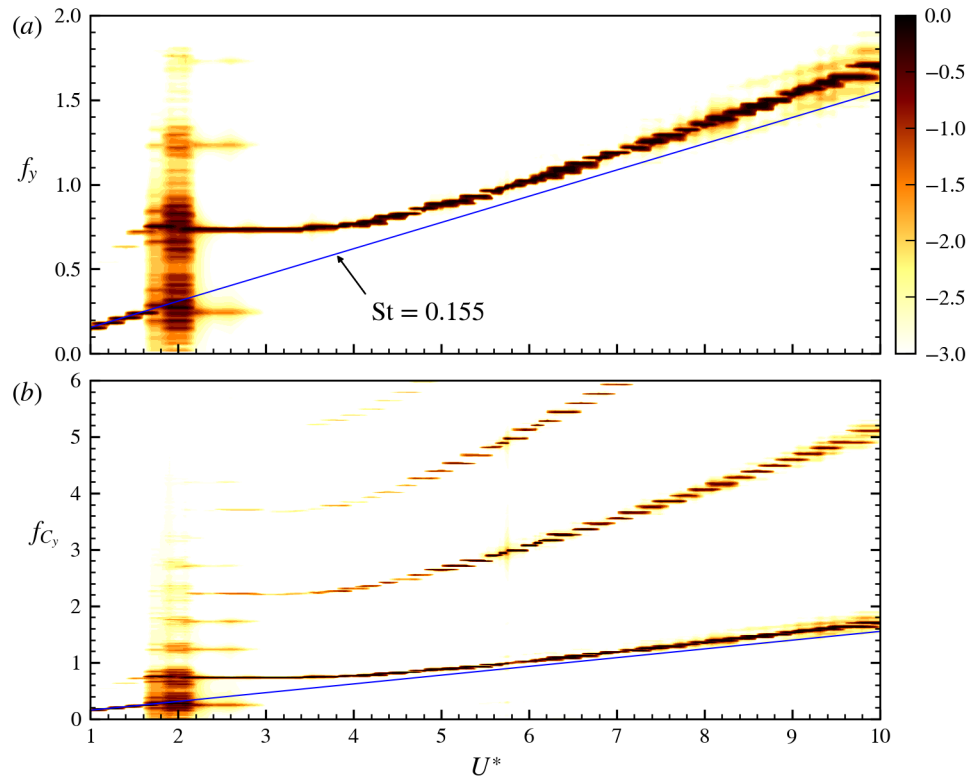


Figure 6.15: (a) Displacement and (b) lift frequency response of the thin plate at $Re = 150$ and $m^* = 3.0$.

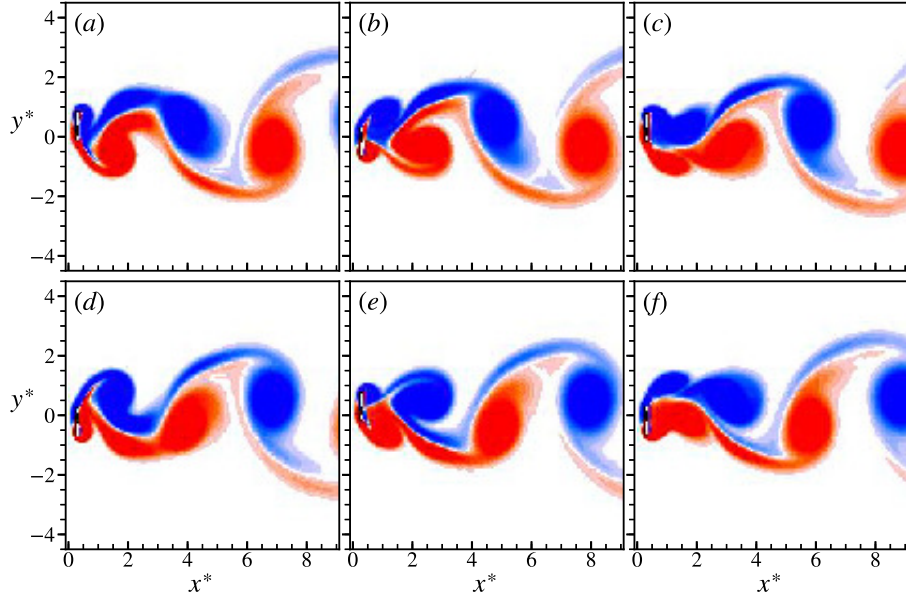


Figure 6.16: Vorticity contours at six time instants for the plate with $m^* = 34.4$ at $U^* = 2.6$ and $Re = 150$. The time instants are shown by filled circular markers in figure 6.17a. The vorticity scale is from -1(blue) to 1(red).

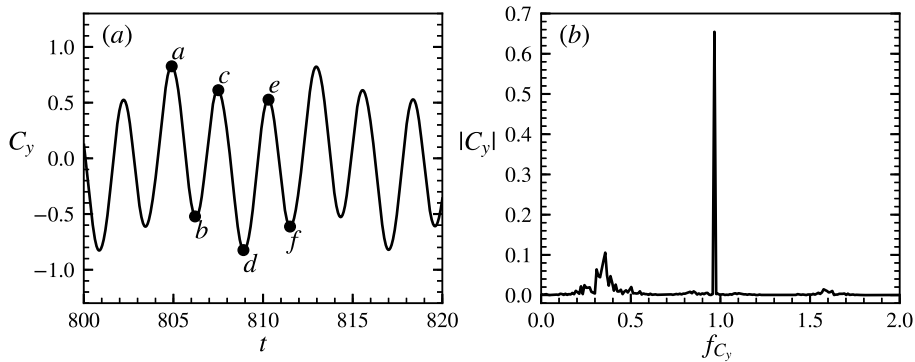


Figure 6.17: (a) Temporal variation of the lift force on the thin plate with $m^* = 34.4$ at $Re = 150$ and $U^* = 2.6$ and (b) FFT of the lift force.

amplitude of the lift force as seen in figure 6.17. Similar vorticity patterns are seen from instant d to f where two counter-clockwise rotating vortices coalesce behind the bottom end of the plate. For $x > 6D$, the vortex structures resembles the 2S vortex shedding mode. Therefore, the vortex shedding pattern at $U^* = 2.6$ is in C(2S) mode. Notice that the similar vortex structures were observed in the experiments at higher Re for $U^* = 2.0$.

The vorticity field calculated at $U^* = 5.8$ is shown in figure 6.18 at six equidistant points in time in one oscillation cycle of the plate. The vortex shedding mode is C(2S) + 2S which matches with that observed in the experiments at $U^* = 4.4$ and 6.2. In one period of oscillation of the plate, one pair of strong vortices separated by a significant distance along the transverse direction is shed. These vortices get shed when the plate

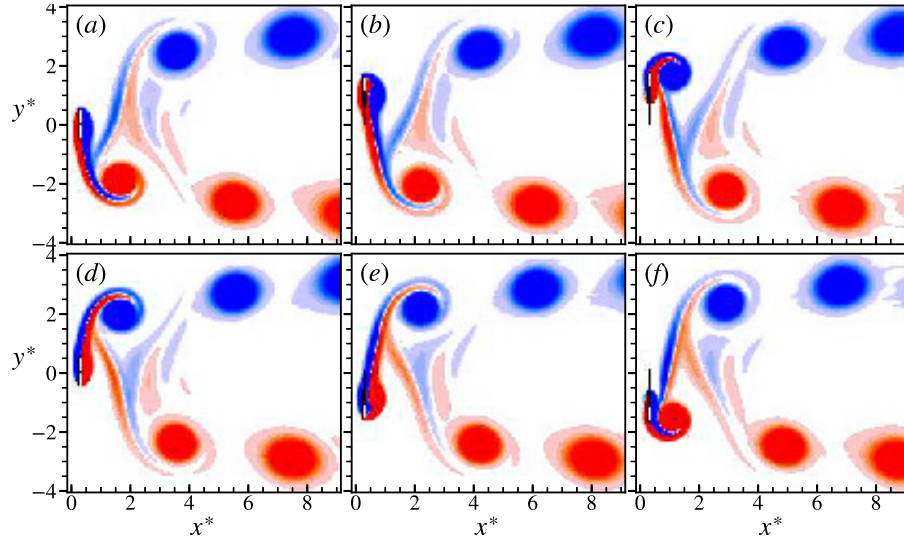


Figure 6.18: Vorticity contours at six equispaced time instants in a cycle of oscillation of the plate with $m^* = 34.4$ at $U^* = 5.8$ and $Re = 150$. The plate is at its mean position at instant a . The vorticity scale is from -1(blue) to 1(red).

is at the maximum distance from its mean location. Another weak vortices pair is shed when the plate is close to its mean location, and therefore these vortices move in the downstream direction close to the x-axis.

The vorticity contours at $U^* = 6.2$ are shown in figure 6.19 at six instants shown by the circular marks in figure 6.20 which shows the temporal variation of the plate displacement. As discussed previously, the displacement amplitude is not stable and switches between low and high value states. The FFT of the displacement and lift force of the plate are shown in figure 6.21a and 6.21b, respectively. The displacement has multiple frequency components which correspond to different vortex shedding patterns. In figure 6.19a and 6.19b, a pair of opposite sign vortices has shed from the top end of the plate, and a single vortex has shed from the bottom end of the plate which is called the P+S vortex shedding mode. The vibration amplitude is close to $0.5D$ when the P+S vortex shedding mode is observed. Similar to $U^* = 5.8$ case, the figure 6.19c and 6.19d shows the C(2S)+2S vortex shedding mode and the vibration amplitude is close to $1.1D$. At instants e and f , when the vibration amplitude is small, the vortex shedding mode is 2S. Notice that the transition from one vortex shedding mode to another is a continuous process and therefore the FFT of the lift force and the displacement show a wide range of frequencies.

6.5 Closure

The flow-induced vibrations of a thin plate kept normal to the incoming flow were studied at high and low Reynolds number using experiments and numerical simulations. The ratio of the width (length along cross-flow direction) to the thickness (length along the flow

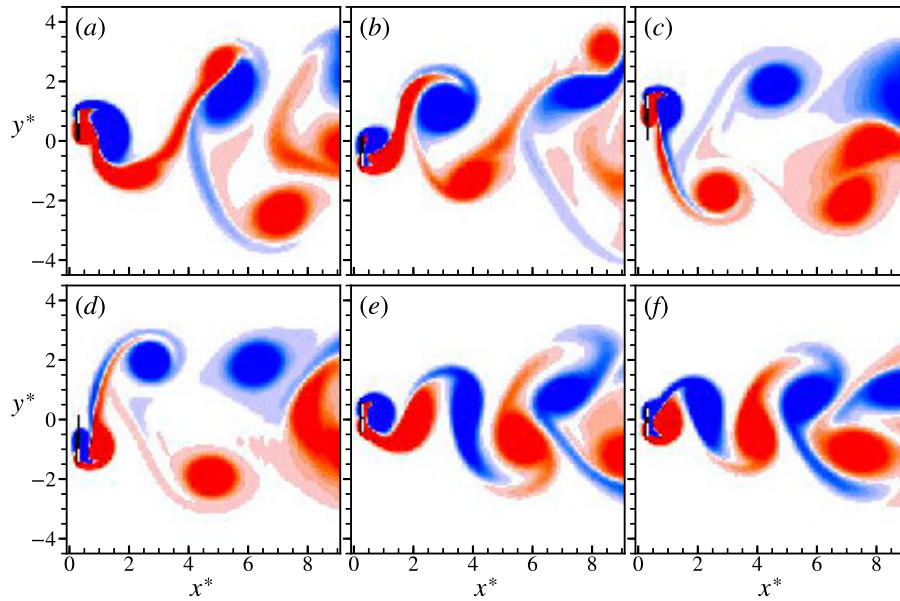


Figure 6.19: Vorticity contours at six time instants, shown by filled circular markers in figure 6.20, for $U^* = 6.2$ and $Re = 150$. The vorticity scale is from -1(blue) to 1(red).

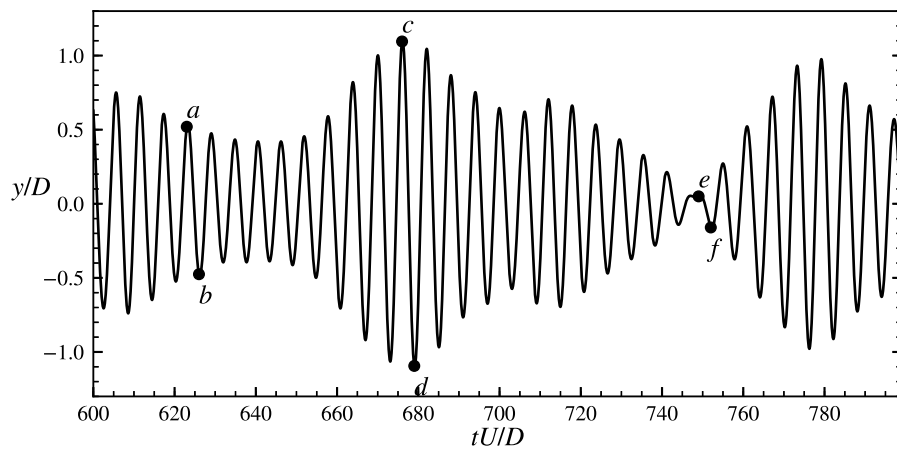


Figure 6.20: Temporal variation of the displacement of the thin plate with $m^* = 34.4$ at $Re = 150$ and $U^* = 6.2$.

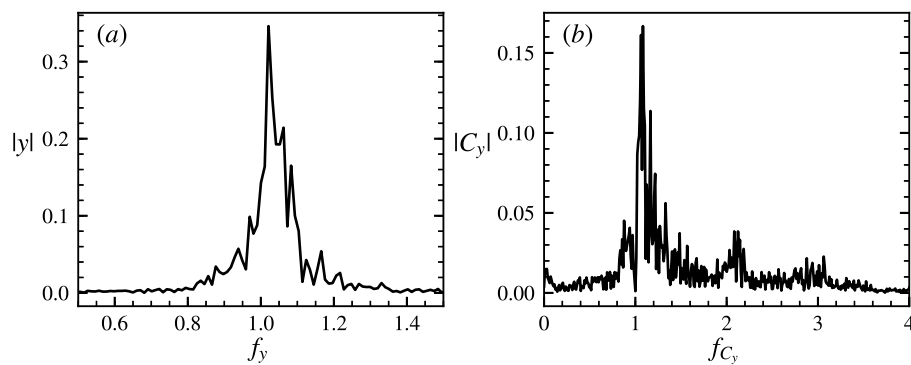


Figure 6.21: Temporal variation of the displacement of the thin plate with $m^* = 34.4$ at $Re = 150$ and $U^* = 6.2$.

direction) is 12.0. The reduced velocity was varied from 1.6 to 10.0. The experiments were conducted in a water channel, and the Reynolds number ranged from 1343 to 8406. The plate motion is found to be dominated by the vortex-induced vibration at all reduced velocities considered in the study. The vibration response of the plate differs from that of a circular cylinder. Although the plate vibration response has three branches, the three branches do not share the characteristics of the three response branches observed in the case of a circular cylinder. In first two branches, the vibration amplitude of the plate increases linearly with the reduced velocity. The two branches differ in the slope of the linear functions. The vortex shedding frequency is locked-in with the natural frequency of the plate. The maximum vibration amplitude of the plate is $1.99D$ observed at the end of the second branch. The plate vibration amplitude is periodic in the two branches meaning it does not change significantly from one cycle to another. In the first branch, the lift force increases with the reduced velocity while the opposite happens in the second branch. The mean phase difference between the lift force and the plate displacement is 0° for the two branches. The vortex shedding mode observed in the first and second branches are $C(2S)$ and $C(2S) + 2S$, respectively. The third branch shows a decrease in the vibration amplitude with increasing reduced velocity. The vibration amplitude loses its periodicity in the third branch, and becomes intermittent in the later part of the branch. The plate motion becomes desynchronized with the flow at the end of the third branch and the vibration amplitude becomes small.

The low Reynolds number case was studied by solving the coupled fluid-structure interaction problem using a spectral-element based solver. The Reynolds number was taken as 150, and the structural damping was neglected. Two mass ratios were studied, one that matched with the experiments ($m^* = 34.4$) and another low value of $m^* = 3.0$, to study the effect of mass. The vibration responses of the plate at lower and higher Reynolds number are very similar. Similar to what was observed in the experiments, there are three branches of the plate vibration response. The first two branches show a linear increment in the vibration amplitude with the reduced velocity. The two branches differ in the slope of the linear increment. The lift force on the plate increase with the reduced velocity in the first branch and the reverse happens in the second branch. The FFT of lift force shows the distribution of the energy over a wide range of frequencies in the first branch which could be attributed to the interaction of the shed vortices behind the plate. The vortex shedding mode is $C(2S)$. In the second branch, the lift force has only the odd harmonics of the fundamental frequency i.e. the natural frequency of the plate and the vortex shedding mode is $C(2S) + 2S$. The vibration amplitude reaches its maximum value of $1.43D$ at the end of the second branch. The maximum vibration amplitude is same for both the mass ratios but occurs at different reduced velocity. The third branch shows a decrease in the vibration amplitude with the increasing reduced velocity. Intermittency is also observed

at for $m^* = 34.4$ case at low Reynolds number. Three vortex shedding modes are seen corresponding to three vibration states in the intermittency region: 2S mode is observed when the vibration amplitude is the smallest, C(2S) + 2S mode is seen when the vibration amplitude is largest, and P+S mode is seen for intermediate amplitude values. The FFT of the lift force and displacement shows three different frequencies corresponding to the three vortex shedding modes. The lower mass ratio case shows larger vibration amplitude in the third branch as compared to $m^* = 34.4$ case.

Chapter 7

Vortex-induced vibration of thin plates: effect of aspect ratio and power extraction

Vortex-induced vibrations of a thin flat plate with various aspect ratios are studied numerically. The plate is free to vibrate only in the transverse direction to the incoming flow. The Reynolds number is kept below 200. Similar to the case of circular cylinder, various response branches have been identified. The 2S vortex shedding phase is observed in the initial branch and 2T mode is observed for upper and lower branches. The peak amplitude of the plate displacement increases with decrease in aspect ratio because the pressure force on the plate becomes more in phase with the velocity. The power extraction from the VIV of plate is also calculated. The plate with aspect ratio 0.2 is found to be optimal. The maximum extraction efficiency is close to 0.19 at $Re = 150$.

7.1 Introduction

Vortex induced vibration (VIV) of bluff bodies is a class of fluid-structure interaction problem which has been studied both experimentally and numerically by many researcher. To motivation to study this phenomenon comes from the flow induced vibration of structures such as building and marine risers which could lead to catastrophic failure. When a bluff body, for example a circular cylinder, is placed in a free-stream flow, vortices gets formed behind the body and get shed from the body in a alternating fashion. The alternate shedding of vortices leads to oscillating lift and drag forces on the body. If the body is free to move in either/both transverse and in-line directions than it starts oscillating in the respective direction. This phenomenon is known as VIV. Some detailed review of the work done on VIV can be found in [Williamson and Govardhan \(2004\)](#), [Sarpkaya \(2004\)](#), [Khalak and Williamson \(1999\)](#), [Gabbai and Benaroya \(2005\)](#), [Bearman \(2011\)](#).

Khalak and Williamson (1999) conducted experiments with an elastically mounted circular cylinder, which could move along the transverse direction to the incoming flow, with low mass-damping value and identified three branches in the response: initial, upper and lower branch. The vortex shedding mode in initial branch was found to be 2S meaning two vortices were shed in one period of the cylinder oscillations. The 2P vortex shedding mode, two pairs of vortices in one period of oscillation, was found in upper and lower branches (Govardhan and Williamson, 2000).

7.2 Problem definition and methodology

7.2.1 Governing equations

The transverse VIV of an elastically mounted flat plate kept normal to the free stream flow is considered. The length and thickness of the rigid plate are D and d , respectively. The free-stream velocity is represented by U . The working fluid is assumed to be incompressible. The plate is free to move along y -direction. The fluid flow is governed by the following non-dimensional Navier-Stokes equations set in the frame of the plate

$$\frac{\partial \mathbf{u}}{\partial t} + (\mathbf{u} \cdot \nabla) \mathbf{u} = \nabla p + \frac{1}{Re} (\nabla^2 \mathbf{u}) + \mathbf{a}_F, \quad (7.1)$$

where \mathbf{a}_F is the acceleration of the plate. The symbol \mathbf{u} and p represent the fluid velocity and kinematic pressure, respectively. The free-stream velocity (U) and the plate length (D) are chosen as reference velocity and length scales for defining the Reynolds number, $Re = UD/\nu$, where ν represents the kinematic viscosity of the fluid. The value of Re is kept low (≤ 200) so that the flow is laminar and two-dimensional (2D).

Let m_{total} be the total mass of the plate system which includes the plate and any other attachment that moves with it, then the mass ratio (m) of the system is defined as ratio of total mass to the mass of the displaced fluid (m_f) i.e $m = m_{total}/m_f$. The mass of the displaced fluid is given as $m_f = \alpha(\rho D^2)$ where the aspect ratio $\alpha = d/D$. The natural frequency of the system in vacuum is given by $f_n = \frac{1}{2\pi} \sqrt{k/m_{total}}$ where k is the spring constant. The reduced velocity is defined as $U_r = U/(f_n D)$. The non-dimensional for the equation of motion of the plate system without any structural damping is given by

$$\ddot{y} + \frac{4\pi^2 y}{U_r^2} = \frac{1}{2\alpha} \frac{C_L}{m}, \quad (7.2)$$

where y and C_L represents the non-dimensional displacement and lift force acting on the plate i.e. the lift coefficient, respectively. The energy of VIV of the plate can be harnessed using a power transducer such as an electromagnetic or piezoelectric generators. The effect of power extraction can be modelled as a damper in the system. The damping model can

have a simple constant damping ratio (CD) or a specially varying electromagnetic damping ratio (EMD) (Soti et al., 2017). The inclusion of power transducer modifies the eq. 7.2 to the following

$$\ddot{y} + \frac{4\pi(\xi + \xi_m)\dot{y}}{U_r} + \frac{4\pi^2 y}{U_r^2} = \frac{1}{2\alpha} \frac{C_L}{m}, \quad (7.3)$$

where ξ and ξ_m represents the constant and electromagnetic damping ratios, respectively. The critical damping for the plate system is given by $c_c = 4\pi m_{total} f_n$ using which the constant damping ratio is defined as $\xi = c/c_c$ where c represents the damping coefficient for the constant damping ratio power transducer. The electromagnetic damping ratio is defined as $\xi_m = \xi_{m0} g^2$ where ξ_{m0} is the electromagnetic damping constant $\xi_{m0} = c_{m0}/c_c$. The parameter $c_{m0} (= \mu_m^2/(RD^4))$ depends upon the magnetic moment μ_m of the magnet used for the electromagnetic generator and load resistance R . The function g is given by the following expression (Soti et al., 2017)

$$g = \left(\frac{2\pi N a^2}{L} \right) \left[\frac{1}{(a^2 + (y_{cm} - L/2)^2)^{3/2}} - \frac{1}{(a^2 + (y_{cm} + L/2)^2)^{3/2}} \right], \quad (7.4)$$

where a , L and N are the non-dimensional radius, non-dimensional length and number of turns of the coil of the electromagnetic power transducer, respectively and y_{cm} is the non-dimensional distance between the coil and the plate centres. The efficiency of the power transducer is defined as the ratio of the power extracted by it to the flow power available across the region occupied by the stationary plate ($\frac{1}{2}\rho U^3 D$). This is also the definition of non-dimensional power. The non-dimensional power is equal to the product of non-dimensional damping force and non-dimensional velocity of the plate

$$P(t) = \frac{8\pi\alpha m(\xi + \xi_m)\dot{y}(t)^2}{U_r}, \quad (7.5)$$

Notice that only one type of power transducer will be used at a time. Since the plate undergoes periodic oscillations, the average power over a period of oscillation (T) can be calculated as

$$\bar{P} = \frac{1}{T} \int_T P(t) dt. \quad (7.6)$$

If the plate displacement is assumed to vary in a sinusoidal fashion with time, $y = A_y \sin(2\pi f_y t)$ where A_y and f_y represents the displacement amplitude and frequency of vibration, respectively, then eq. 7.6 takes the following form

$$\bar{P} = \frac{16\pi^3 \alpha m (\xi + \xi_m) A_y^2 f^2}{U_r^3}. \quad (7.7)$$

where $f = f_y/f_n$ is the normalized vibration frequency of the plate.

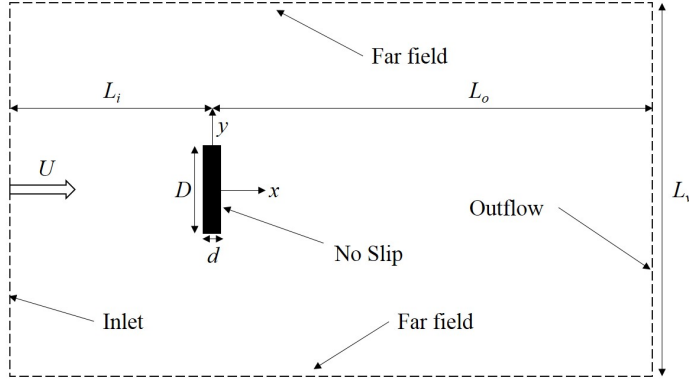


Figure 7.1: Computational domain for the transverse VIV of the plate.

7.2.2 Computational domain and boundary conditions

The computational domain, shown in fig. 7.1, is a rectangle of height L_v . The plate is located mid-way along the transverse (y) direction. The inlet and outlet are located at L_i and L_o distances from the mid section of the plate. The plate surface is considered no-slip boundary. At the inlet, top and bottom boundaries the fluid velocity is prescribed as $u = U, v = -\dot{y}$. The pressure is prescribed and Neumann condition is applied for the fluid velocity at the outlet.

7.2.3 Resolution studies and validation

Various domain sizes were tried to achieve domain independent results. One example of the study carried out for finding appropriate domain height L_v is shown in fig. 7.2. In fig. 7.2, the displacement and power signals for three values of L_v : 40, 60 and 80 are compared. These results correspond to a plate with $\alpha = 0.05$, $m = 2$, $U_r = 5.0$ and $\xi = 0.6$ at $Re = 150$. There is less than 1% change in displacement and power when L_v is increased from 60 to 80. Hence, the value of 60 was chosen for L_v for getting domain independent results while minimizing the computational effort. Similarly, $L_i = 20$ and $L_o = 60$ were found to be sufficient for providing domain independent results.

A similar study was done for finding a suitable mesh for getting mesh independent results. The computational domain was meshed with 720 non-uniform quadrilateral elements. The mesh resolution can be increased by increasing the number of nodes per element. In fig. 7.3, the displacement and power signals for meshes with 6×6 and 8×8 nodes per element are compared. The simulation parameters are the same as used for the results presented in fig. 7.2. The 8×8 node/element mesh shows less than 1% change in the signals. Therefore, 6×6 node/element mesh was chosen for this work.

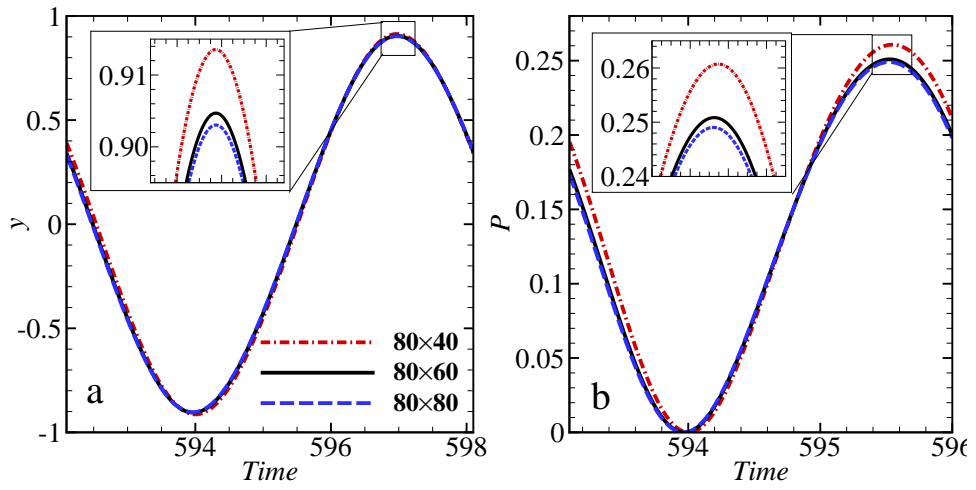


Figure 7.2: Domain independence study.

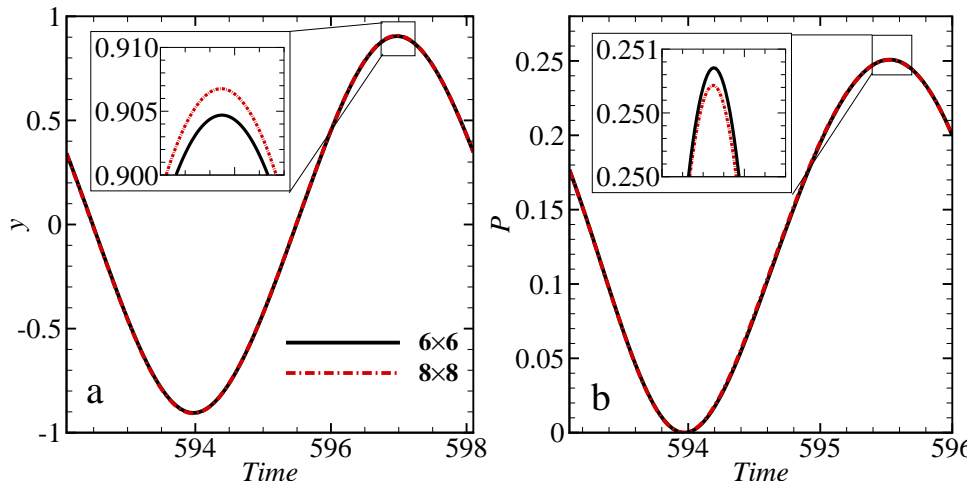


Figure 7.3: Mesh independence study.

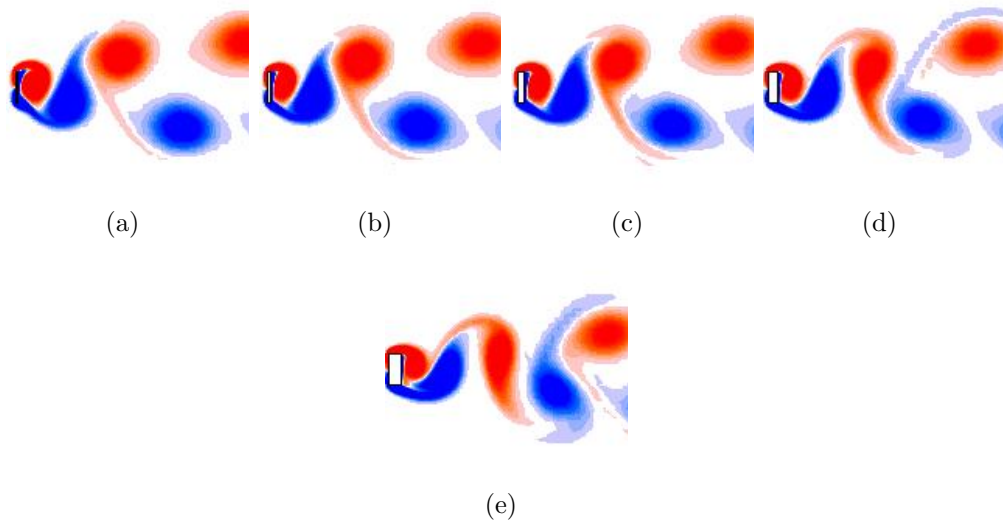


Figure 7.4: Vorticity contours for stationary plates with different thickness a) $\alpha = 0.05$ b) $\alpha = 0.1$, c) $\alpha = 0.2$, d) $\alpha = 0.3$ and e) $\alpha = 0.4$ at $Re = 150$. The vorticity level ranges between -2 (red) to 2 (blue).

7.3 Results

7.3.1 Stationary plates

The lift and Strouhal number for stationary plates will be reported in this section. Five aspect ratio values: 0.05, 0.1, 0.2, 0.3 and 0.4 are chosen for this study. The Reynolds number is taken as 150. The vorticity contours for the five aspect ratio values are plotted in fig. 7.4. The 2S vortex shedding mode is observed for each plate. The size of the recirculation zone is seen to reduce with the increasing aspect ratio (α). The shape of the vortex is circular for the thinnest plate and it becomes stretched as the plate aspect ratio increases. The root mean square (rms) values of drag ($C_{D,rms}$) and lift ($C_{L,rms}$) coefficients and the Strouhal number (St_0) for the stationary plates are plotted in fig. 7.5. The drag is seen to reduce with increasing plate aspect ratio (α) due to the decreasing vortex strength while the lift increases mainly due to a larger surface area normal to y -direction. The Strouhal number increases with the plate aspect ratio. The values of $C_{D,rms}$ reduces by 14.6% and the values of $C_{L,rms}$ and St increases by 150% and 20%, respectively when α is increased from 0.05 to 0.4.

7.3.2 Undamped response

In this section, the transverse vortex-induced vibration (VIV) of undamped plate of aspect ratios $\alpha = 0.05, 0.1, 0.2, 0.3$ and 0.4 will be discussed. The Reynolds number and mass ratio are taken as 150 and 2, respectively. The vibration amplitude (A_y) responses as

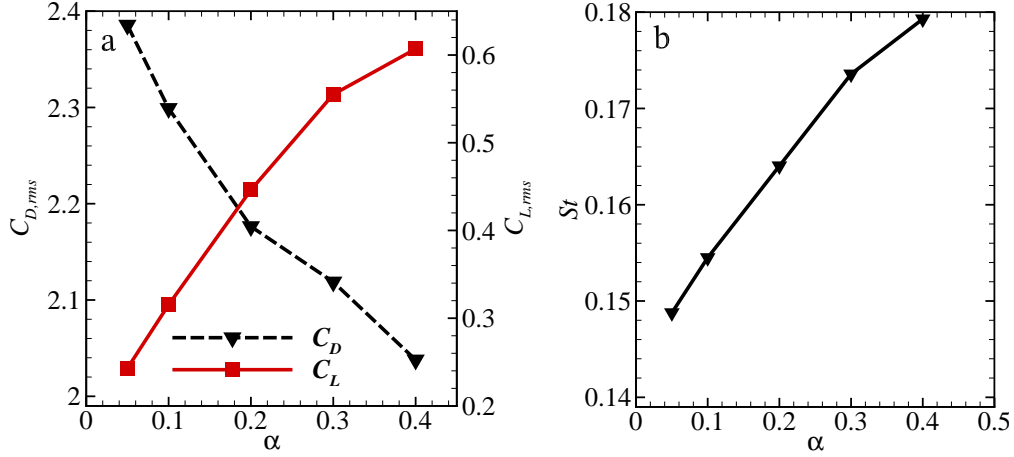


Figure 7.5: (a) RMS drag and lift coefficients and (b) Strouhal number for stationary plates with different thickness at $Re = 150$.

a function of reduced velocity (U_r) for different α values are plotted in fig. 7.6a. The maximum vibration amplitude decreases with increasing aspect ratio of the plate. The maximum values of A_y are 1.46, 1.44, 1.38, 1.34 and 1.19 for aforementioned values of α in increasing order. The reduced velocities corresponding to maximum A_y are 4.4, 5.0, 5.6, 5.8 and 6.2. The synchronization region is also seen to decrease with increase in α . In case of cylinders, the synchronization region increases with decreasing mass ratio. A similar trend is seen here in the case of plates with the mass of the plate increasing with α . The variations of rms lift coefficient ($C_{L,rms}$) with reduced velocity for various values of α are shown in fig. 7.6b. A very similar trend is seen for all α values. For low U_r values (≈ 1.0 -2.5), the vibration amplitude is very small hence the lift values are close to that of the corresponding stationary plates. As U_r is increased, the lift force reaches a peak value for all the α values and then follows a V shape trend. The peak value of lift coefficient increases with increase in α . The phase difference (ϕ) between the lift force and the displacement is shown in fig. 7.6d. Each plate shows a jump in ϕ from 0 to 180° over very narrow range of U_r . The normalized vibration frequency (f), ratio of vibration frequency (f_y) to the natural frequency of the plate (f_n), is plotted in fig. 7.6c. The frequency response of the all the α values can be divided into three regions. In the first region of the low U_r values, the motion is desynchronized from natural frequency as f is quite small compared to 1.0. The frequency increases linearly with U_r in this region. The vibration amplitude is small and increases with U_r . The lift coefficients also do not show much variation from their corresponding values for the stationary cases.

The second region starts with a jump in f and the plate vibration gets locked in with its natural frequency. Notice that f is smaller than 1.0 at lock-in since f_n is larger than the natural frequency in fluid (f_N) due to the added mass effect. The start of the second region can also be characterised by the rapid increase of vibration amplitude and lift coefficient

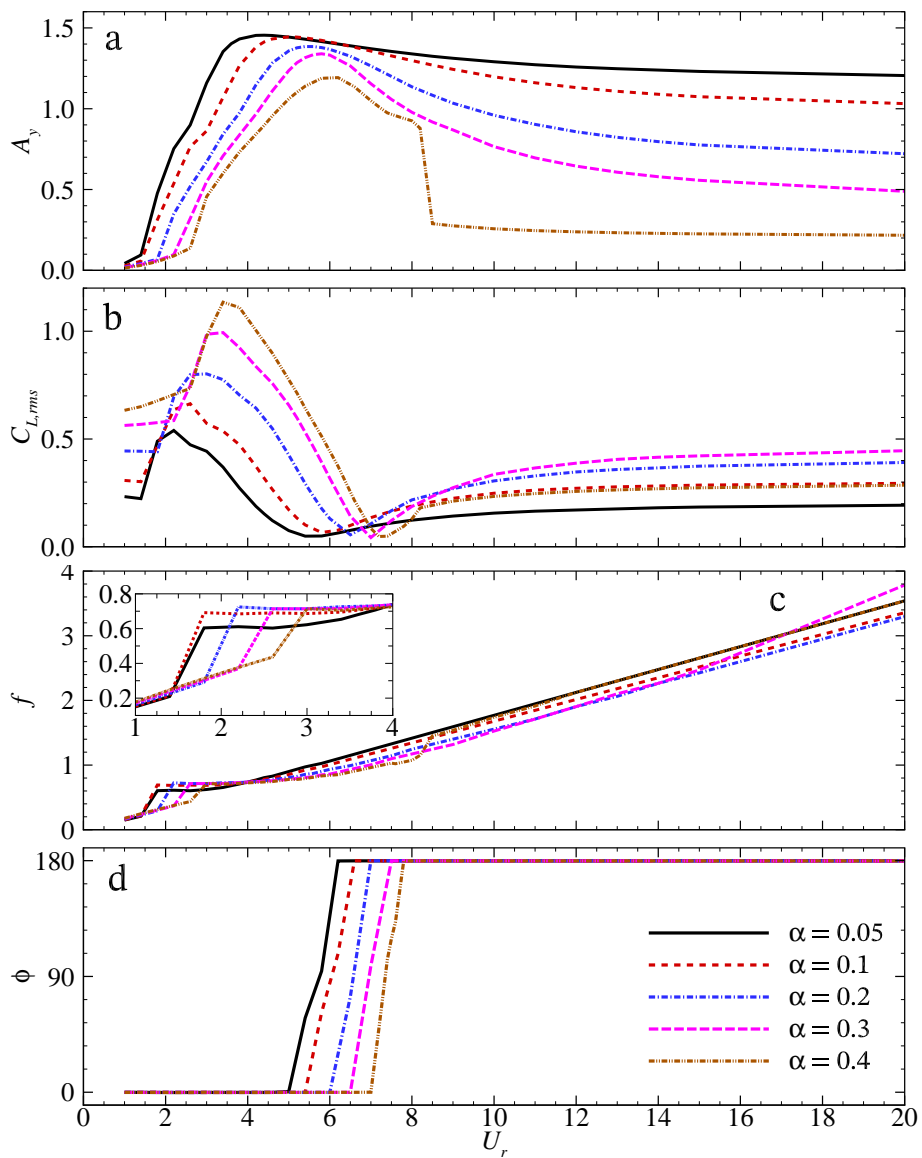


Figure 7.6: a) Displacement amplitude, b) rms lift coefficient, c) normalized vibration frequency and d) phase difference between lift force and displacement versus reduced velocity for various thickness values of the plate for $Re = 150$.

with U_r . The second region ends where the phase difference ϕ jumps to 180° . It is easy to recognise the second region boundary from amplitude response for $\alpha = 0.4$ which shows a sudden decrease in vibration amplitude and corresponding increase in frequency f . For other α values the amplitude decays rather smoothly with U_r and one has to rely upon phase difference data. The lift coefficient reaches its minimum value before the end of the second region where ϕ jumps from 0 to 180° . The second region can be further divided into two subregions: initial branch and upper branch. The initial branch is the initial subregion where the frequency f does not vary with U_r and the lift coefficient increases to its maximum value. The rest of the subregion is defined as the upper branch. In the upper branch, amplitude response is highest and the lift coefficient decreases monotonically to its minimum value. The normalized frequency no longer remains constant in the upper branch and increases with U_r .

In the third region, the phase difference ϕ stays 180° . The vibration frequency f_y becomes constant in this region. The lift coefficient and the vibration amplitude asymptotically approaches a constant value. All the regions are shown in fig. 7.7 for $\alpha = 0.4$.

In fig. 7.6a, it was seen that the maximum displacement amplitude decreases with increasing aspect ratio of the plate. To understand the reason behind this behaviour, the pressure and viscous lift coefficients are plotted in fig. 7.8. The forces are plotted at U_r values when the plates attain maximum vibration amplitude. The motion of the plates in fig. 7.8 is represented as $1 \rightarrow 2 \rightarrow 3 \rightarrow 4 \rightarrow 1$. The viscous force variation with A_y does not show much difference for different aspect ratios. On the other hand, pressure force variation shows a significant change with α . For $\alpha \leq 0.1$, the net pressure force acts along the direction of motion of the plate for most portion of the vibration cycle. This will definitely promote the vibrations. For larger α values the pressure force tends to become in phase with the displacement of the plate. The phase difference (ϕ_p) between pressure force and plate displacement is plotted in fig. 7.9. The circles in fig. 7.9 denote the location of maximum displacement for each aspect ratio. The phase difference ϕ_p at the maximum A_y decreases with increasing aspect ratio of the plate. This is in agreement with the above discussion and hence explains the decrease in vibration amplitude with increasing aspect ratio of the plate.

7.3.3 Wake structure

The wake structures for all the plates considered in this study are quite similar. For any specific plate, the wake structure depends on the region in which U_r falls. The contour plot of amplitude spectral density(ASD) for C_L as a function of reduced velocity and Strouhal number St , normalized by the St_0 , is plotted in fig. 7.10 for $\alpha = 0.4$ at $Re = 150$. Different response branches that were identified in fig. 7.7 are also shown in

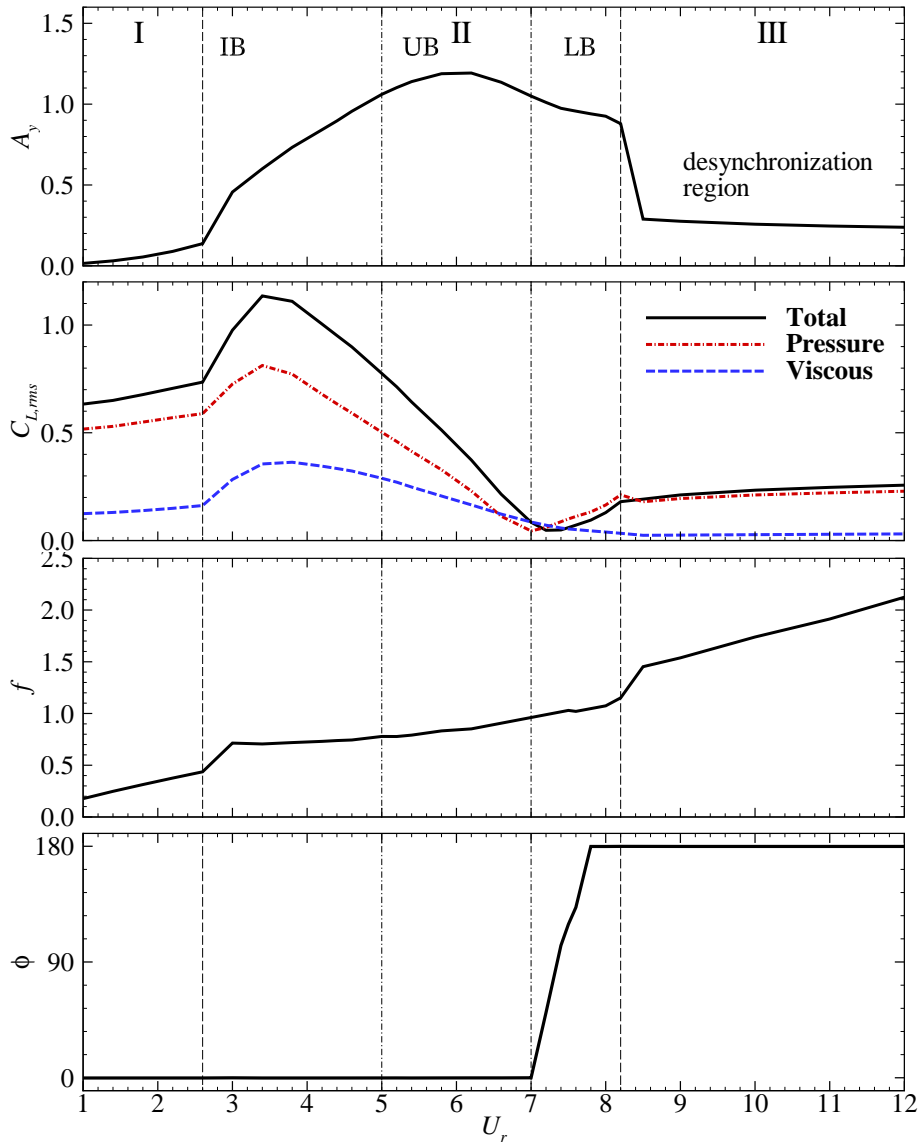


Figure 7.7: Transverse VIV response regions of the plate with $d = 0.4$ (IB - initial branch, UB- upper branch, LB - lower branch).

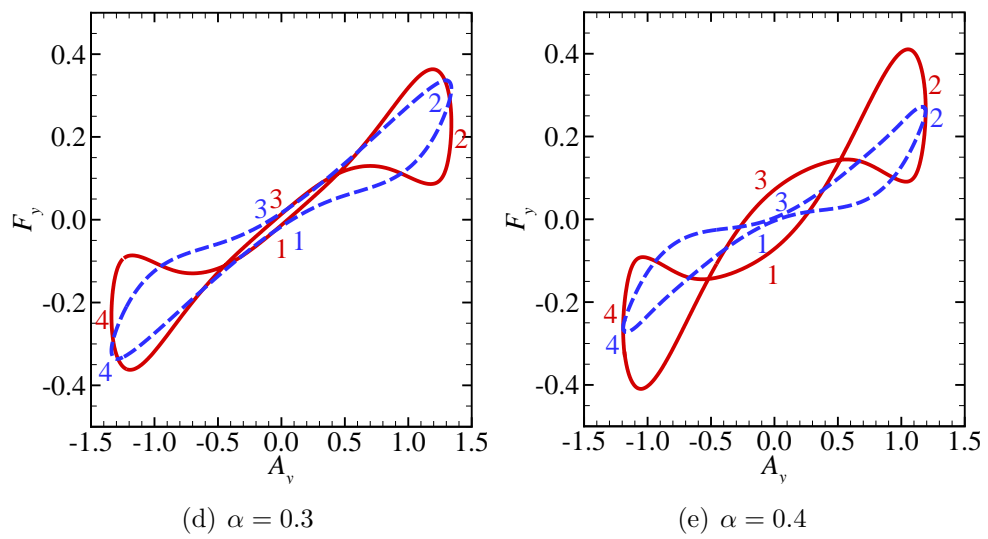
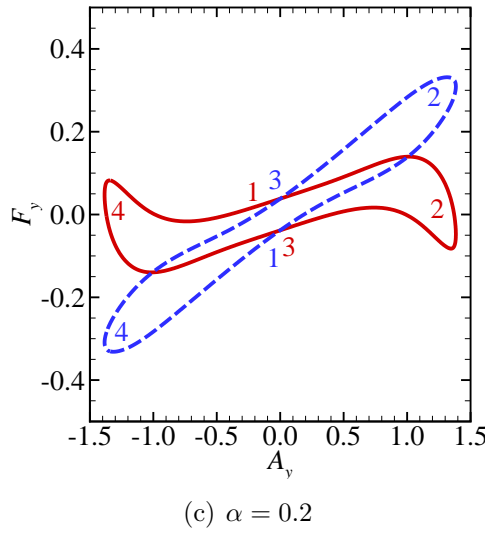
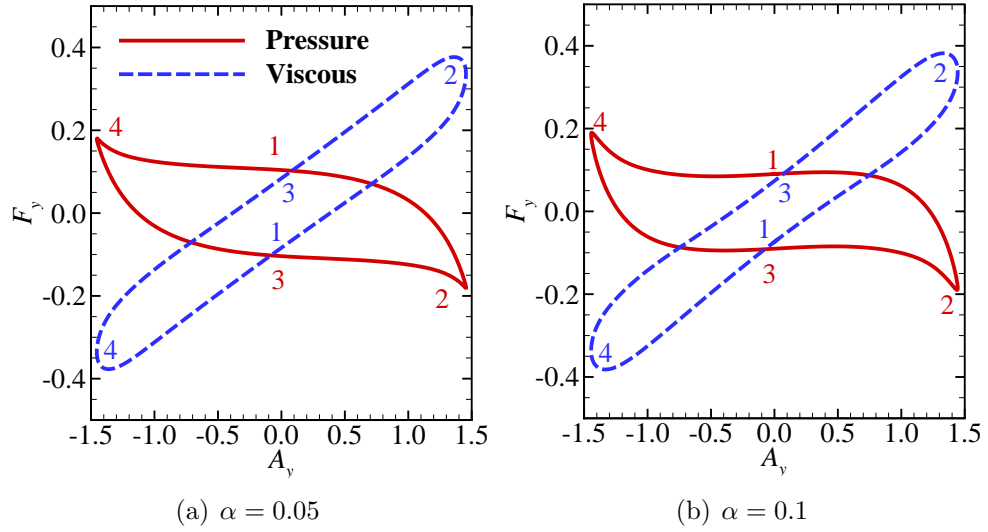


Figure 7.8: Variation of the lift coefficient (pressure and viscous) with the vibration amplitude for different plates.

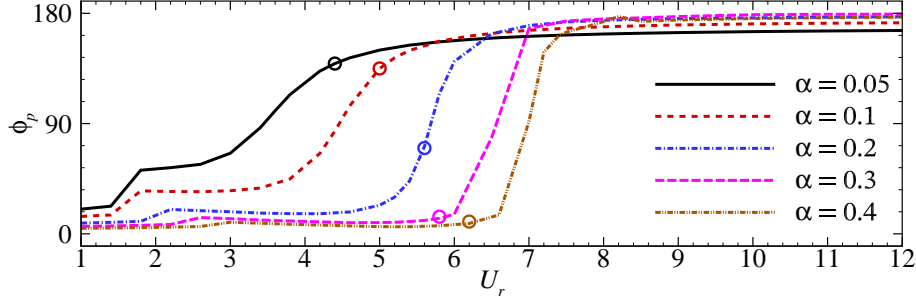


Figure 7.9: Phase difference between pressure force and displacement of the plates for $Re = 150$.

this figure. At the start of the initial branch, the vortex shedding frequency jumps to a value higher than that of the stationary plate case (St_0) and subsequently decreases with U_r . There are two frequency components present in C_L in beginning of the initial branch. The vortex shedding frequency in upper branch is smaller than St_0 and does not vary much with U_r . There is a very weak higher frequency component present in C_L in the upper branch. This higher frequency component becomes more dominant in the lower branch. In the desynchronization region, the vortex shedding frequency becomes equal to St_0 . Wake structures in the each of the response branch will be presented in the subsequent discussion.

The temporal variation of the lift coefficient at $U_r = 3.0$ is plotted in fig. 7.11. The presence of two frequency components, with values $1.33St_0$ and $0.80St_0$, is evident from the the figure. The lift variation is sinusoidal. The lift and displacement are in phase and have equal frequency. The vorticity field for this case is also plotted in fig. 7.11 at six instants shown in C_L plot. The 2S vortex shedding mode is observed i.e two single vortices are being shed in one cycle of oscillations of the plate. Each peak and valley in C_L corresponds a clockwise and counter-clockwise rotating vortex being shed from the plate.

For the upper branch, reduced velocity $U_r = 6.2$ is chosen at which the plate displacement amplitude is maximum. The lift coefficient and the vorticity contours are plotted in fig. 7.12. The vortex shedding mode is 2T i.e two triplet of vortices; primary (P), second (S) and tertiary (T); are shed in one period of oscillations of the plate. At the instant ‘a’ the lift force on the plate is minimum and a counter-clockwise rotating vortex (P_{ccw}) is being formed behind the plate. At a latter instant ‘b’, the primary vortex P_{ccw} has shed and a secondary clockwise rotating vortex (S_{cw}) is developing behind the plate. A local increase in C_L is seen due to the secondary vortex. The local increase in C_L is followed by a local decrease which is related to a tertiary counter-clockwise rotating vortex (T_{ccw}) developing behind the plate. A local maximum of C_L occurs at instant ‘d’ and a primary clockwise rotating vortex (P_{cw}) is being formed behind the plate. Similar to instant ‘b’, a

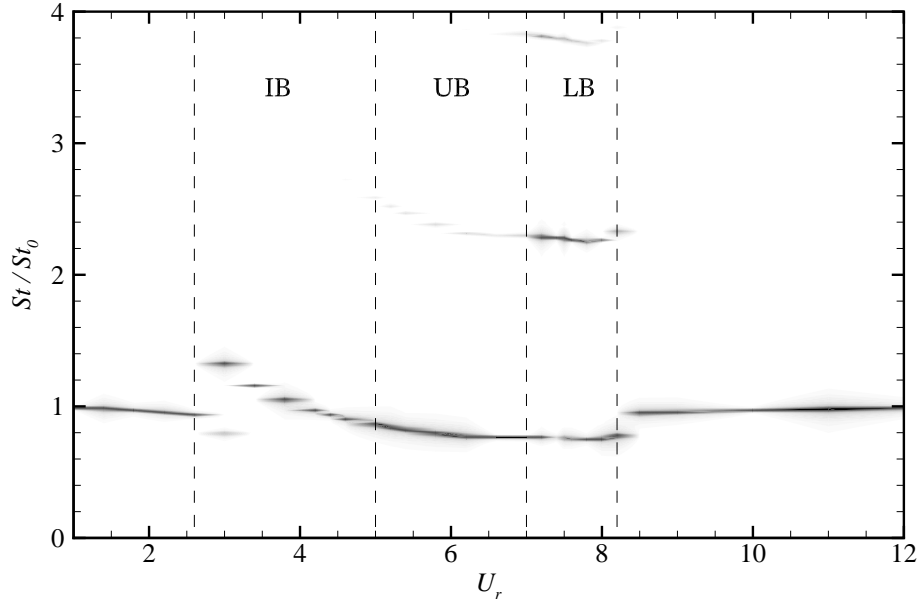


Figure 7.10: Contours of Amplitude spectral density of the lift coefficient for plate with $\alpha = 0.4$ at $Re = 150$ (IB - initial branch, UB- upper branch, LB - lower branch).

local decrease in C_L is seen at instant ‘e’ and corresponds to a secondary counter-clockwise rotating vortex (S_{ccw}) forming behind the plate. At the end of the cycle, instant ‘f’, a tertiary clockwise vortex (T_{cw}) is being developed behind the plate and a corresponding local increase in C_L is seen. The three vortices shed in the initial half of the cycle are also shown in the vorticity contour of instant ‘f’. Therefore in a complete cycle two triplets of vortices are being shed from the plate.

A more dominant high frequency component is present in C_L in the lower branch. The phase difference between the lift force and the displacement transits from 0 to 180° . The temporal variation of the lift force at $U_r = 7.5$ is plotted in fig. 7.13 along with the vorticity contours at six instants in a cycle of oscillation. The vortex shedding mode is same as that in the upper branch i.e 2T. At the instant ‘a’, the plate is approaching its lowest position and a primary counter-clockwise rotating vortex (P_{ccw}) is shedding from the plate. The lift force is maximum at this instant. A local minimum in C_L is observed at instant ‘b’ which is associated to the secondary clockwise rotating vortex (S_{cw}). At the instant ‘c’ when the plate is passing through its mean position, a tertiary counter-clockwise rotating vortex is being shed from the plate and leads to a local maximum in C_L . A similar vortex shedding trend is seen during the remaining half of the plate oscillation cycle. The secondary and tertiary vortex structures dissipate very quickly in the downstream due to low Reynolds number.

The vortex shedding switches back to 2S mode in desynchronization region.

Now the wake structure of the plate with thickness $\alpha = 0.05$ is discussed to demonstrate that same vortex shedding modes are present for all the plates considered in this

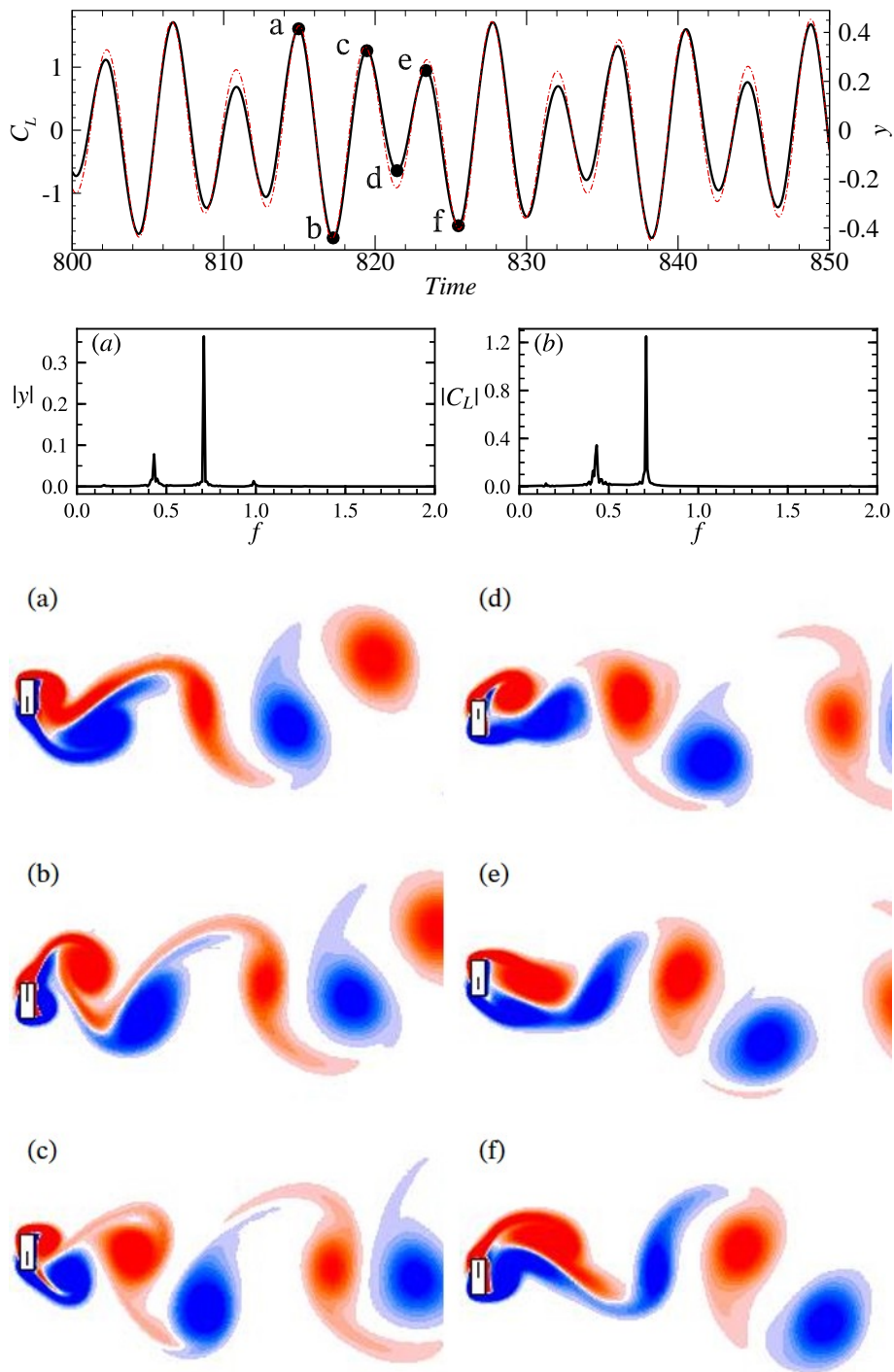


Figure 7.11: Top: Lift coefficient (solid lines) and displacement (broken lines); middle: FFT of displacement and lift force; bottom: Vorticity contours at the instances shown by dots for the plate with $\alpha = 0.4$ at $U_r = 3.0$ and $Re = 150$.

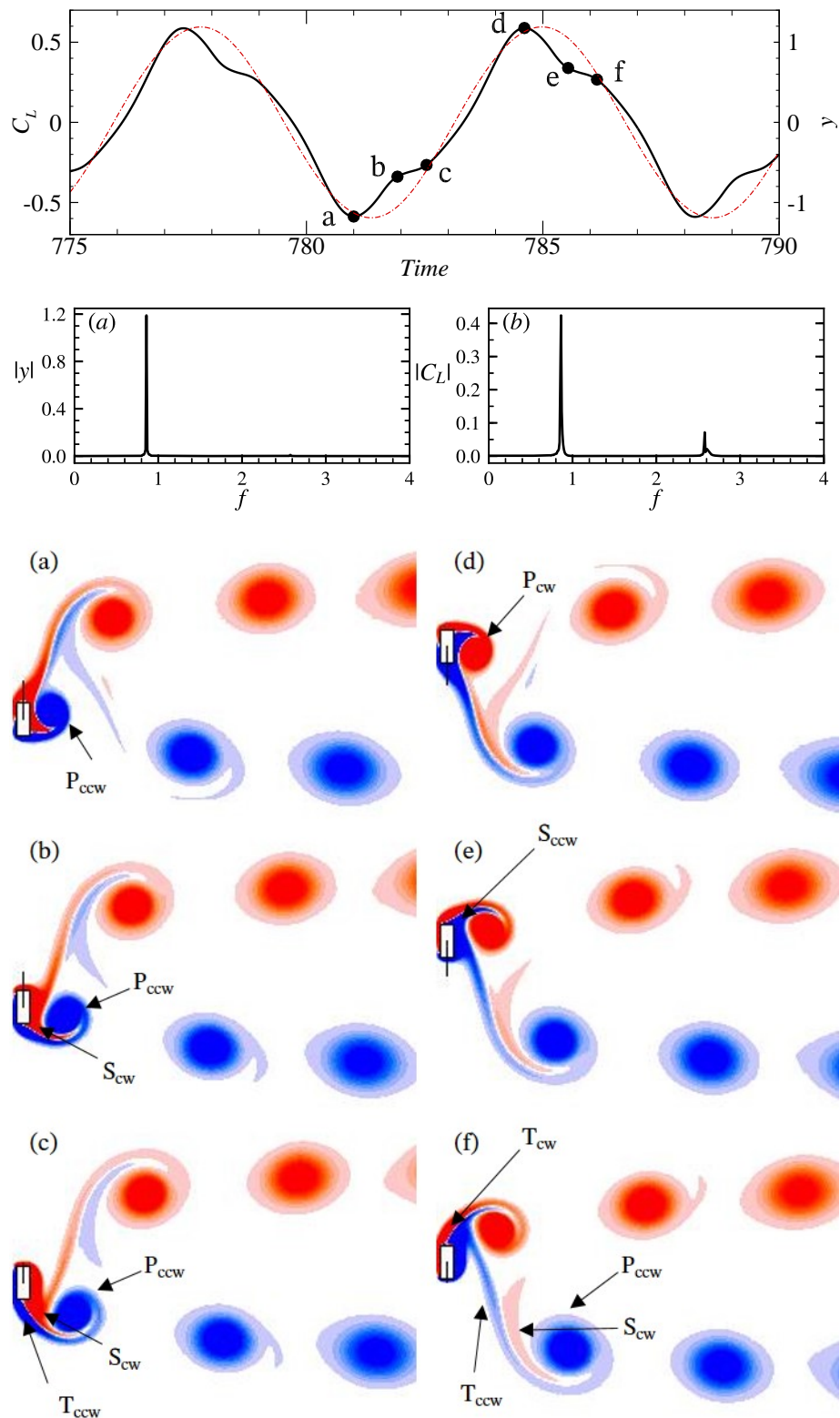


Figure 7.12: Top: Lift coefficient (solid lines) and displacement (broken lines); middle: FFT of displacement and lift force; bottom: Vorticity contours at the instances shown by dots for the plate with $\alpha = 0.4$ at $U_r = 6.2$ and $Re = 150$.

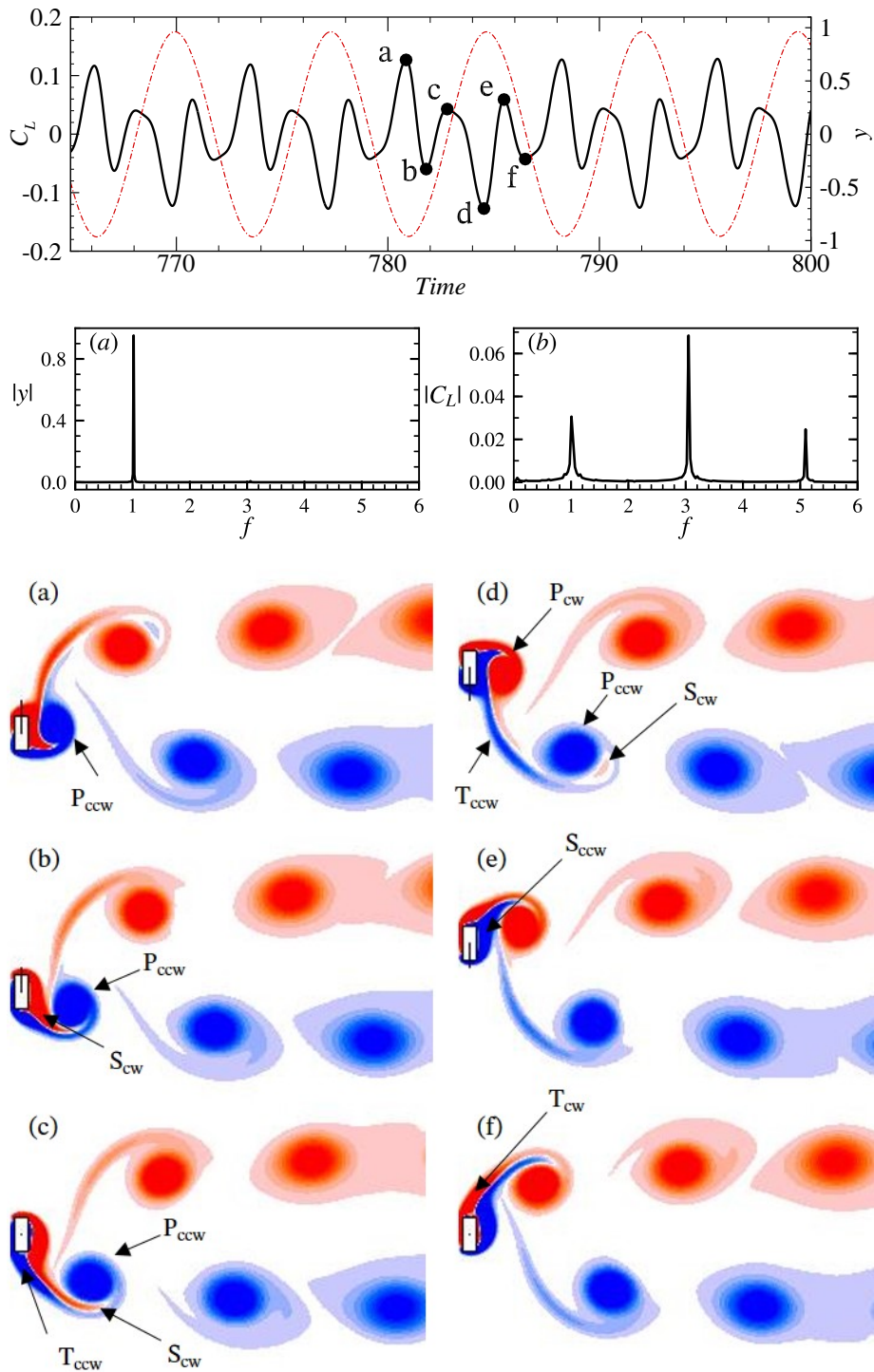


Figure 7.13: Top: Lift coefficient (solid lines) and displacement (broken lines); middle: FFT of displacement and lift force; bottom: Vorticity contours at the instances shown by dots for the plate with $\alpha = 0.4$ at $U_r = 7.5$ and $Re = 150$.

study. The contour plot of amplitude spectral density (ASD) for C_L on the plate with $\alpha = 0.05$ is plotted in fig. 7.15 at $Re = 150$. Different response branches are identified in the figure. Similar to the case of $\alpha = 0.4$, the vortex shedding frequency is higher than that of the stationary plate case in the initial branch and decreases with U_r . Contrary to the case of $\alpha = 0.4$, the value of normalized Strouhal number for $\alpha = 0.05$ is greater than 1 in the upper branch. A weak higher frequency component is also seen for this plate in the upper branch which becomes more dominant in the lower branch. The vortex shedding frequency stays almost constant in the lower branch. Notice that the desynchronization region is absent for this plate. The lift coefficient and vorticity contours for this plate at $U_r = 5.4$ are plotted in fig. 7.15. The considered reduced velocity lies in the lower branch. It is clear from the C_L plot that there is higher frequency component in the lift at three times the frequency of the displacement signal. This ratio of frequencies correlates to the three vortices being shed in half cycle of plate oscillation i.e 2T mode. As seen at instant 'a', the local minimum in C_L is associated with the primary counter-clockwise rotating vortex (P_{ccw}) vortex being shed from the plate. The next local maximum in C_L at instant 'b' is due to the secondary clockwise rotating vortex (S_{cw}) shed from the plate. A tertiary counter-clockwise rotating vortex (T_{ccw}) can be seen being shed from the plate at instant 'c' and this causes a local minimum in C_L . The secondary and tertiary vortices dissipated quickly in the downstream and only the primary vortex can be seen.

To strengthen the evidence of 2T vortex shedding mode, a snapshots of vorticity contours for various plate thickness considered in this study are plotted in fig. 7.16 at $Re = 200$. The three vortices, P_{ccw} , S_{cw} and T_{ccw} , can be easily identified for each plate in the figure. Hence, the following can be concluded for each plate thickness considered in this study: 2S vortex mode is observed in the initial branch and desynchronization region and 2T vortex mode is observed in the upper and lower branches.

7.3.4 Power extraction

In this section, the amount of power that can be extracted from the flow using VIV of the plate will be reported. The constant damping (CD) and electromagnetic damping (EMD) will also be compared against the power output characteristics. The power, eq. 7.5, is proportional to the damping ratio and square of the plate velocity. It can be argued that at a very large damping ratio the plate vibrations will be suppressed completely and consequently there will be no power output. On the other hand, the power output will be zero at zero damping ratio. Some amount of power will be harnessed at any intermediate values of damping ratio due to a non-zero vibration amplitude of the plate. Therefore for any reduced velocity, there should exist an optimal damping ratio (ξ_{opt}) at which the harnessed power will be maximum. The average power (\bar{P}) as a function of damping ratio (ξ) is plotted in fig. 7.17a for the plate with $\alpha = 0.2$ at $U_r = 5.8$ and $Re = 150$.

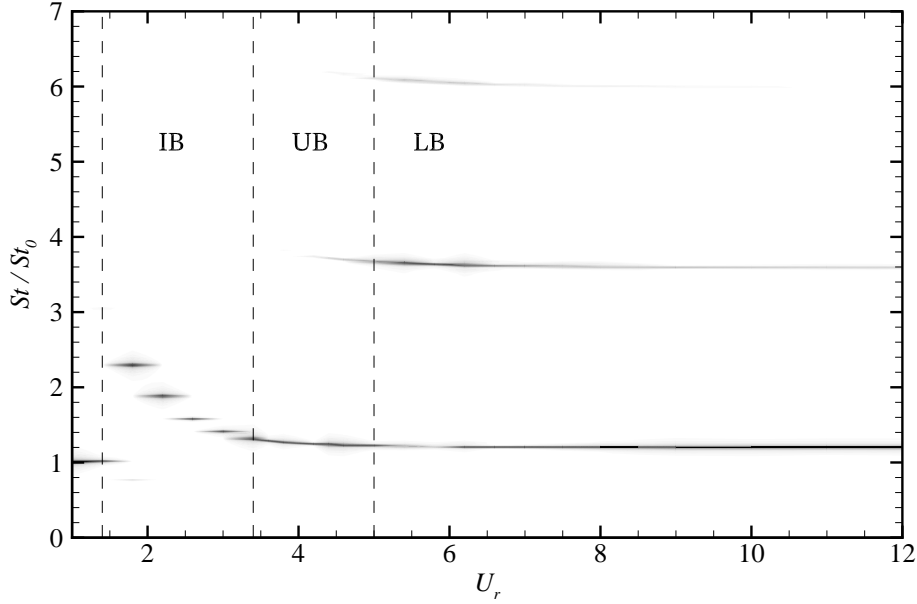


Figure 7.14: Contours of Amplitude spectral density of the lift coefficient for plate with $\alpha = 0.05$ at $Re = 150$ (IB - initial branch, UB- upper branch, LB - lower branch).

The vibration amplitude (A_y) of the plate is also plotted in the figure. The vibration amplitude decreases monotonically with ξ . The value of optimal damping is $\xi_{opt} = 0.36$. The vibration amplitude of the plate also depends strongly on the reduced velocity. At any value of damping ratio, an optimal reduced velocity should exist due to the lock-in phenomena. The average power (\bar{P}) as a function of reduced velocity is plotted in fig. 7.17b for the same plate at $\xi = 0.36$ and $Re = 150$. The maximum average power is obtained at $U_r = 5.8$. The preceding arguments leads to a conclusion that there is a combination of reduced velocity and damping ratio at which the extracted average power will attain a global maximum value (\bar{P}_{max}). The values of optimal damping and reduced velocity and the corresponding global maximum average power (\bar{P}_{max}) will depend on the aspect ratio of the plate.

The global maximum average power (\bar{P}_{max}) as a function of aspect ratio (α) is plotted in fig. 7.18 for different mass ratios of the plate. The value of (\bar{P}_{max}) is maximum for $\alpha = 0.2$.

7.4 Closure

Vortex-induced vibration of a thin plate with one degree of freedom in transverse direction to the incoming flow was analysed numerically. The aspect ratio of the plate was varied from 0.05 to 0.4. The peak amplitude of the plate is found to increase with decreasing aspect ratio which was related to the phase of pressure force with respect to displacement. The maximum values of displacement amplitude are 1.46, 1.44, 1.38, 1.34 and 1.19 for α

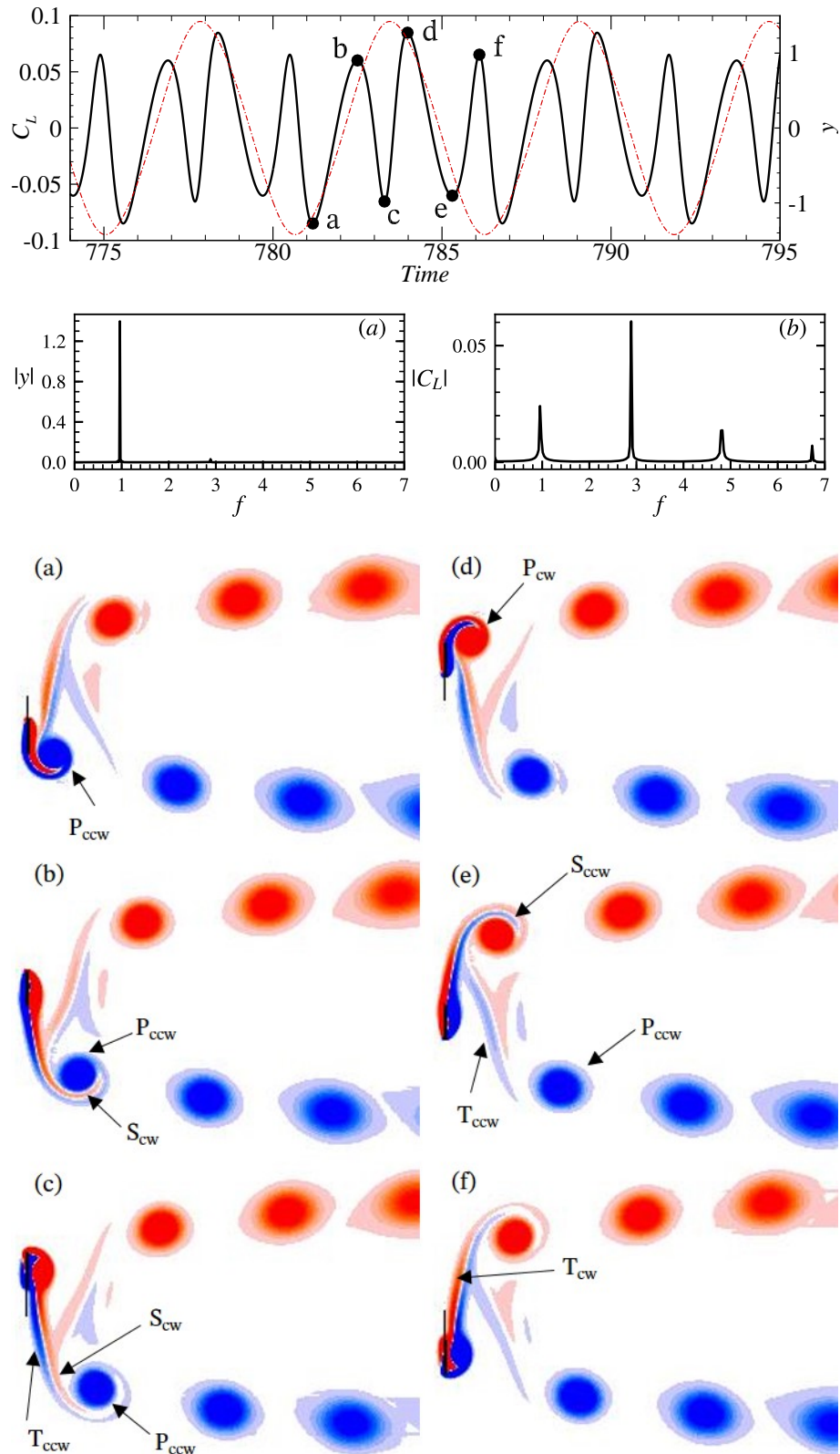


Figure 7.15: Top: Lift coefficient (solid lines) and displacement (broken lines); middle: FFT of displacement and lift force; bottom: Vorticity contours at the instances shown by dots for the plate with $\alpha = 0.05$ at $U_r = 5.4$ and $Re = 150$.

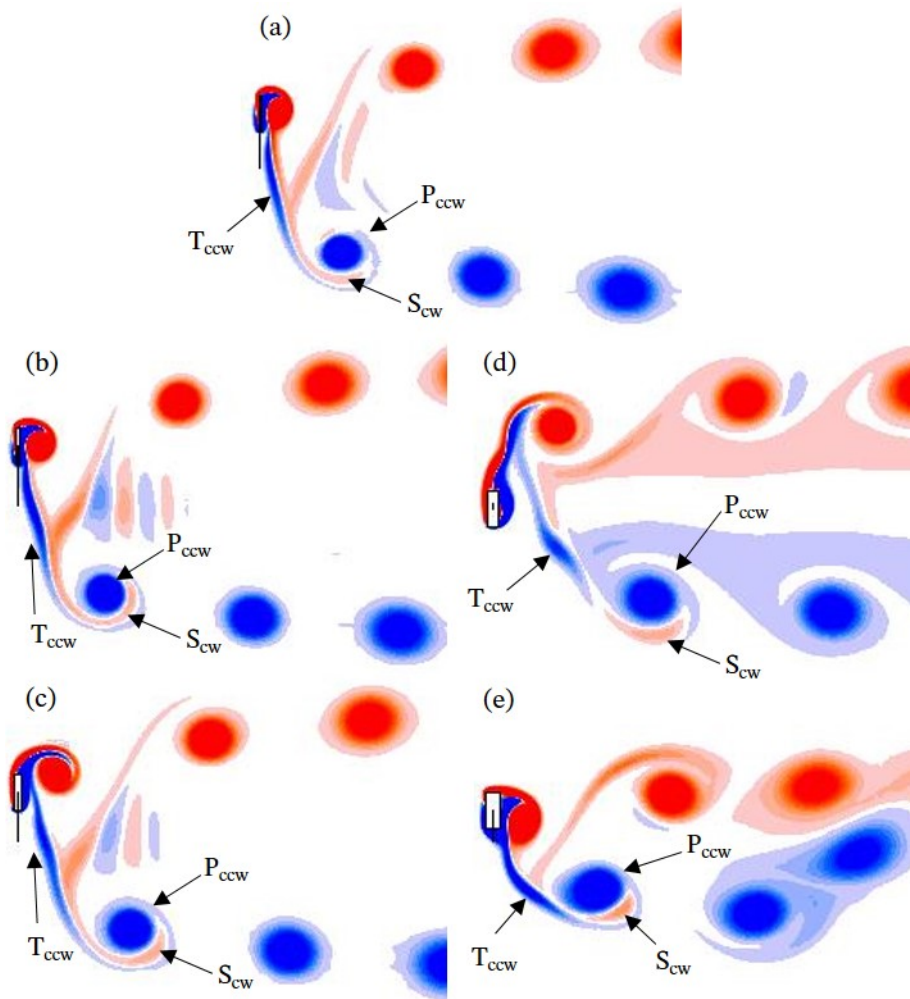


Figure 7.16: Vorticity contour for (a) $\alpha = 0.05$, (b) $\alpha = 0.1$, (c) $\alpha = 0.2$, (d) $\alpha = 0.3$ and (e) $\alpha = 0.4$ at $Re = 200$.

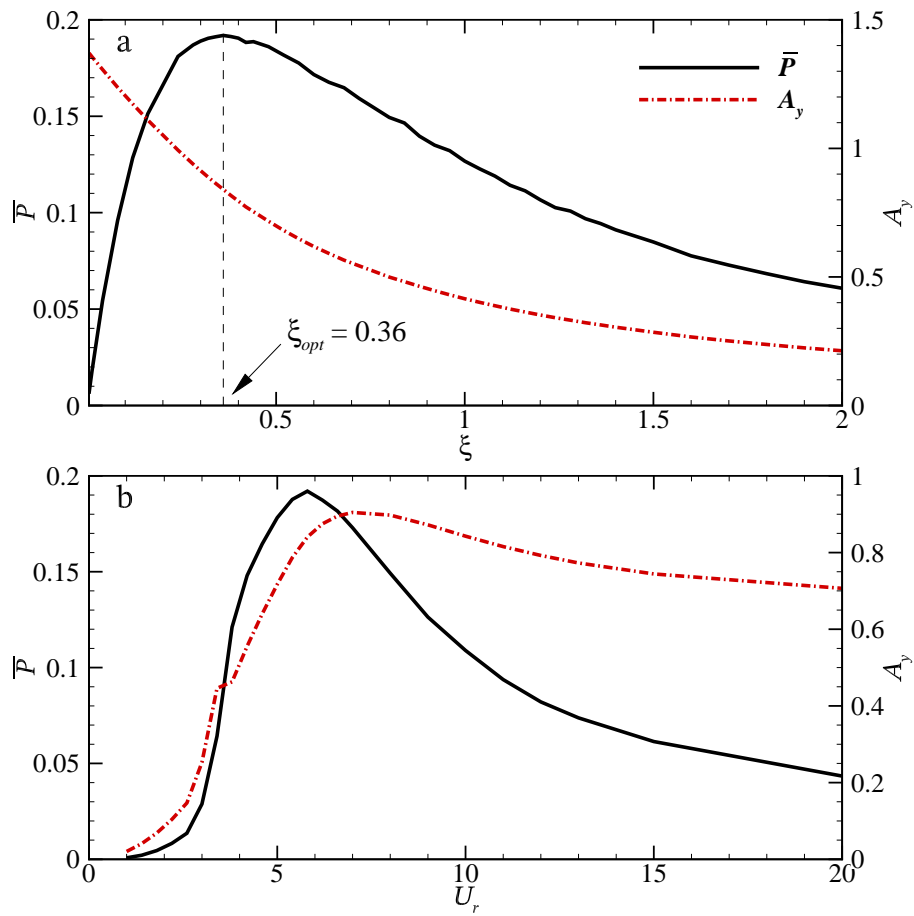


Figure 7.17: (a) Average power versus damping ratio at $U_r = 5.8$ and (b) Average power versus reduced velocity at $\xi = 0.36$ for CD case for the plate with $\alpha = 0.2$ at $Re = 150$.

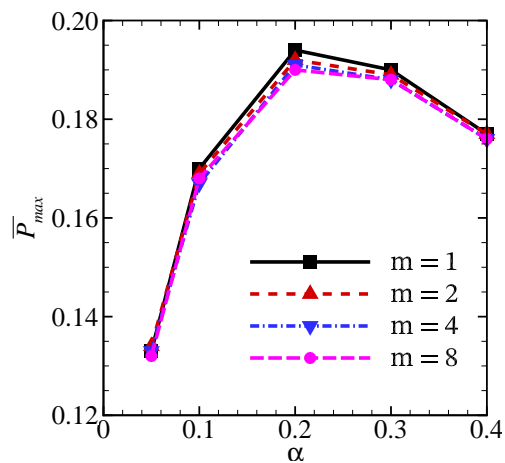


Figure 7.18: maximum average power versus aspect ratio of the plate for different mass ratios at $Re = 150$.

= 0.05, 0.1, 0.2, 0.3 and 0.4, respectively at $Re= 150$. Three response branches; initial, lower and upper, were observed for the plate. The power extraction from VIV of plate was also considered. The plate with aspect ratio 0.2 is found to extract maximum amount of power among all the aspect ratios.

Chapter 8

Heat transfer enhancement using flow-induced deformation

Flow-induced deformation of thin flexible structures coupled with convective heat transfer has potential applications in energy harvesting and is important for understanding functioning of several biological systems. We numerically demonstrate large-scale flow-induced deformation as an effective passive heat transfer enhancement technique. An in-house, strongly-coupled fluidstructure interaction (FSI) solver is employed in which flow and structure solvers are based on sharp-interface immersed boundary and finite element method, respectively. In the present work, we validate convective heat transfer module of the in-house FSI solver against several benchmark examples of conduction and convective heat transfer including moving structure boundaries. The thermal augmentation is investigated as well as quantified for the flow-induced deformation of an elastic thin plate attached to lee side of a rigid cylinder in a heated channel laminar flow. We show that the wake vortices past the plate sweep higher sources of vorticity generated on the channel walls out into the high velocity regions promoting the mixing of the fluid. The self-sustained motion of the plate assists in convective mixing, augmenting convection in bulk and near the walls; and thereby reducing thermal boundary layer thickness as well as improving Nusselt number at the channel walls. We quantify the thermal improvement with respect to channel flow without any bluff body and analyze the role of Reynolds number, Prandtl number and material properties of the plate in the thermal augmentation.

8.1 Introduction

Fluidstructure interaction (referred as FSI hereafter) of flexible thin structures immersed in a flow coupled with convective heat transfer enhances thermal transport, which could be utilized to improve the thermal performance of engineering as well as biological systems. Examples of engineering systems include, energy harvesting devices in microsystems

(Beeby et al., 2006) and microelectronics cooling using piezoelectric fans. Examples of biological systems include, thermoregulation in elephants via flapping of their large ears (Weissenböck et al., 2010) and thermal transport enhancement in microchannels using oscillating synthetic cilia (Mills et al., 2012).

While analyzing the FSI of the flexible thin structures without heat transfer, several previous numerical studies ignored internal stresses and thickness of the structure, and considered it as a membrane (see review by Shelley and Zhang (2011)). Zheng et al. (2010) considered the internal stresses in the structure in their FSI model; however, they considered small-scale deformation of the structure and neglected geometric non-linearity in the structure solver. In the context of large-scale deformation, Baaijens (2001) presented numerical analysis of the FSI of slender bodies placed in a channel flow; however, this study ignored inertial terms in the governing equation of the structure domain. Similarly, Vigmostad et al. (2010) showed capability of simulating thin, flexible structures using a sharp-interface Cartesian grid method. A FSI benchmark involving large-scale flow-induced deformation was proposed by Turek and Hron (2006). In this benchmark, an elastic plate attached to the lee side of a rigid cylinder develops self-sustained oscillation in 2D laminar channel flow. The FSI studies of flexible thin structures by Dunne and Rannacher (2006), Heil et al. (2008), Bhardwaj and Mittal (2012), Lee and You (2013) and Tian et al. (2014) showed validation of their respective solvers against the benchmark proposed by Turek and Hron (2006).

The other class of FSI numerical studies considered coupled convective heat transfer; however, these studies ignored the flexibility of the immersed structure and considered it rigid. These studies demonstrated heat transfer enhancement and can be conveniently categorized in passive and active techniques (Webb and Kim, 2005; Bergles, 2011), which either harness flow energy or utilize external source of energy to augment the heat transfer, respectively. The flow past bluff, rigid bodies such as, rectangular cylinder (Valencia, 1995), inclined square cylinder (Yoon et al., 2009), triangular cylinder (Chatterjee and Mondal, 2012), wings (Biswas and Chattopadhyay, 1992; Hiravennavar et al., 2007; Fiebig et al., 1989) in a channel, conical (Fan et al., 2011) and louvered strip inserts (Fan et al., 2012) in a tube, and flow in wavy-wall channel (Wang and Chen, 2002) were utilized as a passive technique. On the other hand, the heat transfer improvement via oscillating bluff bodies inside the channel (Celik et al., 2010; Beskok et al., 2012) was shown as the active technique. Recently, Mills et al. (2012) considered an array of oscillating synthetic cilia to show heat transfer enhancement in microchannels, however, they did not consider flow-induced deformation in their model.

Very few numerical studies which considered FSI of the flexible structures coupled with convective heat transfer were reported. For instance, Khanafer et al. (2010) simulated a heated flexible cantilever attached to a square cylinder in a channel. Very re-

cently, [Soti and Bhardwaj \(2013\)](#) demonstrated heat transfer enhancement via large-scale flow-induced deformation in the FSI benchmark at Reynolds number, $Re = 100$. They compared effectiveness of various configurations obtained from FSI benchmark using top-down approach (table 8.1). Similarly, [Shi et al. \(2014\)](#) showed thermal improvement in the FSI benchmark at $Re = 204.8 - 327.7$.

In addition, there is limited availability of numerical FSI benchmarks involving large-scale deformation coupled with convective heat transfer. In this context, the objective of the present work is twofold: first, numerically demonstrate and quantify the largescale flow-induced deformation as an effective passive heat transfer enhancement technique. Second, we provide benchmark results which will serve as validation data for FSI solvers coupled with convective heat transfer. Since several previous numerical studies ([Dunne and Rannacher, 2006](#); [Heil et al., 2008](#); [Bhardwaj and Mittal, 2012](#); [Lee and You, 2013](#); [Tian et al., 2014](#)) used FSI benchmark proposed by [Turek and Hron \(2006\)](#) to validate FSI solvers, we propose an extension of this FSI benchmark to account for coupled convective heat transfer in the present work.

In present work, we built upon our previous work ([Soti and Bhardwaj, 2013](#)) and employ a sharp-interface immersed boundary method based flow and heat transfer solver with finite-element based structural dynamics solver (section 8.2). First, we perform code validation for the heat transfer module of the in-house FSI solver (Section 8.3). Second, we consider convective heat transfer in FSI benchmark problem proposed by [Turek and Hron \(2006\)](#) and explain role of vortex dynamics in enhanced mixing of the fluid in Section 8.4.1. The mechanism of thermal augmentation via large-scale flow-induced deformation is described in Section 8.4.2. The quantification of the heat transfer improvement is analyzed by calculating and comparing the effectiveness of various configurations (table 8.1) with respect to pumping power required in the channel in Section 8.4.3. Finally, we quantify the influence of several relevant parameters such as Prandtl number, Reynolds number, Youngs modulus and channel length in Sections 8.4.4, 8.4.5, 8.4.6 and 8.4.7, respectively.

8.2 Computational model

An in-house FSI solver based on sharp-interface immersed boundary method is employed to simulate the fluid dynamics, heat transfer and structure dynamics. The governing equations of the flow domain are solved on a fixed Cartesian (Eulerian) grid while the movement of the immersed structure surfaces is tracked in Lagrangian framework. As reviewed by [Mittal and Iaccarino \(2005\)](#), the immersed boundary method is relevant for 3D complex moving boundaries on a Cartesian grid. Since governing equations are solved on body non-conformal, Cartesian grid, there is no need of re-meshing with deforming or

Table 8.1: Cases considered by [Soti and Bhardwaj \(2013\)](#) and in present work to quantify heat transfer augmentation via flow-induced deformation.

Cases	Configuration
CHL	Channel flow without bluff body
CYL	Channel flow with a stationary and rigid cylinder
CRP	Channel flow with a stationary and rigid cylinder with a rigid plate attached on its lee side
CDP	Channel flow with a stationary and rigid cylinder with a deformable plate attached on its lee side

moving immersed structures in the fluid domain. The FSI solver employed in the present study was developed by Mittal and co-workers ([Zheng et al., 2010](#); [Mittal et al., 2008](#); [Seo and Mittal, 2011b](#); [Mittal et al., 2011](#)) and later developed for large-scale flow-induced deformation by [Bhardwaj and Mittal \(2012\)](#). The flow is governed by unsteady, viscous and incompressible NavierStokes equations:

$$\frac{\partial v_i}{\partial x_i} = 0, \quad (8.1)$$

$$\frac{\partial v_i}{\partial t} + \frac{\partial v_i v_j}{\partial x_j} = -\frac{\partial p}{\partial x_i} + \frac{1}{Re} \frac{\partial^2 v_i}{\partial x_j^2}, \quad (8.2)$$

where $i, j = 1, 2, 3$ and v_i, t, p and Re are fluid velocity vector, time, pressure and Reynolds number, respectively. These equations are discretized in space using a cell-centered, collocated (non-staggered) arrangement of primitive variables v_i, p and a second-order, central difference scheme is used for all spatial derivatives. In addition, the face center velocities are computed ([Zang et al., 1994](#)), which results in discrete mass conservation to machine accuracy. The implementation details can be found in previous and recent papers by Mittal and co-workers ([Zheng et al., 2010](#); [Mittal et al., 2008](#); [Seo and Mittal, 2011b](#); [Mittal et al., 2011](#)). Here we provide the methodology briefly. The unsteady NavierStokes equation is marched in time using a fractional-step scheme ([Mittal et al., 2008](#); [Chorin, 1968b](#)) which involves two steps: solving an advectiondiffusion equation followed by a pressure Poisson equation. During the first step, both the convective and viscous terms are treated implicitly using CrankNicolson scheme to improve the numerical stability. In the second step, the pressure Poisson equation is solved with the constraint that the final velocity be divergence-free. Once the pressure is obtained, the velocity field is updated to its final value in the final sub-step. A fast geometric multigrid solver ([Press et al., 1992](#)) is used to solve the pressure Poisson equation. A sharp-interface immersed boundary method based on multi-dimensional ghost-cell methodology ([Mittal et al., 2008](#)) is utilized and the immersed structure boundary is represented using unstructured grid with triangular

elements in Cartesian volume grid of the flow domain.

The structure dynamics was simulated using an open-source finite-element solve [Tahoe](#)[©]. The governing equations for the structure are the Navier equations (momentum balance equation in Lagrangian form) and are written in non-dimensional form as:

$$\rho_s \frac{\partial^2 d_i}{\partial t^2} = \frac{\partial \sigma_{ij}}{\partial x_j} + \rho_s f_i, \quad (8.3)$$

where i and j range from 1 to 3, ρ_s is the dimensionless density of the structure with respect to the fluid density, d_i is the displacement component in the i direction, σ is the Cauchy stress tensor and f_i is the body force component in the i direction. The structure solver was implicitly (two-way) coupled with the flow solver using a partitioned (segregated) approach by [Bhardwaj and Mittal \(2012\)](#). The implicit coupling ensures numerical stability at low structure-fluid density ratio ([Zheng et al., 2010](#)). The implementation details of the coupling can be found in Refs. ([Bhardwaj and Mittal, 2012](#); [Bhardwaj et al., 2014](#)). The structural solver [Tahoe](#)[©] was coupled with a compressible flow solver in ([Bhardwaj et al., 2014](#)). No slip boundary conditions are applied for the velocity at the fluidstructure interface which represents continuity of the velocity at the interface,

$$v_{i,f} = \dot{d}_{i,s}, \quad (8.4)$$

where subscripts f and s denote fluid and structure, respectively. In addition, the balance of forces is applied at the interface,

$$\sigma_{ij,f} n_j = \sigma_{ij,s} n_j, \quad (8.5)$$

where n_j is the local surface normal pointing outward from the surface. The pressure loading on the structure surface exposed to the fluid domain is calculated at the current location of the structure using interpolated fluid pressure via bilinear interpolation, as described by [Mittal et al. \(2008\)](#).

The heat transfer inside the fluid is governed by the following dimensionless energy equation:

$$\frac{\partial T}{\partial t} + v_i \frac{\partial T}{\partial x_i} = \frac{1}{Pe} \frac{\partial^2 T}{\partial x_j^2}, \quad (8.6)$$

where Pe is Peclet number and T is dimensionless temperature, defined in terms of dimensional temperature T^* , reference wall temperature T_w^* and reference temperature T_{ref}^* , as follows,

$$T = \frac{T^* - T_{ref}^*}{T_w^* - T_{ref}^*}, \quad (8.7)$$

T_{ref}^* is taken as inlet temperature of the fluid in all simulations unless specified otherwise.

The thermal boundary conditions are described as follows (fig. 8.1). The temperature is considered as uniform at the inlet. The fluidstructure interface is insulated and channel walls are at constant temperature. Zero Neumann temperature boundary conditions are applied at the outlet. The heat transfer augmentation is characterized using instantaneous Nusselt numbers at the channel wall, which is defined as follows (Bejan, 2004):

$$Nu(x, t) = \frac{2H}{T_m - 1} \left. \frac{\partial T}{\partial y} \right|_{wall}, \quad (8.8)$$

where $2H$ is the dimensionless hydraulic diameter of the channel. The bulk mean temperature, T_m , is defined as (Bejan, 2004):

$$T_m(x, t) = \frac{\int_0^H uT dy}{\int_0^H u dy}, \quad (8.9)$$

where u stands for dimensionless axial velocity component. Time-average Nusselt number (Nu_{avg}) over one period of oscillation, τ , for time-periodic flow is expressed as:

$$Nu_{avg}(x) = \frac{1}{\tau} \int_t^{t+\tau} Nu(x, t) dt. \quad (8.10)$$

Time- and space-average Nusselt number (Nu_{mean}) over surface area A is defined as:

$$Nu_{mean} = \frac{1}{A} \int \int_A Nu_{avg}(x) dA. \quad (8.11)$$

8.3 Code validation

The flow solver was extensively validated by Mittal et al. (2008) against several benchmark problems such as flow past a circular cylinder, sphere, airfoil and suddenly accelerated circular cylinder and normal plate and was used to simulate 3D biological flows involving FSI (Zheng et al., 2010; Mittal et al., 2011). The capability of simulating large-scale flowinduced deformation with implicit (two-way) coupling in the FSI solver was implemented by Bhardwaj and Mittal (2012). We briefly present validation results for this module in Section 8.3.1 for the sake of completeness of the validation of the model. The validation studies carried out in the present work for convective heat transfer module are described in subsequent subsections.

8.3.1 Large-scale flow-induced deformation

The flow-induced deformation module in the in-house FSI solver was validated by Bhardwaj and Mittal (2012) against the FSI benchmark proposed by Turek and Hron (2006).

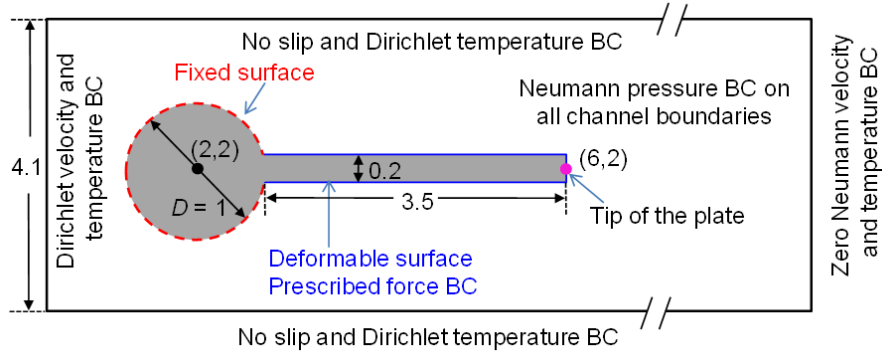


Figure 8.1: Schematic and boundary conditions (BC) of the FSI benchmark problem with heat transfer. The FSI benchmark was first proposed by Turek and Hron (2006) and later Bhardwaj and Mittal (2012) validated their FSI solver with the benchmark. In present work, coupled convective heat transfer is considered with insulated cylinder and plate in a heated channel. Adapted with permission from (Bhardwaj and Mittal, 2012). Copyright (2011) Professor Rajat Mittal.

In the benchmark, a $3.5D \times 0.2D$ elastic plate attached on the lee side of a rigid cylinder is placed inside a channel of width $4.1D$, where D is the cylinder diameter (fig. 8.1). The fluid is considered to be Newtonian and incompressible. The plate is considered to be of Saint VenantKirchhoff material, which accounts for geometric-nonlinearity for a linear elastic material (Fung, 1993). The boundary conditions for the benchmark problem are shown in fig. 8.1. At the inlet, a fully developed parabolic velocity profile with mean velocity $U_m = 1$ is applied and no slip boundary conditions are applied at the channel walls and immersed structure boundaries. At the outlet, zero Neumann boundary condition is applied for the velocity. Note that the thermal boundary conditions shown in fig. 8.1 will be used later in the discussion. The Reynolds number, dimensionless Youngs modulus, structure-fluid density ratio and Poissons ratio are 100, 1.4×10^3 , 10 and 0.4, respectively. The minimum grid sizes in x and y directions are $\Delta x_{min} = 0.0231$ and $\Delta y_{min} = 0.02$, respectively, and time step is $\Delta t = 0.01$. The validation in Ref. Bhardwaj and Mittal (2012) was conducted for time-varying position of the tip of the plate (fig. 8.2) and oscillation frequency, after the plate reaches self-sustained periodic oscillation state. The position as well as frequency was in good agreement with published results of Turek and Hron (2006).

8.3.2 Conduction heat transfer

We present validation of 1D unsteady and 2D steady heat conduction cases against analytical model (Incropera and De Witt, 2007). The temperature in these cases is governed

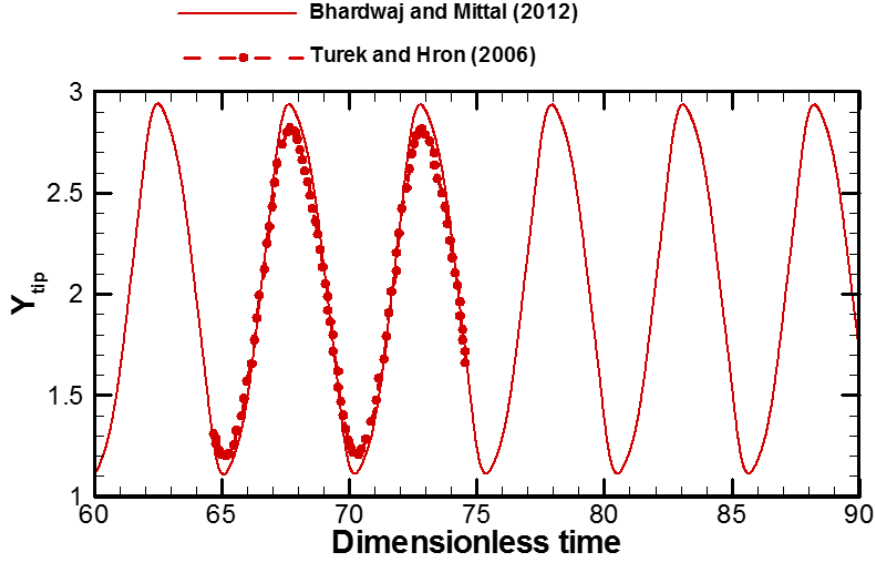


Figure 8.2: Comparison between the present work and published results of [Turek and Hron \(2006\)](#) for the stationary-state time-variation of X and Y displacement of the tip of the plate. Adapted with permission from ([Bhardwaj and Mittal, 2012](#)). Copyright (2011) Professor Rajat Mittal.

by the heat conduction equation,

$$\frac{\partial T^*}{\partial t^*} = \alpha \frac{\partial^2 T^*}{\partial x_j^{*2}}, \quad (8.12)$$

where α is thermal diffusivity of the material. The dimensionless form of eq. 8.12 with a reference velocity and length renders eq. 8.6 with flow velocity set to zero. The reference velocity in both cases is taken as 1 m/s. In 1D unsteady case, the reference length, the reference wall temperature (T_w^*) and reference temperature (T_{ref}^*) are taken as the slab length, right wall temperature and initial slab temperature, respectively. The left as well as right boundary is at $T_w = 1$ (fig. 8.3a). The grid-size and time-step are 1.5×10^{-2} and 1×10^{-4} , respectively. In fig. 8.3b and c, we note good agreement between numerical and analytical results at different time instances for $Pe = 1$ and $Pe = 4$, respectively.

In 2D steady-state case, a square block of dimension 1×1 with a circular hole of diameter $D = 0.5$ at its center (fig. 8.4a) is considered with $Pe = 1$ and $Re = 1$. The reference length, reference wall temperature (T_w^*) and reference temperature (T_{ref}^*) are taken as the block size, right wall temperature and left wall temperature, respectively. The left and right boundaries of the block are kept at temperatures 0 and 1, respectively with top and bottom boundaries insulated. A uniform heat flux $q''_w = 1$ is applied along the boundary of the hole. The unsteady heat conduction equation (eq. 8.6) was solved with uniform grid-size and time-step 1.5×10^{-2} and 1×10^{-3} , respectively, until steady

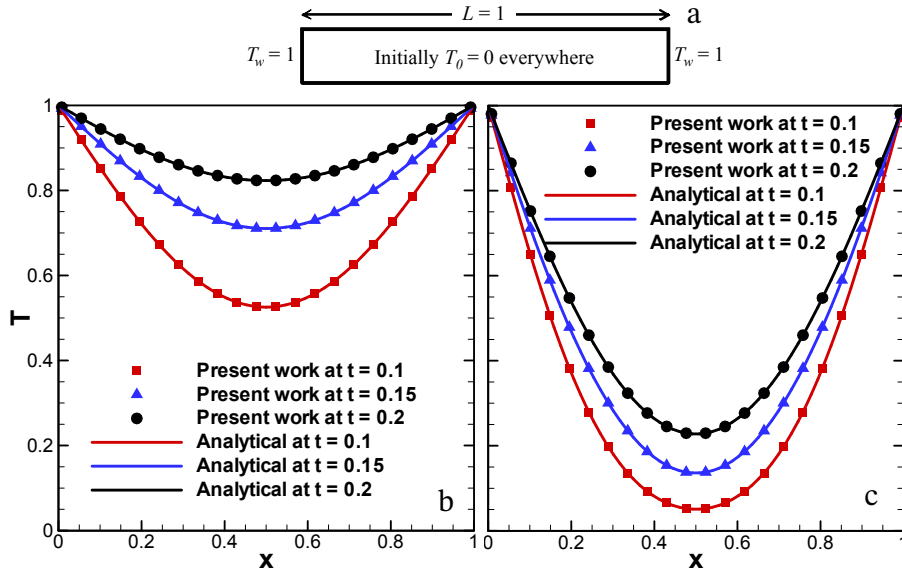


Figure 8.3: Schematic of 1D conduction heat transfer in a slab with initial and boundary conditions (a) Comparisons of simulated time- and space-varying temperature in the slab for Peclet numbers, $Pe = 1$ (b), and $Pe = 4$ (c) with 1D analytical theory.

state is reached. In fig. 8.4c, we plot the temperature variation along the x -axis at $y = 0.5$, calculated by our numerical simulation and [MATLAB](#) partial differential equation solver. The comparison is in good agreement and verifies our calculations. A qualitative comparison of isotherms is shown in fig. 8.4a and b.

8.3.3 Convective heat transfer without bluff body

We validate convective heat transfer module with analytical model given in Ref. ([Bejan, 2004](#)) for steady-state channel flow with constant wall temperature and constant wall heat flux, respectively. In this validation, we consider a $20H \times H$ channel and dimensional reference temperature T_{ref}^* is taken as wall temperature for constant wall temperature case. At inlet, a fully-developed parabolic velocity is applied with maximum value of $1.5U_m$ at the center, U_m being the mean velocity. Zero Neumann velocity boundary condition is applied at outlet. The Reynolds number, based on the mean velocity and channel hydraulic diameter ($2H^*$), and Prandtl number are taken as 200 and 1, respectively. A uniform inlet temperature, $T_{in} = 1$ and 0 is considered for constant wall temperature ($T_w = 0$) and constant wall heat flux ($q''_w = 1$) cases, respectively. Zero Neumann boundary condition is applied for temperature at the outlet. Simulation is performed till steady state on a 512×64 uniform grid with $\Delta x_{min} = 0.04$ and $\Delta y_{min} = 0.02$ with time step equal to 0.02. Local Nusselt numbers (Nu) (eq. 8.8) calculated using the present numerical model and analytical expressions (eqs. (3.111)-(3.114) in Ref. ([Bejan, 2004](#))) are compared in fig. 8.5. The fully developed values of $Nu = 7.54$ and 8.23 are obtained for the constant

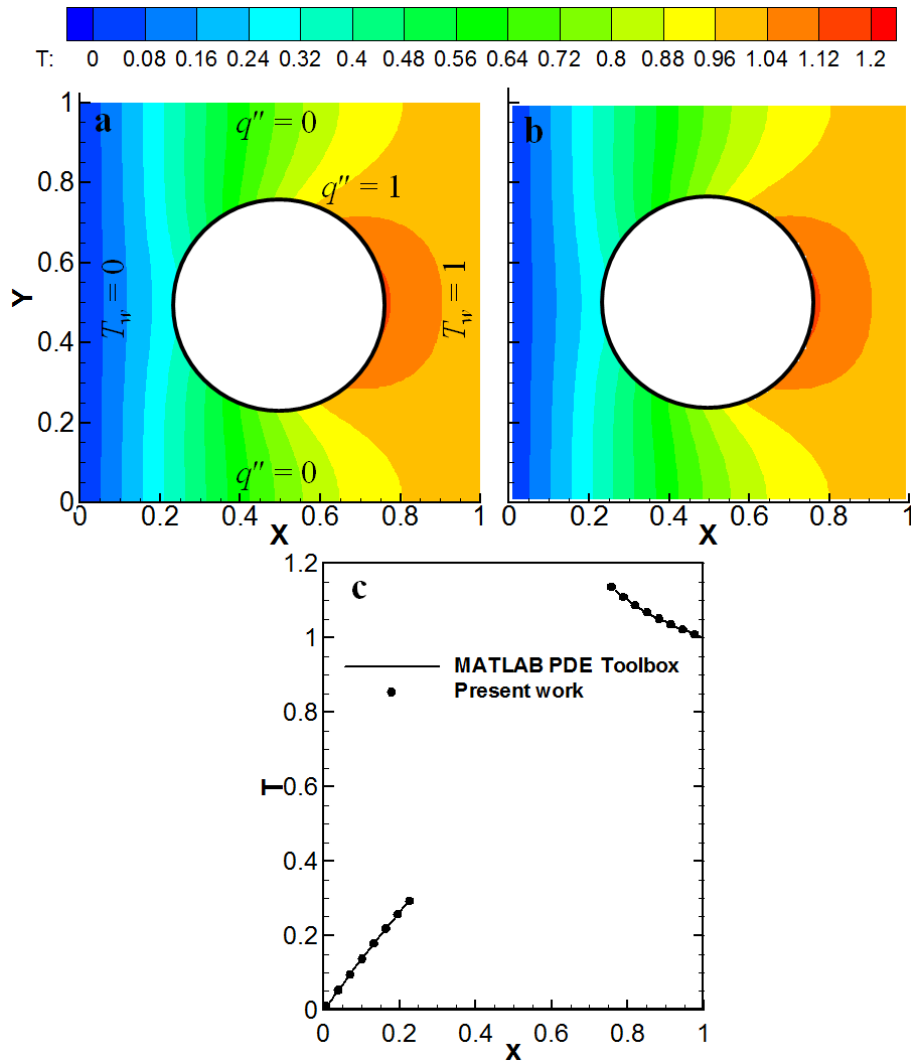


Figure 8.4: 2D conduction heat transfer in a square block with boundary conditions shown in (a). Qualitative comparison of isotherms for $Pe = 1$ obtained using (a) MATLAB PDE Toolbox, and (b) the present numerical model. (c) Comparison of steady-state x -varying temperature at $y = 0.5$.

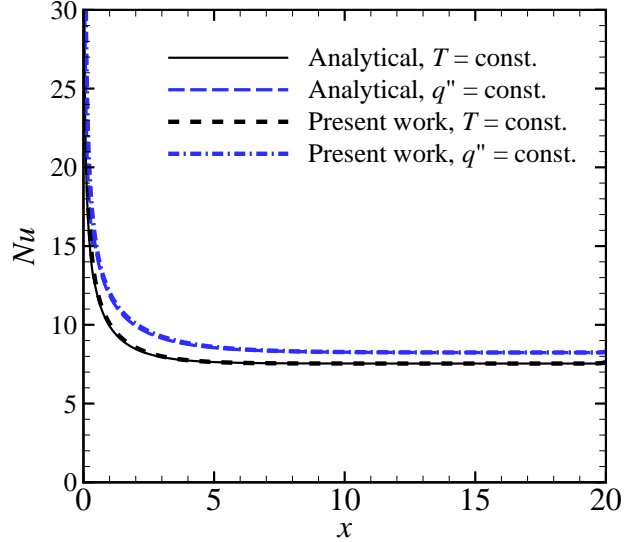


Figure 8.5: Comparison of local Nusselt number along channel length with analytical theory. Two cases, constant wall temperature and constant wall flux are considered.

wall temperature and constant wall heat flux cases, respectively. These values as well as space-variation of Nu match well with the analytical theory and verify the convective heat transfer module.

8.3.4 Convective heat transfer with stationary immersed boundary

We validate convective heat transfer module with an immersed stationary boundary for free stream flow around a heated cylinder (diameter $D = 1$) in a $40D \times 20D$ domain. The computational domain and boundary conditions are shown in fig. 8.6a. The simulations are performed for a range of Reynolds number. The Reynolds number (Re) based on free stream velocity and the cylinder diameter is varied in range of 80-200, keeping Prandtl number constant, $Pr = 0.7$. We utilize a 384×384 non-uniform grid with $\Delta x_{min} = 0.005$ and $\Delta y_{min} = 0.005$, and $\Delta t = 0.0025$. The simulated local Nusselt number for $Re = 120$ is compared with published numerical (Patnana et al., 2010) and experimental (Eckert, 1952) results in fig. 8.6b. The comparisons are in good agreement and therefore, verify our calculations. Comparisons of mean Nusselt numbers calculated at different Re are shown in table 8.2 and the maximum error in our calculations is around 3% as compared to the published results.

8.3.5 Convective heat transfer with moving immersed boundary

In order to validate the FSI solver for convective heat transfer with moving boundary, we consider a transversely oscillating heated cylinder of diameter $D = 1$ in a $40D \times 10D$

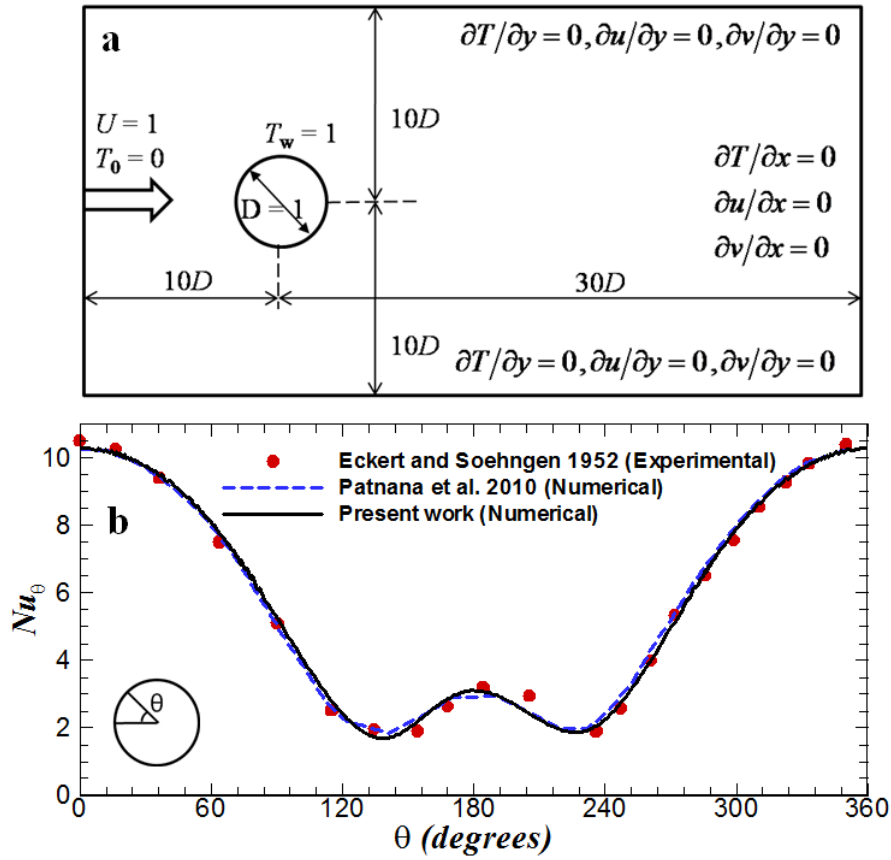


Figure 8.6: (a) Schematic and boundary conditions for flow past a heated and stationary cylinder. (b) Comparison of local Nusselt number for $Re = 120, Pr = 0.7$ as function of azimuthal angle (shown in inset) at the surface of the cylinder with published numerical and experimental results.

Table 8.2: Time- and space- averaged Nusselt number (Nu_{mean}) for flow around a stationary heated cylinder.

Re	Present work	Knudsen and Katz (1958)	Žukauskas (1972)	Churchill and Bernstein (1977)
80	4.58	4.67	4.56	4.64
100	5.14	5.19	5.10	5.16
120	5.66	5.65	5.59	5.62
200	7.39	7.16	7.21	7.19

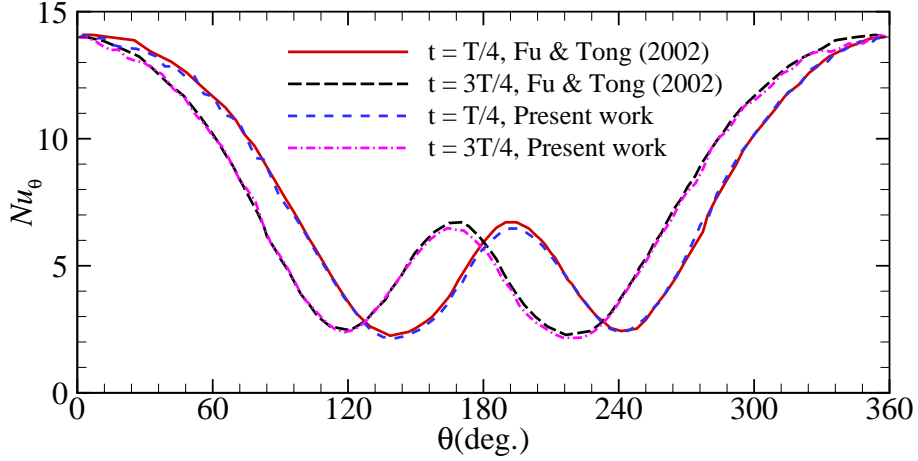


Figure 8.7: Comparison of local Nusselt number as function of azimuthal angle (shown in inset of fig. 8.6b) at the surface of a transversely oscillating cylinder with numerical results of [Fu and Tong \(2002\)](#) for $Re = 200$ and $Pr = 0.71$. Results are compared at different time instances, $t = \tau/4$ and $3\tau/4$, where τ is the time-period of the oscillation of the cylinder.

channel ([Fu and Tong, 2002](#)). The cylinder is located midway between the channel walls at a distance of $10D$ from the inlet. The dimensionless oscillation frequency, amplitude of the transverse velocity of the cylinder, Reynolds number and Prandtl number are 0.2, 0.5, 200 and 0.71, respectively (case 2 in Ref. ([Fu and Tong, 2002](#))). We employed a 256×256 nonuniform grid with $\Delta x_{min} = 0.01$ and $\Delta y_{min} = 0.01$, and $\Delta t = 0.0025$. The local Nusselt numbers at surface of the cylinder calculated in present work and by [Fu and Tong \(2002\)](#) at different time instances are compared in fig. 8.7. The average Nusselt number values from the present work and from [Fu and Tong \(2002\)](#) differ by 0.56% and 0.62% at $t = T/4$ and $t = 3T/4$, respectively. The present calculations are in good agreement with [Fu and Tong \(2002\)](#) and thus verify the present numerical model for convective heat transfer with moving immersed boundary.

8.4 Results and discussion

We demonstrate heat transfer enhancement via large-scale flow-induced deformation in the FSI benchmark proposed by [Turek and Hron \(2006\)](#). The flow boundary conditions and relevant parameters of the benchmark are discussed in Section 8.3.1. The thermal boundary conditions and associated simulation parameters are described as follows. At the inlet and channel walls, Dirichlet boundary condition for the temperature, $T_0 = 0$ and $T_w = 1$, are applied, respectively. Zero Neumann boundary condition is applied for temperature at the channel outlet and the fluidstructure interface. The temperature is zero initially in a $4.1D \times 41D$ channel and Prandtl number is taken as 1 in the simulation.

We utilize a 384×160 non-uniform grid with $\Delta x_{min} = 0.0231$ and $\Delta y_{min} = 0.02$, and

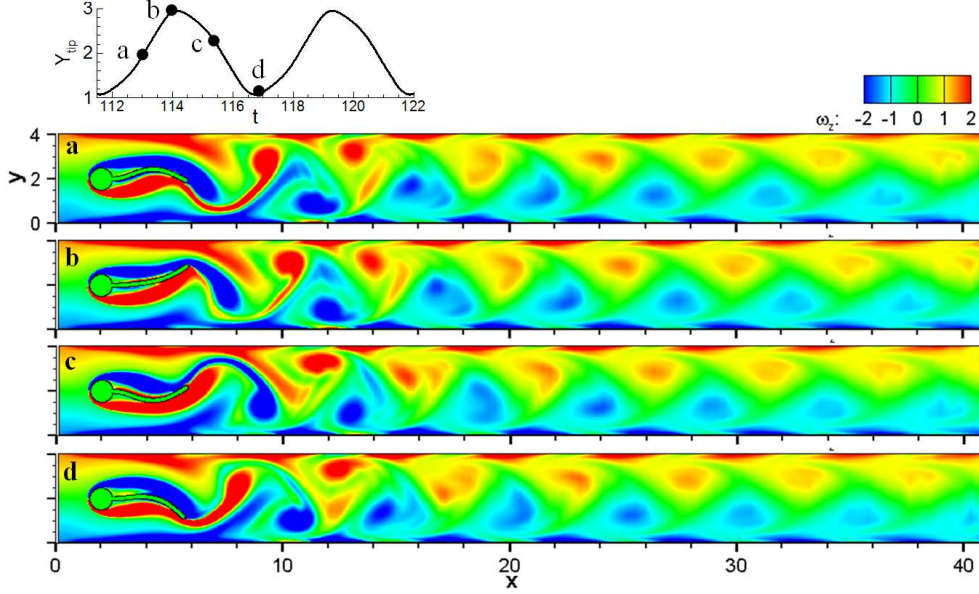


Figure 8.8: Vorticity contours in a channel with a cylinder attached to an elastic plate at different time instances for $Re = 100$. The time instances are shown in the inset as black dots on time-varying position of the tip of the plate during a typical cycle of the plate oscillation.

$\Delta t = 0.01$. The grid convergence study was performed in Ref. (Bhardwaj and Mittal, 2012) for the FSI benchmark, and 256×128 grid was deemed adequate for resolving the flow field coupled with the structure dynamics. In the present work, in order to resolve the thermal field in the downstream of the channel, we perform the grid convergence study for three grids keeping the grid resolution near the cylinder and plate same as those in Ref. (Bhardwaj and Mittal, 2012) and add more grid points in the downstream. Four different grids: 256×128 (baseline), 320×160 (fine), 384×160 (finer) and 512×160 (finest) are selected, and differences in the amplitude (frequency) of the plate obtained using the fine grid with respect to baseline grid, finer grid with respect to fine grid and the finest grid with respect to the finer grid are 2.2% (2.6%), 0.0% (0.0%) and 0.0% (0.0%), respectively. Similarly, the respective differences in the mean Nusselt number, (eq. 8.11), are 4.8%, 4.3% and 2%, respectively. Since deviations in the results obtained using the finer grid are small, we employ the finer grid (384×160) in all simulations presented in this work.

8.4.1 Enhanced mixing of the fluid due to FSI

The vorticity contours are plotted in fig. 8.8 after the flow field reaches time-periodic state. The four plots (a)(d) in fig. 8.8 correspond to four time instances in a typical cycle of the oscillation of the plate, as shown by the black dots in inset of fig. 8.8. As shown in fig. 8.8a and b, the fluid accelerates near the cylinder in lower half of the channel due to

partial blockage by the plate in upper half. The clockwise (fig. 8.8b) and counter-clockwise (fig. 8.8d) vortices generated due to the motion of the plate interact with the bottom and top channel wall, respectively. The flow induces a wave-like deformation in the plate and the plate attains self-sustained periodic oscillation with plateau amplitude after a short time (Bhardwaj and Mittal, 2012). The vorticity generated on the cylinder surface is almost annihilated by the wall vorticity from the wall closest to it, as evidenced by the residual vorticity footprint downstream. The cross-annihilation of vorticity of a particular sign with the vorticity of opposite sign generated on the cylinder or wall surfaces, results in descending strength of the vortices as they advect along the channel length. Thus, the wake vortices sweep the higher sources of vorticity generated on the channel walls out into the high velocity regions which aids in the mixing of the fluid in the bulk as well as near the channel walls.

8.4.2 Thermal augmentation due to FSI

The isotherms and instantaneous Nusselt numbers at the channel walls are plotted in fig. 8.9 and 8.10, respectively, after the flow as well as temperature field reach the time-periodic state. The four plots (a)-(d) in fig. 8.9 and 8.10 corresponds to four time instances of the oscillation (black dots in inset of fig. 8.8). The isotherms in fig. 8.9 qualitatively indicate reduction in thermal boundary layer thickness at the locations of the convected vortices described in Section 8.4.1. In order to confirm this trend quantitatively, we plot temperature profile at the four instances at $x = 8$ and 27 in fig. 8.11. The change in temperature gradient at the walls at these instances confirms the effect of the convected vortices. The enhanced mixing of the fluid described in Section 8.4.1 assists in augmenting convection in the bulk as well as near the channel walls. The peaks of the instantaneous Nusselt numbers at the channel walls ($x \lesssim 8$) in fig. 8.10 are signature of the reduction in the thermal boundary layer thickness due to the convected vortices. The height of the local peaks decrease due to decrease in strength of the vortices along the channel length as described in Section 8.4.1. The influence of decreasing strength of vortices can be seen through temperature profiles plotted at $x = 8$ and 27 in fig. 8.11a and b, respectively. The temperature gradients at the walls are larger at $x = 8$ as compared to those at $x = 27$, which implies larger Nusselt numbers at the former location. Overall, the vortices increase mixing in the channel as hot fluid near the channel walls moves towards the center of the channel and get replenished by relatively colder fluid. The interaction of the vortices with the channel wall helps in reducing thermal boundary layer thickness.

The local fluid acceleration caused by the presence of cylinder also aids in improving heat transfer, however, this effect is regional. Due to upward motion of the plate (fig. 8.8a and b), the fluid rushes through the lower half of the channel resulting in the fluid acceleration near the cylinder region, which reduces the thermal boundary layer thickness

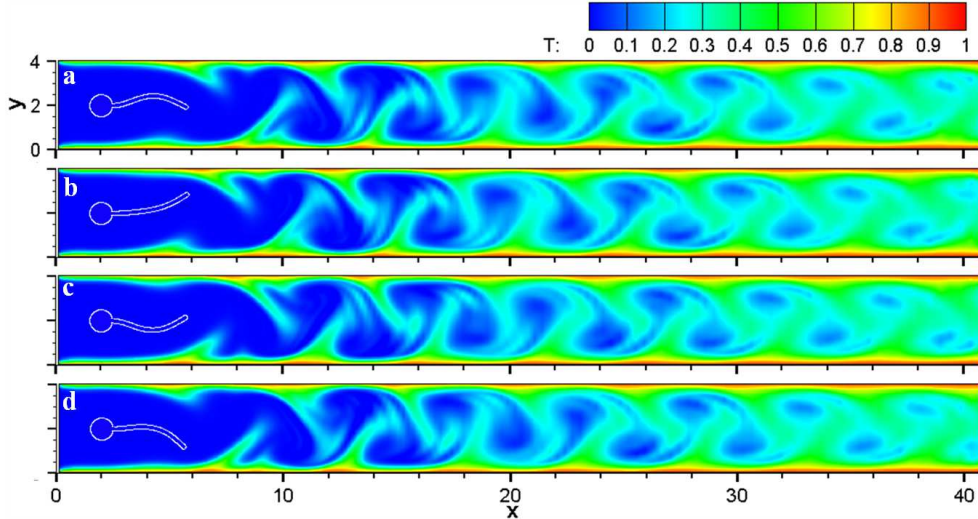


Figure 8.9: Isotherms in a channel with a cylinder attached to an elastic plate at different time instances for $Re = 100$ and $Pr = 1$. The time instances are shown in the inset of fig. 8.8 as black dots on time-varying position of the tip of the plate during a typical cycle of the plate oscillation.

(fig. 8.9b, at $x \approx 6$) and improves the Nusselt number (Nu_{bw}) regionally at the bottom wall (fig. 8.10b, at $x \approx 6$). Similarly, downward motion of the plate (fig. 8.8b-d) improves the Nusselt number (Nu_{tw}) regionally at the top wall (fig. 8.10d, at $x \approx 6$). The peaks at $x \approx 2$ for the top as well as bottom wall are caused by the accelerating fluid due to blockage by the cylinder (fig. 8.10a-d).

8.4.3 Quantification of augmentation in heat transfer

In order to quantify the heat transfer enhancement achieved in the case described in Section 8.4.2 - the flow past rigid cylinder attached with deformable plate in a heated channel (referred as CDP hereafter) - we performed simulations for three additional configurations listed in Table 8.1. These cases correspond to a channel flow without bluff body (CHL), channel flow past a rigid cylinder (CYL) and channel flow past a rigid cylinder attached with rigid plate (CRP), with same simulation parameters as those used in CDP. The vorticity contours and isotherms for all configurations at $t = 80$ are plotted in figs. 8.12 and 8.13, respectively. We note that the vortices are present in CYL and CDP (fig. 8.12b and d, respectively) and strength of the vortices decreases in stream-wise direction. However the vortices are stronger, closer to the walls and convect much further in the downstream in CDP as compared to those in CYL. The flow is steady in CHL and the rigid plate inhibits flow-instabilities to suppress the vortex shedding in CRP. As illustrated by isotherms in CYL and CDP in fig. 8.13b and d, respectively, interaction of the vortices with the channel wall helps in reducing the thermal boundary layer and thereby augmenting heat transfer. In order to quantify the augmentation, we plot stream-

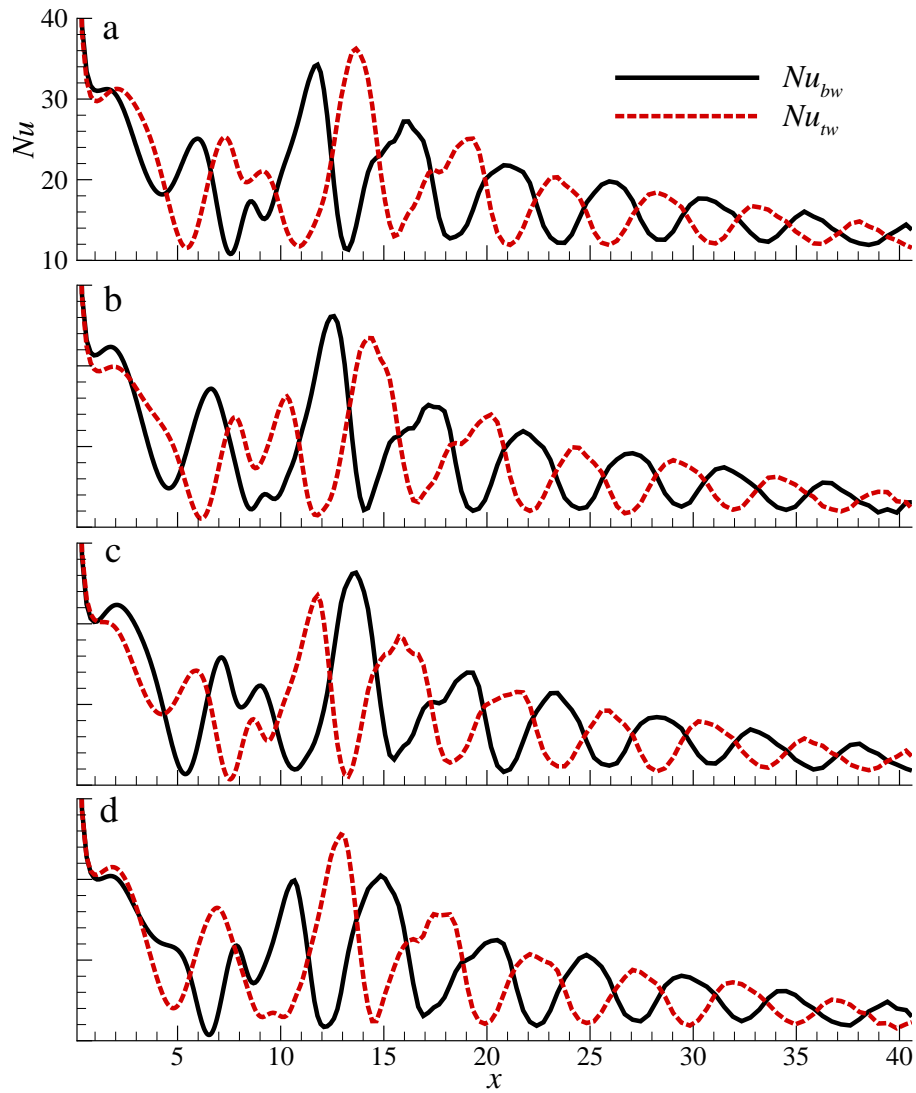


Figure 8.10: Instantaneous Nusselt numbers at the bottom ($Nu_{bw}(x, t)$) and top ($Nu_{tw}(x, t)$) channel walls at different time instances, $Re = 100$, $Pr = 1$. The time instances are shown in the inset of fig. 8.8 as black dots on time-varying position of the tip of the plate during a typical cycle of the plate oscillation.

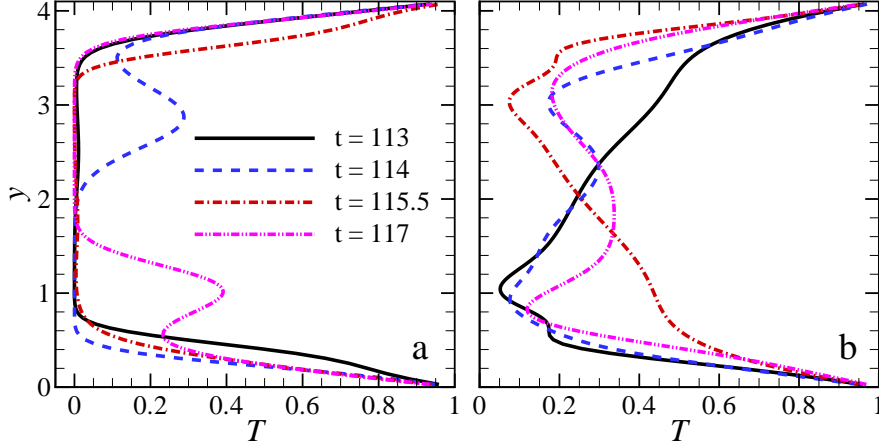


Figure 8.11: Variation of temperature in a channel with a cylinder attached to an elastic plate along y -axis at (a) $x = 8$ and (b) $x = 27$ for $Re = 100$, $Pr = 1$. The time instances are shown in the inset of fig. 8.8 as black dots on time-varying position of the tip of the plate during a typical cycle of the plate oscillation.

wise variation of time-averaged Nusselt number (Nu_{avg} , eq. 8.10) for the above cases in fig. 8.14. We note that the Nu_{avg} decreases monotonically along the channel for CHL case while a local peak occurs at the location of the cylinder ($x \approx 2$) in rest of other cases. The local peaks occur due to partial blockage of the flow by the cylinder, as explained in Section 8.4.2. The vortex shedding in CYL helps in improving the Nusselt number at all stream-wise locations and Nu_{avg} improves by 18% at $x \approx 40$, as compared to that in CHL and CRP. The results indicate significant increase in Nu_{avg} in CDP due to the enhanced convection as explained in Sections 8.4.1 and 8.4.2. With respect to CHL, the maximum enhancement is around 137% at $x \approx 10.6$ and 57% at channel outlet ($x \approx 40$). The regional thermal improvement, for instance at $x \approx 10.6$, implies that large-scale deformation could be leveraged to cool spatially-varying peak thermal loading on a surface, for instance, hotspots on electronic chips (Hamann et al., 2007). The time- and space-averaged Nusselt number (Nu_{mean} , eq. 8.11) for all four configurations is compared using bar charts in fig. 8.15a (first set of red bars) and Nusselt number is 69%, 41% and 54% larger in CDP as compared to that in CHL, CYL and CRP, respectively. We note that the augmentation in CDP is the largest; however, power required in pumping the fluid may be different in these cases. We define dimensionless pumping power (P) required to maintain a given flow rate Q in a channel of width H , as follows,

$$P = Q \left[\int_0^H p_{inlet}(y) dy - \int_0^H p_{outlet}(y) dy \right], \quad (8.13)$$

where p_{inlet} and p_{outlet} are pressures per unit span wise length across the channel inlet and outlet, respectively. The flow rate Q per unit span wise length is same in all cases and

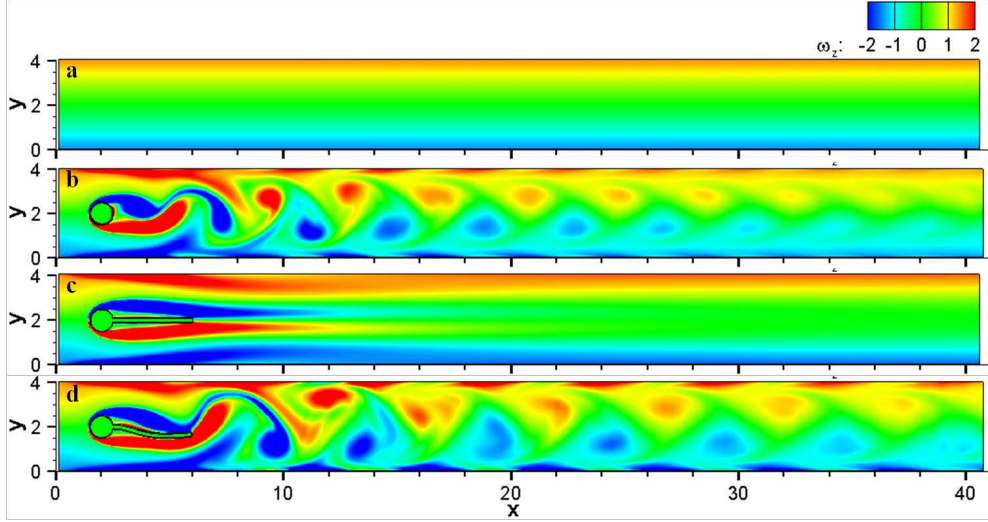


Figure 8.12: Vorticity contours obtained at $t = 80$, for configurations CHL, CYL, CRP and CDP, defined in table 8.1 at $Re = 100$.

defined as,

$$Q = \int_0^H u(y)dy, \quad (8.14)$$

In time-periodic flows, the average pumping power (P_{avg}) is time-average of the instantaneous pumping power over a period of oscillation. The dimensionless pumping power required in different cases is plotted in fig. 8.15b (first set of red bars), which shows that the thermal enhancements in CYL, CRP and CDP are achieved at expense of more energy required in pumping of the fluid in the channel. It is worthwhile to compare the effectiveness of CYL, CRP and CDP with respect to CHL and we use the following metric for the comparison among these configurations. We define efficiency index (η) (Yang, 2003),

$$\eta = \frac{\eta_h}{\eta_f}, \quad (8.15)$$

where η_h and η_f are enhancement factors for the heat transfer and pumping power, respectively, defined as follows (Yang, 2003),

$$\eta_h = \frac{Nu_{mean}}{Nu_{mean} \text{ for channel}}, \quad (8.16)$$

$$\eta_f = \frac{P_{avg}}{P_{avg} \text{ for channel}}, \quad (8.17)$$

We plot the efficiency indices for CYL, CRP and CDP in fig. 8.15c (first set of red bars), which shows that CDP is 10% and 6% more efficient than CYL and CRP, respectively. Therefore, large-scale flow-induced deformation helps in the thermal augmentation as compared to a case in which a rigid bluff body is employed as vortex generator.

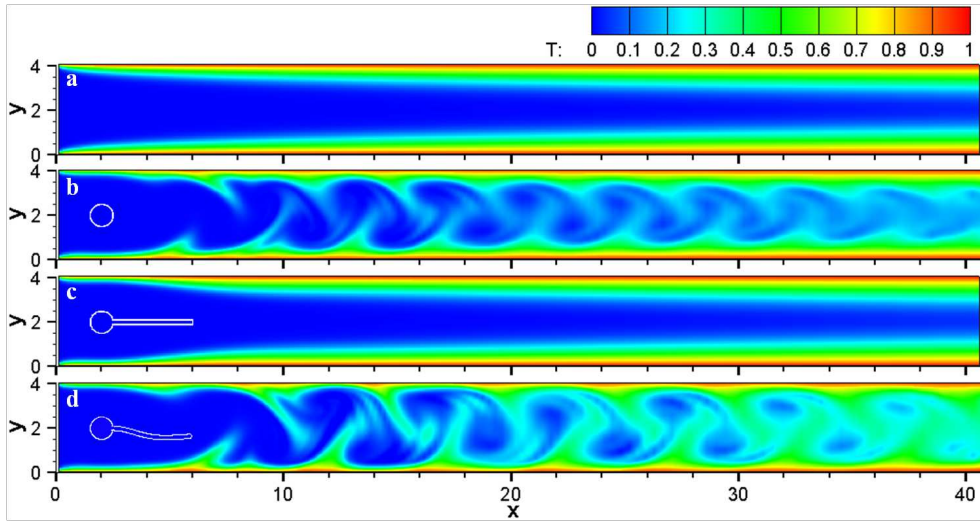


Figure 8.13: Isotherms obtained at $t = 80$, for configurations CHL, CYL, CRP and CDP, defined in table 8.1 at $Re = 100$, and $Pr = 1$.

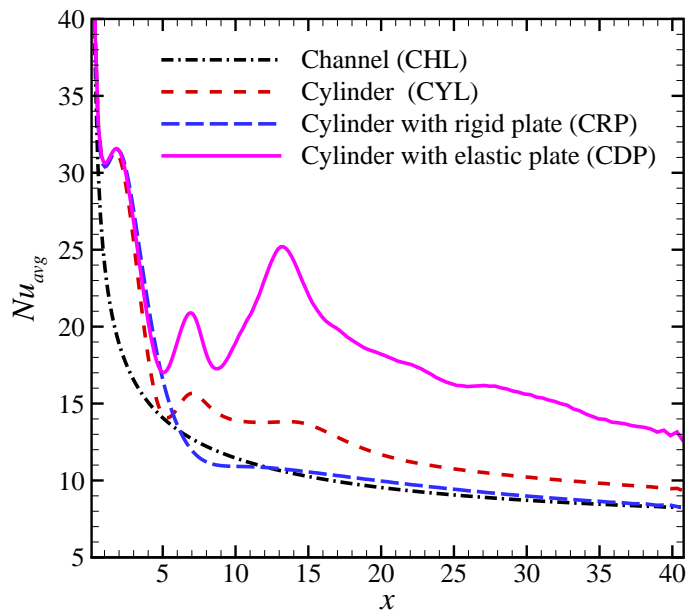


Figure 8.14: Time-averaged Nusselt number (Nu_{avg}) for $Re = 100$ and $Pr = 1$, for configurations CHL, CYL, CRP and CDP, defined in table 8.1.

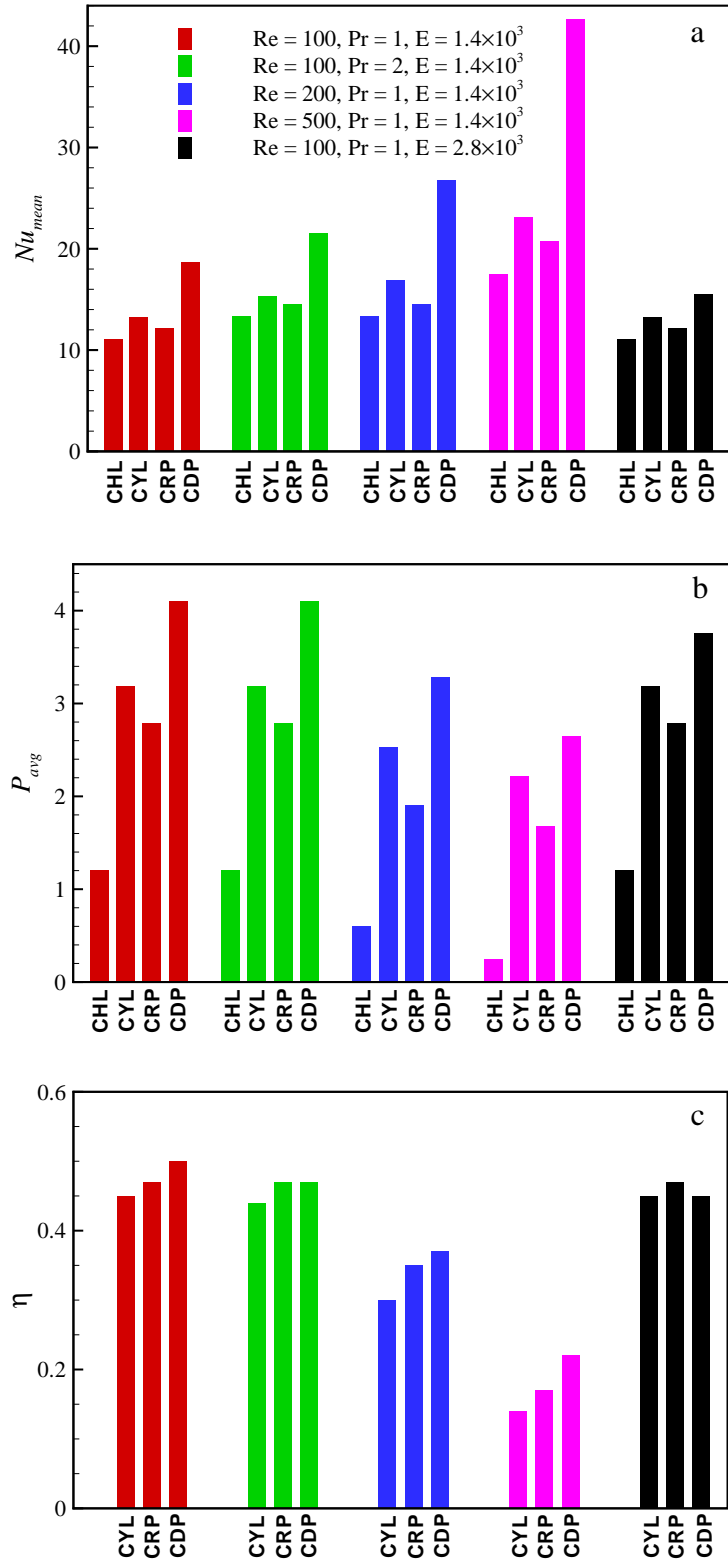


Figure 8.15: (a) Time- and space-average Nusselt number, (b) Time-average pumping power, and (c) efficiency index for configurations CHL, CYL, CRP and CDP, defined in table 8.1. The Reynolds number, Prandtl number and Young Modulus of the plate are varied in separate cases keeping other two parameters as constant.

8.4.4 Effect of Prandtl number

In this and the following sections, we perform additional simulations to assess the influence on Prandtl number (Pr), Reynolds number (Re), Youngs modulus (E) and channel length. In order to assess the effect of Pr , we increase it to $Pr = 2$, in CHL, CYL, CRP and CDP keeping all other parameters same. Nu_{mean} , P_{avg} and η for these four simulations are plotted using second set of green bars in fig. 8.15a-c, respectively. At $Pr = 2$, the Nu_{mean} increases in all configurations as compared to the respective baseline cases (first set of red bars vs. second set of respective green bars in fig. 8.15a) due to decrease in thermal boundary layer thickness at larger Prandtl number (Bejan, 2004). However, pumping power is same as compared to the respective baseline cases and the improvement in η in CDP ($Pr = 2$) is 6% as compared to CYL ($Pr = 2$), which is lower than that in the baseline case (10%, first set of red bars in fig. 8.15a). Therefore, larger Prandtl number assists in achieving the enhancement, however, it is less efficient than the baseline case (CDP, $Pr = 1$).

8.4.5 Effect of Reynolds number

The effect of Reynolds number is studied by increasing it to $Re = 200$ and 500 in CHL, CYL, CRP and CDP keeping all other parameters same. Nu_{mean} , P_{avg} and η for these eight simulations are plotted in fig. 8.15a-c, respectively. Third set of blue bars and fourth set of magenta bar show results for $Re = 200$ and 500 , respectively. At $Re = 200$, Nu_{mean} improves due to larger convection, pumping power reduces due to smaller pressure drop needed at larger Re , however, the efficiency index decreases for all configurations (compare first set of red bars vs. third set of respective blue bars in fig. 8.15a-c, respectively). Note that η decreases because relative to CHL case the increase in Nu_{mean} for other cases is not in proportion to the decrease in P_{avg} . In particular, vortex shedding (not shown here) occurs behind the tip of the rigid plate in CRP case as compared to that in baseline CRP ($Re = 100$). The efficiency index in the CDP is around 23% more compared to CYL ($\eta = 0.30$ to 0.37) for $Re = 200$, which is larger than the baseline case (10%, $\eta = 0.45$ to 0.50). We see similar trends for $Re = 500$ with forth set of magenta bars in fig. 8.15. Larger thermal enhancement is achieved with lower pumping power at $Re = 500$ as compared to $Re = 200$. Nu_{mean} increases by around 59% and η decreases by 40% for the former as compared to the latter in the CDP case. Overall, larger Reynolds number helps in achieving larger thermal augmentation at lower pumping power, however, it is less efficient than the baseline case (CDP, $Re = 100$).

8.4.6 Effect of Youngs modulus

We increase Youngs modulus to $E = 2.8 \times 10^3$ in CDP and keep all other parameters same in CHL, CYL, CRP and CDP. Nu_{mean} , P_{avg} and η for these four simulations are plotted using fifth set of black bars in fig. 8.15a-c, respectively. Since Youngs modulus is associated with the deformation of the plate, the results in only CDP are influenced. Due to 17% reduction in the amplitude of the oscillating plate (Bhardwaj and Mittal, 2012), Nu_{mean} and P_{avg} decrease, which results in lower η . η in the CDP is same as that in CYL at $E = 2.8 \times 10^3$. Hence, larger Youngs modulus impedes the enhancement as well as costlier with respect to CHL. Overall, the Nusselt number ($Nu_{mean} = 42.7$) and efficiency index ($\eta = 0.5$) are the largest for CDP with $Re = 500$, $Pr = 1$, $E = 1.4 \times 10^3$ and CDP with $Re = 100$, $Pr = 1$, $E = 1.4 \times 10^3$, respectively for the simulations presented in fig. 8.15.

8.4.7 Effect of channel length

Finally, we examined effect of channel length by varying it to $L = 61$ in the baseline case (CDP, $L = 41$, $Re = 100$, $Pr = 1$, $E = 1.4 \times 10^3$, $Nu_{mean} = 18.71$). The mean Nusselt number decreases by 5.5% ($Nu_{mean} = 16.69$) for 49% longer channel ($L = 61$). Since strength of the vortices decrease as they convect in the downstream, the mean Nusselt number decreases marginally along the channel length. The pumping power increases by 47% in the latter case and the efficiency index is 0.49, same as in the baseline case. Note that the Nusselt number is dependent on the channel length and plateau Nusselt number for an infinitely long channel is 7.54 (Bejan, 2004).

8.5 Closure

We demonstrate effective thermal enhancement in a laminar, incompressible heated channel flow via large-scale flow-induced deformation of an elastic thin plate attached on lee side of a rigid cylinder. The in-house fluidstructure interaction (FSI) solver with convective heat transfer is based on a sharp-interface immersed boundary method. The flow solver is strongly-coupled with an open-source structure dynamics solver using partitioned approach. In the present work, several validations are carried out against benchmark examples of conduction and convective heat transfer including moving structure boundaries, in order to test the convective heat transfer module of the FSI solver. The mechanism to achieve thermal augmentation via large-scale flow-induced deformation is as follows. The wake vortices generated due to the self-sustained motion of the plate sweep higher sources of vorticity generated on the channel walls out into the high velocity regions which aids in the mixing of the fluid in the bulk as well as near the channel walls. Due to the enhanced

mixing, the hot fluid near the channel walls moves towards the center of the channel and get replenished by relatively colder fluid. The interaction of the vortices with the channel wall helps in reducing thermal boundary layer thickness and thereby increasing Nusselt number at the channel walls. The thermal improvement is quantified via testing of three additional configurations, namely, channel flow without bluff body; channel flow with a stationary and rigid cylinder; and channel flow with a stationary and rigid cylinder with a rigid plate attached on its lee side. Simulation results suggest that larger Prandtl number and Reynolds number promote the thermal enhancement, however, with lesser efficiency. On the other hand, larger Youngs modulus impedes the enhancement as well as requires larger pumping power. The numerical data presented will help to design better thermal augmentation systems involving large-scale flow-induced deformation of thin flexible structures. Overall, the large-scale flow-induced deformation harnesses available flow energy and does not require any external power sources to achieve the thermal augmentation. The large regional thermal improvements could be leveraged to cool non-uniform peak thermal loading on a surface.

Chapter 9

Convective Heat Transfer Augmentation by a Fin-like Thin, Elastic Plate in a Laminar Channel Flow

The flow-induced deformation of a thin, elastic plate is utilized to augment convective heat transfer in a pulsating channel flow. An in-house Fluid-structure Interaction (FSI) model is employed to solve the coupled fluid dynamics, heat transfer and structure dynamics. The FSI model utilizes a sharp-interface immersed-boundary method to solve flow as well as thermal field, and a finite-element method to solve structural dynamics. Numerical simulations show that a vortex forms due to the separating shear layers at the plate tip as the plate deforms, and the vortex interacts with the heated channel walls. The coupling of the vortex structure with the transient convective heat transfer and the non-linear dynamics of the plate is investigated. The heat transfer augmentation from the heated channel wall due to the associated vortex dynamics is quantified. Numerical results are quantified in terms of the plate displacement and the Nusselt number at the channel wall. The effects of plate rigidity, channel height, and Reynolds number on the effectiveness of the augmentation are investigated. We found that the rigid plate is more effective at a smaller channel height when compared to the elastic one and an optimal channel height exists to achieve the largest thermal augmentation in case of the elastic plate.

9.1 Introduction

The use of fins to improve heat transfer in engineering systems such as heat-sinks ([Akhilesh et al., 2005](#)), radiators, I.C. engines is very common. The present work examines improvements or changes in thermal augmentation, which are possible if a deformable, fin-like

structure instead of a rigid one is employed. In biology, employing flexible structures to improve heat transfer is common; for example, elephants thermoregulate their bodies by flapping their large ears (Weissenböck et al., 2010), and thermal transport enhancement by oscillating cilia (Mills et al., 2012). For such problems, the flow as well as the convective heat transfer is coupled with structural dynamics during large-scale, flow-induced deformation of the structure. The problem is computationally challenging and involves moving structure boundaries inside a fluid domain. The flow is highly unsteady with geometric and material non-linearity in the structure domain. The coupling of the governing equations of the fluid and structure domains brings additional complexity to the system of equations.

Previous numerical studies on the thermal augmentation either harnessed flow energy or utilized an external source of energy to augment the heat transfer, which are categorized as passive or active techniques (Webb and Kim, 2005; Bergles, 2011), respectively. In the former, bluff bodies such as a rectangular cylinder (Valencia, 1995), an inclined square cylinder (Yoon et al., 2009), a triangular cylinder (Chatterjee and Mondal, 2012), and wings (Hiravennavar et al., 2007) were used as vortex-generators to enhance the heat transfer. Similarly, conical inserts in a tube (Fan et al., 2011), and flow in wavy-wall channel (Wang and Chen, 2002; Ramgadia and Saha, 2012) were also utilized to improve the heat transfer. In the latter, oscillating bluff bodies inside the channel (Celik et al., 2010; Beskok et al., 2012) and the pulsating of a cross-flow fluid jet in a channel (Chandratilleke et al., 2010) were utilized as thermal augmentation techniques.

In the context of utilizing FSI for thermal augmentation, Fu and Yang (2001) showed that a swinging plate in a heated channel enhances heat transfer which scales with the plate amplitude. Similarly, previous studies have demonstrated that the oscillation of a plate improves heat transfer from a heat sink due to enhanced convective mixing (Dey and Chakraborty, 2009; Yu et al., 2013). Recently, Mills et al. (2012) considered an array of oscillating synthetic cilia to show heat transfer enhancement in microchannels; however, they did not consider flow-induced deformation of cilia in their model. Shoele and Mittal (2014) investigated the thermal enhancement that occurs due to the flow-induced fluttering motion of a flexible reed inside a heated channel; the reed had zero-thickness and was inextensible. Soti et al. (2015) demonstrated heat transfer enhancement through large-scale, flow-induced deformation in the FSI benchmark problem that was proposed by Turek and Hron (2006). In this benchmark, an elastic plate that is attached to the lee side of a rigid cylinder develops self-sustained oscillation in a two-dimensional (2D) laminar channel flow. In this study (Soti et al., 2015), the plate was aligned along the flow, and the cross-flow configuration was not considered for quantifying thermal augmentation. Ali et al. (2015) demonstrated heat transfer enhancement by installing deformable panels in a channel flow. As an extension of the work of Soti et al. (2015), Joshi et al. (2015)

recently investigated heat transfer augmentation by using twin deformable thin plates in a heated channel that had a laminar pulsating flow. However, the blockage caused by the twin plates in the channel resulted in a large pressure drop, thereby, reducing the effectiveness of the thermal augmentation.

In this work, a proof-of-concept investigation is performed by harnessing the energy of the existing flow field in order to assess the effectiveness of the thermal augmentation of a fin-like elastic plate in a cross-channel pulsating flow. The present work is built upon our previous works (Soti et al., 2015; Joshi et al., 2015). In the present work, we investigate the interaction of vortex dynamics with convective heat transfer during the deformation of the elastic plate in a pulsating channel flow. A state-of-the-art FSI solver (section 9.2) is employed to solve the governing equations for flow field, structural dynamics and temperature field. Numerical results that demonstrate thermal augmentation are discussed in section 9.5.

9.2 Computational model

An in-house FSI solver is employed for numerical simulation of the fluid flow, heat transfer, and structural dynamics of a thin, elastic plate that is placed in a laminar pulsating channel flow. The FSI solver was developed by Mittal and co-workers (Mittal et al., 2008; Zheng et al., 2010; Seo and Mittal, 2011b; Mittal et al., 2011), and capability to simulate the large-scale, flow-induced deformation was implemented and validated by Bhardwaj and Mittal (2012) against the FSI benchmark proposed by Turek and Hron (2006). Recently, the convective heat transfer module in the solver was validated by Soti et al. (2015) for the cases of moving immersed boundaries. The complete details of the method can be found in the previous papers (Soti et al., 2015; Mittal et al., 2008; Zheng et al., 2010; Seo and Mittal, 2011b; Mittal et al., 2011; Bhardwaj and Mittal, 2012); here, the methodology is described briefly. In this solver, a sharp-interface immersed-boundary method that is based on a multi-dimensional ghost-cell methodology (Mittal et al., 2008) is utilized; the immersed structure boundary is represented by using unstructured triangular elements grids. The flow and thermal field is solved on a stationary Cartesian grid, while the motion of the immersed structure surfaces is captured by using interface tracking.

In the flow solver, the unsteady, viscous, and incompressible Navier-Stokes equations are discretized in space by using a cell-centered, collocated arrangement that is based on primitive variables; velocity components and pressure. All spatial derivatives are discretized using a second-order central-difference scheme. The unsteady Navier-Stokes equation is marched in time using a two-step fractional-step scheme (Mittal et al., 2008; Chorin, 1968b). During the first step, the momentum equations are solved using the Crank-Nicolson scheme for both the convective and viscous terms for better numerical

stability. The pressure Poisson equation is solved in the second step with the constraint of a divergence-free final velocity. A fast geometric multigrid solver (Press et al., 1992) is used to solve the pressure Poisson equation. The velocity field is updated in the final sub-step with the pressure obtained from the solution of the pressure Poisson equation.

An open source finite-element solver, [Tahoe](#)[©], is employed to solve the structural dynamics and is implicitly coupled with the flow solver by using a partitioned approach. The implicit coupling ensures numerical stability for low structure-fluid density ratios (Zheng et al., 2010). No slip and balance of forces are applied at the fluid-structure interface as boundary conditions. The implementation details of the implicit coupling can be found in Bhardwaj and Mittal (2012). The convective heat transfer is governed by the energy equation (Soti et al., 2015). The fluid-structure interface is considered to be insulated, and the channel walls are kept at a constant temperature. Zero Neumann temperature boundary conditions are applied at the channel outlet.

The heat transfer enhancement is quantified using the instantaneous Nusselt number given in eq. 8.8 with the definition of bulk mean temperature modified to (Guo and Sung, 1997)

$$T_m(x, t) = \frac{\int_0^H |u|T dy}{\int_0^H |u| dy}, \quad (9.1)$$

The rest of the parameters such as pinging power (Q), efficiency (η) etc. are same as defined in chapter 8.

9.3 Simulation Setup

The computational domain along with the applied boundary conditions is shown in fig. 9.1. An elastic plate of height h and thickness $0.1h$ is mounted normal to the bottom wall of the channel. The plate is kept at a distance of $4h$ from the inlet. The channel length, L , is taken to be $12h$, based on a domain length independence study presented in the section 9.4. A fully developed, parabolic, pulsating velocity profile is applied at the channel inlet

$$u(y, t) = 2U \frac{y(H-y)}{H^2} \{1 - \cos(2\pi ft)\}, \quad (9.2)$$

where U is the maximum flow velocity at the center of the channel. The plate height (h) and the maximum velocity (U) are taken as the reference length and reference velocity for the non-dimensionalization, respectively. The fluid is considered to be Newtonian and incompressible, whereas, the plate is assumed to consist of St. Venant Kirchhoff material. The frequency of pulsation is taken to be $f = 0.1$ in all simulations. The non-dimensional values of $T_0 = 0$ and $T_w = 1$ are prescribed for the temperature at the channel inlet and walls, respectively. A zero Neumann boundary condition is applied at the channel

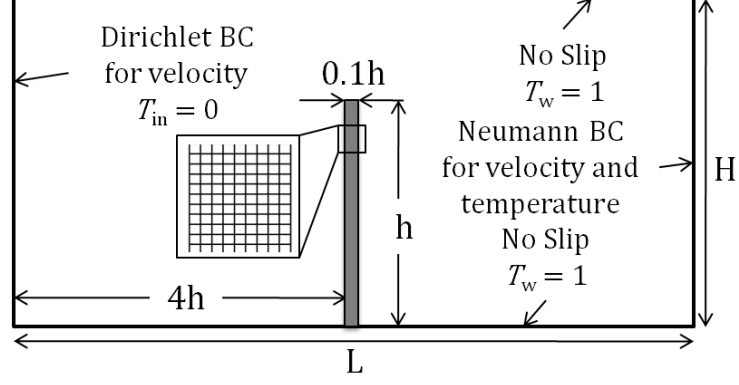


Figure 9.1: Computational domain and boundary conditions.

outlet for the velocity as well as for the temperature. The Prandtl number, dimensionless Young's modulus, Poisson ratio, and structure-fluid density ratio are considered to be 1, 1.0×10^3 , 0.45 and 10, respectively, which is in line with previous related studies (Turek and Hron, 2006; Bhardwaj and Mittal, 2012).

9.4 Domain and Grid Size Independence Study

The domain length independence study is performed on the largest channel height of $H = 8$. We consider three channel lengths $L = 12, 16$ and 20 , with the same grid resolution near the plate in all cases. The mean Nusselt numbers (Nu_{mean}) integrated over $x = 0-12$ for one pulsation cycle in these cases are 22.07, 22.40 and 22.47, respectively. The maximum difference is less than 2%, and, hence, we choose a channel length of $L = 12$ for our simulations in order to reduce computational cost. The left column of fig. 9.2 shows the effect of domain length on the time-varying x and y displacement of the tip of the plate over a flow oscillation cycle. The following three grids were considered for the grid independence study: (a) 256×160 , (b) 384×192 , and (c) 512×256 . The minimum mesh cell sizes for grids (a), (b), and (c) are $\Delta x = \Delta y = 0.01$, $\Delta x = \Delta y = 0.078$ and $\Delta x = \Delta y = 0.005$, respectively. The mean Nusselt numbers for grids (a), (b), and (c) were 22.09, 22.03 and 22.07, respectively. The maximum difference is less than 0.3%. For the widest domain simulations, the 384×192 mesh was employed. The right column of fig. 9.2 shows the effect of grid resolution on the time-varying x and y displacement of the tip of the plate over a flow oscillation cycle.

9.5 Results and Discussion

The thermal augmentation by flow-induced deformation is demonstrated for a thin, elastic plate in a laminar pulsating channel flow by using 2D numerical simulations. The aug-

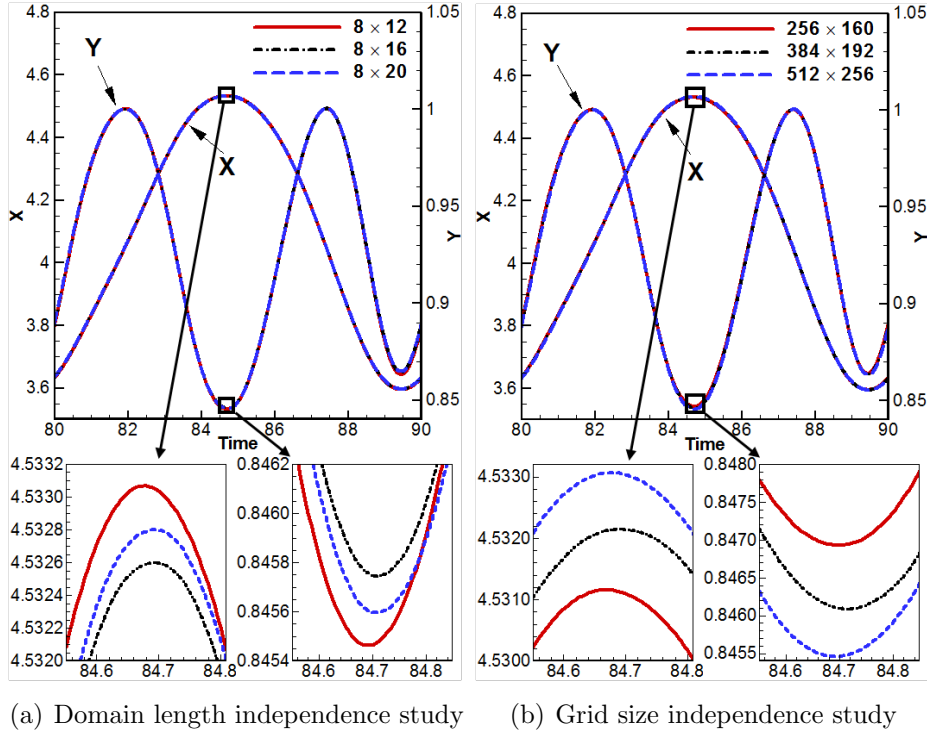


Figure 9.2: (a) Domain length independence and (b) Grid size independence study: Time variation of x and y coordinates of tip of the plate is plotted for one cycle of pulsation for different channel lengths and grid resolutions.

mentation is discussed in a baseline case ($H = 3$ and $Re_H = 400$), and the effects of plate rigidity, channel height, and Reynolds number are studied by systematically varying the parameters in the baseline case. The following three configurations are considered in order to quantify the thermal augmentation: (a) pulsating channel flow without a bluff body (CHL); (b) pulsating channel flow with a rigid plate (CRP); and (c) pulsating channel flow with a deformable plate (CDP). The following metrics are used to quantify thermal augmentation: (a) Instantaneous Nusselt number ($Nu(x, t)$); (b) time-averaged Nusselt number (Nu_{avg}) in a pulsation cycle; and (c) time- and space-averaged Nusselt number (Nu_{mean}) in a pulsation cycle and over the channel wall. The pumping power required in different configurations is calculated, and an efficiency index is used in order to assess the effectiveness of the thermal augmentation.

9.5.1 Mechanism of Thermal Augmentation in a Baseline Case

In this section, a baseline case is considered for a channel of height $H = 3$, in order to examine in detail the thermal augmentation due to large-scale flow-induced deformation. A non-uniform Cartesian grid is used in the channel with 384 grid points along channel length ($\Delta x_{min} = \Delta y_{min} = 0.0078$). The grid size independence study is presented in section 9.4. The results of the baseline case are presented in terms of the position of the

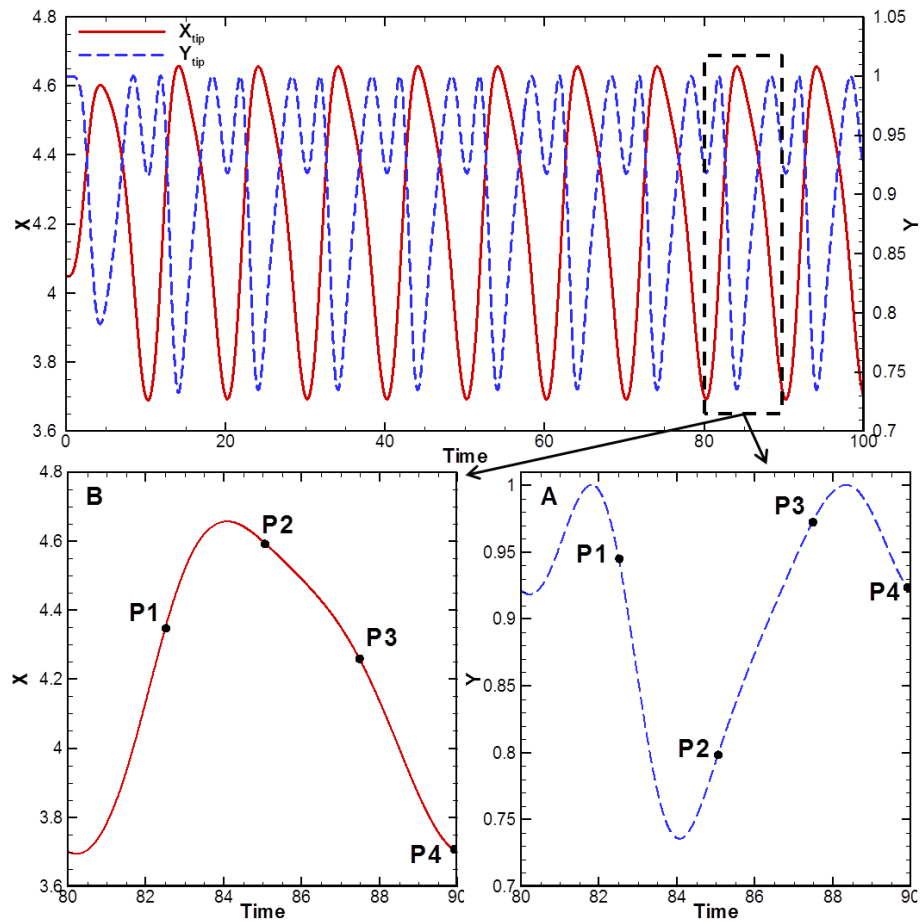


Figure 9.3: Time variation of x and y coordinates of the tip of the plate over a pulsation cycle for a channel height of $H = 3$ and $Re_H = 400$.

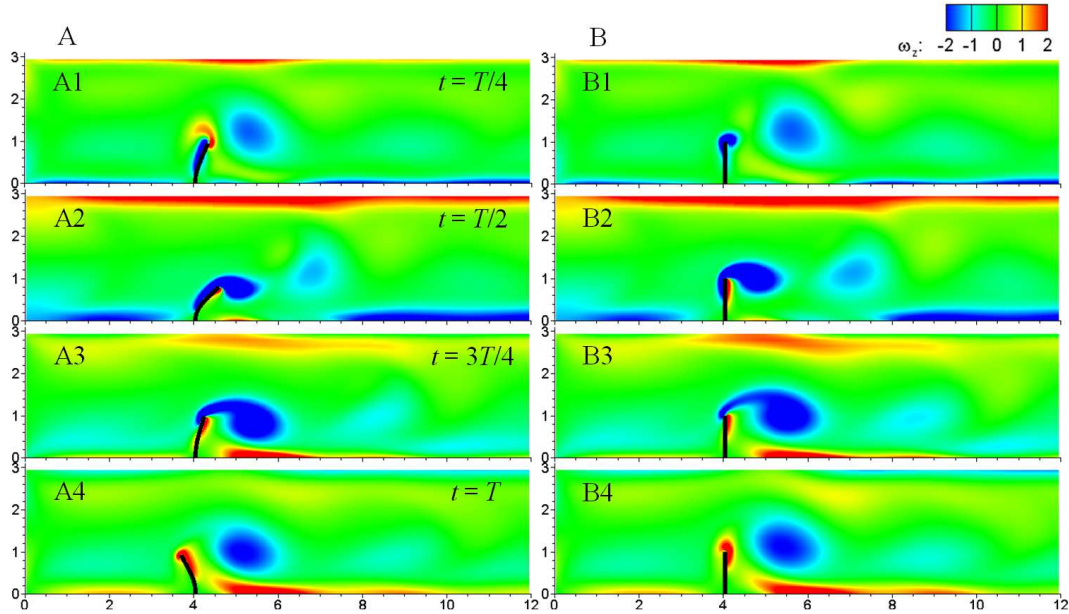


Figure 9.4: Vorticity contours for channel height $H = 3$ and $\text{Re}_H = 400$ with A) an elastic and B) a rigid plate. Plots are shown at four equispaced times (P1-P4 from fig. 9.3) over a pulsation cycle.

time-varying plate tip, vorticity contours, and isotherms. The time-dependent x and y coordinates of the tip of the plate, initially located at $(4.05h, h)$, are plotted in fig. 9.3 for a typical flow pulsation cycle. The pulsating flow sets the plate into a time-periodic motion. The centerline velocity increases from zero to its maximum value of U during the first half of the cycle, causing the plate to bend in the downstream direction of the channel, as plotted in the insets of fig. 9.3. The flow decelerates during the second half of the cycle and the plate returns toward its initial position. Note that the plate overshoots its initial position due to its inertia. The vorticity and temperature contours are plotted in fig. 9.4A and fig. 9.5A, respectively. The four frames correspond to instances at equal time intervals, shown in the insets of fig. 9.3 ($P1 = T/4$, $P2 = 2T/4$, $P3 = 3T/4$ and $P4 = T$) for a typical cycle of pulsating flow. The flow velocity magnitude increases over the range $0 < t < T/2$, where T is the time period of the pulsation, causing the plate to deform due to fluid dynamic forces. A vortex forms from the separating shear layer at the tip of the plate during this period. For $T/2 < t < T$, the flow velocity magnitude decreases and the plate moves backward toward its initial position. A vortex sheds within this interval from the tip of the plate, as shown in fig. 9.4 (A3-A4). The shed vortex influences heat transfer, shown by the isotherms in fig. 9.5A, and is quantified by the instantaneous Nusselt number (Nu). The position of the vortex corresponds to a thinner thermal boundary layer, implying larger Nu , plotted in fig. 9.6A at the corresponding instances at equal time intervals. The time-varying locations of the peaks of the Nusselt number in fig. 9.6A correspond to the time-varying position of the vortex.

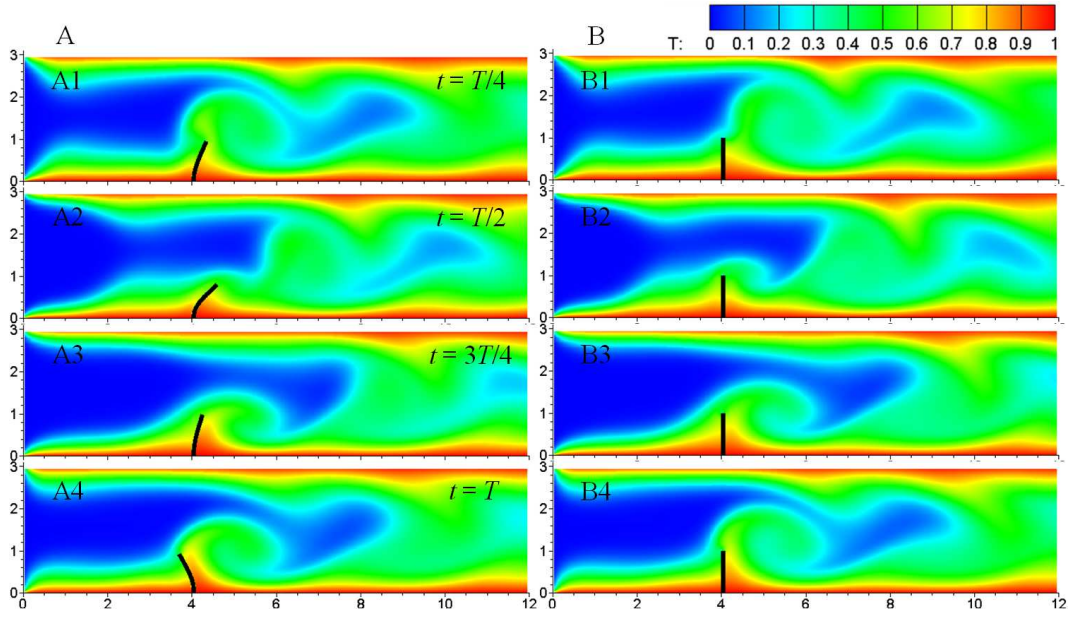


Figure 9.5: Temperature contours for channel height $H = 3$ and $Re_H = 400$ with A) an elastic and B) a rigid plate. Plots are shown at four equispaced times over a pulsation cycle.

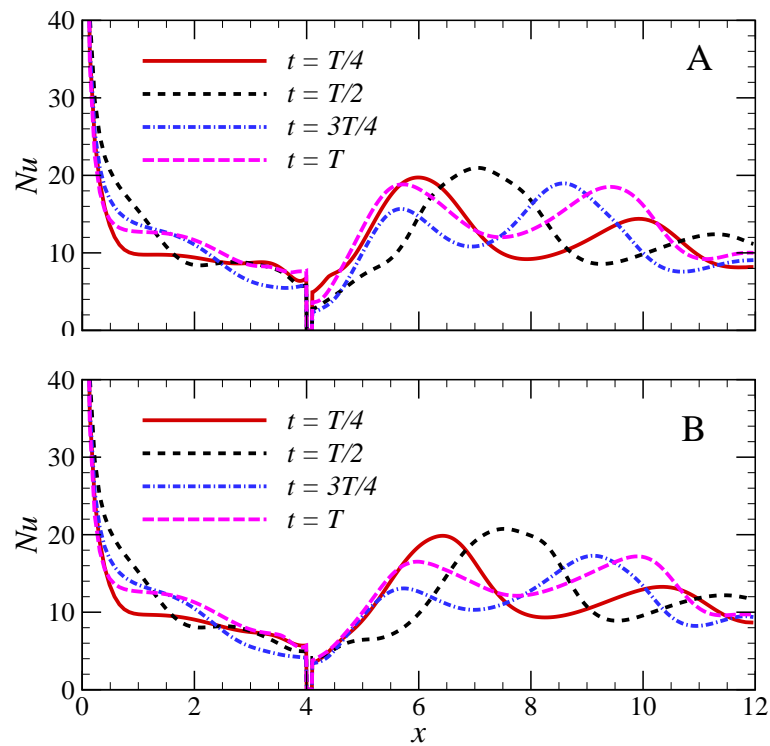


Figure 9.6: Instantaneous Nusselt number for channel height $H = 3$ and $Re_H = 400$ with A) an elastic and B) a rigid plate. Plots are shown at four equispaced times over a pulsation cycle.

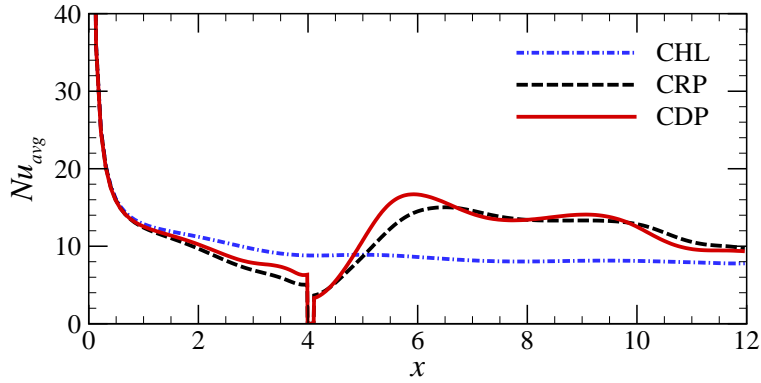


Figure 9.7: Time-averaged Nusselt numbers for channel height $H = 3$ at $Re_H = 400$. Three cases are compared: (a) pulsating channel flow without a bluff body (CHL); (b) pulsating channel flow with a rigid plate (CRP); and (c) pulsating channel flow with a deformable plate (CDP).

9.5.2 Effect of Plate Rigidity

In order to investigate the effect of plate rigidity, the simulations are repeated with a rigid plate but otherwise with the parameters as for the baseline case (section 9.5.1). The vorticity and temperature contours are shown at equal time intervals (shown in insets of fig. 9.3, $P1 = T/4$, $P2 = 2T/4$, $P3 = 3T/4$ and $P4 = T$) in fig. 9.4B and fig. 9.5B, respectively. As shown in fig. 9.4(B1-B4), a vortex sheds from the tip of the rigid plate, similar to the one described in section 9.5.1. However, a significant difference between the two cases is in the position of the vortex with respect to the channel wall. The vortex moves closer to the lower wall in the case of the elastic plate, due to plate deformation. The effect of the plate deformation on the heat transfer is qualitatively demonstrated by isotherms plotted in fig. 9.5A and fig. 9.5B for both cases. The instantaneous Nusselt numbers for the rigid plate are plotted in fig. 9.6B. At all instances, the Nusselt number is larger than for the rigid plate for $5 < x < 6.5$ than for the elastic plate. Also, the peaks in Nu are higher for the elastic plate when compared to the rigid one for $x > 8$. The time-averaged Nusselt number (Nu_{avg}) is compared in fig. 9.7 for three configurations: CHL, CRP, and CDP. The time-averaged Nusselt number in CDP is larger than that in CRP for $4.5 < x < 6$, which implies larger thermal enhancement near the bottom plate. The time- and space-averaged Nusselt numbers (Nu_{mean}) in the cases of CDP and CRP are 22% and 18% larger, respectively, than those in CHL.

9.5.3 Effect of Channel Height

The effect of the channel height (H) on thermal augmentation is studied by varying the height through the sequence $H = 2h, 3h, 6h$ and $8h$, while keeping the Reynolds number the same, that is, at $Re_H = 400$. For these domains with varying height, 160 and 192

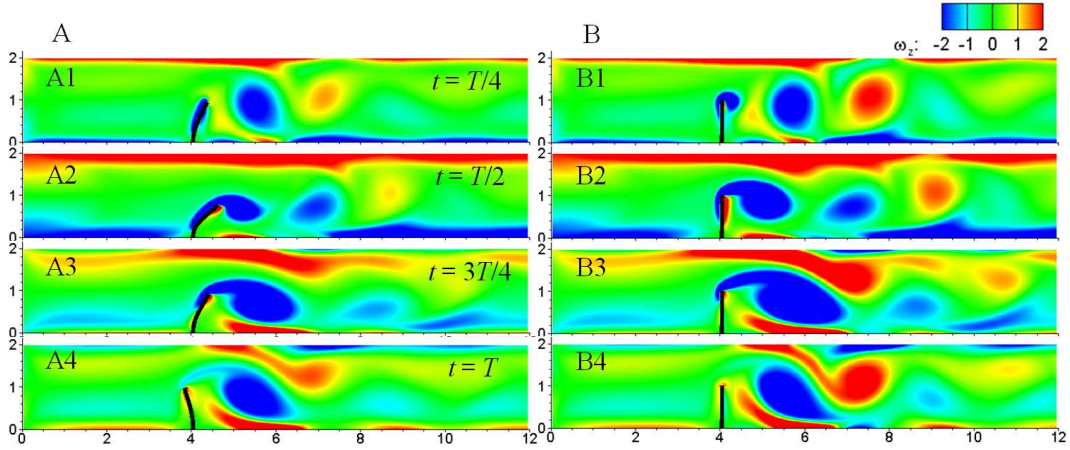


Figure 9.8: Vorticity contours for channel height $H = 2$ and $Re_H = 400$ with A) an elastic and B) a rigid plate. Plots are shown at four equispaced times over a pulsation cycle.

grid points are used along channel height for $H = 2h, 3h$, and $H = 6h, 8h$, respectively. The vorticity contours for the elastic and rigid plate cases, when the channel height is reduced to $H = 2h$, are plotted in fig. 9.8A and fig. 9.8B, respectively. A clockwise rotating vortex (blue contours in fig. 9.8) is shed from the tip of the plate in both cases, similar to the one reported for the baseline case in section 9.5.1. The vortex is more stretched in the streamwise direction in the case of the rigid plate when compared to the elastic plate. In contrast to the baseline case, strong counter-clockwise rotating vortices are present in both cases (red contours in fig. 9.8), which shed from the top channel wall. The vortices shed from the tip of the plate drift vorticity that is generated on the channel walls in the downstream, which enhances the fluid mixing. The mixing is larger in the case of the rigid plate, and is caused by its stronger wake vortices. The strength of these vortices is weaker in the case of the elastic plate because the bending of the plate reduces instantaneous blockage in the channel. The corresponding isotherms in fig. 9.9 show that a larger amount of cold fluid is directed toward the lower channel wall with the rigid plate, again due to the flow induced by the stronger vortex that is in closer proximity to the upper wall.

The instantaneous Nusselt number is plotted for the rigid and elastic plates at the four instances in fig. 9.10. The highest peaks in Nusselt numbers (Nu) at $t = T/4$ near $x = 6.5$ are caused by the clockwise rotating vortices being shed from the tips of the plates. The magnitude of this peak is higher for the rigid plate because of the larger vortex strength in that case. At $t = T/2$, the clockwise rotating vortex located near $x = 7.0$ is closer to the lower channel wall for the elastic plate than for the rigid plate (fig. 9.8(B1-B2)). This results in a larger peak value of Nu for the elastic plate at $t = T/2$. The peak values of Nu are higher for the rigid plate for the remaining two instances of $t = 3T/4$ and $t = T$, as shown in fig. 9.10A and B. Overall, the time-averaged Nusselt number (Nu_{avg}), plotted

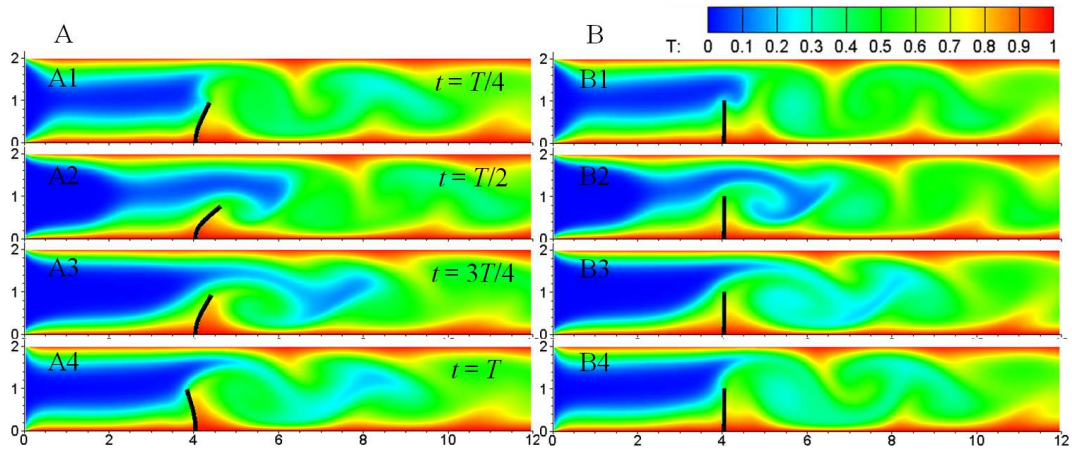


Figure 9.9: Temperature contours for channel height $H = 2$ and $Re_H = 400$ with A) an elastic and B) a rigid plate. Plots are shown at four equispaced times over a pulsation cycle.

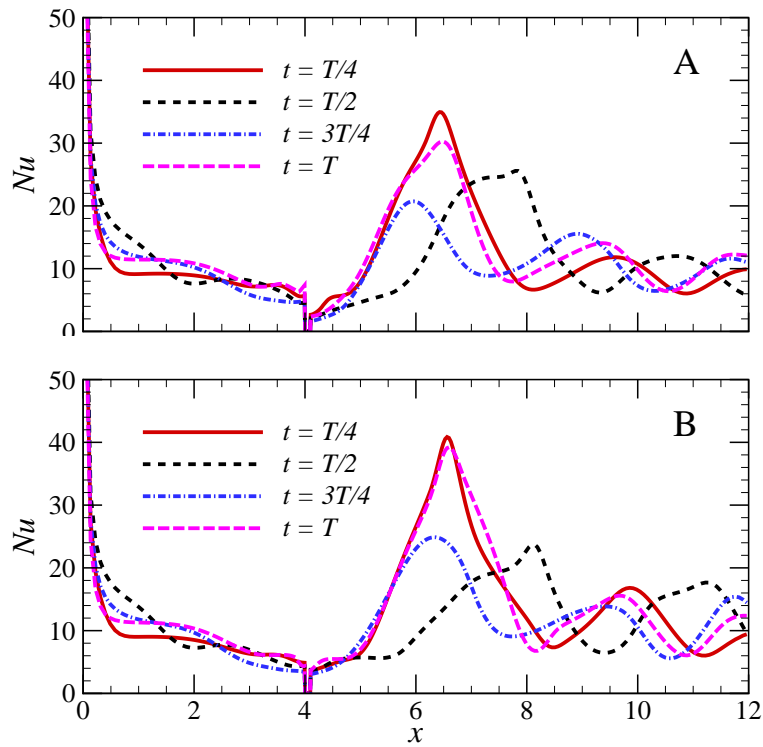


Figure 9.10: Instantaneous Nusselt number for channel height $H = 2$ and $Re_H = 400$ with A) an elastic and B) a rigid plate. Plots are shown at four equispaced times over a pulsation cycle.

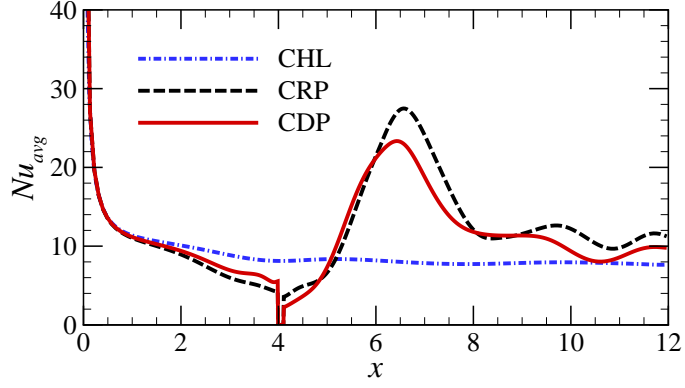


Figure 9.11: Time-averaged Nusselt numbers for channel height $H = 2$ at $\text{Re}_H = 400$. Three cases are compared: (a) pulsating channel flow without a bluff body (CHL); (b) pulsating channel flow with a rigid plate (CRP); and (c) pulsating channel flow with a deformable plate (CDP).

in fig. 9.11, is larger in CRP for $x > 6.2$ and is around 17% larger in CRP than CDP at $x \approx 6.5$.

The channel width is further varied to $H = 3h, 6h$, and $8h$, again keeping the Reynolds number constant at $\text{Re}_H = 400$ for different configurations CHL, CRP, and CDP-defined in section 9.5.2. An efficiency index is used to quantify the effectiveness of the thermal augmentation with respect to the channel flow (CHL), and is defined in chapter 8. The time and space-averaged Nusselt number (Nu_{mean}), the average pumping power (P_{avg}), and the efficiency index (η) are plotted in the top, middle, and bottom rows of fig. 9.12, respectively. CRP produces a larger Nu_{mean} for a channel height of $H = 2h$ when compared to CDP. As explained above, this is because of higher blockage in the channel, which creates a secondary vortex that directs fluid toward the lower channel wall. This brings the primary vortex closer to the lower wall and results in larger heat transfer enhancement. The elastic plate, on the other hand, deforms and reduces the blockage. A channel height, $H = 3$, results in a larger mean Nusselt number, lower pumping power and, thus, better efficiency in CDP. At $H = 8$, Nu_{mean} for CDP is marginally smaller than for CHL, however, it is still more efficient than for CRP. This is due to the smaller blockage that leads to the moving away of the vortices from bottom wall. In summary, these results indicate that an optimal channel height exists to achieve higher thermal augmentation by using a deformable plate rather than a rigid plate at a fixed Reynolds number.

9.5.4 Effect of Reynolds Number

The Reynolds number based on the channel height (Re_H) is varied to $\text{Re}_H = 400, 600$, and 1200 for all channel heights; three different configurations-CHL, CRP and CDP-

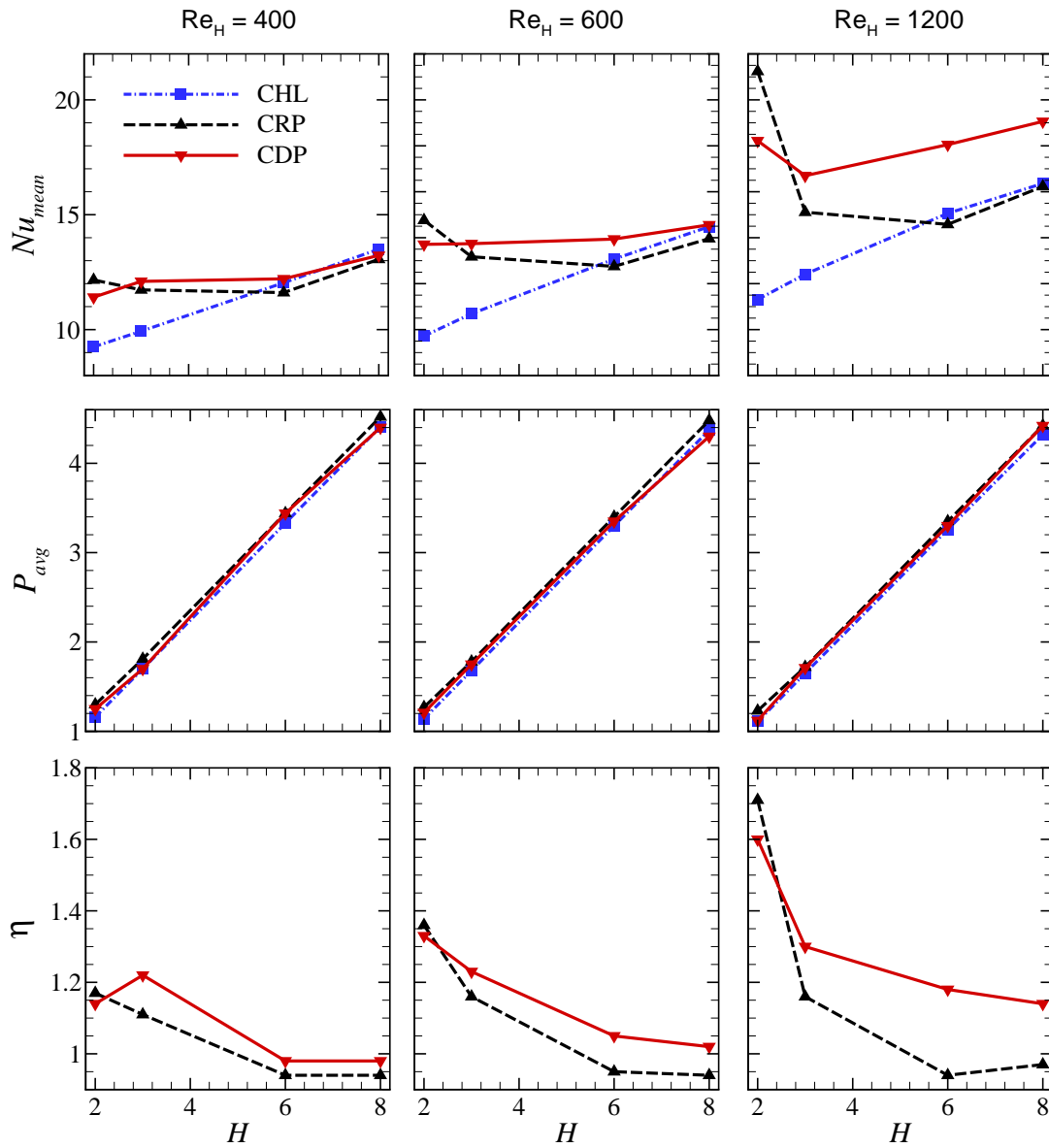


Figure 9.12: Variation of mean Nusselt number (top row), pumping power (middle row) and efficiency index (bottom row) with channel height. The data for three Reynolds numbers is plotted columnwise: $Re_H = 400$ (left column), 600 (middle column), 1200 (right column).

are considered. Other simulation parameters are maintained as described in section 9.3. Note that the maximum Reynolds number based on leaflet height (Re_h) and time-averaged centerline velocity ($U/2$) is lesser than or equal to 200 in all simulation cases, in order to avoid 3D effects. The mean Nusselt numbers, the average pumping power, and the efficiency index are plotted in the top, middle, and bottom rows of fig. 9.12, respectively, for different Re_H . The data for $Re_H = 400, 600,$ and 1200 are plotted in the left, middle, and right columns of fig. 9.12, respectively. At the lowest channel height ($H = 2$) for all cases of Re_H , CRP performs better in terms of the mean Nusselt number, which may be attributed to the vortex dynamics explained in section 9.5.3. The efficiency indices however become lesser than CDP at $Re_H \geq 600$. At $H \geq 3$, CDP performs the best for all Re_H in terms of the mean Nusselt number as well as the efficiency index.

9.6 Closure

The vortex dynamics and associated convective heat transfer augmentation by an elastic plate attached to a channel wall are investigated in a heated channel that has pulsating inlet velocity. The flow field, thermal field and plate dynamics are solved by an in-house FSI solver. The FSI solver couples a sharp-interface immersed-boundary method for flow simulation with a finite-elementbased structural dynamics solver. An implicit partitioned approach is utilized to ensure the numerical stability of the solver for low structure-fluid density ratios. We describe the vortex formation from the separating shear layer at the plate tip, which are created as the plate deforms during the inflow phase of the flow oscillation. The interaction of the vortex with the vorticity generated at the channel walls is described, including the induction of secondary separation. This leads to enhanced fluid mixing and convection in the bulk as well as at the walls, reduces the thermal boundary layer thickness, and enhances heat transfer at the channel walls, in particular. The time-varying instantaneous Nusselt number at the wall confirms the thermal augmentation. The effects of the plate rigidity, channel height, and Reynolds number on thermal augmentation are discussed. Our 2D numerical simulations show that an optimal channel height exists in order to achieve larger thermal augmentation with a deformable plate at a given Reynolds number; the efficiency of the thermal augmentation increases with the Reynolds number. The present results provide insights into the designing and utilizing of flexible plates that are potentially useful in dissipating large, non-uniform, and cyclic heat loads.

Chapter 10

Energy transfer to a flexible plate kept behind a circular cylinder

10.1 Introduction

In the present work we focus on the possibility of harnessing flow energy using a deformable plate kept downstream to a circular cylinder. This can be done by attaching a piezoelectric patch to the plate ([Akcabay and Young, 2012](#)). The patch can convert deformation of the plate into electrical energy. A rigid splitter plate was utilized in previous studies to reduce drag force on the cylinder. [Kwon and Choi \(1996\)](#) used a splitter plate attached to the cylinder. They numerically studied the effect of length of the splitter plate on drag reduction at Reynolds numbers in the range of 80-160. They found a critical length of the plate, which is proportional to the Reynolds number, beyond which the vortex shedding completely disappears. There was also an optimum length of the plate at which minimum drag on the cylinder occurred. This optimum length was equal to the size of the time-average separation bubble. [Hwang et al. \(2003\)](#) studied the effect of gap between the upstream end of the splitter plate and the lea side of the cylinder on drag reduction. The length of plate was taken equal to the cylinder diameter. They found an optimal gap for the maximum drag reduction. Their numerical results showed a monotonic decrease in the drag coefficient (C_D) and Strouhal number (St) when gap was increased from zero to an optimal value. There was a sudden increase in both C_D and St beyond this optimal value. The sudden increase in these values was associated to the sudden decrease in the size of the separation bubble. 14.7% reduction in drag was reported for $Re = 100$ when compared to the case of cylinder without the splitter plate. [Bao and Tao \(2013\)](#) used two short splitter plates of length $0.3D$ attached symmetrically on the rear side of the cylinder. They varied the attachment angle and found an optimal range for maximum drag reduction. They also noticed increased drag reduction due to increase in the length of the plates.

Some authors have also consider the possibility of harnessing energy from flow induced deformations of flexible structures. [Tang et al. \(2009\)](#) studied flutters of a flexible cantilever plate and concluded that some amount of work is done by the fluid on the plate. They proposed a design, which they called a flutter-mill, to convert this work done by the fluid into electrical energy. The fluid forces in their work were calculating using the unsteady lumped vortex model. [Michelin and Doaré \(2013\)](#) studied the efficiency of the electrical power generation due to flutter of a flexible flag attached with piezoelectric patches. They used a semi-analytical approach where the fluid forces were modelled assuming potential flow and Euler-Bernoulli model was used for the flag. A maximum 12% efficiency was reported for the largest mass ratio and flow velocity considered in their work. [Pan et al. \(2014\)](#) numerically studies the deformation behaviour of a flexible plate of fixed length kept behind a D-cylinder. The plate was modelled using the linear beam theory. The plate remained stationary for small distances between the plate and cylinder for the Reynold number less than 150. The oscillation amplitude of the plate was found to increase with the Reynolds number. They also calculated the kinetic and strain energy of the plate and found that more energy could be extracted when the plate is placed at a distance which does not affect the vortex shedding from the cylinder. One question that remains answered is: what is the optimal length of the plate which gives maximum energy extraction per unit length of the plate?

10.2 Problem Definition and methodology

We consider a plate of length L and thickness d that is kept at a distance G behind a cylinder of diameter D . The cylinder-plate system is kept in a free stream flow with velocity U . The Reynolds number is based on the cylinder diameter and free stream velocity, $Re = \rho_f U D / \mu$. The plate is assumed to be made of Saint Venant-Kirchhoff material. The problem is governed by the following parameters: Reynolds number, Young's modulus (E), bending stiffness (k), density ratio (ρ_s / ρ_f) and distance G of the plate from the cylinder.

The bending vibrations of the plate are described by the following equation

$$EI \frac{\partial^4 y}{\partial x^4} + \rho_s A \frac{\partial^2 y}{\partial t^2} = 0 \quad (10.1)$$

where E, I, ρ_s, A are the Young Modulus, second moment of area of the cross-section, density and cross section area of the plate. L is the length of the plate. The solution of eq. 10.1 can be written as a standing wave $y(x, t) = w(x)u(t)$. This leads to the following

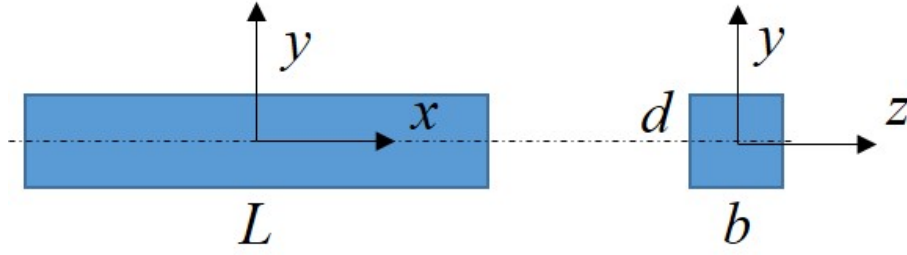


Figure 10.1: Dimensions of the plate.

characteristic equation that relates the circular frequency ω to the wave number λ

$$\omega^2 = \frac{EI}{\rho_s A} \lambda^4 \quad (10.2)$$

and the spatial variation is given by:

$$w(x) = C_1 \sin(\lambda x) + C_2 \cos(\lambda x) + C_3 \sinh(\lambda x) + C_4 \cosh(\lambda x) \quad (10.3)$$

The unknown coefficients can be found by applying appropriate boundary conditions(BC). If b and d represents the plate width and thickness, respectively then

$$I = \frac{bd^3}{12}, A = bd$$

therefore

$$\omega = \left(\sqrt{\frac{E}{12\rho_s}} \right) d\lambda^2 \quad (10.4)$$

Let us consider the case of a hinged plate. The boundary conditions are

$$w(0) = 0; w''(0) = 0; w''(L) = 0; w'''(L) = 0; \quad (10.5)$$

The first two conditions correspond to zero displacement and zero bending moment at the hinge point, respectively. The last two BCs correspond to zero moment and force at the free end, respectively. Applying eq. 10.5 to eq. 10.3 leads to the following set of equations

$$-C_1 \sin(\lambda L) + C_3 \sinh(\lambda L) = 0 \quad (10.6)$$

$$-C_1 \cos(\lambda L) + C_3 \cosh(\lambda L) = 0 \quad (10.7)$$

Table 10.1: Values of α_n for a hinged/fixed plate

n	α_n (hinged)	α_n (fixed)
1	3.93	1.88
2	7.07	4.69
3	10.21	7.86

Equations 10.6 and 10.7 have solutions only if determinant of the following matrix is zero

$$\begin{vmatrix} -\sin(\lambda L) & \sinh(\lambda L) \\ -\cos(\lambda L) & \cosh(\lambda L) \end{vmatrix} = 0 \quad (10.8)$$

which gives

$$\cos(\lambda L)\sinh(\lambda L) - \sin(\lambda L)\cosh(\lambda L) = 0 \quad (10.9)$$

Equation 10.9 has infinite solutions which can be written as $\lambda_n L = \alpha_n$. The values of α_n are given in table 10.1. Hence the natural frequencies ($f = \omega/2\pi$) of the plate are given by

$$f_n = \frac{\alpha_n^2 d}{2\pi L^2} \sqrt{\frac{E}{12\rho_s}} \quad (10.10)$$

If we compare eq. 10.10 with the expression $f = (\alpha_n^2/2\pi)\sqrt{k/m}$ then the bending stiffness (per unit width) of the plate is given by

$$k = \frac{3EI}{L^3} = \frac{E}{4} \left(\frac{d}{L}\right)^3 \quad (10.11)$$

The expression of natural frequency in terms of bending stiffness is given by

$$f_n = \frac{\alpha_n^2}{2\pi} \sqrt{\frac{k}{3\rho_s d L}} \quad (10.12)$$

The computational domain, a rectangle of size $50D \times 40D$, is shown in fig. 10.2. The cylinder is kept at a distance $20D$ from the inlet and midway along the the vertical direction. The left boundary is specified with the free steam velocity U . Zero-Neumann boundary condition is applied for the fluid velocity at the right boundary. The top and bottom boundaries are supplied with zero shear boundary condition. No-slip boundary condition is applied at the cylinder and plate surfaces. Zero-Neumann boundary condition is used for pressure at all boundaries.

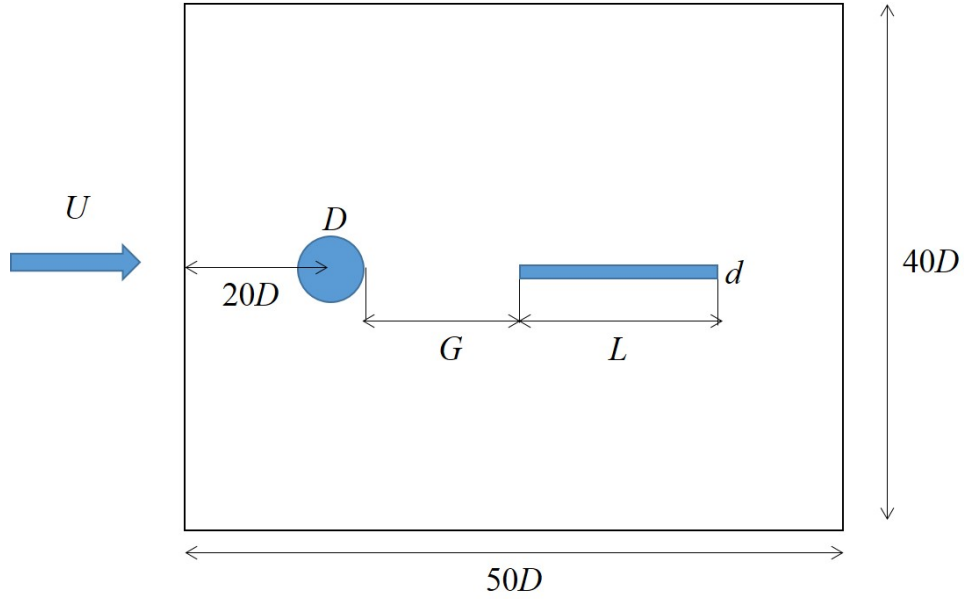


Figure 10.2: Computational domain for VIV of a circular cylinder.

10.3 Results and Discussion

We study the effects of various parameters such as gap G , Length L and thickness d of the plate on the energy transferred to it from the fluid. We also investigate the effect of these parameters on drag coefficient for the cylinder. we have also considered the effect of boundary condition at the constrained end of the plate.

10.3.1 Effect on Drag

In this section we examine the possibility of drag reduction on the cylinder due to the deformable plate. In past, drag reduction was achieved by keeping a rigid plate in the wake of the cylinder. [Kwon and Choi \(1996\)](#) studied the effect of length of the splitter plate attached to the cylinder. They found a critical length for the splitter plate beyond which the vortex shedding suppresses completely. For $Re = 100$ the critical length was reported to be $3D$. Following their work, we take a flexible plate of length $3D$ and study its effects on drag reduction. We take two types of boundary conditions for the upstream end of the plate: a) hinged and b) fixed which alters the natural frequency of the plate. Young's modulus of the plate is kept at $E = 1.4 \times 10^3$ and density ratio is taken as 10. Two values of plate thickness, $d = 0.1$ and 0.2 are considered which affects the values of plate natural frequency and bending stiffness. Natural frequency of four different plates are listed in table [10.2](#). Note that the natural frequency in fluid is going to be smaller because of the added-mass effect.

The variations of drag coefficient for the cylinder and Strouhal number with gap G is

Table 10.2: Natural frequencies of hinged and fixed plates.

Boundary condition	thickness d	Natural frequency f
Fixed	0.10	0.13
Fixed	0.20	0.27
Hinged	0.10	0.09
Hinged	0.20	0.19

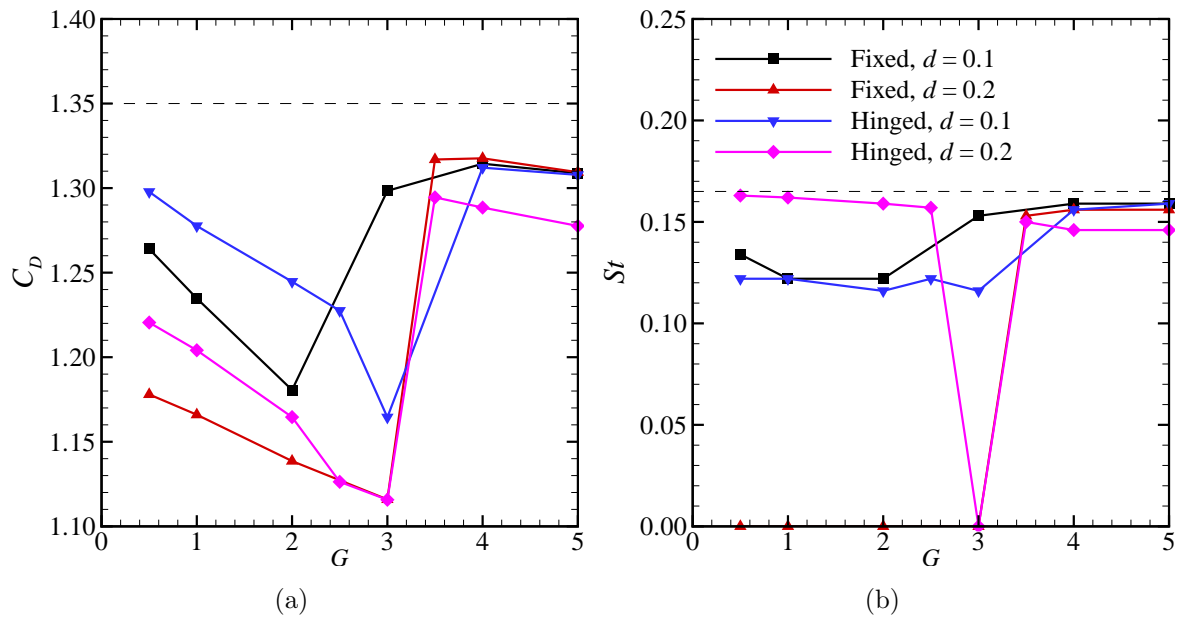


Figure 10.3: (a) Drag coefficient and (b) Strouhal number versus G for four cases mentioned in table 10.2.

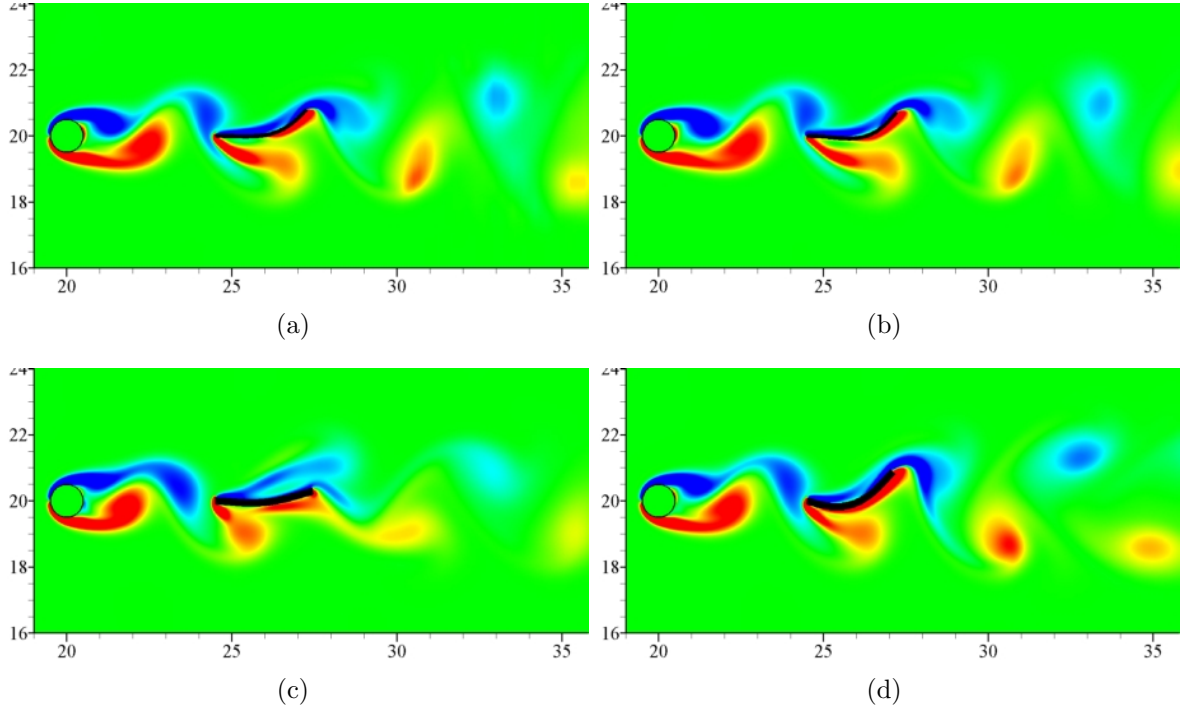


Figure 10.4: Vorticity contours for (a) a fixed plate with $d = 0.1$, (b) a hinged plate with $d = 0.1$, (c) a fixed plate with $d = 0.2$ and (d) a hinged plate with $d = 0.2$ at $G = 4$.

shown in fig. 10.3. The dotted horizontal lines show corresponding values for an isolated cylinder in free stream flow at $\text{Re} = 100$. The largest drag reduction (17%) is achieved by both fixed and hinged plates of thickness $d = 0.2$ at $G = 3$. As seen in fig. 10.3b, the fixed plate with $d = 0.2$ does not oscillate till $G > 3$ and suppresses the vortex shedding completely. On the other hand, the rigid plate with $d = 0.1$ is seen to oscillate for all values of G because of its low bending stiffness. On the other hand, hinged plates are seen to oscillate for all values of G except in the case of $d = 0.2$ and $G = 3$. These trends of C_D for flexible plates are similar to the one observed for rigid splitter plate case.

The vorticity contours for four cases are shown in fig. 10.4 for $G = 4$. The 2S vortex shedding mode is observed in all the cases. For this large value of G , we observe that the vortex shedding takes place behind the cylinder and then the shedded vortex interact with the plate.

10.3.2 Energy transfer

In this section we discuss the energy transfer to the plates and its dependence on the gap G . The y -amplitude of oscillation of the downstream end of the plates are plotted in fig. 10.5a. The fixed plate with $d = 0.2$ does not deform for $G \leq 3$ but the thinner fixed plate is seen to deform at all values of G . The maximum displacement for the thinner fixed plate occurs at $G = 3$ and its displacement is always larger than the $d = 0.2$ plate. For

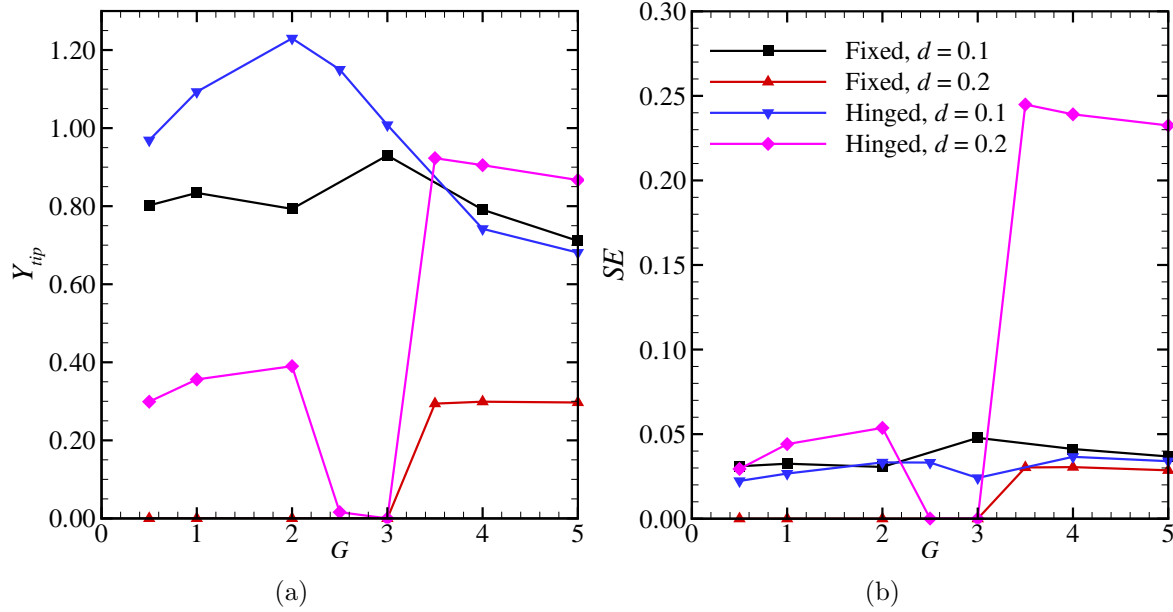


Figure 10.5: (a) Y-coordinate of right end and (b) Strain energy of the plate versus G for four cases.

the hinged plates, the maximum displacement occurs at $G = 2$ and 3 for $d = 0.1$ and 0.2 , respectively. There is a local maxima for thicker hinged plate at $G = 2$.

The average strain energies (SE) over a cycle of oscillation of the plates are plotted in fig. 10.5b. Surprisingly, the largest strain energy is produced in the thick hinged plate at $G = 3$ when it has the largest displacement. Rest three configurations give nearly same amount of SE which is around 5 times less than that of thick hinged plate. Notice that the maximum strain energy in all cases corresponds to the maximum displacement. The kinetic (KE) and total (TE) energies for these cases are plotted in fig. 10.6. Again, the maxima of KE coincides with the maximum tip displacements. We notice the similarities between the tip displacement and SE, KE and TE plots. This indicates that one can correlate the Total energy extraction with the tip displacement of a plate but the same is not true when comparing two different types of plate. Although the thin hinged plate shows a larger displacement but more energy is extracted by the thicker hinged plate. The higher energy level for the thick plate can be a due to the lock-in situation since the natural frequency of this plate is close to the vortex shedding frequency.

10.4 Closure

A flexible plate kept behind a cylinder at various locations was studied from energy extraction point of view. Different plate properties and fixing arrangement were considered. An Immersed Boundary method based FSI solver was used to simulate the flow and structure

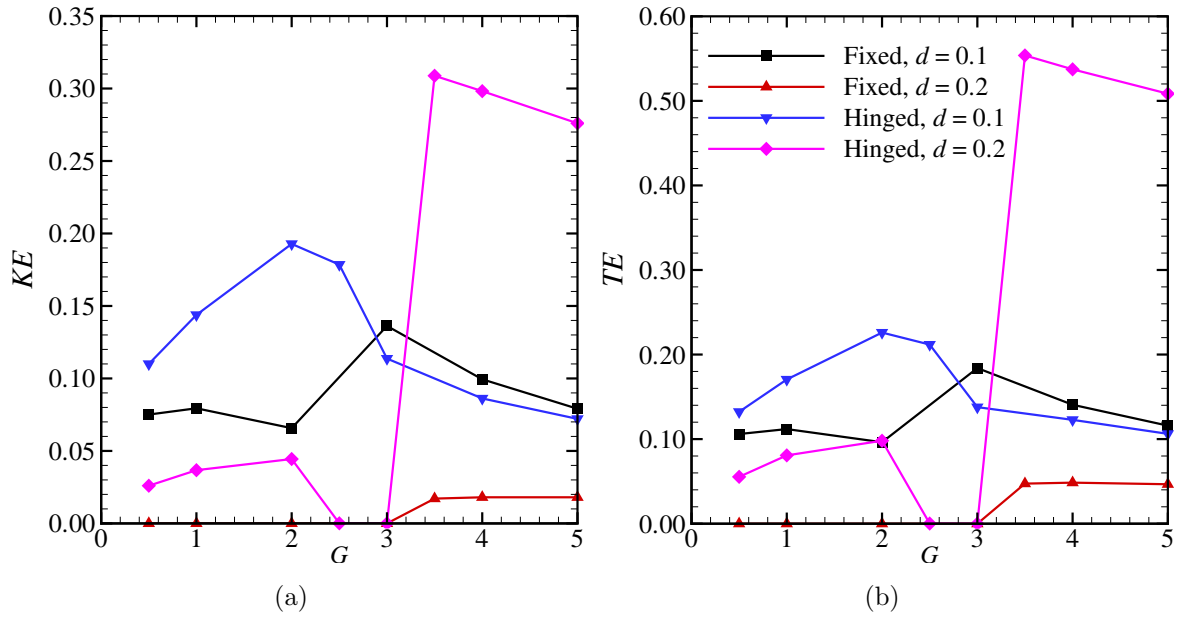


Figure 10.6: (a) Kinetic and (b) total energy of the plate versus G for four cases.

dynamics. The energy extraction is quantified in terms of the strain and kinetic energy of the plate. Results show that there is an optimal distance at which maximum power is transferred to the plate from the fluid. We also see a optimal distance for the maximum drag reduction. The maximum drag reduction is obtained when the plate completely attenuates the vortex shedding.

Chapter 11

Conclusions and future work

11.1 Conclusions

The fluid-solid interaction (FSI) was investigated by numerical and experimental methods for their applications in renewable energy and heat transfer enhancement. Two classes of FSI problems were investigated: Vortex-induced vibration (VIV) and flow induced deformation (FID). The numerical solutions of VIV problems were obtained using a spectral-element based solver because of its computational efficiency for these class of problem. All the VIV problems were solved in the reference frame of the body and therefore, no re-meshing was required. Since the mesh is fixed, the linear system arising from the discretization of the governing equations has a constant coefficient matrix which can be inverted before starting the solution process. This and the fact that the spectral-element methods need less number of elements due to their higher order spatial accuracy, makes the solution of VIV problems very efficient. Experiments were also performed on VIV of a circular cylinder in a water channel for high Re situation.

A sharp interface immersed boundary (IB) method based solver was used for simulating flow FID of flexible structures. Since the IB method uses a fixed Cartesian grid, the problem of re-meshing for continuously changing domain, due to the deforming bodies, is overcome easily. Notice that the coefficient matrix of the linear system arising from the discretization of the governing equations will no longer be constant since the position of the immersed boundaries (IB) keep changing with time. The IB solver was modified and validated for the heat transfer applications. The FSI solver was also made more efficient by accelerating the implicit coupling between the fluid and structure solver using Aitken's method. Before this modification, one had to choose a suitable under-relaxation parameter of the implicit coupling for each new FSI problem. The under-relaxation parameter had to be small enough so that the implicit coupling does not diverge and big enough to reduce the number of iterations required for reaching a desired residual level. The Aitken's method introduces a variable under-relaxation parameter based on previous

implicit coupling iterations. With this modification, one can now start any FSI problem with a sufficiently small under-relaxation parameter and then the Aitken's method can determine its optimal values for faster convergence. A speed-up of 2.7 was obtained for the benchmark cylinder-flag problem.

VIV of a circular cylinder was studied numerically to investigate power extraction at low Reynolds number. In literature, power extraction process had been modelled as a constant damping system. For the first time, a more realistic electromagnetic power transducer was used. It was modelled as a spatially variable damping system. It was found that the average extracted power was independent to the nature of damping, i.e. both constant and electromagnetic damping systems produced same amount of average power. On the other hand, temporal variation of power and displacement of the cylinder were very different. A maximum of 13% efficiency was obtained at $Re = 150$. The VIV of the circular cylinder was also examined in a water channel facility at Monash University for high Re situation. A eddy current based damping mechanism was introduced into the existing VIV setup. The effects of damping on VIV of circular cylinder were investigated. The extracted power was found to increase with Reynolds number due to a increase in vibration amplitude.

Since the extracted power was observed to increase with Re VIV of plate with low aspect ratio was also investigated. In literature, researches had only focused on high aspect ratio cases such as square cylinders. Therefore, this study also reported the VIV of thin plates for the first time. Various response branches and lock-in region were identified. The thin plates showed a larger vibrations response as compared to circular cylinder and therefore showed much better power extraction capability. Interestingly, an optimal aspect ration of 0.2 was found to extract maximum average power. The maximum extraction efficiency was close to 19% at $Re = 150$.

For the first time, flow induced deformation of a flexible plate was demonstrated as a passive means of enhancing heat transfer in a laminar channel flow. Numerical simulations of a flexible plate, fixed to the lee side of a circular cylinder, kept in a laminar channel flow were performed using IB method. The IB solver was also validated for heat transfer problems. The flexible structure was found to outperform other methods for enhancing heat transfer such as use of a circular cylinder. The effects of Reynolds number and plate material property were also investigated. Another problem of a flexible plate attached to the channel wall was also investigated. In this problem, a pulsating flow was applied at the channel entrance so that the flexible plate would undergo periodic vibrations. The effects of channel height and plate rigidity were the main focus. It was found that there is an optimal channel height for obtaining maximum heat transfer enactment using flexible plate. The rigid plate was found to perform better in small channel height case.

The FSI benchmark cylinder-flag problem was revisited for its application in flow

energy extraction. This time the flexible plate was kept at some distance behind the cylinder and the whole structure was kept in a free-stream of fluid. The energy extraction was evaluated in terms of the strain and total (kinetic plus strain) energy of the flexible plate. An optimal gap between the cylinder and plate was found to produce maximum energy of the plate. The plate energy was found to be a very strong function of the plate natural frequency due to the ‘lock-in’ phenomenon. The plate energy was maximum when its natural frequency was close to the vortex shedding frequency. Since the strain energy is a function of plate deformation and bending stiffness, it was found that an optimal bending stiffness exists for maximum strain energy.

11.2 Future work

Few research problems encountered during the course of this research, some of which can be a PhD topic in itself and some I look forward to investigate in future, are listed here.

- Optimization of the shape of the bluff body for maximizing its flow energy extraction capability. Two body shapes were investigated in the present work. One can look at other geometries such as aerofoil. On the other hand, evolutionary algorithms are promising in optimization problems whose solution can be tricky. One can couple the flow solver with an evolutionary algorithm to drive optimal bluff body shapes for power extraction although that can become a PhD topic itself.
- Development of a spectral-element based immersed boundary solver. The immersed boundary method is very attractive because of the re-meshing issue faced with body-fitted meshes. Also, meshing a complex geometry can be very time consuming. The Cartesian mesh, on the other hand, is not efficient. Usually, refinement is required only near the immersed boundaries but a Cartesian mesh ends up wasting a lot of nodes in far field regions and also produces cells with very large side ratios. An immersed boundary spectral-element based solver with variable element order can easily overcome these shortcomings.
- Producing a better initial guess of the position and velocity of the immersed boundary for implicit coupling. The Aitken’s method has accelerated the FSI convergence but still there is scope for further improvement. A better initial guess will surely result in even faster solution of FSI problems. One way could be to use the history of immersed boundary to predict its location at the next time step.
- Development of an immersed boundary solver for two-fluid/two-medium problems. The diffused interface immersed boundary method is only first order accurate near immersed boundary. A second order accurate solution is possible since the two

fluids can be solved individually using the sharp interface IB method and then their solution can be coupled at the interface using a similar implicit coupling approach. This was tried for simple heat conduction problems with multiple materials. Some problems did not converge when the IB method could not satisfy the compatibility condition for Poisson's equation. The level set method was implemented into the existing IB solver for solving free-surface flows but a similar compatibility condition halted the progress. This problem can be a separate PhD topic on its own.

Publications under the candidature

Journal publications

1. Soti, A. K., Thompson, M. C., Sheridan, J., and Bhardwaj, R. (2017). Harnessing electrical power from vortex-induced vibration of a circular cylinder. *J. Fluids Struct.*, 70:360-373.
2. Kundu, A., Soti, A. K., Thompson, M. C., Bhardwaj, R. (2017). The Response of an Elastic Splitter Plate Attached to a Cylinder to Laminar Pulsatile Flow. *J. Fluids Struct.* 68:423-443.
3. Joshi, R. U., Soti, A. K., and Bhardwaj, R. (2015). Numerical study of heat transfer enhancement by deformable twin plates in laminar heated channel flow. *Comput. Therm. Sci.: Int. J.*, 7(5-6).
4. Soti, A. K., Bhardwaj, R., and Sheridan, J. (2015). Flow-induced deformation of a flexible thin structure as manifestation of heat transfer enhancement. *Int. J. Heat Mass Transfer*, 84:1070-1081.
5. Soti, A. K., Zhao, J., Thompson, M. C., Sheridan, J., and Bhardwaj, R. Damping effects on vortex-induced vibration of a circular cylinder and implications for power extraction. *J. Fluids Struct.* (Reviewers comments received).
6. Soti, A. K., Zhao, J., Thompson, M. C., Sheridan, J., and Bhardwaj, R. (under preparation). Vortex-induced vibration of a thin plate. *J. Fluid Mech.*
7. Soti, A. K., Thompson, M. C., Sheridan, J., and Bhardwaj, R. (under preparation). Vortex-induced vibration of thin plates: effect of aspect ratio and power extraction. *J. Fluid Mech.*
8. Soti, A. K., Thompson, M. C., Sheridan, J., and Bhardwaj, R. (under preparation). Convective Heat Transfer Augmentation by a Fin-like Thin, Elastic Plate in a Laminar Channel Flow. *Int. J. Heat Mass Transfer*.

9. Soti, A. K., Thompson, M. C., Sheridan, J., and Bhardwaj, R. (under preparation). Energy transfer to a flexible plate kept behind a circular cylinder. *J. Fluids Struct.*

Conferences

1. Soti, A. K., Thompson, M. C., Sheridan, J., Bhardwaj, R., Electrical Power Generation from Vortex-Induced Vibrations of a Circular Cylinder, *20th Australasian Fluid Mechanics Conference*, Australasian Fluid Mechanics Society, 2016.
2. Kundu, A., Soti, A. K., Joshi, R. U., Bhardwaj, R., Effect of Pulsatile flow on flow-induced deformation of an elastic plate, *5th International and 41st National Conference on Fluid Mechanics and Fluid Power (NCFMFP)*, December 12-14, 2014, IIT Kanpur, India.
3. Soti, A. K. and Bhardwaj, R., Numerical study of heat transfer enhancement via flow-induced deformation of elastic plate in channel flow, *Proceedings of the 22nd National and 11th International ISHMT-ASME Heat and Mass Transfer Conference*, December 28-31, 2013, IIT Kharagpur, India.
4. Soti, A. K. and Bhardwaj, R., Numerical Investigation of Fluid structure interaction of elastic Leaflet in Incompressible Channel Flow, *Proceedings of 40th National Conference on Fluid Mechanics and Fluid Power (NCFMFP)*, December 12-14, 2013, NIT Hamirpur, Himachal Pradesh, India.
5. Bailoor, S., Soti, A. K., Bhardwaj, R., Nguyen, T.D., Effectiveness of Eye armor during blast loading, *Proceedings of the ASME 2013 Summer Bioengineering Conference*, Sunriver, Oregon, WA, June 26-29, 2013.
6. Bhardwaj, R. and Soti, A. K., A Strongly Coupled Fluid-Structure Interaction Solver with Application to Cardiovascular Flows, *Proceedings of 39th National Conference on Fluid Mechanics and Fluid Power (NCFMFP)*, Surat, India 2012.

Bibliography

- Akaydin, H., Elvin, N., and Andreopoulos, Y. (2010). Wake of a cylinder: a paradigm for energy harvesting with piezoelectric materials. *Experiments in Fluids*, 49(1):291–304.
- Akcabay, D. T. and Young, Y. L. (2012). Hydroelastic response and energy harvesting potential of flexible piezoelectric beams in viscous flow. *Physics of Fluids (1994-present)*, 24(5):054106.
- Akhilesh, R., Narasimhan, A., and Balaji, C. (2005). Method to improve geometry for heat transfer enhancement in pcm composite heat sinks. *Int. J. Heat Mass Transfer*, 48(13):2759–2770.
- Ali, S., Habchi, C., Menanteau, S., Lemenand, T., and Harion, J.-L. (2015). Heat transfer and mixing enhancement by free elastic flaps oscillation. *Int. J. Heat Mass Transfer*, 58:250–264.
- Baaijens, F. P. (2001). A fictitious domain/mortar element method for fluid-structure interaction. *Int. J. Numer. Methods Fluids*, 35(7):743–761.
- Bao, Y., Huang, C., Zhou, D., Tu, J., and Han, Z. (2012). Two-degree-of-freedom flow-induced vibrations on isolated and tandem cylinders with varying natural frequency ratios. *J. Fluids & Struct.*, 35:50–75.
- Bao, Y. and Tao, J. (2013). The passive control of wake flow behind a circular cylinder by parallel dual plates. *Journal of Fluids and Structures*, 37:201–219.
- Barrero-Gil, A., Pindado, S., and Avila, S. (2012). Extracting energy from vortex-induced vibrations: a parametric study. *Applied mathematical modelling*, 36(7):3153–3160.
- Barrero-Gil, A., Sanz-Andres, A., and Roura, M. (2009). Transverse galloping at low reynolds numbers. *J. Fluids & Struct.*, 25(7):1236–1242.
- Bearman, P. (2011). Circular cylinder wakes and vortex-induced vibrations. *J. Fluids & Struct.*, 27(5):648–658.

- Beeby, S. P., Tudor, M. J., and White, N. (2006). Energy harvesting vibration sources for microsystems applications. *Meas. Sci. Technol.*, 17(12):175–195.
- Bejan, A. (2004). *Convection Heat Transfer*. Wiley.
- Bergles, A. E. (2011). Recent developments in enhanced heat transfer. *Heat Mass Transfer*, 47(8):1001.
- Bernitsas, M. M., Raghavan, K., Ben-Simon, Y., and Garcia, E. (2008). Vivace (vortex induced vibration aquatic clean energy): A new concept in generation of clean and renewable energy from fluid flow. *Journal of offshore mechanics and Arctic engineering*, 130(4):041101.
- Beskok, A., Raisee, M., Celik, B., Yagiz, B., and Cheraghi, M. (2012). Heat transfer enhancement in a straight channel via a rotationally oscillating adiabatic cylinder. *Int. J. Therm. Sci.*, 58:61–69.
- Bhardwaj, R. and Mittal, R. (2012). Benchmarking a coupled immersed-boundary-finite-element solver for large-scale flow-induced deformation. *AIAA*, 50(7):1638–1642.
- Bhardwaj, R., Ziegler, K., Seo, J. H., Ramesh, K., and Nguyen, T. D. (2014). A computational model of blast loading on the human eye. *Biomech. Model. Mechanobiol.*, 13(1):123–140.
- Biswas, G. and Chattopadhyay, H. (1992). Heat transfer in a channel with built-in wing-type vortex generators. *Int. J. Heat Mass Transfer*, 35(4):803–814.
- Canuto, C., Hussaini, M. Y., Quarteroni, A., and Zang, T. A. (2006). *Spectral Methods - Fundamentals in Single Domains*. Springer Verlag.
- Carli, D., Brunelli, D., Bertozzi, D., and Benini, L. (2010). A high-efficiency wind-flow energy harvester using micro turbine. In *Power electronics electrical drives automation and motion (SPEEDAM), 2010 international symposium on*, pages 778–783. IEEE.
- Celik, B., Raisee, M., and Beskok, A. (2010). Heat transfer enhancement in a slot channel via a transversely oscillating adiabatic circular cylinder. *Int. J. Heat Mass Transfer*, 53(4):626–634.
- Chandratilleke, T., Jagannatha, D., and Narayanaswamy, R. (2010). Heat transfer enhancement in microchannels with cross-flow synthetic jets. *Int. J. Thermal Sci.*, 49(3):504–513.
- Chatterjee, D. and Mondal, B. (2012). Forced convection heat transfer from an equilateral triangular cylinder at low reynolds numbers. *Heat Mass Transfer*, 48(9):1575–1587.

- Chorin, A. J. (1968a). Numerical solution of the Navier–Stokes equations. *Math. Comp.*, pages 745–762.
- Chorin, A. J. (1968b). Numerical solution of the navier-stokes equations. *Math. Comput.*, 22(104):745–762.
- Churchill, S. and Bernstein, M. (1977). A correlating equation for forced convection from gases and liquids to a circular cylinder in crossflow. *J. of Heat Transfer*, 99:300–306.
- Dai, H., Abdelkefi, A., Yang, Y., and Wang, L. (2016). Orientation of bluff body for designing efficient energy harvesters from vortex-induced vibrations. *Applied Physics Letters*, 108(5):053902.
- Degroote, J., Haelterman, R., Annerel, S., Bruggeman, P., and Vierendeels, J. (2010). Performance of partitioned procedures in fluid–structure interaction. *Comput. Struct.*, 88(7):446–457.
- Dey, S. and Chakraborty, D. (2009). Enhancement of convective cooling using oscillating fins. *Int. Commun. Heat Mass Transfer*, 36(5):508–512.
- Donoso, G., Ladera, C., and Martin, P. (2009). Magnet fall inside a conductive pipe: motion and the role of the pipe wall thickness. *Eur. J. Phys.*, 30(4):855.
- Donoso, G., Ladera, C., and Martin, P. (2010). Magnetically coupled magnet–spring oscillators. *European Journal of Physics*, 31(3):433.
- Dunne, T. and Rannacher, R. (2006). Adaptive finite element approximation of fluid–structure interaction based on an eulerian variational formulation. In *Fluid-structure interaction*, pages 110–145. Springer.
- Eckert, E. (1952). Distribution of heat-transfer coefficients around circular cylinders in crossflow at reynolds numbers from 20 to 500. *Trans. ASME*, 74:343–347.
- Fan, A., Deng, J., Guo, J., and Liu, W. (2011). A numerical study on thermo-hydraulic characteristics of turbulent flow in a circular tube fitted with conical strip inserts. *Appl. Therm. Eng.*, 31(14):2819–2828.
- Fan, A., Deng, J., Nakayama, A., and Liu, W. (2012). Parametric study on turbulent heat transfer and flow characteristics in a circular tube fitted with louvered strip inserts. *Int. J. Heat Mass Transfer*, 55(19):5205–5213.
- Favier, J., Revell, A., and Pinelli, A. (2014). A lattice boltzmann–immersed boundary method to simulate the fluid interaction with moving and slender flexible objects. *J. Comput. Phys.*, 261:145–161.

- Feng, C. (1968). The measurement of vortex induced effects in flow past stationary and oscillating circular and D-section cylinders. Master's thesis, University of British Columbia, Canada.
- Fiebig, M., Brockmeier, U., Mitra, N., and Gü termann, T. (1989). Structure of velocity and temperature fields in laminar channel flows with longitudinal vortex generators. *Numer. Heat Transfer*, 15(3):281–302.
- Fu, W.-S. and Tong, B.-H. (2002). Numerical investigation of heat transfer from a heated oscillating cylinder in a cross flow. *Int. J. Heat Mass Transfer*, 45(14):3033–3043.
- Fu, W.-S. and Yang, S.-J. (2001). A numerical study of effects of the swinging amplitude of fins on heat transfer characteristics in a flow. *Heat Mass Transfer*, 38(1):55–63.
- Fung, Y.-C. (1993). *Foundations of Solid Mechanics*. Springer-Verlag, New York.
- Gabbai, R. and Benaroya, H. (2005). An overview of modeling and experiments of vortex-induced vibration of circular cylinders. *J. Sound Vib.*, 282(3):575–616.
- Govardhan, R. and Williamson, C. (2000). Modes of vortex formation and frequency response of a freely vibrating cylinder. *Journal of Fluid Mechanics*, 420:85–130.
- Govardhan, R. and Williamson, C. (2006). Defining the modified griffin plotin vortex-induced vibration: revealing the effect of reynolds number using controlled damping. *J. Fluid Mech.*, 561:147–180.
- Griffin, O. (1980). Vortex-excited cross-flow vibrations of a single cylindrical tube. *J. of Pressure Vessel Technol.*, 102(2):158–166.
- Guo, Z. and Sung, H. J. (1997). Analysis of the nusselt number in pulsating pipe flow. *Int. J. Heat Mass Transfer*, 40(10):2486–2489.
- Hamann, H. F., Weger, A., Lacey, J. A., Hu, Z., Bose, P., Cohen, E., and Wakil, J. (2007). Hotspot-limited microprocessors: Direct temperature and power distribution measurements. *IEEE J. Solid-State Circuits*, 42(1):56–65.
- Heil, M., Hazel, A. L., and Boyle, J. (2008). Solvers for large-displacement fluid–structure interaction problems: segregated versus monolithic approaches. *Comput. Mech.*, 43(1):91–101.
- Hiravennavar, S., Tulapurkara, E., and Biswas, G. (2007). A note on the flow and heat transfer enhancement in a channel with built-in winglet pair. *Int. J. Heat Mass Transfer*, 28(2):299–305.

- Hobbs, W. B. and Hu, D. L. (2012). Tree-inspired piezoelectric energy harvesting. *Journal of Fluids and Structures*, 28:103–114.
- Hou, G., Wang, J., and Layton, A. (2012). Numerical methods for fluid-structure interaction: a review. *Commun. Comput. Phys.*, 12(02):337–377.
- Hover, F., Techet, A., and Triantafyllou, M. (1998). Forces on oscillating uniform and tapered cylinders in cross flow. *J. Fluid Mech.*, 363:97–114.
- Hwang, J.-Y., Yang, K.-S., and Sun, S.-H. (2003). Reduction of flow-induced forces on a circular cylinder using a detached splitter plate. *Physics of Fluids (1994-present)*, 15(8):2433–2436.
- Incropera, F. P. and De Witt, D. P. (2007). *Fundamentals of Heat and Mass Transfer*. John Wiley and sons Inc, Hoboken, NJ.
- Jauvtis, N. and Williamson, C. H. K. (2004). The effect of two degrees of freedom on vortex-induced vibration at low mass and damping. *J. Fluid Mech.*, 509:23–62.
- Joshi, R. U., Soti, A. K., and Bhardwaj, R. (2015). Numerical study of heat transfer enhancement by deformable twin plates in laminar heated channel flow. *Comput. Therm. Sci.: Int. J.*, 7(5-6).
- Karniadakis, G. E., Israeli, M., and Orszag, S. A. (1991). High-order splitting methods of the incompressible Navier-Stokes equations. *J. Comput. Phys.*, 97:414–443.
- Karniadakis, G. E. and Sherwin, S. J. (1999). *Spectral/hp Element Methods for CFD*. Oxford University Press, England, 1st edition.
- Khalak, A. and Williamson, C. (1999). Motions, forces and mode transitions in vortex-induced vibrations at low mass-damping. *J. Fluids & Struct.*, 13(7-8):813–851.
- Khalak, A. and Williamson, C. H. K. (1997). Fluid forces and dynamics of a hydroelastic structure with very low mass and damping. *J. Fluids & Struct.*, 11(8):973–982.
- Khanafer, K., Alamiri, A., and Pop, I. (2010). Fluid–structure interaction analysis of flow and heat transfer characteristics around a flexible microcantilever in a fluidic cell. *Int. J. Heat Mass Transfer*, 53(9):1646–1653.
- Klamo, J. T. (2009). The application of controlled variable magnetic eddy current damping to the study of vortex-induced vibrations. *Exp. Fluids*, 47(2):357–367.
- Knopper, L. D., Ollson, C. A., et al. (2011). *Health effects and wind turbines: A review of the literature*. BioMed Central.

- Knudsen, J. G. and Katz, D. L. (1958). Fluid dynamics and heat transfer.
- Kwon, K. and Choi, H. (1996). Control of laminar vortex shedding behind a circular cylinder using splitter plates. *Physics of Fluids (1994-present)*, 8(2):479–486.
- Lee, H., Hourigan, K., and Thompson, M. (2013). Vortex-induced vibration of a neutrally buoyant tethered sphere. *Journal of Fluid Mechanics*, 719:97–128.
- Lee, J. and Bernitsas, M. (2011). High-damping, high-reynolds viv tests for energy harnessing using the vivace converter. *Ocean Engineering*, 38(16):1697–1712.
- Lee, J. and You, D. (2013). Study of vortex-shedding-induced vibration of a flexible splitter plate behind a cylinder. *Phys. Fluids*, 25(11):110811.
- Leontini, J. S., Lo Jacono, D., and Thompson, M. C. (2011). A numerical study of an inline oscillating cylinder in a free stream. *Journal of Fluid Mechanics*, 688:551–568.
- Leontini, J. S., Lo Jacono, D., and Thompson, M. C. (2013). Wake states and frequency selection of a streamwise oscillating cylinder. *Journal of Fluid Mechanics*, 730:162–192.
- Leontini, J. S., Stewart, B. E., Thompson, M. C., and Hourigan, K. (2006a). Wake state and energy transitions of an oscillating cylinder at low Reynolds number. *Physics of Fluids*, 18(6):067101 (9 pages).
- Leontini, J. S., Thompson, M. C., and Hourigan, K. (2006b). The beginning of branching behaviour of vortex-induced vibration during two-dimensional flow. *Journal of Fluids and Structures*, 22(6):857–864.
- Leontini, J. S., Thompson, M. C., and Hourigan, K. (2007). Three-dimensional transition in the wake of a transversely oscillating cylinder. *Journal of Fluid Mechanics*, 577:79–104.
- Lo Jacono, D., Leontini, J. S., Thompson, M. C., and Sheridan, J. (2010). Modification of three-dimensional transition in the wake of a rotationally oscillating cylinder. *Journal of Fluid Mechanics*, 643:349–362.
- Luo, H., Dai, H., de Sousa, P. J. F., and Yin, B. (2012). On the numerical oscillation of the direct-forcing immersed-boundary method for moving boundaries. *Comput. Fluids*, 56:61–76.
- MATLAB. PDE toolbox release 2009a, the MathWorks, inc., Natick, MA, <http://www.mathworks.in/products/pde/>.

- Mehmood, A., Abdelkefi, A., Hajj, M., Nayfeh, A., Akhtar, I., and Nuhait, A. (2013). Piezoelectric energy harvesting from vortex-induced vibrations of circular cylinder. *Journal of Sound and Vibration*, 332(19):4656–4667.
- Michelin, S. and Doaré, O. (2013). Energy harvesting efficiency of piezoelectric flags in axial flows. *Journal of Fluid Mechanics*, 714:489–504.
- Mills, Z. G., Aziz, B., and Alexeev, A. (2012). Beating synthetic cilia enhance heat transport in microfluidic channels. *Soft Matter*, 8(45):11508–11513.
- Mittal, R., Dong, H., Bozkurttas, M., Najjar, F., Vargas, A., and von Loebbecke, A. (2008). A versatile sharp interface immersed boundary method for incompressible flows with complex boundaries. *J. Comput. Phys.*, 227(10):4825–4852.
- Mittal, R. and Iaccarino, G. (2005). Immersed boundary methods. *Annu. Rev. Fluid Mech.*, 37:239–261.
- Mittal, R., Zheng, X., Bhardwaj, R., Seo, J. H., Xue, Q., and Bielamowicz, S. (2011). Toward a simulation-based tool for the treatment of vocal fold paralysis. *Frontiers physiol.*, 2:19.
- Mittal, S. and Singh, S. (2005). Vortex-induced vibrations at subcritical re. *J. Fluid Mech.*, 534:185–194.
- Morse, T., Govardhan, R., and Williamson, C. (2008). The effect of end conditions on the vortex-induced vibration of cylinders. *J. Fluids & Struct.*, 24(8):1227–1239.
- Nemes, A., Zhao, J., Jacono, D. L., and Sheridan, J. (2012). The interaction between flow-induced vibration mechanisms of a square cylinder with varying angles of attack. *J. Fluid Mech.*, 710:102–130.
- Nishi, Y., Ueno, Y., Nishio, M., Quadrante, L. A. R., and Kokubun, K. (2014). Power extraction using flow-induced vibration of a circular cylinder placed near another fixed cylinder. *Journal of Sound and Vibration*, 333(10):2863–2880.
- Pan, D., Shao, X., Deng, J., and Yu, Z. (2014). Simulations of passive oscillation of a flexible plate in the wake of a cylinder by immersed boundary method. *European Journal of Mechanics-B/Fluids*, 46:17–27.
- Park, K.-H., Min, J. K., Kim, J.-K., Park, S.-H., and Ha, M. Y. (2013). A study on a flexible wing with up–down vibration in a pulsating flow of cooling air to improve heat transfer efficiency. *Heat Mass Transfer*, 49(10):1459–1470.

- Parkinson, G. and Smith, J. (1964). The square prism as an aeroelastic non-linear oscillator. *Q. J. Mech. Appl. Maths*, 17(2):225–239.
- Patnana, V. K., Bharti, R. P., and Chhabra, R. P. (2010). Two-dimensional unsteady forced convection heat transfer in power-law fluids from a cylinder. *Int. J. Heat Mass Transfer*, 53(19):4152–4167.
- Peskin, C. S. (1972). Flow patterns around heart valves: a numerical method. *J. Comput. Phys.*, 10(2):252–271.
- Peskin, C. S. (1977). Numerical analysis of blood flow in the heart. *J. Comput. Phys.*, 25(3):220–252.
- Peskin, C. S. (2002). The immersed boundary method. *Acta Numer.*, 11:479–517.
- Placzek, A., Sigrist, J.-F., and Hamdouni, A. (2009). Numerical simulation of an oscillating cylinder in a cross-flow at low reynolds number: Forced and free oscillations. *Computers & Fluids*, 38(1):80–100.
- Prasanth, T. and Mittal, S. (2008). Vortex-induced vibrations of a circular cylinder at low reynolds numbers. *J. Fluid Mech.*, 594:463–491.
- Press, W. H., Flannery, B. P., Teukolsky, S. A., Vetterling, W. T., and Kramer, P. B. (1992). *Numerical recipes: The Art of Scientific Computing*. Cambridge University Press, New York.
- Ramgadia, A. G. and Saha, A. K. (2012). Fully developed flow and heat transfer characteristics in a wavy passage: Effect of amplitude of waviness and reynolds number. *Int. J. Heat Mass Transfer*, 55(9):2494–2509.
- Sareen, A., Zhao, J., Lo Jacono, D., Sheridan, J., Hourigan, K., and Thompson, M. C. (2017). Vortex induced vibration of a rotating sphere. *Under consideration for publication in Journal of Fluid Mechanics*.
- Sarpkaya, T. (1978). Fluid forces on oscillating cylinders. *ASCE J. Waterway Port Coast. Ocean Div.*, 104:275–290.
- Sarpkaya, T. (2004). A critical review of the intrinsic nature of vortex-induced vibrations. *J. Fluids & Struct.*, 19(4):389–447.
- Schieber, D. (1975). Optimal dimensions of rectangular electromagnet for braking purposes. *IEEE Transactions on magnetics*, 11(3):948–952.
- Sen, S. and Mittal, S. (2015). Effect of mass ratio on free vibrations of a square cylinder at low reynolds numbers. *J. Fluids & Struct.*, 54:661–678.

- Seo, J. H. and Mittal, R. (2011a). A high-order immersed boundary method for acoustic wave scattering and low-mach number flow-induced sound in complex geometries. *Journal of computational physics*, 230(4):1000–1019.
- Seo, J. H. and Mittal, R. (2011b). A sharp-interface immersed boundary method with improved mass conservation and reduced spurious pressure oscillations. *J. Comput. Phys.*, 230(19):7347–7363.
- Shelley, M. J. and Zhang, J. (2011). Flapping and bending bodies interacting with fluid flows. *Annu. Rev. Fluid Mech.*, 43:449–465.
- Shi, J., Hu, J., Schafer, S. R., and Chen, C.-L. C. (2014). Numerical study of heat transfer enhancement of channel via vortex-induced vibration. *Appl. Therm. Eng.*, 70(1):838–845.
- Shoole, K. and Mittal, R. (2014). Computational study of flow-induced vibration of a reed in a channel and effect on convective heat transfer. *Phys. Fluids*, 26(12):127103.
- Soti, A. K. and Bhardwaj, R. (2013). Numerical study of heat transfer enhancement via flow-induced deformation of elastic plate in channel flow. In *Proceedings of the 22nd National and 11th International ISHMT-ASME Heat and Mass Transfer Conference*.
- Soti, A. K., Bhardwaj, R., and Sheridan, J. (2015). Flow-induced deformation of a flexible thin structure as manifestation of heat transfer enhancement. *Int. J. Heat Mass Transfer*, 84:1070–1081.
- Soti, A. K., Thompson, M. C., Sheridan, J., and Bhardwaj, R. (2017). Harnessing electrical power from vortex-induced vibration of a circular cylinder. *J. Fluids & Struct.*, 70:360–373.
- Tahoe. An open source c++ finite element solver, which was developed at Sandia National Labs, CA. <http://sourceforge.net/projects/tahoe/>.
- Tang, L., Païdoussis, M. P., and Jiang, J. (2009). Cantilevered flexible plates in axial flow: energy transfer and the concept of flutter-mill. *Journal of Sound and Vibration*, 326(1):263–276.
- Thompson, M. C., Hourigan, K., Cheung, A., and Leweke, T. (2006). Hydrodynamics of a particle impact on a wall. *Applied Mathematical Modelling*, 30(11):1356–1369.
- Tian, F.-B., Dai, H., Luo, H., Doyle, J. F., and Rousseau, B. (2014). Fluid–structure interaction involving large deformations: 3d simulations and applications to biological systems. *J. Comput. Phys.*, 258:451–469.

- Tornberg, A.-K. and Engquist, B. (2004). Numerical approximations of singular source terms in differential equations. *J. Comput. Phys.*, 200(2):462–488.
- Turek, S. and Hron, J. (2006). Proposal for numerical benchmarking of fluid-structure interaction between an elastic object and laminar incompressible flow. In *Fluid-structure interaction*, pages 371–385. Springer.
- Valencia, A. (1995). Heat transfer enhancement in a channel with a built-in rectangular cylinder. *Heat Mass Transfer*, 30(6):423–427.
- Van Kan, J. (1986). A second-order accurate pressure-correction scheme for viscous incompressible flow. *SIAM J. Sci. Statist. Comput.*, 7(3):870–891.
- Vermeer, L., Sørensen, J. N., and Crespo, A. (2003). Wind turbine wake aerodynamics. *Progress in aerospace sciences*, 39(6):467–510.
- Vigmostad, S. C., Udaykumar, H. S., Lu, J., and Chandran, K. B. (2010). Fluid–structure interaction methods in biological flows with special emphasis on heart valve dynamics. *Int. J. Numer. Methods Biomed. Eng.*, 26(3-4):435–470.
- Wang, C.-C. and Chen, C.-K. (2002). Forced convection in a wavy-wall channel. *Int. J. Heat Mass Transfer*, 45(12):2587–2595.
- Wang, D.-A., Chiu, C.-Y., and Pham, H.-T. (2012). Electromagnetic energy harvesting from vibrations induced by kármán vortex street. *Mechatronics*, 22(6):746–756.
- Webb, R. L. and Kim, N.-H. (2005). *Principles of Enhanced Heat Transfer*. Taylor & Francis, New York.
- Weissenböck, N. M., Weiss, C. M., Schwammer, H. M., and Kratochvil, H. (2010). Thermal windows on the body surface of african elephants (*loxodonta africana*) studied by infrared thermography. *J. Therm. Biol.*, 35(4):182–188.
- Williamson, C. and Govardhan, R. (2004). Vortex-induced vibrations. *Annu. Rev. Fluid Mech.*, 36:413–455.
- Williamson, C. H. K. and Roshko, A. (1988). Vortex formation in the wake of an oscillating cylinder. *J. Fluids & Struct.*, 2(4):355–381.
- Wong, K. W. L., Zhao, J., Lo Jacono, D., Thompson, M. C., and Sheridan, J. (2017). Experimental investigation of flow-induced vibration of a rotating circular cylinder. *Under consideration for publication in Journal of Fluid Mechanics*.
- Xiao, Q. and Zhu, Q. (2014). A review on flow energy harvesters based on flapping foils. *Journal of fluids and structures*, 46:174–191.

- Yang, S.-J. (2003). Numerical study of heat transfer enhancement in a channel flow using an oscillating vortex generator. *Heat Mass Transfer*, 39(3):257–265.
- Ye, T., Mittal, R., Udaykumar, H., and Shyy, W. (1999a). An accurate cartesian grid method for viscous incompressible flows with complex immersed boundaries. *J. Comput. Phys.*, 156(2):209–240.
- Ye, T., Mittal, R., Udaykumar, H., and Shyy, W. (1999b). A cartesian grid method for viscous incompressible flows with complex immersed boundaries. In *14th Computational Fluid Dynamics Conference*, page 3312.
- Yoon, D.-H., Yang, K.-S., and Choi, C.-B. (2009). Heat transfer enhancement in channel flow using an inclined square cylinder. *J. Heat Transfer*, 131(7):074503.
- Yu, Y., Simon, T., and Cui, T. (2013). A parametric study of heat transfer in an air-cooled heat sink enhanced by actuated plates. *Int. J. Heat Mass Transfer*, 64:792–801.
- Zang, Y., Street, R. L., and Koseff, J. R. (1994). A non-staggered grid, fractional step method for time-dependent incompressible navier-stokes equations in curvilinear coordinates. *J. Comput. Phys.*, 114(1):18–33.
- Zhao, J., Leontini, J. S., Jacono, D. L., and Sheridan, J. (2014a). Fluid–structure interaction of a square cylinder at different angles of attack. *J. Fluids & Struct.*, 747:688–721.
- Zhao, J., Leontini, J. S., Lo Jacono, D., and Sheridan, J. (2014b). Chaotic vortex induced vibrations. *Phys. Fluids*, 26(12):121702.
- Zhao, J., Leontini, J. S., Lo Jacono, D., and Sheridan, J. (2014c). Fluid–structure interaction of a square cylinder at different angles of attack. *J. Fluid Mech.*, 747:688–721.
- Zhao, M. (2015). Flow-induced vibrations of square and rectangular cylinders at low reynolds number. *Fluid Dyn. Res.*, 47(2):025502.
- Zhao, M., Cheng, L., and Zhou, T. (2013). Numerical simulation of vortex-induced vibration of a square cylinder at a low reynolds number. *Phys. Fluids*, 25(2):023603.
- Zheng, X., Xue, Q., Mittal, R., and Beilamowicz, S. (2010). A coupled sharp-interface immersed boundary-finite-element method for flow-structure interaction with application to human phonation. *J. Biomech. Eng.*, 132(11):111003.
- Žukauskas, A. (1972). Heat transfer from tubes in crossflow. *Advances in heat transfer*, 8:93–160.